Analysis of recommended localized human exposure limits for radiofrequency fields in the frequency range, 6 GHz to 300 GHz

Authors

G Gajda, J Paradis, E Lemay, M Zhuk, G. McGarr, P Bellier, J McNamee

Consumer & Clinical Radiation Protection Bureau, Health Canada
775 Brookfield Road, Ottawa, ON, Canada, K1A 1C1

Approval

Martel, Narine Digitally signed by Martel, Narine
Date: 2021.02.01 12:40:25 -05'00'

Narine Martel, Director CCRPB

EXECUTIVE SUMMARY

To help protect the health and safety of Canadians from radiofrequency electromagnetic fields (RFEMF), Health Canada continuously monitors and assesses the scientific literature, conducts research and provides recommendations on safe human exposure levels in its publication Safety Code 6 - *Limits of Human Exposure to Radiofrequency Electromagnetic Energy in the Frequency Range from 3 kHz to 300 GHz*. The Code is periodically revised to reflect new knowledge in the scientific literature. The current version of Safety Code 6 includes exposure limits applicable to radiofrequency fields above 6 GHz which are based on whole body exposure scenario (ie. the RF field exposes the entire body). Since forthcoming technologies will begin to utilize frequencies above 6 GHz for devices which may be held close to the body, Health Canada deemed it necessary to provide recommendations for localized human exposure limits in this frequency range. Localized human exposure limits are based on exposure scenarios where the radiofrequency source is held close to the body and only a small area is exposed. Two international organizations, the International Commission on Non-Ionizing Radiation Protection (ICNIRP) and the Institute of Electrical and Electronics Engineers (IEEE) have recently published guidelines with new localized exposure limits in the 6 to 300 GHz frequency range (ICNIRP, 2020; IEEE, 2019). Health Canada has evaluated these new safety limits as part of its process to develop an official Health Canada recommendation for localized exposures in this frequency range.

In this report, the scientific basis supporting the ICNIRP (2020) guidelines for localized exposure limits in the 6 to 300 GHz frequency range have been summarized to provide context. The guidelines include new quantities for evaluating localized exposures to frequencies above 6 GHz for basic restrictions, namely the absorbed power density applicable to continuous exposures and absorbed energy density for pulsed exposures. ICNIRP (2020) also specifies a new spatial averaging area of 4 cm^2 for localized exposures above 6 GHz and an additional spatial averaging area of 1 cm^2 for frequencies above 30 GHz to account for smaller beam diameters that can be produced by devices emitting higher frequencies to address emerging technologies. The IEEE (2019) standard introduced a new quantity, the “epithelial power density”, for evaluation against dosimetric reference levels (akin to basic restrictions) and specifies the same spatial averaging scheme as ICNIRP (2020) and the same localized exposure limits for continuous exposures. However, the IEEE (2019) standard specifies different requirements than ICNIRP (2020) for pulsed exposures. IEEE (2019) specifies a peak power density limit for a reference window of 100 ms and a fluence limit (energy density limit per pulse) that is applicable above 30 GHz. The latter appears to be excessively restrictive and has been rejected because it does not behave according to the accepted Pennes heat exchange model. Aside from the fluence limit, ICNIRP (2020) provides safety limits that are more conservative than IEEE (2019). Therefore, the detailed analysis in this report focuses on the ICNIRP (2020) guidelines.

Based upon a systematic review approach, Health Canada has identified two adverse health outcomes that are relevant to localized exposure to millimeter-wave RFEMF. These are a heat-pain sensation, which demonstrates an absolute threshold temperature of ~42-43 ^oC, and tissue damage which can occur when skin or cornea are heated and maintained at temperatures at or above 43 ^oC. Other adverse health effects

are theoretically possible if localized exposure to millimeter wave RFEMF heats the core body temperature by more than 1 °C, however such effects are unlikely to occur from millimeter-wave RFEMF without first exceeding the heat-pain sensation temperature threshold in Type 1 tissues as most energy will be deposited in superficial tissues due to the limited penetration depth of millimeter wave RFEMF. Therefore, Health Canada is in agreement with ICNIRP that the primary adverse health effects to be avoided as millimeter-wave RFEMF intensity increases are a heat-pain sensation and thermal tissue damage to Type 1 tissues (e.g. skin/cornea).

Based upon an analysis of millimeter-wave RFEMF studies and complementary research (e.g. hyperthermia and non-RFEMF tissue heating) on temperature thresholds for the occurrence of heat-pain sensation and thermal tissue damage (Section 4.2), Health Canada concludes that the ICNIRP 'Operational Adverse Health Effect Threshold' (OAHET) of 41 °C is a conservative estimate of the minimum temperature where adverse health effects (heat-pain sensation or thermal tissue damage) may occur. Based upon an analysis of complementary evidence of resting (normothermal) Type 1 tissue temperatures, Health Canada considers the normothermal temperature of skin and cornea to range between 33-36 °C. Therefore, Health Canada considers the ICNIRP OAHET value of 41 °C to be at least 5 °C above normothermal Type 1 tissue temperatures. With the application of 10-fold and 2-fold safety margins in the ICNIRP (2020) localized exposure limits for the uncontrolled and controlled environments, ICNIRP intends to limit the maximum localized tissue temperature increase at the maximum allowable exposure limits to 0.5 °C and 2.5 °C, respectively. These temperature increases are well below the threshold for all known adverse health effects from millimeter-wave RFEMF. It is important to note that modest temperature increases (1-2 °C) to Type 1 tissues are routinely experienced in our daily lives from a variety heat sources. Small deviations from the targeted tissue temperature elevations under unique/exotic exposures scenarios will still maintain Type 1 tissue temperature elevations below the threshold for adverse effects.

To assess if the recommended localized exposure limits above 6 GHz specified in ICNIRP (2020) result in localized tissue temperatures below the OAHET and respect the intended conservativeness (i.e. provide the intended reduction factors), numerical modelling was employed using an approximate Gaussian beam model. This model can be used to estimate temperature increases in human tissues by: i) determining the wave propagation across multiple tissue layers by assuming the incident EMF is a plane wave, from which the absorbed EMF is calculated as a function of depth in the tissue, ii) accounting for the effect of a finite beam diameter by multiplying the depth distribution of absorbed EMF by a Gaussian transverse distribution, and iii) solving the Pennes Bio Heat Transfer Equation in all layers by considering the effect of heat diffusion, heat transport by blood perfusion and convective heat loss at the air-skin boundary. As a representation of human superficial tissues: a 3-layer model composed of skin, subcutaneous adipose tissue (SAT) and muscle was considered for frequencies between 6 GHz and 60 GHz and a 4-layer model composed of epidermis, dermis, SAT, and muscle was considered for frequencies above 60 GHz up to 200 GHz. The numerical model allowed an evaluation of the impact of time- and spatial-averaging, for both continuous and pulsed exposures.

Through application of the numerical model, temperature estimates indicating a temperature increase higher than ICNIRP's OAHET were considered non-conservative, otherwise the limits were considered

conservative. This analysis was done for a variety of beam diameters, frequencies and exposure durations. The results demonstrated that ICNIRP's localized exposure limits in the 6 to 300 GHz frequency range were not sufficiently conservative for all exposure scenarios. The level of non-conservatism was especially pronounced for short pulse exposures at frequencies of 30 GHz or higher and with small beam diameters. Under certain worst-case exposure conditions, tissue temperature elevations were estimated to be as much as 3.57 times higher than ICNIRP's target temperature increases of 0.5 ^{o}C and 2.5 ^{o}C for uncontrolled and controlled environments, respectively, translating to a localized tissue temperature increase of ~1.79 ^{o}C for uncontrolled environment exposures and ~8.93^{o}C for controlled environment exposures. In addition, for the controlled environment (e.g. occupational), temperatures could exceed the OAHET of 41 ^{o}C and could possibly lead to a heat-pain sensation or tissue damage. It is important to note that the worst-case exposure conditions that resulted in these temperatures elevations can be addressed by modifications to the ICNIRP (2020) localized exposure limits.

Based upon the observed non conservatism in the ICNIRP (2020) localized exposure limits under certain exposure scenarios, Health Canada recommends the application of the ICNIRP (2020) localized exposure limits with some modifications. These modifications are intended to help ensure that localized tissue temperature increases from exposures to RFEMF are kept well below the scientifically established thresholds of health effects. If Health Canada's recommended modifications to the ICNIRP localized exposure limits are applied, the associated maximum (worst-case) tissue temperature increases would be ~0.77 ^{o}C for uncontrolled environment and ~3.85 ^{o}C for controlled environment, which are below the threshold of all established adverse health effects for localized exposure to radiofrequency fields in the 6 to 300 GHz frequency range.

Recommendations:

For localized exposure to RFEMF at frequencies in the 6 to 300 GHz frequency range, Health Canada recommends using the:

- ICNIRP (2020) Guidelines, **Table 2**, for occupational and general public exposure scenarios, in the frequency range >6 GHz to 300 GHz, applicable to CW or quasi-CW exposures,) where:
    - **Note 5** of Table 2 is modified to: "Local S_{ab} is to be averaged over a square 4-cm^2 surface area of the body. Above 30 GHz, an additional constraint is imposed, such ***that the spatial peak*** exposure is restricted to two times that of the 4-cm^2 restriction."
- ICNIRP (2020) Guidelines, **Table 3**, for occupational and general public exposure scenarios, in the frequency range >6 GHz to 300 GHz, applicable to any pulse, group of pulses, or subgroup of pulses in a train, where:
    - **Note 4** of Table 3 is modified to: "Local U_{ab} is to be averaged over a square 4-cm^2 surface area of the body. Above 30 GHz, an additional constraint is imposed, such ***that the spatial peak*** exposure is restricted to 72[0.025+0.975(t/360)$^{0.5}$] kJ/m^2 for occupational and 14.4[0.025+0.975(t/360)$^{0.5}$] kJ/m^2 for general public exposure."
    - **Note 5** of Table3 is modified to: "Exposure from any pulse, group of pulses, or subgroup of pulses in a train, as well as from the summation of exposures (including non-pulsed EMF), delivered in t s, ***where t is the sum of all periods in which there is non-zero***

exposure, must not exceed these levels." (i.e. all pulses are glued together within any 6-minute reference period).

- ICNIRP (2020) Guidelines, **Table 6**, for occupational and general public exposure scenarios, in the frequency range >6 GHz to 300 GHz, applicable to CW or quasi-CW exposures, where:
  - **Note 7** of Table 6 is modified to: "For frequencies of >30 GHz to 300 GHz, ***the spatial peak*** exposure must not exceed twice that of the square 4-cm^2 restrictions."
- ICNIRP (2020) Guidelines, **Table 7**, for occupational and general public exposure scenarios, in the frequency range >6 GHz to 300 GHz, applicable to any pulse, group of pulses, or subgroup of pulses in a train, where:
  - **Note 2** of Table 7 is modified to: "f_M is frequency in MHz; f_G is frequency in GHz; t is time interval in seconds, such that exposure from any pulse, group of pulses, or subgroup of pulses in a train, as well as from the summation of exposures (including non-pulsed EMF), delivered in t seconds, ***where t is the sum of all periods in which there is non-zero exposure***, must not exceed these levels." (i.e. all pulses are glued together within any 6-minute reference period).
  - **Note 7** of Table 5 is modified to: "For frequencies of >30GHz to 300 GHz, ***the spatial peak*** exposure must not exceed $275/f_G^{0.177}$ X $0.72[0.025+0.975(t/360)^{0.5}]$ kJ/m^2 for occupational and $55/f_G^{0.177}$ X $0.72[0.025+0.975(t/360)^{0.5}]$ kJ/m^2 for general public exposure."

The recommendations above can be reproduced in a simplified table format where the information in ICNIRP pertaining to frequencies below 6 GHz can be removed because it was not subject to this evaluation:

Basic restrictions for local electromagnetic field exposure above 6 GHz up to 300 GHz

Exposure Scenario	Exposure Duration (t)	Local Absorbed Energy Density [kJ/m^2]	Local Absorbed Power Density [W/m^2]
Controlled Environment	0 sec < t < 360 sec	36 $[0.05+0.95(t/360)^{0.5}]$	NA
	t ≥ 6 min	NA	100
Uncontrolled Environment	0 sec < t < 360 sec	7.2 $[0.05+0.95(t/360)^{0.5}]$	NA
	t ≥ 6 min	NA	20

Notes:

1. "NA" signifies "not applicable" and does not need to be taken into account when determining compliance.
2. "t" is time in seconds, and restrictions must be satisfied for all values of t between >0 s and <360 s, regardless of the temporal characteristics of the exposure itself.
3. Local absorbed power density exposures are to be averaged over 6 min.
4. Local absorbed power density is to be averaged over a square 4-cm^2 surface area of the body. Above 30 GHz, an additional constraint is imposed, such that the spatial peak exposure is restricted to two times that of the 4-cm^2 restriction.
5. Local absorbed energy density is to be averaged over a square 4-cm^2 surface area of the body. Above 30 GHz, an additional constraint is imposed, such that the spatial peak exposure is restricted to $72[0.025+0.975(t/360)^{0.5}]$ kJ/m^2 for controlled environment and $14.4[0.025+0.975(t/360)^{0.5}]$ kJ/m^2 for uncontrolled environment exposure.

6. Exposure from any pulse, group of pulses, or subgroup of pulses in a train, as well as from the summation of exposures (including non-pulsed EMF), delivered in t s, where t is the sum of all periods in which there is non-zero exposure, must not exceed these levels.

Reference Levels for local electromagnetic field exposure above 6 GHz up to 300 GHz

Exposure Scenario	Exposure Duration (t)	Local Incident Energy Density [kJ/m^2]	Local Incident Power Density [W/m^2]
Controlled Environment	0 sec < t < 360 sec	$275/f_G^{0.177}$ X $0.36[0.05+0.95(t/360)^{0.5}]$	NA
	t ≥ 6 min	NA	$275/f_G^{0.177}$
Uncontrolled Environment	0 sec < t < 360 sec	$55/f_G^{0.177}$ X $0.36[0.05+0.95(t/360)^{0.5}]$	NA
	t ≥ 6 min	NA	$55/f_G^{0.177}$

Notes:

1. "NA" signifies "not applicable" and does not need to be taken into account when determining compliance.
2. f_G is frequency in GHz; t is time interval in seconds, such that exposure from any pulse, group of pulses, or subgroup of pulses in a train, as well as from the summation of exposures (including non-pulsed EMF), delivered in t seconds, where t is the sum of all periods in which there is non-zero exposure, must not exceed these levels.
3. Incident energy density is to be calculated over time t,
4. Incident power density is to be averaged over 6 min.
5. For frequencies of >6 GHz to 300 GHz: (a) within the far-field zone, compliance is demonstrated if the incident power density, averaged over a square 4-cm^2 projected body surface space, does not exceed the above reference level values; plane-wave equivalent incident power density may be substituted for the incident power density; (b) within the radiative near-field zone, compliance is demonstrated if the incident power density, averaged over a square 4-cm^2 projected body surface space, does not exceed the above reference level values; and (c) within the reactive near-field zone reference levels cannot be used to determine compliance, and so basic restrictions must be assessed.
6. For frequencies of >6 GHz to 300GHz: (a) within the far-field or radiative near-field zone, compliance is demonstrated if the incident energy density, averaged over a square 4-cm^2 projected body surface space, does not exceed the above reference level values; (b) within the reactive near-field zone, reference levels cannot be used to determine compliance, and so basic restrictions must be assessed.
7. For frequencies of >30 GHz to 300 GHz, the spatial peak incident power density exposure must not exceed twice that of the square 4-cm^2 restrictions
8. For frequencies of >30GHz to 300 GHz, the spatial peak incident energy density exposure must not exceed $275/f_G^{0.177}$ X $0.72[0.025+0.975(t/360)^{0.5}]$ kJ/m^2 for controlled environment and $55/f_G^{0.177}$ X $0.72[0.025+0.975(t/360)^{0.5}]$ kJ/m^2 for uncontrolled environment exposure.

Table of Contents

1.0 Overview of Safety Code 6 limits 10
1.1 References 11
2.0 Purpose 12
3.0 International guidelines and standard for limiting exposures to radiofrequency electromagnetic radiation 12
3.1 ICNIRP (2020) High Frequency Guidelines (100 kHz to 300 GHz) 12
3.1.1 Whole-body exposure limits basis 14
3.1.2 Localized exposure limits basis 14
3.1.3 Localized exposure limits at frequencies above 6 GHz 15
3.1.4 Assumptions underpinning the ICNIRP limits 16
3.2 IEEE (2019) Standard for Safety Levels with Respect to Human Exposure 17
3.2.1 Whole-body exposure limits basis 18
3.2.2 Localized exposure limits basis above 6 GHz 18
3.2.3 Assumptions underpinning the IEEE limits 20
3.3 Comparison between the new ICNIRP Guidelines and IEEE Standard 21
3.4 Relevance of proposed international Guidelines and Standards 23
3.5 References 25
4.0 Assessment of potential adverse health effects from exposure to RFEMF at frequencies from 6 to 300 GHz 27
4.1 Identification of adverse health effects from RFEMF in the 6 to 300 GHz frequency range 27
4.2 Threshold of temperature-related adverse health effects 86
4.3 Normothermal temperature range of skin and cornea (Type 1 tissues) 92
4.4 Thermoregulatory processes 93
4.5 Conclusions 96
4.6 References 98
5.0 Evaluation of ICNIRP (2020) Local Exposure Basic Restrictions (> 6 GHz) Using the Approximate Gaussian Beam Model 115
LIST OF ACRONYMS 115
TABLE OF SYMBOLS 116
5.1 Background: OAHET basic restrictions for 6 -300 GHz 117
5.2 Definitions 117

5.3 Assessing ICNIRP's Basic Restrictions 119
5.3.1 Exposure & thermal model: 119
5.3.2 Tissue Models 120
5.3.3 Wide beams versus narrow beams 121
5.3.4 Evaluation Metrics 122
5.3.5 Spatial averaging considerations 123
5.4 Single isolated pulse and CW 124
5.4.1 Wide beams 124
5.4.2 Narrow beams 128
5.4.3 General results, single isolated pulse & CW 130
5.4.4 Isolated groups of pulses 134
5.5 Continuous Pulse Trains 137
5.5.1 TR response to pulsed exposure 137
5.5.4 General results – Continuous pulse trains 140
5.5.4 Discussion – continuously pulsed exposures and ICNIRP OBRs 146
5.6 References 147
6.0 Recommendations regarding the use of the localized exposure limits for frequencies > 6 GHz . 148
Appendix A - Validity of PBHTE in computational dosimetry 153
A.1 Review of the ICNIRP Thermal Workshop 153
A.2 Scientific Evaluation of the Pennes BHTE and Computational Dosimetry 154
A.3 References 158
Appendix B - Validity of the approximate unpolarised Gaussian model as an RF exposure model in computational dosimetry 162
B.1 Assessment of the transmitted PD as function of Grazing Angle and polarization state 163
B.2 Variation of transmitted power density coefficient in human skin 168
B.3 References 172
Appendix C - Minimum beam diameter as function of frequency for typical telecommunication antennas 173
C.1 Estimated beam diameters of typical single elements 174
C.1.1 Half-wave dipole 174
C.1.2 Rectangular aperture antenna element 175
C.2 Theoretical beam diameters for antenna arrays 177

C.2.1 Antenna arrays and super-directivity 177
C.2.2 The far zone 178
C.2.3 Uniform linear array 182
C.2.4 The broadside array 186
C.2.5 The end-fire array 189
C.2.6 Comparison between broadside and end-fire configuration 191
C.3 Simulated power density beam diameters and associated SAR spot sizes in near-field 194
C.3.1 Vertical broadside array of 3 dipoles 194
C.3.2 Single dipole versus small array of 3 dipoles (end-fire configuration) 200
C.3.3 SAR spot sizes versus power density beam widths for a single dipole 202
C.4 Conclusion 206
C.5 References 206
Appendix D.1 - Finite difference solution of the dynamic BHTE 209
D.1.1 Coordinate system & assumptions: 209
D.1.2 1D BHTE 209
D.1.3 3D BHTE 211
Appendix D.2 - Solutions of the BHTE for very short exposure durations 212
Appendix D.3 – Continuous pulse trains in the steady state 214
D.3.1 Conditions for maximum peak TR in the steady state 214
D.3.2 Maximum peak TR in the context of the 360 s reference period 215
Appendix D.4 - Spatial distribution of temperature-rise for extremely narrow beams 220
Appendix D.5 - Spatial averaging power and energy densities: 221
Appendix D.6 - Sasaki tissue parameter data base 222
D.6.1 Dielectric properties 222
D.6.2 Thermal/physical properties: 222
Appendix D.7 - Test of ICNIRP (2020) Table3 - Note 5 interpretation 223
D.7.1 2-pulse group 223
D.7.2 3-pulse group 226
D.7.3 N-pulse group 227
D.7.4 Discussion: Test of ICNIRP (2020) Table 3 - Note 5 229
D.7.5 Conclusion 230
Appendix E – List of excluded papers from scientific literature analysis in section 4.0 231

1.0 Overview of Safety Code 6 limits

Health Canada's mandate regarding human exposure to radiofrequency electromagnetic energy from wireless devices is to carry out research into possible health effects, monitor the scientific literature related to such effects, and develop exposure guidelines. The current version of these exposure guidelines is specified in a document entitled: Limits of Human Exposure to Radiofrequency Electromagnetic Energy in the Frequency Range from 3 kHz to 300 GHz - Safety Code 6 (2015)[1]. The exposure limits in Safety Code 6 are based on a review of published scientific studies, including both internal and external authoritative reviews of the scientific literature, as well as Health Canada's own research. The Code is periodically revised to reflect new knowledge in the scientific literature. The current version of Safety Code 6 reflects the scientific literature published up to August 2014. Since the publication of Safety Code 6 in 2015, Health Canada scientists have continued to review and assess emerging science and do not consider that the scientific literature published since 2014 necessitates changes to the exposure limits in the existing version of Safety Code 6.

Safety Code 6 specifies exposure limits in terms of *Basic Restrictions* and *Reference Levels*, at frequencies ranging from 3 kHz to 300 GHz. *Basic Restrictions* are maximum allowable internal electrical quantities in the body, arising from exposure to incident external fields, that prevent the occurrence of all established adverse health effects. *Reference Levels* are more easily measured or calculated quantities (i.e. externally applied electric field strength, magnetic field strength and power density or resulting body current), that when respected, ensures compliance with the underlying basic restrictions in Safety Code 6.

At frequencies below 10 MHz, intense radiofrequency EMF exposure can cause peripheral nerve stimulation (PNS). **At frequencies from 100 kHz to 300 GHz**, intense radiofrequency EMF exposure can cause excessive tissue heating. The limits found in Safety Code 6 (2015) are set below the thresholds for the occurrence of these adverse health effects with additional safety margins applied.

At frequencies between 100 kHz and 6 GHz, Safety Code 6 specifies specific absorption rate (SAR)-based *Basic Restrictions* to prevent the occurrence of established adverse effects in humans related to tissue heating. The threshold for thermal effects from whole body radiofrequency field exposure in humans is based on observations of adverse effects in animal studies (e.g. slowing response, stoppage of performing tasks (D'Andrea, 2007)) at a whole-body average (WBA) SAR of approximately 4 W/kg, which results in a core body temperature rise of approximately 1^{o}C. Studies performed on human volunteers have shown that the human body is equipped with adequate response mechanisms (e.g. sweating, increased blood flow) to dissipate heat from RF exposures (Adair 2003, Walters 2000, 2004, Nelson 2003) at much higher levels. WBA SAR exposure at levels up to 5 W/kg (Adair and Berglungd (1986), Adair (2001), Taberski (2014), Brockow (2007), or even as high as 6 to 8 W/kg (Hirata 2008, Nelson 2013) are required to cause a 1^{o}C body core temperature rise in the human body. Howeverto be conservative, the WBA SAR assumed to

[1]https://www.canada.ca/content/dam/hc-sc/migration/hc-sc/ewh-semt/alt_formats/pdf/consult/_2014/safety_code_6-code_securite_6/final-finale-eng.pdf

represent a 1°C core body temperature increase in humans in Safety Code 6 was set at 4 W/kg. Through the application of a 50-fold safety margin, the WBA SAR *Basic Restriction* in Safety Code 6 has been established at 0.08 W/kg. The peak spatially averaged SAR (pk-SAR) limit in Health Canada's Safety Code 6 is 1.6 W/kg (averaged over 1 g of tissue for the head, neck and trunk) and is intended to prevent an excessive temperature increase in small volumes of tissue at the site of exposure.

At frequencies above 6 GHz, power density is used (as opposed to SAR) because the RFEMF is mainly absorbed in the superficial tissues (e.g. skin) given that the penetration depth is shallow for higher frequencies. Through the application of a 50-fold safety margin, the whole-body average power density *limits* in Safety Code 6 for frequencies above 6 GHz have been established at 10 W/m^2 up to 150 GHz and then progressively increase up to 20 W/m^2 at 300 GHz.

The current version of Safety Code 6 (2015) does not specify *Basic Restrictions* or *Reference Level* limits for localized exposure to radiofrequency fields at frequencies above 6 GHz since this was not an expected exposure scenario at the time of its revision. The **application of a whole-body average power density limit for localized exposure** above 6 GHz would lead to an unnecessarily restrictive limit because localized exposures can i) tolerate higher temperature increases because skin heating is not as severe as the entire human body being heated (which could lead to heat stress) and ii) smaller exposed areas can shed heat faster than if the entire body was heated (blood perfusion and heat diffusion to other surrounding areas). Since localized exposures are expected from emerging wireless devices that will utilize frequencies above 6 GHz, Health Canada has undertaken a review of the scientific literature, assessed recently published international guidelines and standards and conducted numerical modelling to develop science-base advice regarding recommended human exposure limits for localized exposure to radiofrequency fields at frequencies from 6 to 300 GHz.

1.1 References

Adair ER, Berglund LG. 1986. On the thermoregulatory consequences of NMR imaging. Magn Reson Imaging 4:321–333.

Adair ER, Mylacraine KS, Cobb BL. Partial-body exposure of human volunteers to 2450MHz pulsed or CW fields provokes similar thermoregulatory responses. Bioelectromagnetics 22:246-259; 2001.

Adair ER, Mylacraine KS, Allen SJ. Thermophysiological consequences of whole body resonant RF exposure (100 MHz) in human volunteers. Bioelectromagnetics 24: 489-501; 2003.

Brockow T, Wagner A, Franke A, Offenbächer M, Resch KL. A randomized controlled trial on the effectiveness of mild water-filtered near infrared whole-body hyperthermia as an adjunct to a standard multimodal rehabilitation in the treatment of fibromyalgia. Clin J Pain 23:67-75; 2007.

D'Andrea JA, Ziriax JM, Adair ER. Radio frequency electromagnetic fields: mild hyperthermia and safety standards. Prog Brain Res. 2007; 162:107-135. doi:10.1016/S0079-6123(06)62007-4

Hirata A, Asano T, Fujiwara O. FDTD analysis of body-core temperature elevation in children and adults for whole-body exposure. Phys Med Biol 53:5223-5238; 2008.

Nelson DA, Walters TJ, Ryan KL, Emerton KB, Hurt WD, Ziriax JM, Johnson LR, Mason PA. Interspecies extrapolation of skin heating resulting from millimeter wave irradiation: modeling and experimental results. Health Phys. 84(5):608-615; 2003.DOI:10.1097/00004032-200305000-00006

Nelson DA, Curran AR, Nyberg HA, Marttila EA, Mason PA, Ziriax JM. High-resolution simulations of the thermophysiological effects of human exposure to 100 MHz RF energy. Phys Med Biol 58:1947-1968; 2013.

Taberski K, Klose M, Grote K, El Ouardi A, Streckert J, Hansen VW, Lerchl A. Noninvasive assessment of metabolic effects of exposure to 900 MHz electromagnetic fields on Djungarian Hamsters (Phodopus sungorus). Radiat Res 181:617-622; 2014.

Walters, Effects of blood flow on the skin heating induced by millimeter wave irradiation in humans, Health Phys. 86(2):115-120;2004

Walters, Heating and pain sensation produced in human skin by millimeter waves: comparison to a simple thermal model, Health Phys. 78(3):259-267;2000

2.0 Purpose

The purpose of this report is to document Health Canada's review and analysis of: a) the scientific literature related to health effects of RFEMF at frequencies from 6 to 300 GHz, b) the scientific basis for recently published international guidelines and standard for localized exposure to radiofrequency electromagnetic radiation at frequencies above 6 GHz (i.e. ICNIRP, 2020; IEEE, 2019), and c) the results of numerical modelling conducted by Health Canada to assess temperature elevations associated with localized exposure to millimeter wave EMF at the maximum recommended exposure levels in the recently published international exposure guidelines. The analysis presented in this report supports Health Canada's recommendation regarding the appropriateness of applying the new localized exposure limits for frequencies above 6GHz contained within updated international guidelines.

3.0 International guidelines and standard for limiting exposures to radiofrequency electromagnetic radiation

3.1 ICNIRP (2020) High Frequency Guidelines (100 kHz to 300 GHz)

In March of 2020, ICNIRP published a revised version of their high frequency guidelines (100 kHz to 300 GHz) based upon an evaluation of the scientific literature (ICNIRP, 2020). The ICNIRP 2020 guidelines

replaced the previous version of the document, published in 1998. The new guidelines include 2 appendices: Appendix A - "Background Dosimetry" describes the rationale for the derivation of recommended exposure limits, spatial-averaging and time-averaging requirements, and Appendix B - "Health Risk Assessment Literature" where ICNIRP describes how it reviewed and assessed relevant scientific literature and identified the scientifically substantiated adverse health effects associated with exposures to RFEMF. ICNIRP has also published a review of complementary literature pertaining to thermal adverse health effects (Sienkiewicz et al., 2016). These documents inform the scientific basis where biological tissue damage thresholds and dosimetry assumptions are evaluated supporting the development of *Basic Restrictions* and *Reference Levels*. Since the goal of this report is to analyze the scientific validity and the level of health protection of updated international exposure limits for localized exposure at frequencies above 6 GHz, the scientific basis and assumptions made by ICNIRP have been summarized below.

The purpose of the new ICNIRP High Frequency RFEMF Guidelines (ICNIRP, 2020) is to provide exposure limits for protection of all people against substantiated adverse health effects from RFEMF exposures. Medical RF exposures as well as exposures as part of volunteers participating in research are considered outside the scope of the ICNIRP 2020 guidelines. ICNIRP has reviewed the scientific literature concerning health effects of RFEMF exposures on biological systems and identified health effects which they considered both harmful and scientifically substantiated. This means that ICNIRP considered the identified adverse health effects to be independently replicated, of sufficient scientific quality and consistent both within and across multiple streams of scientific evidence. In cases where there was insufficient scientific literature on the direct impact of RFEMF exposures on certain health outcomes, ICNIRP used indirect scientific evidence related to the primary effect of exposure (e.g. heating) to the same related health effect (e.g. pain). From this information, ICNIRP established "operational adverse health effect thresholds" (OAHET) which correspond to the lowest exposure level known to cause an adverse health effect.

The ICNIRP 2020 Guidelines state that, according to major international reviews of the scientific literature on RFEMF and health, conducted by the World Health Organization (WHO), the Scientific Committee on Emerging and Newly Identified Health Risks (SCENIHR), and additional scientific reviews by ICNIRP, the only adverse health effects which have been substantiated from RFEMF in the 3 kHz to 300 GHz frequency range are: i) nerve stimulation, ii) membrane permeabilization, and iii) tissue heating. Nerve stimulation can occur from exposure to RFEMF at frequencies below 10 MHz. Exposure limits to protect against nerve stimulation are already recommended in the ICNIRP Low Frequency Guidelines (ICNIRP, 2010). Membrane permeabilization has been demonstrated from intense ultra-short pulses in cell culture experiments, but this effect would only be possible if the exposures greatly exceed the existing exposure limits for nerve stimulation and thermal effects. Therefore, in the context of localized exposure limits at frequencies above 6 GHz, ICNIRP only considered thermal effects to be relevant for the derivation of exposure limits.

ICNIRP concluded that adverse thermal effects are related to absolute tissue or body temperature, but that it was not feasible to establish RFEMF exposure limits based upon absolute temperature because it is dependent on many environmental factors (external temperature, humidity, level of exertion, clothing, etc.) that are outside the scope of the guidelines. Therefore, ICNIRP's strategy was to derive limits based

upon limiting temperature elevation for conservative, yet realistic, exposure scenarios and considering normal initial human body temperatures. The derivation of *Reference Levels* encompasses highly unlikely, worst-case exposure conditions that predicts an associated *Basic Restriction* dose or dose rate limit (e.g. in the case of rapid temperature rise, adiabatic boundary conditions—rather than realistic exposures which considers the body's ability to remove RF-induced heat were applied).

3.1.1 Whole-body exposure limits basis

ICNIRP considered the normal human body core temperature in a state of normothermia (when no thermoregulatory systems are actively engaged to increase or decrease body temperature) to be typically 37^{o}C ± 1^{o}C. ICNIRP based its whole body average (WBA) exposure limits on adverse health effects related to cardiovascular load for thermoregulation (e.g. tissue heating) and a cascade of functional changes in tissues (e.g. brain, heart or kidneys) that result from such heating where the OAHET for WBA RFEMF exposures between 100 kHz to 300 GHz was set at a core body temperature increase of 1^{o}C. Recent theoretical and experimental research has shown that a WBA-specific absorption rate (SAR) of 6 W/Kg (between 100 kHz and 6 GHz) for over an hour in a 28^{o}C environment is required to increase core body temperature by 1^{o}C (a higher WBA-SAR would be required for children and small stature adults as they can dissipate heat more efficiently). As a conservative measure, ICNIRP selected 4 W/Kg as the SAR corresponding to the OAHET for frequencies between 100 kHz to 300 GHz.

ICNIRP chose a reduction factor of 10 to set the Basic Restriction limit (of 0.40 W/kg) for occupational exposures due to the large scientific uncertainty and variation of thermal baseline, thermoregulation capacity and core temperature health threshold across the population. ICNIRP chose a reduction factor of 50 to set the Basic Restriction limit (of 0.08 W/kg) for the general public because they cannot be expected to be aware of exposures and related risk mitigation measures.

3.1.2 Localized exposure limits basis

Inside the human body, some tissues are normally at a temperature that is slightly different than the average core body temperature. Therefore, ICNIRP defined two types of tissues based upon their location and normothermal temperature ranges. ICNIRP defined Type 1 tissues as the upper arm, forearm, hand, thigh, leg, foot, pinna, cornea, anterior parts of the eye, epidermal, dermal, fat, muscle and bone which typically range in temperature less than 33 ^{o}C to 36 ^{o}C depending on the specific tissue. ICNIRP defined Type 2 tissues as the head, remainder of the eye (less the cornea and anterior parts of the eye), abdomen, back, thorax, pelvis and testes (essentially excluding any tissue defined as Type 1) which typically range in temperature less than 38.5 ^{o}C depending on the specific tissue. ICNIRP adopted a 41 ^{o}C absolute temperature value as a conservative value to protect against tissue damage and thermal pain for partial body (localized) exposures. Based upon the normothermal temperatures of both tissue types, ICNIRP set the OAHET from RFEMF exposures at +5 ^{o}C and +2 ^{o}C above the normothermal temperatures for Type 1 and Type 2 tissues, respectively.

3.1.3 Localized exposure limits at frequencies above 6 GHz

Since the purpose of this document is to assess localized exposure limits above 6 GHz available in international guidelines and standard, this section summarizes ICNIRP's localized exposure limits above 6 GHz. The other exposure limits of the guidelines (ICNIRP, 2020) are not summarized in this report.

In the frequency range between 6 GHz and 300 GHz, tissue heating occurs mainly in the superficial tissues of the human body as approximately 86% of the power is absorbed within the first 8 mm of skin and sub-cutaneous tissue (Sasaki et al. 2017). Since RFEMF energy is deposited predominantly in superficial tissues, ICNIRP concluded that the use of a cubic pk-$SAR_{(10g)}$ limit was not an appropriate metric. Instead, ICNIRP established recommended exposure limits in terms of absorbed power density (S_{ab}) as it was more appropriate for the assessment of temperature elevation in superficial tissue in relation to RFEMF exposure. Furthermore, since RFEMF exposures in this frequency range are largely superficial, ICNIRP concluded that the 5^{o}C OAHET for Type 1 would also restrict temperature elevation for the OAHET of Type 2 tissues. ICNIRP chose an averaging area of 4 cm^2 to remain consistent with the dimensions of the pk-$SAR_{(10g)}$ based averaging volume for frequencies below 6 GHz. Since antennas above 30 GHz can emit radiation patterns with smaller beam diameters, ICNIRP specified an additional criterion of 1 cm^2 averaging area for RFEMF exposures in the 30 to 300 GHz frequency range and permitted exposures to be twice as high as the spatially-averaged limits for a 4 cm^2 area. ICNIRP concluded that the absorbed power density (S_{ab}) of 200 W/m^2 was required to exceed the OAHET of both Type 1 and Type 2 tissues for the head & torso and limbs (averaged over a 6-minute time interval). To account for rapid temperature rises from exposure durations shorter than 6 minutes, ICNIRP concluded that an absorbed energy density limit (U_{ab}) of $72x[0.05 + 0.95x(t/360)^{0.5}]$ kJ/m^2 averaged over 4 cm^2 and an additional absorbed energy density limit of $144x[0.025 + 0.975x(t/360)^{0.5}]$ kJ/m^2 averaged over of 1 cm^2 for frequencies equal to and greater than 30 GHz was required to exceed the OAHET of both tissue types from short exposure durations. ICNIRP applied a reduction factor of 2 to set the *Basic Restriction* limit for occupational exposures due to scientific uncertainty and variation of thermal baseline and thermoregulation capacity across the population. ICNIRP applied a reduction factor of 10 to set the *Basic Restriction* limit for the general public because they cannot be expected to be aware of exposures and related risk mitigation measures.

ICNIRP also derived *Reference Level* limits based on a combination of measurement studies and computational dosimetry approaches that aim to provide an equivalent level of protection as the *Basic Restrictions* based on "worst-case" exposure scenarios. The table 3.1 below summarize the recommended human exposure limits outlined in the ICNIRP guidelines (ICNIRP, 2020) for localized exposures above 6 GHz.

Table 3.1: Summary of ICNIRP basis and limits for localized exposures between 6 GHz and 300 GHz

OAHET	Exposure scenario	Reduction Factor	Time Base [sec]	Frequency Range [GHz]	Aver. Area	Basic Restrictions U_{ab} or S_{ab} [kJ/m^2] or specified	Reference Levels U_{inc} or S_{inc} [kJ/m^2] or specified
Both Type 1 (5°C) and Type 2 (2°C)	Controlled (work place)	2	< 360	6 to 300	4 cm^2	$36[0.05+0.95(t/360)^{0.5}]$	$275\ f_G^{-0.177}$ x $0.36[0.05+0.95(t/360)^{0.5}]$
				30 to 300	1cm^2	$72[0.025+0.975(t/360)^{0.5}]$	$275\ f_G^{-0.177}$ x $0.72[0.025+0.975(t/360)^{0.5}]$
			> 360	6 to 300	4 cm^2	100 W/m^2	$275\ f_G^{-0.177}$ W/m^2
				30 to 300	1cm^2	200 W/m^2	$550\ f_G^{-0.177}$ W/m^2
	General Public	10	< 360	6 to 300	4 cm^2	$7.2[0.05+0.95(t/360)^{0.5}]$	$55\ f_G^{-0.177}$ x $0.36[0.05+0.95(t/360)^{0.5}]$
				30 to 300	1cm^2	$14.4[0.025+0.975(t/360)^{0.5}]$	$55\ f_G^{-0.177}$ x $0.72[0.025+0.975(t/360)^{0.5}]$
			> 360	6 to 300	4 cm^2	20 W/m^2	$55\ f_G^{-0.177}$ W/m^2
				30 to 300	1cm^2	40 W/m^2	$110\ f_G^{-0.177}$ W/m^2

Notes:

* f_G is frequency expressed in GHz.
* t is time in seconds, and restrictions must be satisfied for all values of t between >0 and <360 s, regardless of the temporal characteristics of the exposure itself.
* Local S_{ab} (absorbed power density) and U_{ab} (absorbed energy density) are averaged over a 4-cm^2 (6-300 GHz) and additionally over 1-cm^2 (>30-300 GHz) square area, approximating the body surface.
* Within the far-field or radiative near-field zone, local S_{inc} (incident power density) and U_{inc} (incident energy density) are averaged over a 4-cm^2 (6-300 GHz) and additionally over 1-cm^2 (>30-300 GHz) square area.
* Within the reactive near-field zone, reference levels cannot be used to determine compliance, and so basic restrictions must be assessed.
* U_{ab} and U_{inc} is to be calculated over time t, as specified above.
* S_{ab} and S_{inc} exposures are to be averaged over 6 min.

3.1.4 Assumptions underpinning the ICNIRP limits

ICNIRP has developed recommended human exposure limits for localized exposure to RFEMF at frequencies from 6 to 300 GHz that are based upon several assumptions and conclusions. These include: a) the conclusion that thermal effects are the first adverse health effect to be manifested as RFEMF exposure levels increase in intensity; b) the choice of 41°C as an appropriate absolute threshold for the OAHET; c) the assumed normothermal range of Type 1 and Type 2 tissue temperatures and the conclusion that a 5°C and 2°C temperature increase in Type 1 and Type 2 tissues, respectively, from external heating correspond to the OAHET; d) the absorbed power density associated with causing a 5°C and 2°C temperature increase in Type 1 and Type 2 tissues, respectively; e) the choice of reduction factors for

occupational and non-occupational exposures; and f) the choice of time- and spatial-averaging conditions. Sections 4 and 5 of this report describe Health Canada's evaluation of the assumptions/conclusions made by ICNIRP when developing these limits in an effort to validate if these limits afford adequate protection against the established health effects of localized RFEMF exposure at frequencies above 6 GHz.

3.2 IEEE (2019) Standard for Safety Levels with Respect to Human Exposure

In February of 2019, IEEE published a revised version of their *Standard for Safety Levels with Respect to Human Exposure to Electric, Magnetic, and Electromagnetic Fields, 0 Hz to 300 GHz* (IEEE, 2019) based upon a comprehensive review of the scientific literature. IEEE's International Committee on Electromagnetic Safety (ICES) and the literature review working group (LRWG) conducted the scientific review and concluded that the previous 2005 version (IEEE, 2005) appeared to be sufficiently protective based on expert groups' reviews. However, IEEE indicated that major changes in limits in this standard are the DRLs and ERLs above 6 GHz based on recent thermal modeling studies. IEEE has documented their rationale and summary of the literature for the identification of levels of exposure associated with adverse effects in annex B and C of their revised standard. The information found in these anexes forms the basis for the development of *Dosimetric Reference Limits* (DRL) and *Exposure Reference Levels* (ERL) which are akin to ICNIRP's *Basic Restrictions* and *Reference Levels* respectively.

The purpose of the new IEEE standard (IEEE, 2019) is to provide science-based exposure criteria to protect against established adverse health effects in humans associated with exposures to electric, magnetic and electromagnetic fields in the frequency range of 0 Hz to 300 GHz. IEEE has identified two tiers of permissible exposure values: i) the unrestricted tier for which the specified permissible exposure values do not require the need for a safety program and ii) the restricted tier for which a safety program is required as a mitigation measure to allow higher values of permissible exposures (i.e. by a factor of 5 with respect to unrestricted tier). The unrestricted tier's limits would be applicable for exposures by the general public and the restricted tier's limits would be applicable to persons in a controlled occupational environment such as workers. The IEEE's proposed limits do not apply to patients undergoing procedures for medical diagnosis or treatment or to informed volunteers in medical or scientific research studies.

IEEE reviewed the scientific literature to refine and update parts of their standards but considered that the fundamental basis found in the previous edition are still valid in terms of recognized adverse health effects. For frequencies below a 100 kHz, the IEEE concludes that intense tissue exposures above human exposure limits can lead to electrostimulation which causes a range of reaction like pain stimulation, muscle excitation, alteration of synaptic activity in the brain, cardiac excitation and induced potentials or forces on moving particles (e.g. blood flow). For frequencies between 100 kHz and 300 GHz, IEEE concludes that intense tissue exposures above human exposure limits can lead to tissue heating and whole-body heating as a predominating effect. IEEE has investigated the possibility of adverse health effects associated with chronic low level exposure but found that the weight-of-evidence provides no credible indication of adverse effects and that no biophysical mechanisms have been scientifically validated to date.

3.2.1 Whole-body exposure limits basis

IEEE's ICES' literature review working group (LRWG) recently reviewed the scientific literature and could not find reliable evidence that would change the scientific basis for the adverse health effect threshold levels for whole body exposures. The threshold for Whole-Body Averaged (WBA) SAR of 4 W/kg for established adverse effects remains the same as the previous version of the IEEE standard (IEEE, 2005). The adoption of this threshold was based on disruption of animal and nonhuman primates' behavior in laboratory setting and the hypothesis that it might extrapolate to human beings. Since IEEE has chosen the same safety factors (aka reduction factors in ICNIRP) as ICNIRP for the unrestricted and restricted tier, the whole-body exposure limits are consistent with the new ICNIRP guidelines (ICNIRP, 2020). Therefore, there is no need to expand on the rationale for such limits.

3.2.2 Localized exposure limits basis above 6 GHz

IEEE recognized that there is only limited experimental human data related to human tissue heating by RF energy for frequencies above 6 GHz. IEEE has considered the available human exposure data in combination with modeling studies using theoretical models for heating of tissue (i.e. the Pennes Bio Heat Transfer Equation) for threshold setting. Several recent authors (Foster K.R. *et al.,*2017; Foster K.R. *et al.,*2016; Morimoto R. *et al.*, 2016; Sasaki K. *et al.*, 2015) have generated useful theoretical data from those models which have also been considered in the ICNIRP guidelines. IEEE has concluded that, since SAR measurements or computations are still practical up to 6 GHz, that the transition frequency determined as 3 GHz in the previous IEEE standard (IEEE, 2005) is now changed to 6 GHz in the current version (IEEE, 2019).

The ERL and DRL for local exposure in the frequency range of 6 GHz to 300 GHz were chosen to maintain a similar peak temperature increase in tissue produced by RF exposure across the transition frequency and to maintain the fivefold safety factor ratio in exposure between unrestricted and restricted exposure conditions. IEEE considered several computational modeling studies reviewed in (Foster K.R. *et al.,*2017) establishing a heating factor of approximately 0.25 °C/(W/kg), in the frequency range 100 kHz to 6 GHz. Using this heating factor, IEEE estimates a resulting peak temperature increase of approximately 2.5 °C at the localized head & torso DRL below 6 GHz for restricted exposure conditions. IEEE recognized that many environmental and biological factors can affect the estimation of steady-state temperature increases but assume that continuous exposure at restricted exposures limits should result in peak temperature increases of this order. IEEE assumes an initial skin temperature of 34 °C under ordinary room ambient conditions and a thermal pain threshold of ~ 44 °C, this would mean that there is approximately a safety factor of 3 to 5 built into the restricted exposure limits. To remain consistent, IEEE used the same maximum temperature increase in the skin (~ 2 °C to 3 °C) threshold over the entire frequency range to determine the ERL and DRL for restricted exposure conditions. IEEE considered the studies from the following authors to determine such limits (Foster K.R. *et al.,*2017; Hashimoto Y. *et al.*, 2017; Laakso I. *et al.*, 2017; Sasaki K. *et al.*, 2017). The ERL and DRL for unrestricted exposure conditions are obtained by applying the safety factor of 5 for all frequencies.

IEEE has introduced the quantity of epithelial power density at body surface expressed in units of W/m^2 which can be used for assessing compliance with the local exposure DRL at frequencies between 6 GHz and 300 GHz. IEEE chose a value of 100 W/m^2 as DRL for restricted exposure conditions and 20 W/m^2 for unrestricted environment, which is aligned with the values provided by the new ICNIRP guidelines (ICNIRP, 2020). The epithelial power density is to be spatially averaged over any square area with a size of 4 cm^2 and, for smaller exposed areas (< 1 cm^2 as defined by −3 dB contours relative to the peak exposure) at frequencies above 30 GHz, this quantity is averaged over 1 cm^2 for comparison against twice the DRL value.

The new IEEE standard (IEEE, 2019) no longer considers the nature of the exposure environment (restricted versus unrestricted) as a basis for the averaging time for exposure. The averaging time of exposure is considered to be related to the thermal time constant which is dependent on the volume of the exposed tissue. Therefore, IEEE considers 30 min averaging time for whole-body exposure and 6 min for local exposure.

As opposed to the DRL which is expressed in term of an in situ quantity (e.g. epithelial power density), the ERL is expressed in terms of incident power density which is intended to ensure that the DRL is not exceeded. The DRL and ERL incorporate conservative safety factors that take into account biological and dosimetry uncertainties in laboratory studies and the variability of dose response within the human population. Because the incident power density is conservatively derived from the epithelial power density, it is possible to exceed an ERL while still complying with the DRL. The ERL increases as the frequency is reduced to 6 GHz, to account for the smaller transmittance into tissue at lower frequencies and the deeper penetration of energy into tissue.

IEEE recognizes that the lack of consideration given to short pulses in previous standards allowed the peak power density to rise arbitrarily, even when the average power density complied with the standard. So for exposures to pulsed RF fields in the range of 6 GHz to 300 GHz, peak power density limits are provided to prevent unintentionally high local exposure in terms of epithelial energy density. Therefore, in pulsed conditions (pulse widths less than 100 ms), the ERL, as averaged over any 100 ms, is reduced by a factor of five. Additionally, for intense pulses in the millimeter-wave frequency range (30 GHz to 300 GHz), IEEE introduces a maximum local incident energy density per pulse (or fluence) limit of 0.2 $\tau^{1/2}$ kJ/m^2 and 1 $\tau^{1/2}$ kJ/m^2, averaged over 1 cm^2 square area, for unrestricted and restricted exposure conditions respectively (where τ is the pulse width in s). The table 3.2 below summarizes IEEE's DRL and ERL for localized exposures above 6 GHz.

Table 3.2: Summary of IEEE basis and limits for localized exposures between 6 GHz and 300 GHz

Max ΔT^oC (pain)	Exposure scenario	SF	Time Base [sec]	Frequency Range [GHz]	Aver.Area	Dosimetric Reference Limits (DRLs)	Exposure Reference Levels (ERLs)
(10^oC) Skin start at 34^oC. Pain start at 44^oC	restricted (work place)	3 - 5	Fluence	30 to 300	1 cm^2	-	1 $\tau^{1/2}$ kJ/m^2
			Peak PD < 100ms	6 to 300	4 cm^2	20 W/m^2	55 $f_G^{-0.177}$ W/m^2
				30 to 300	1cm^2	40 W/m^2	110 $f_G^{-0.177}$ W/m^2
			> 360	6 to 300	4 cm^2	100 W/m^2	275 $f_G^{-0.177}$ W/m^2
				30 to 300	1cm^2	200 W/m^2	550 $f_G^{-0.177}$ W/m^2
	Un-restricted (General Public)	15 - 25	Fluence	30 to 300	1 cm^2	-	0.2 $\tau^{1/2}$ kJ/m^2
			Peak PD < 100ms	6 to 300	4 cm^2	4 W/m^2	11 $f_G^{-0.177}$ W/m^2
				30 to 300	1cm^2	8 W/m^2	22 $f_G^{-0.177}$ W/m^2
			> 360	6 to 300	4 cm^2	20 W/m^2	55 $f_G^{-0.177}$ W/m^2
				30 to 300	1cm^2	40 W/m^2	110 $f_G^{-0.177}$ W/m^2

Notes:

* f_G is frequency expressed in GHz.
* τ is the pulse width in seconds.
* Epithelial power density and Incident power density exposures are to be averaged over 6 min.
* The peak power density limit (Peak PD) applies to the summation of all incident energy density of a pulse train in any period of 100 ms divided by 6 minutes.
* Local epithelial power density and Incident power density energy density are averaged over a 4-cm^2 (6-300 GHz) and additionally over 1-cm^2 (>30-300 GHz) square area **if the beam is smaller than 1 cm^2** (as defined by the contour of the -3dB surface plot), approximating the body surface.
* The fluence limit is applied to any pulse of duration τ within a pulse train (or single pulse) and is averaged over 1 cm^2.

3.2.3 Assumptions underpinning the IEEE limits

IEEE has developed recommended human exposure limits for localized exposure to RFEMF at frequencies from 6 to 300 GHz that are based upon several assumptions and conclusions. These include: a) the conclusion that thermal effects are the first adverse health effect to be manifested as RFEMF exposure levels increase in intensity; b) the conclusion that 44^oC represents the threshold for thermal pain sensation); c) the assumed normothermal range of superficial tissue temperatures is 10^oC lower than the threshold for thermal pain sensation); d) the absorbed power density associated with causing a 10^oC temperature increase in superficial tissues; e) the choice of safety factors for exposures in restricted and unrestricted environments; and f) the choice of time- and spatial-averaging conditions. Sections 4 of this report describe Health Canada's evaluation of the assumptions/conclusions made by IEEE when developing these limits in an effort to validate if these limits afford adequate protection against the established health effects of localized RFEMF exposure at frequencies above 6 GHz.

3.3 Comparison between the new ICNIRP Guidelines and IEEE Standard

ICNIRP and IEEE have both recently published updated RFEMF exposure guidelines and standard which introduce new exposure limits for localized exposure that could be applicable to exposure scenarios from new and emerging technologies. In an effort to simplify the analysis of those new localized exposure limits, it is worth looking at the similarities and differences between these two publications.

As described above in sections (3.1) and (3.2), a few similarities can be identified in the guidance provided. Namely, the transition frequency (ie the frequency between local SAR and area-averaged absorbed power density) that used to be 3 GHz in the IEEE standard was modified to match the ICNIRP transition frequency of 6 GHz. The proposed basic restrictions and reference levels in the ICNIRP Guidelines (ICNIRP, 2020) are the same as the proposed dosimetric reference limits (DRLs) and exposure reference levels (ERLs) in the IEEE standard (IEEE, 2019) for Continuous Wave (CW) exposures averaged over 6 minutes. This can likely be explained by the fact that they both used similar maximum temperature increases in the body for the development of those limits, even if different approaches were taken to arrive at the maximum temperature increases. ICNIRP defined a targeted operational adverse health effect threshold (OAHET) for two types of tissues with a maximum 5^{o}C for type 1 tissue and a maximum 2^{o}C for type 2 tissue and then applied a reduction factor of 10 for uncontrolled environment. Since the skin is typically the limiting factor for exposures above 6 GHz, this means that the target maximum temperature increase in the skin for such environment is about 0.5^{o}C. IEEE identified approximately 10^{o}C temperature elevation in the skin as a pain threshold which is divided by a safety factor between 15 to 25 for the unrestricted tier. If an average reduction factor of 20 is applied, this means that the target maximum temperature increase in the skin for the unrestricted tier is approximately 0.5^{o}C which is equivalent to the maximum temperature increase associated with the ICNIRP limit. Furthermore, both guidance documents propose to use a square averaging area of 4 cm^2 for exposures in the frequency range of 6 GHz - 300 GHz and to additionally apply a square averaging area of 1 cm^2 for exposures in the frequency range of 30 GHz - 300 GHz to be compared with a doubling of the limit provided at 4 cm^2. IEEE stipulates that the 1 cm^2 averaging area criterion is only needed for beam size defined by a -3dB (from the peak) contour plot indicating that the beam is smaller than 1 cm^2. That could be identified as a small difference between the two publications but, in essence, this does not make a big difference because this criterion is required for small beams only.

The main differences between the ICNIRP guidelines (ICNIRP, 2020) and the IEEE standard (IEEE, 2019) for localized exposures above 6 GHz lie in their recommended exposure limits for short exposure durations (i.e. less than 6 minutes). ICNIRP applies a fluence limit to the absorbed energy density and incident energy density for any pulse, group of pulses, or subgroup in a pulse train in addition to the CW limit. IEEE, on the other hand, i) maintains the same fixed power density limit applied for CW exposures and averages the pulses over 6 minutes, ii) divides that fixed power density limit by 5 which would apply to the sum of the energies of all pulses within any period of 100 ms period divided by 6 minutes (aka instantaneous peak power density restrictions), and iii) applies an additional fluence limit to the incident energy density for intense pulses. To illustrate the differences between the recommended limits from both documents, the following graph has been generated to show the ratio between the IEEE limits (not including the additional fluence limit) and ICNIRP limits.

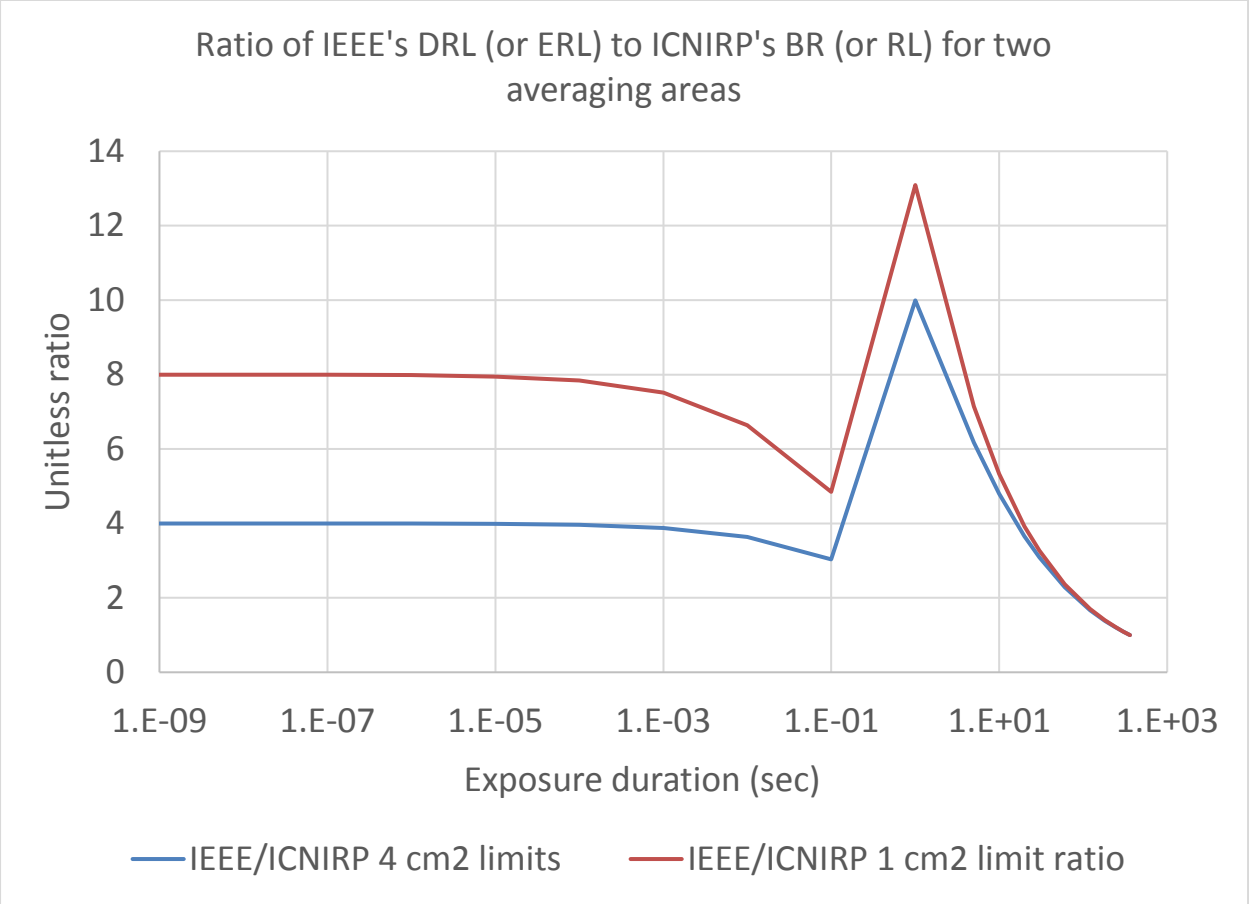

Figure 3.1: Evaluation of the ratio between IEEE and ICNIRP's proposed limits (not considering IEEE's fluence limit)

The ratio for limit comparison was defined by dividing either the IEEE's DRL by the ICNIRP's basic restrictions or by dividing IEEE's ERL by ICNIRP's reference levels. These ratios are exactly the same because both ICNIRP and IEEE used the same transmission coefficient as a function of frequency, (which can be found by dividing the basic restrictions by the reference levels) which appear to be $0.3636*(f_G)^{0.177}$. This simplifies the analysis because i) there is no need to generate graphs for a series of frequencies and, ii) since both IEEE and ICNIRP use the same reduction factor of 5 between uncontrolled environment and controlled environment, Figure 3.1 is valid for both environments. As can be seen on such figure, when we do not consider the additional IEEE fluence limit, the ratio is always above 1 for exposure durations less than 360 seconds which indicates that ICNIRP's proposed limits are more conservative. The IEEE and ICNIRP limits agree on the CW limit averaged over 360 seconds where the ratio reaches unity.

IEEE's further recommends, *for intense pulses (such as in certain military weapons systems) in the millimeter-wave frequency range (30 GHz to 300 GHz),* a specific maximum local incident energy density per pulse limit of 0.2 $\tau^{1/2}$ kJ/m^2 for the uncontrolled environment tier and 1 $\tau^{1/2}$ kJ/ m^2 for the controlled environment tier to be averaged over 1 cm^2. This fluence limit per pulse appears to be very low when compared to ICNIRP's fluence limit as can be seen on figure 3.2.

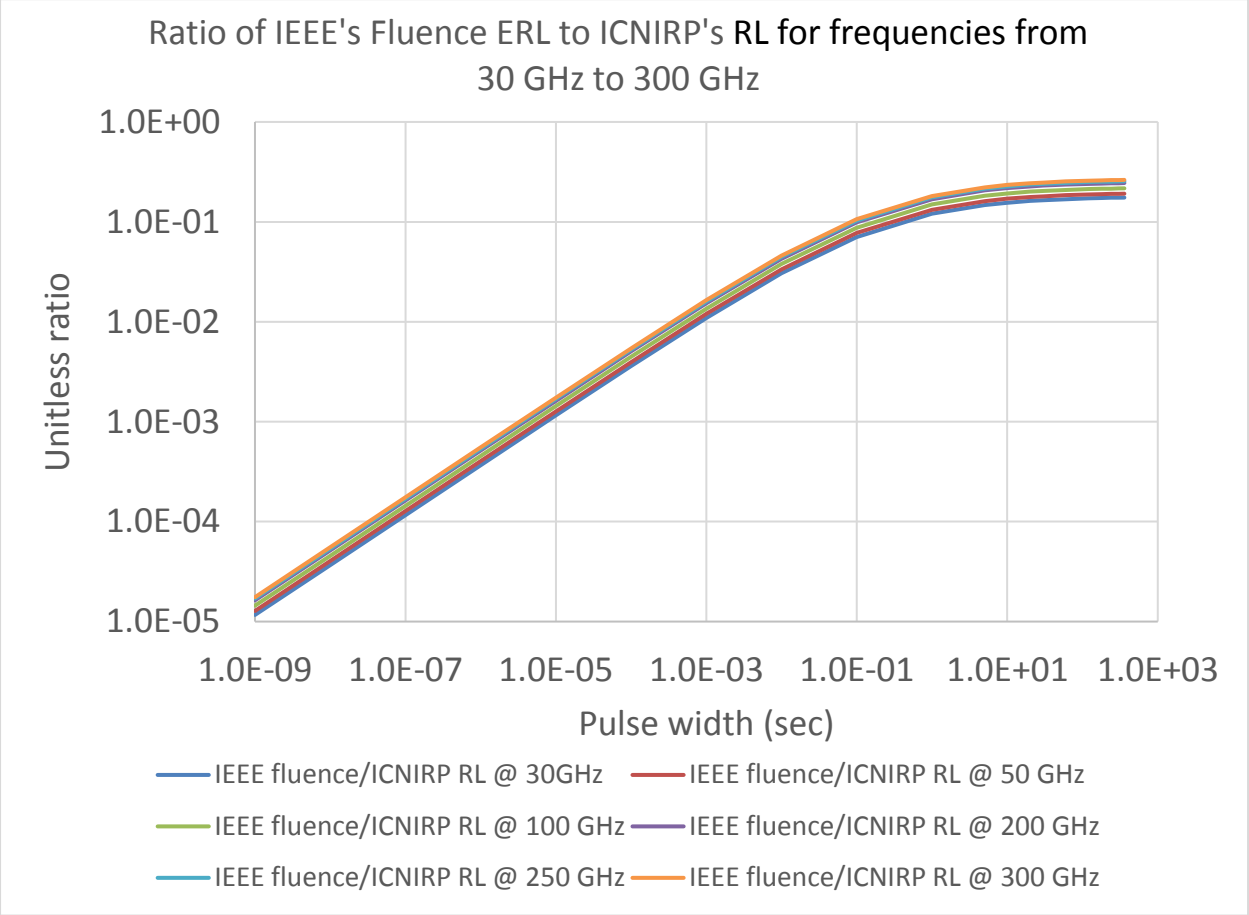

Figure 3.2: Evaluation of the fluence ratio between IEEE and ICNIRP's proposed limits.

According to figure 3.2, IEEE's ERL fluence limits appear to be several orders of magnitude smaller than the one proposed by ICNIRP for single pulses of short duration. This fluence limit ratio reaches a value between 0.17 to 0.26, depending on frequency, if we assume a single pulse with a duration of 360 seconds. The basis for this additional fluence limit is unclear and difficult to reconcile with the other applicable ERLs proposed by IEEE, as seen in figure 3.1, which appear to be less conservative than the limits proposed by ICNIRP.

3.4 Relevance of proposed international Guidelines and Standards

The IEEE (IEEE, 2019) and ICNIRP (ICNIRP, 2020) RFEMF limits show some similarities and differences as described in the previous sections. There appears to be agreement on the basic restrictions (or DRLs) and reference levels (or ERL) for exposure duration averaged over 6 minutes. They have both used the same transmission coefficient to convert basic restrictions into reference levels value and defined an additional measurement averaging area for small beams widths for frequencies above 30 GHz. However, there seems to be significant discrepancies between IEEE and ICNIRP when it comes to proposing limits for pulses or for exposure duration less than 360 seconds.

ICNIRP proposes a fluence limit (or absorbed energy density) for short exposures less than 360 seconds that varies as the sum of a fixed value and a value proportional to the square root of the exposure time. For exposure durations longer or equal to 360 seconds, a fixed power density (or absorbed power density) is applied. The net effect of this approach, means that i) for very short exposure durations (when the square root becomes almost zero) a fixed energy density limit is applied, ii) for intermediate exposure durations an energy density limit that varies as the square root of time is applied and iii) for long exposure durations a fixed power density limit is applied.

IEEE, on the other hand, applies a fixed power density limit averaged over 6 minutes for any exposures (including exposure less than 360 seconds) and, as an instantaneous peak power density restriction, applies a fixed power density limit divided by 5 averaged over 6 minutes for any exposures to a pulse train in any period of 100 msec. Additionally, IEEE applies a fluence limit per pulse (only for ERL) which appear to be several orders of magnitude smaller than their instantaneous peak power density restriction. If the fluence limit is not considered, the net effect of the IEEE approach is that i) for very short exposure durations (less than 100 msec) a fixed energy density limit is proposed which is 5 times less then for intermediate exposure durations, ii) for intermediate exposure durations (from 100 msec to 360 sec) a fixed energy density limit is proposed and iii) for long exposure durations a fixed power density limit is proposed. If IEEE's proposed fluence limit is considered, it becomes difficult to reconcile with the other limits because they appear to be much lower.

Based on computational dosimetry approaches (see section 5), some fundamental principles were observed when solving the 3D BHTE in a volume of tissue. For starters, some fundamental principles should be considered when assessing both the IEEE and ICNIRP exposure limits. First, the elaboration of a limit as function of exposure time, either as absorbed energy density or as absorbed power density, depends mainly on the characteristic times involved in the thermal diffusion and transfer mechanisms. The absorbed energy density in human tissue required to increase the temperature of the skin by a set value depends on many factors (e.g. tissue layer thicknesses, blood perfusion, etc.) which varies across the population. Second, it is important to consider the volume in which the energy is absorbed, which will depend largely on the frequency and beam diameter or SAR spot size (i.e. penetration depth and exposed area, respectively). The exposed tissue volume (and how close this exposed volume is to the skin-air interface) will be a determining factor for the two main characteristic times involved in heat diffusion and heat transport. The characteristic time related to natural heat diffusion is very short (of the order of 1 s) and the one related to heat transport by blood flow is much longer (in the 100s of seconds).

Based on the above principles, one would expect that the temperature elevation over very short exposure durations (less than the characteristic time for thermal diffusion) would be related to the total absorbed energy. It would be independent of the exposure duration because the energy does not have time to be diffused or transported out of the volume over the short period of time. (For a more thorough discussion, see Appendix D.2 of Chapter 5.) As the exposure duration increases (longer than the diffusion characteristic time but shorter than 5 times the blood transport characteristic time), the amount of energy required to reach the same set temperature elevation should be higher and vary as a function of exposure time because as energy is poured into the volume, some of it is being diffused and transported (by blood

flow) out of the volume. Finally, when the exposure duration is sufficiently long, a steady state equilibrium is reached between the rate of energy deposited in the volume and the rate of energy being diffused and transported out of the volume, which means that a fixed power density limit would be appropriate.

The new ICNIRP (ICNIRP, 2020) localized exposure limits above 6 GHz appear to be based on these fundamentals of thermal transfer mechanisms whereas this is not the case of the new IEEE standard's (IEEE, 2019) time dependant limits. Furthermore, aside from the IEEE fluence limit which tends towards null as the pulse width gets shorter, this analysis has found that the limits in the IEEE standard are less conservative than that of ICNIRP. For these reasons, the remainder of this report is focussed on the analysis of tissue temperature effects associated with the new ICNIRP guidelines.

3.5 References

Foster, K. R., Ziskin, M. C., and Balzano, Q., "Thermal modeling and the next generation of radiofrequency limits," Health Physics, vol. 113, pp. 41–53, 2017. (B432 – Foster K.R. *et al.,*2017)

Foster, K. R., Ziskin, M. C., and Balzano, Q., "Thermal response of human skin to microwave energy: A critical review," Health Physics, vol. 111, no. 6, pp. 528–541, 2016. (B433 – Foster K.R. *et al.,*2016)

Hashimoto, Y., Hirata, A., Morimoto, R., Aonuma, S., Laakso, I., Jokela, K., and Foster, K., "On the averaging area for incident power density for human exposure limits at frequencies over 6 GHz," Physics in Medicine and Biology, vol. 62, pp. 3124–3138, 2017. (B577 – Hashimoto Y. *et al.*, 2017)

ICNIRP. Guidelines for limiting exposure to electromagnetic fields (100 kHz to 300 GHz). Health Phys 118(5):483-524; 2020.

ICNIRP. Guidelines for limiting exposure to time-varying electric and magnetic fields (1 Hz to 100 kHz). Health Phys 99:818–836; 2010.

IEEE Standard C95.1™-2019, IEEE Standard for Safety Levels with Respect to Human Exposure to Electric, Magnetic, and Electromagnetic Fields, 0 Hz to 300 GHz. 2019.

IEEE Standard C95.1™-2005, IEEE Standard for Safety Levels with Respect to Human Exposure to Radio Frequency Electromagnetic Fields, 3 kHz to 300 GHz. 2005.

Laakso, I., Morimoto, R., Heinon, J., Jokela, K., and Hirata, A., "Human exposure to pulsed fields in the frequency range from 6 to 100 GHz," Physics in Medicine and Biology, vol. 62, no 17, pp. 6980–6992, 2017. (B801 – Laakso I. *et al.*, 2017)

Morimoto, R., Laakso, I., De Santis, V., and Hirata, A., “Relationship between peak spatial averaged specific absorption rate and peak temperature elevation in human head in frequency range of 1-30 GHz,” Physics in Medicine and Biology, vol. 61, pp. 5406–5425, 2016. (B1038 – Morimoto R. *et al.*, 2016)

Sasaki, K., Isimura, Y., Fujii, K., Wake, K., Watanabe, S., Kojima, M., Suga, R., and Hashimoto, O., “Dielectric property measurement of ocular tissues up to 110 GHz using 1 mm coaxial sensor,” Physics in Medicine and Biology, vol. 60, pp. 6273–6288, 2015. (B1251 – Sasaki K. *et al.*, 2015)

Sasaki, K., Mizuno, M., Wake, K., and Watanabe, S., “Monte Carlo simulations of skin exposure to electromagnetic field from 10 GHz to 1 THz,” Physics in Medicine and Biology, vol. 62, pp. 6993–7010, 2017. (B1252 – Sasaki K. *et al.*, 2017)

Sienkiewicz Z, van Rongen E, Croft R, Ziegelberger G, Veyret B. A Closer Look at the Thresholds of Thermal Damage: Workshop Report by an ICNIRP Task Group. Health Phys. 2016 Sep;111(3):300-6.

4.0 Assessment of potential adverse health effects from exposure to RFEMF at frequencies from 6 to 300 GHz

4.1 Identification of adverse health effects from RFEMF in the 6 to 300 GHz frequency range

The WHO defines health as "…a state of complete physical, mental and social well-being and not merely the absence of disease or infirmity."[2] For the purpose of this analysis, an adverse health effect is defined as a detectable bio-physical change that results in impairment in the physical health of an exposed individual or of his or her offspring. Impacts on mental health (e.g. fear/anxiety related to exposure) or social well-being (e.g. property values, social justice) are not directly and exclusively dependent upon or related to RFEMF exposure. These outcomes are beyond the scope of this analysis and are best dealt with through policy considerations. It is important to note that biological effects or changes (e.g. small temperature changes) may occur upon exposure to RFEMF without the occurrence of an adverse health effect, even with indefinite exposure. Health Canada's review and recommendations are intended to identify thresholds for, and prevent the occurrence of, established adverse health effects, but not necessarily the occurrence of biological responses that do not result in adverse health outcomes.

Recently, ICNIRP (2020) and IEEE (2019) have published revised recommended human exposure limits for RFEMF. Both of these non-governmental organizations reported that they have reviewed and evaluated the scientific literature to identify the scientifically substantiated/established adverse health effects associated with RFEMF in the 6 to 300 GHz frequency range. In addition, these organizations reference reviews by the WHO (WHO 2014), the Scientific Committee on Emerging and Newly Identified Health Risks (SCENIHR, 2015) and the Swedish Radiation Safety Authority (SSM 2015, 2016, 2018). Both IEEE and ICNIRP have concluded that no other adverse health effects would occur, as the intensity of RFEMF exposure increases in the frequency range from 6 to 300 GHz, without first causing either a heat-pain sensation or thermal tissue damage. Since both of these effects are related to excessive tissue heating, both IEEE and ICNIRP have derived their recommended human exposure limits in the 6 to 300 GHz frequency range based upon limiting the magnitude of localized tissue or whole-body temperature increases from RFEMF exposure.

While Health Canada values the scientific assessments conducted by both ICNIRP, IEEE and other international health organizations, an independent evaluation of the scientific literature was conducted. To evaluate potential adverse health effects from RFEMF in the frequency range between 6 to 300 GHz, Health Canada conducted a review of the relevant scientific literature. Since such a small number of studies were found for each potential adverse health outcome, endpoint, frequency, animal model and exposure duration, a quantitative meta-analysis of these results was not deemed appropriate. Instead, Health Canada has conducted a systematic analysis whereby all relevant scientific literature was identified through a systematic approach in accordance with systematic review principles (Rooney et al., 2016) using a narrative systematic review approach. The purpose of this analysis was to answer the question: "Does exposure to RFEMF in the 6 to 300 GHz frequency range adversely affect health in humans or mammals?".

[2] Preamble to the Constitution of the World Health Organization (April, 1948).

To aid in answering this question, the following PECO (Participants, Exposure, Comparator, Outcome) was applied:

Participants: Human or other mammalian studies were included. Studies conducted in insects, plants or cell cultures were not included.

Exposure: Radiofrequency electromagnetic fields in the 6 to 300 GHz frequency range.

Comparator: Human or other mammalian subjects/samples and non-exposed samples maintained under similar time- and environmental conditions (e.g. sham conditions).

Outcome: The outcomes considered were any adverse health effect (e.g. change in a biophysical endpoint leading to impairment of physical health of an individual or their offspring).

Methods:

Search strategy and selection criteria

English and French language scientific articles were searched using PubMed (https://www.ncbi.nlm.nih.gov/pubmed/) on January 27, 2020 using the following terms: [(("electromagnetic"[Title/Abstract] OR "electro magnetic"[Title/Abstract] OR "electro-magnetic"[Title/Abstract] OR "microwave"[Title/Abstract] OR "radiowave"[Title/Abstract] OR "radio wave"[Title/Abstract] OR "radio-wave"[Title/Abstract] OR "radiofrequency"[Title/Abstract] OR "radio frequency"[Title/Abstract] OR "radio-frequency"[Title/Abstract] OR "cellular phone"[Title/Abstract] OR "cell phone"[Title/Abstract] OR "smartphone"[Title/Abstract] OR "smart phone"[Title/Abstract] OR "smart-phone"[Title/Abstract] OR "Wifi"[Title/Abstract] OR "Wi-Fi"[Title/Abstract] OR "smart meter"[Title/Abstract] OR "mobile phone"[Title/Abstract] OR "mobile telephone"[Title/Abstract] OR "base station"[All Fields] OR "GSM"[Title/Abstract] OR "cell tower"[Title/Abstract] OR "UMTS"[Title/Abstract] OR "mobile communication"[Title/Abstract]) AND ("English"[Language] OR "French"[Language])) NOT ("ablation"[Title/Abstract])]. EMF-Portal (https://www.emf-portal.org/en) was also searched on January 27, 2020 using the following criteria: [Topics=Experimental studies, Epidemiology studies, Review/Surveys/Summaries; Frequency Selection=radiofrequency (above 10 MHz), mobile phone related frequencies, low frequency (below 10 MHz)]. A search update, via alerts, was performed up until July 17, 2020. We supplemented the electronic database searches with manual searches for published studies in previous review articles and websites of international agencies (e.g., WHO, IEEE). Furthermore, the references within included studies were screened to identify other possibly relevant publications. Across all searches, we included scientific articles if they consisted of original quantitative research published in a peer-reviewed journal, while we excluded studies that calculated effects with simulations or statistical models instead of actual measurements in humans or other mammals. The screening of the titles, abstracts, and full texts for eligibility, and the selection of studies to be included were conducted by two reviewers.

All studies that assessed bio-physical outcomes in human or other mammalian models in response to RFEMF exposure in the 6 to 300 GHz frequency range in comparison to time- and environmental-matched conditions (e.g. sham control) were included. Studies were excluded if one or more of the following conditions were not met:

- the article did not contain original data (e.g. review article, editorial, commentary, letter to editor),
- the article was not published in a peer-reviewed journal
- the subjects/samples were not exposed to RFEMF in the 6 to 300 GHz frequency range,
- the article was not conducted in humans or other mammals (e.g. cell culture or protein in solution).
- the article was written in a language other than English or French.

In vitro studies were excluded as they do not provide direct evidence of adverse health effects in animals or humans. Articles were also excluded if they were studies on co-exposure to RFEMF and any other potentially beneficial or detrimental chemical or physical exposure, were related to a human medical intervention (e.g. radiofrequency ablation), a medical device (e.g. electromagnetic interference) or if the exposure consisted of an electromagnetic pulse (EMP) or ultra-wide band (UWB) radiation. Case studies were also excluded.

Approach for assessing Risk-of-Bias

The risk-of-bias of included human and mammalian studies were assessed according to the systematic review principles outlined by Rooney et al. (2016). Each study was independently evaluated by two reviewers across several domains, including: 1. Study design (participant selection and/or randomization and allocation concealment); 2. Blinding (during exposure and/or during endpoint assessment); 3. Attrition/exclusion (loss of subjects, samples or data-points); 4. Exposure assessment (e.g. confidence in quantification of RFEMF dose and/or dose rate measurement/calculation, information on heterogeneity of exposure across tissue/body and peak intensity); 5. Selective reporting (e.g. incomplete reporting of outcome data); 6. Conflict of interest (e.g. could funding source introduce bias into studied outcomes); and 7. Other biases (e.g. includes quality of endpoint assessment techniques, sensitivity of assays, statistical approach, temperature monitoring and control, description of sham conditions, number of independent experiments or subjects). Some quality features, such as lack of blinding, may impact ratings in more than one domain. Risk of bias for each domain was rated as “Low risk of bias”, “Probably low risk of bias”, “Probably high risk of bias” or “High risk of bias”. Discrepancies between reviewer evaluations were discussed with respect to the study merits and limitations to develop a jointly agreed upon classification. When multiple studies assessed the same potential adverse health outcome, an overall risk-of-bias was developed based upon evaluations across all studies. Similarly, each study was classified with an ‘Overall study risk-of-bias’ based upon biases in each of the seven domains.

Approach for assessing the Quality and Strength of Evidence

The available human and mammalian studies on bio-physical effects from exposure to millimeter-wave (6 to 300 GHz) RFEMF fall into 7 general categories, including: 1) skin temperature changes, heat-pain

sensation and cardiovascular effects, 2) hypoalgesic (pain suppression) effects, 3) immune system effects, 4) ocular effects, 5) reproductive system effects, 6) cancer and genotoxicity and 7) other studies. Since most studies within a given category used different exposure conditions (frequency, location, duration, intensity) and many assessed a diverse assortment of endpoints, it was not possible to extract data and conduct a quantitative meta-analysis from the aggregated study findings. Therefore, a narrative assessment was performed. An assessment of the quality and strength of evidence was conducted for each potential adverse health outcome. The body of evidence was assessed separately for human and mammalian animal studies. The ratings for the Quality of Evidence were “High”, “Moderate”, “Low” and “Very Low”. The initial Quality of Evidence rating for human experimental studies and mammalian studies was set as “High”. The quality of evidence for each potential adverse health outcome was considered for downgrading based upon: 1) Risk-of-bias across studies; 2) Indirectness (e.g. how comparable is the evidence to the PECO?); 3) Inconsistency (e.g. how comparable were results across subjects within a study or between studies?); and 4) Imprecision (How precise are the effect estimates? This can be influenced by participant number or number of occurrences of an event). Publication bias was not assessed, as meaningful quantitative analysis of the raw data could not be performed due to the diverse nature of the exposure conditions and endpoints assessed, resulting in an insufficient number of studies for each outcome. For each evaluated potential adverse health outcome, the Strength of Evidence for each health endpoint was determined by considering: 1) Quality of Evidence; 2) Direction of effect; 3) Confidence in effect; and 4) Other compelling attributes of the data that may influence certainty (e.g. evidence from complimentary research). The Strength of Evidence was rated as either “Sufficient Evidence”, “Limited Evidence”, “Insufficient Evidence” or “Evidence of lack of toxicity”.

Results

Analysis of the search results: A total of 88187 articles were identified in PubMed and 16292 were identified in EMF-Portal. After title screening, 4602 unique records were identified. After abstract and full-text screening based upon the requirements to meet the appropriate frequency range, include original data, include an appropriate time- and environment-matched sham control, an additional 4394 studies were excluded. A total of an additional 107 articles were excluded as they were cell culture studies, resulting in a total of 101 articles meeting all requirements for inclusion in the review (Figure 4.1). A list of studies/articles relevant to the 6 to 300 GHz frequency range that were excluded can be found in Appendix E. Of the 101 included studies, 10 were conducted in humans and 91 were conducted in other mammals.

Figure 4.1. PRISMA flowchart of the study selection process.

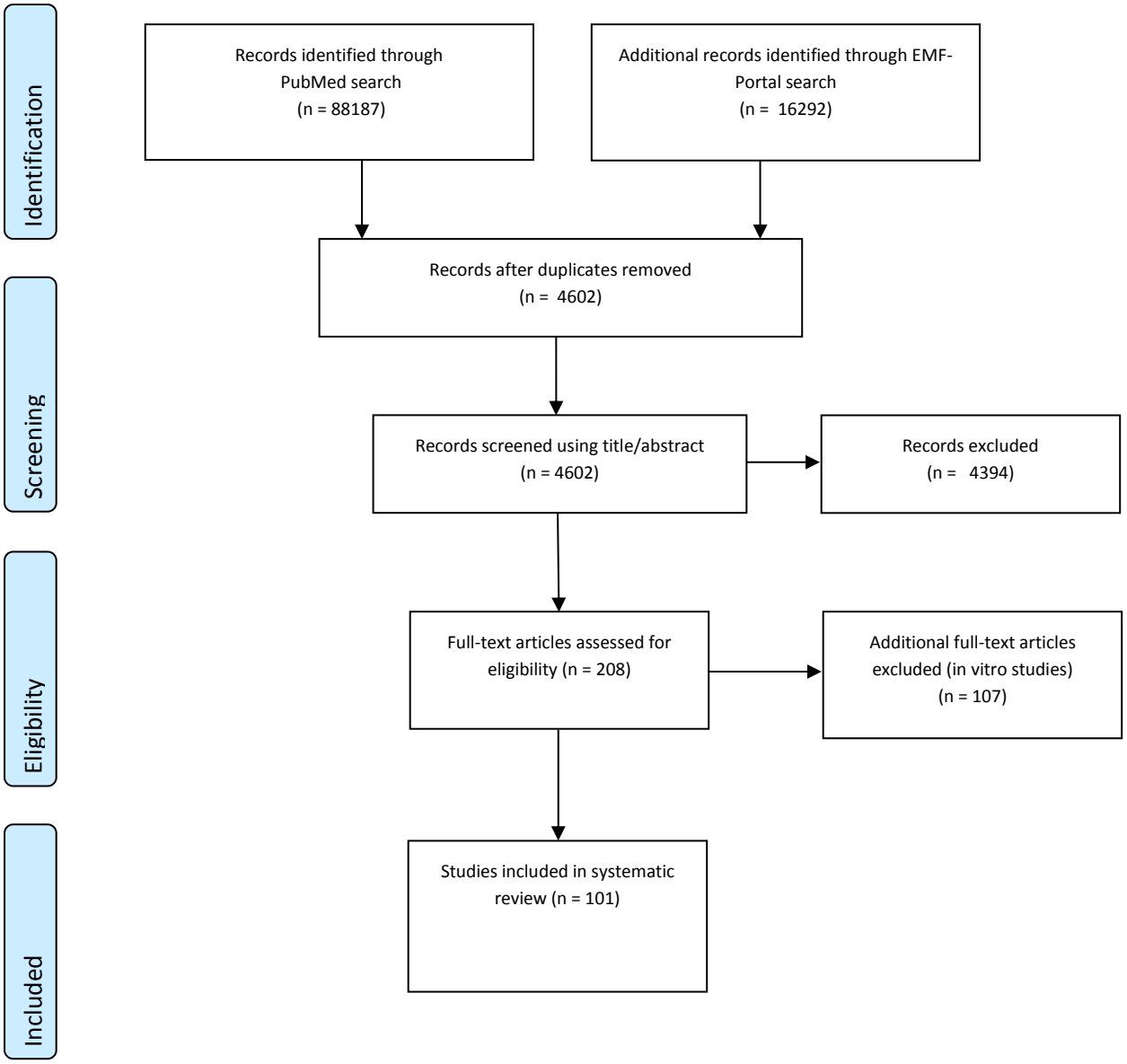

Summary of evidence:

Human Studies:

Of the 10 identified studies on human responses to RFEMF in the 6 to 300 GHz frequency band, most have been conducted by two research groups and have focussed on skin temperature changes and the threshold of perceived warmth and heat pain sensation. No human studies were identified that assessed endpoints such as cancer, ocular effects, reproductive system effects, cognitive effects, impacts on the immune system, non-specific symptoms or any other adverse health outcomes in response to exposure to RFEMF in the 6-300 GHz frequency range. The included studies on human outcomes are outlined in Table 4.1.

Skin temperature changes, pain and warmth sensation in human studies

Studies by Ziskin and colleagues assessed skin temperature changes in human volunteers in response to 42.25 GHz RFEMF and investigated the influence of beam diameter, temperature kinetics and skin blood perfusion on the maximum skin temperature response (Alekseev et al., 2003, 2005). The authors reported that increasing beam diameter resulted in higher peak temperatures at the center of the beam at the same incident power density. The authors also found that beam diameter had no influence on temperature kinetics for short exposures (< 3 s), presumably since such exposures deposited energy (resulting in heat) substantially faster than the rate at which heat could be transferred to adjacent tissues or the external environment. Occlusion of blood perfusion in well perfused tissues was found to result in similar temperature responses as observed in poorly perfused tissues, highlighting the important role of blood perfusion in modulating tissue temperature in response to RFEMF exposure. This group also reported that a 30 min exposure of 42.25 GHz RFEMF at a power density of 250 W/m^2 to the chest skin could induce a peripheral hypoalgesic response towards a cold pain sensation in the hand (Radzievsky et al., 1999). It is unclear if the authors controlled for distraction, which has previously been demonstrated to influence pain thresholds. The authors speculated that these effects may be associated with the activation of peripheral nerves within the skin (possibly through an opioid signalling pathway), resulting in a systemic hypoalgesic response. Alternatively, it is possible that localized exposure to the chest caused an activation of peripheral nerves within the skin that resulted in a systemic increase in peripheral skin blood perfusion, which provided protection against cold pain in the cold pressor test by maintaining warmth in the exposed tissue through an increased rate of blood flow. Partyla et al. (2017) followed-up on these observations, exposing the chests of human subjects to either broadband “noise” RFEMF in the 50 to 75 GHz frequency range or 42.25 GHz RFEMF for 30 min at a power density not exceeding 172 W/m^2. The authors then administered the cold pressor test under double-blind conditions. The authors reported no changes in the pain threshold, time to onset of cold pain or “increasing pain” in RFEMF exposed subjects in relation to the placebo control group.

A series of studies on the kinetics of skin temperature elevation and the thresholds of either a warmth sensation or a heat pain sensation were conducted at Brooks Air Force Base (TX, USA). These studies exposed human volunteers to 7.5, 10, 35 or 94 GHz RFEMF, at a range of power densities, for times ranging from 3 s to 3 min. The authors reported that a skin warmth sensation on the back occurred at lower incident power densities at higher frequencies. At 94 GHz, the authors reported that skin warmth was

perceived at a power density of 45 W/m^2 for 10 s exposure (Blick et al., 1997). The authors also reported that a heat pain sensation was perceived at a power density threshold of ~12500 W/m^2 (for a 3 s exposure) which was associated with a ~10^{o}C skin temperature increase from baseline to 43.9^{o}C (Walters et al., 2000). The impact of blood perfusion on skin temperature elevation was also assessed by this group. The Pennes bioheat equation (PBHE), with no blood perfusion term included in the model, was found to provide an accurate estimation of skin temperature elevation for exposure times less than 3 s in humans, monkeys and rats. However, for longer exposures the steady state temperature elevation was best estimated when a moderate blood flow term was included in the modelling and species differences in maximum temperature responses appeared to coincide with peripheral blood perfusion capacity (Nelson et al., 2003). Walters et al. (2004) confirmed these findings in human volunteers by assessing skin temperature elevation from RFEMF in relation to blood perfusion rates and identified a biphasic temperature response. The authors reported that small changes in skin blood perfusion could produce substantial alterations in skin heating.

Early work by Hendler and Hardy (1960) using human subjects reported a warmth sensation could be perceived on the forehead with a 0.02^{o}C temperature increase at a depth of 150-200 µm below the skin surface at the location of peripheral nerve receptors for both infrared light and 10 GHz RFEMF. Gustrau and Bahr (2002) measured the skin temperature elevation on the forearm of human subjects during exposure to 77 GHz RFEMF over a 15 min time period. The authors reported that exposure at 10 W/m^2 caused a 0.1^{o}C temperature elevation while exposure at 100 W/m^2 caused a 0.7^{o}C temperature elevation.

Table 4.1: Summary of human study characteristics.

Source	***Frequency of RFEMF***	***Exposure duration and intensity***	***Tissue exposed***	***Findings***
Alekseev et al., 2003	*42.25 GHz*	*0.3 to 55 s; 550-2080 W/m^2*	*Forearm skin*	*Measured skin temperatures were similar to those modelled using 2-D PBHE. Increasing beam diameter led to higher peak temperature increase at the same incident power density. Beam diameter had no influence on temperature kinetics for exposures less than 3 s.*
Alekseev et al., 2005	*42.25 GHz*	*0 to 20 min; 550-2080 W/m^2*	*Forearm and middle finger skin*	*Increasing blood perfusion was found to decrease maximum tissue temperature increase. Occlusion of blood perfusion resulted in similar temperature responses in tissues with differing basal blood flow.*
Blick et al., 1997	*7.5, 10, 35 and 94 GHz*	*10 s; 0-200 W/m^2*	*Skin on back*	*Skin warmth perception thresholds (195 W/m^2 at 7.5 GHz; 45 W/m^2 at 94 GHz) were reported in terms of incident power density across a wide frequency spectrum.*

Gustrau and Bahr, 2002	*77 GHz*	*15 min; 10 or 100 W/m^2*	*Forearm skin*	*Measured skin temperatures were similar to those modelled using PBHE (skin with fat layer). Exposure at 10 W/m^2 caused less than a 0.1^{o}C temperature increase whereas exposure at 100 W/m^2 caused a 0.7^{o}C peak skin temperature increase.*
Hendler and Hardy, 1960	*10 GHz, 2.5 kHz pulsed*	*140 s; 170 W/m^2*	*Forehead skin*	*Threshold of warmth sensation was reported to be a 0.02^{o}C temperature increase at a depth of 150-200 µm below the skin surface.*
Nelson et al., 2003	*94 GHz, 1 kHz pulsed*	*3 s or 3 min; 1750 or 10000 W/m^2*	*Forearm skin*	*Measured skin temperature increases (~7^{o}C) for high power density (10 kW/m^2 for 3s) RFEMF exposure were similar to those predicted using PBHE model with no blood flow. Low power density (1750 W/m^2) RFEMF exposure caused an ~8^{o}C temperature increase over 3 min that reached steady state, which was most similar to a moderate blood flow model (17mL/100g/min). The results suggested the PBHE model should adjust for variable blood flow during longer duration exposures.*
Partyla et al., 2017	*42.25 GHz*	*30 min; <172 W/m^2*	*Chest*	*RFEMF exposure had no effect on pain tolerance, time to onset of cold pain or increasing pain threshold under double-blind conditions.*
Radzievsky et al., 1999	*42.25 GHz, continuous*	*30 min; 250 W/m^2*	*Chest*	*RFEMF exposure caused a ~1.6^{o}C temperature increase in chest skin after 5min, but subjects could not perceive this temperature increase. RFEMF exposure caused a delay in cold pain sensation in the hand and an increase in pain tolerance. No changes were noted in heart rate or blood pressure in response to RFEMF exposure.*
Walters et al., 2000	*94 GHz, 1 kHz pulsed*	*3 s; 9000 to 17500 W/m^2*	*Mid-back*	*The average power density to evoke a threshold sensation of pain was 12500 W/m^2 for a 3 s exposure. This corresponds to a mean increase in surface temperature of 9.9^{o}C from pre-exposure skin temperature (34.0^{o}C) to a threshold temperature of 43.9^{o}C at the end of 3 s.*
Walters et al., 2004	*94 GHz, 1 kHz pulsed*	*4 s or 3 min; 1750 or 10000 W/m^2*	*Forearm skin*	*RFEMF exposure caused a bi-phasic temperature response, with the second phase resulting from local alterations in blood flow. Reduced blood flow resulted in increased peak tissue temperatures.*

Risk-of-bias assessment for human studies on skin temperature changes, pain and warmth sensations

Table 4.2: Summary of risk-of-bias judgements (low risk, probably low risk, probably high risk, high risk) for each determinant for each included human study.

Source	Study design	Blinding	Attrition/exclusion	Exposure assessment	Selective reporting	Conflict of interest	Other	Overall study Risk of Bias
Alekseev et al., 2003								
Alekseev et al., 2005								
Blick et al., 1997								
Gustrau and Bahr, 2002								
Hendler and Hardy, 1960								
Nelson et al., 2003								
Partyla et al., 2017								
Radzievsky et al., 1999								
Walters et al., 2000								
Walters et al., 2004								
Overall Risk of Bias by domain								

Risk of bias categories: low risk (green), probably low risk (yellow), probably high risk (orange), high risk (red).

All human studies were experimental studies whereby either skin temperature measurements or thermal perception thresholds were assessed in volunteers, with a relatively small number of subjects. While skin temperature changes are fundamentally important for the possible occurrence of a heat-pain sensation or temperature-induced tissue damage (See section 4.2), tissue temperature changes are not considered a direct adverse health outcome by themselves. Similarly, a warmth sensation may be evidence of a biological effect, but it is not considered an adverse health effect. Thus, the quality and strength of evidence for skin temperature changes and a warmth sensation were not assessed as these are not adverse health outcomes. Although complimentary research has demonstrated tissue damage can occur from elevated tissue temperatures (See section 4.2), no relevant human studies assessed tissue damage in response to millimeter-wave RFEMF exposure (likely due to ethical reasons). The only adverse health effect identified from the available human RFEMF studies relates to the occurrence of a heat pain sensation in human skin from high intensity RFEMF exposure in one study (Walters et al., 2000), where skin temperature exceeded 43^{o}C.

Quality and Strength of Evidence for Heat-Pain sensation from millimeter-wave RFEMF exposure

The initial Quality of Evidence rating for human experimental studies was assumed to be "High". However, only one study with 10 subjects assessed the heat-pain threshold in humans from 94 GHz RFEMF (Walters et al., 2000). This study did not indicate blinding of the researchers or the subjects in the experimental protocol. The lack of blinding is of lower concern for studies that measure skin temperature or blood perfusion due to the direct nature of the measurement, but it is of greater concern for studies that are based on subjective perceptions of pain thresholds, where knowledge/expectations of exposure may alter perceived response thresholds such as in the case of this study. This study also failed to implement statistical analysis as the authors simply reported temperature measurement data and a pain threshold response in relation to various exposure conditions. For these reasons, the Risk of Bias for this adverse health outcome was rated as "Probably Low", resulting in a downgrade by one level in the Quality of Evidence. The Quality of Evidence was further downgraded by one level for Indirectness as the exposure levels required to elicit these effects are far above existing human exposure limits and are unlikely to be experienced by humans. No other downgrades were implemented for Inconsistency or Imprecision. The overall Quality of Evidence for an association between millimeter-wave RFEMF exposure and a heat-pain sensation was therefore rated as "Low". Complimentary research using other heat sources has demonstrated the occurrence of a heat-pain response in humans when skin temperature exceeds 42-43^{o}C (See section 4.2). Therefore, the Strength of Evidence for an association between millimeter-wave RFEMF exposure and a heat-pain sensation was rated as "Sufficient" based upon an established mechanism. It is important to note that there is no evidence from existing studies of an altered heat-pain sensation when skin temperature does not exceed 42^{o}C.

Table 4.3: Summary of findings, quality of evidence, and strength of evidence for human studies assessing heat pain sensation in response to millimeter-wave RFEMF exposure.

Factor	**Rating**	**Basis**
Risk of Bias across Studies	-1	All subjects were exposed to the same treatment, making the randomization of allocation redundant. No information was provided regarding concealment of exposure conditions and blinding of researchers was lacking. No statistics were applied.
Indirectness	-1	Direct data on humans. The exposure levels required to elicit these effects are far above existing Canadian and international exposure limits and are considered unlikely to be experienced in normal living and working environments.
Inconsistency	0	Responses were similar across subjects. Results are consistent with complementary research on heat pain (See section 4.2).

Imprecision	0	Only one human study conducted using RFEMF.
Overall Quality of Evidence	Low	"High" + (-2) = "Low"
Summary of findings from qualitative analysis	N/A	A consistent exposure-response relationship was observed that was dependent on skin temperature changes.
Overall Strength of Evidence	Sufficient	While only one study was conducted in humans, the results are biologically plausible and consistent with complementary heat pain results from non-RFEMF studies (Section 4.2).

Mammalian Studies

A total of 91 studies were identified and included for analysis that assessed health or biological effects in experimental animals after exposure to RFEMF in the 6 to 300 GHz frequency range. Most of these studies fall into one of the following categories: i) RFEMF-induced skin and colonic temperature elevation and impacts on the cardiovascular system (e.g. heart rate and blood pressure); ii) hypoalgesic effects of RFEMF; iii) ocular temperature elevation, corneal damage and cataracts; iv) immune system; v) reproductive system effects; vi) cancer and genotoxicity; and (vii) other studies.

Temperature elevation and cardiovascular outcomes

A series of studies examined the impact of millimeter-wave RFEMF exposure on cardiovascular outcomes such as heart rate, blood pressure, respiratory rate and skin blood perfusion in anesthetized rats. Frei et al. (1989) assessed the physiological and thermoregulatory responses of rats exposed to 9.3 GHz RFEMF. The authors found the time required to increase colonic temperature by 1^{o}C increased by ~50% compared to exposures at frequencies below 6 GHz (at the same incident power density of 300 or 600 W/m^2), while ipsilateral subcutaneous and tympanic temperatures were markedly higher than colonic temperature, when compared to exposures at frequencies below 6 GHz (Frei et al. 1988). Heart rate was found to increase during exposure by 20 beats per minute relative to pre-exposure, but no differences were found between continuous and pulsed RFEMF exposure at the same time-averaged power density. This study concluded that the frequency markedly affected the heat distribution and physiological responses of irradiated animals. In a related study, Frei et al. (1992) exposed rats to 9.3 GHz RFEMF at a power density of either 590 or 790 W/m^2 in both the E- and H-orientation and found that while orientation affected the absorbed dose rate, when exposures were corrected for dose rate there were no differences in heart rate or mean arterial pressure between exposures in the E- or H-orientation. In a follow-up study, Frei et al. (1995) exposed anesthetized rats to 35 GHz RFEMF at an intensity of 750 W/m^2 until death. During exposure the authors monitored temperature at 5 sites and monitored cardiovascular and respiratory changes. The authors found that ipsilateral subcutaneous and tympanic temperatures were markedly higher than colonic and tail temperatures and mean arterial pressure was found to increase until a subcutaneous temperature of 42^{o}C (and a colonic temperature of 40.3^{o}C) was reached, then declined until circulatory shock occurred at a mean arterial pressure of 75 mmHG. Similar results were observed at 10,

35 and 94 GHz (Jauchem et al., 1999, 2000; Millenbaugh et al., 2006), however exposure at higher frequencies caused a greater ratio of skin/subcutaneous tissue heating relative to colonic temperature elevation. Millenbaugh et al (2006) concluded that core body heating was the primary determinant of hemodynamic collapse, however excessive superficial heating could exacerbate colonic heating and induce circulatory failure at a lower colonic temperature once a colonic temperature threshold was exceeded.

A series of studies was undertaken to understand the mechanisms and factors involved in the circulatory shock induced by intense RFEMF exposure. Ryan et al. (1996) exposed anesthetized rats to 35 GHz RFEMF at a power density of 750 W/m^2 until mean arterial pressure dropped to 75 mmHg (the threshold for circulatory shock in rats), then ceased exposure and treated the animals with either saline or L-NAME (a nitric oxide synthase inhibitor). L-NAME treatment caused a slight increase in mean arterial pressure but did not alter survival time. In a related study, Ryan et al. (1997b) pre-treated rats for 14 days with L-NAME, then exposed anesthetized animals to 35 GHz RFEMF at 750 W/m^2 until their mean arterial pressure reached 75 mmHg. The authors reported that pre-treatment with L-NAME caused a greater initial increase in mean arterial pressure and decreased the time for mean arterial pressure to drop to 75mmHg, but also did not alter survival time. Ryan et al. (1997c) tested whether co-treatment with SNAP, a nitric oxide donor, could modulate the hypotension induced by RFEMF exposure. Based on this series of studies, the authors reported that exogenous nitric oxide had no effect on modulating RFEMF induced hypotension. The authors concluded that nitric oxide does not appear to be responsible for the hypotensive response to 35 GHz RFEMF exposure.

Jauchem et al. (1997) exposed male rats to 35 GHz RFEMF at a power density of 750 W/m^2 and co-treated them with esmolol, a β-1 adrenoreceptor antagonist, to examine the role of the sympathetic nervous system on the heat stress response. Esmolol was found to decrease heart rate, but mean arterial pressure was found to decline to 75 mmHg at a lower subcutaneous/colonic temperature. In a similar study, Jauchem et al. (2004) co-treated 35 GHz RFEMF-exposed rats with diphendramine and cimetidine, H-1 and H-2 histamine receptor antagonists, respectively. Pre-treatment caused decreased initial mean-arterial pressure and delayed the depression of mean arterial pressure after RFEMF heating, however it did not alter survival time. The authors concluded that histamine receptors do not mediate the hypotensive response to RFEMF heating. Ryan et al., (2002) co-treated 35 GHz RFEMF-exposed rats with the platelet-activating factor (PAF) antagonist, WEB 2086, either before or after RFEMF exposure, to explore whether PAF was associated with the hypotensive state associated with microwave heating. The authors found that treatment with a PAF receptor antagonist did not change the survival time, the RFEMF temperature elevation kinetics or mean arterial pressure changes, leading them to conclude that PAF is not associated with the hypotensive response induced by intense RFEMF exposure.

Ryan et al. (1997a) assessed the impact of age on the circulatory hypotension from intense RFEMF exposure at 35 GHz, concluding that the age of rats does not alter the thermal or cardiorespiratory responses to microwave heating. Kalns et al. (2000) assessed an oxidative stress biomarker (3-nitrotyrosine, 3-NT) in rats after either short-term (up to 20 min) or prolonged (20 to ~45min) exposure to 35 GHz RFEMF and found that 3-NT increased in lung, liver and blood plasma after short exposures at 750

W/m^2, however prolonged exposure only resulted in increased 3-NT in blood plasma. The authors concluded that oxidative stress occurs in many organs in response to microwave heating, however systemic oxidative stress does not appear to be correlated to circulatory failure from intense RFEMF exposure. Sypniewska et al. (2010) assessed plasma proteins from 35 GHz RFEMF-exposed rats and rats exposed to environmental heat, where colonic temperatures reached 41^{o}C. The authors reported altered expression of several proteins in blood plasma associated with inflammation, oxidative stress and energy metabolism and the release of macrophage-activating mediators from both environmental heat and RFEMF exposure. In a related study, Jauchem et al. (2016) assessed skin histology and liver enzymes and electrolytes in the blood of rats exposed to 35 GHz RFEMF for short (~19 min) or prolonged exposure (~38 min) at 750 W/m^2 relative to sham controls. The authors reported changes in serum glucose, creatinine, uric acid and anion gap from prolonged RFEMF exposure that are consistent with changes observed during heat-stroke from environmental heat. Histology revealed hemorrhage and congestion of blood vessels in the dermis and subcutis of irradiated skin in the absence of a tissue burn.

Zavgorodny et al. (2000) assessed the potential antihypertensive effects of millimeter-wave RFEMF in spontaneously-hypertensive rats by monitoring their heart rate and mean arterial pressure after repeated daily exposure of the rat ear or knee joint to 42.253 GHz RFEMF at a power density of 500 W/m^2 for 15 min/day for up to 10 days. The authors reported that RFEMF exposure reduced both mean arterial blood pressure and heart rate, with effects occurring more rapidly with exposure to the ear.

Table 4.4: Summary of mammalian study characteristics on cardiovascular endpoints

Source	***Species***	***Frequency***	***Exposure duration and intensity***	***Tissue exposed***	***Findings***
Frei et al., 1989	*Rat, female*	*9.3 GHz, continuous and pulsed at 0.5 kHz*	*10 to 45 min per cycle; 300 or 600 W/m^2, WBA-SAR of 9.3 or 18.6 W/kg*	*Whole body*	*Ipsilateral subcutaneous and tympanic temperatures were markedly elevated above colonic temperature as core body temperature was increased from 38.5 to 39.5^{o}C by RFEMF exposure. Mean arterial pressure and respiratory rate remained unchanged as colonic temperature increased from 38.5 to 39.5^{o}C, but heart rate increased as colonic temperature increased. No differences were observed between continuous and pulsed RFEMF exposure of the same magnitude.*
Frei et al., 1992	*Rat, male*	*9.3 GHz*	*~15 min, until a colonic temperature of 39.5^{o}C*	*Whole body*	*Ipsilateral subcutaneous temperature and tail temperature were markedly elevated above contralateral subcutaneous, tympanic and colonic temperatures. No significant differences were observed between E- and H-*

			was achieved; 590 or 790 W/m^2, WBA-SAR of 12.5 W/kg		*field orientation. Mean arterial pressure and heart rate increased significantly during irradiation.*
Frei et al., 1995	*Rat, male*	*35 GHz*	*32 to 69 min (until death); 750 W/m^2, WBA-SAR of 13.0 W/kg*	*Whole body*	*Ipsilateral subcutaneous temperature was markedly elevated above contralateral subcutaneous, tail and colonic temperatures. Mean arterial pressure increased at subcutaneous temperature increases below 41.5^{o}C, but then decreased at temperatures above 42^{o}C. Heart rate increased continuously as temperature increased. Death occurred at a subcutaneous temperature of 48.0^{o}C and colonic temperature of 40.3^{o}C.*
Jauchem et al., 1997	*Rat, male*	*35 GHz*	*0 to 80 min (until death); 750 W/m^2, WBA-SAR of 13 W/kg*	*Whole body*	*Co-treatment with esmolol, a β1-adrenoreceptor antagonist, caused a decreased heart rate. Mean arterial pressure reached 75 mmHg at a lower subcutaneous and colonic temperature, but had a minimal effect on subcutaneous and colonic temperature increases. Esmolol co-treatment decreased survival time from continuous RFEMF induced exposure.*
Jauchem et al., 1999	*Rat, male*	*94 GHz*	*0 to ~40 min (until death); 750 W/m^2*	*Whole body*	*Ipsilateral subcutaneous temperature increased to a greater extent and more quickly than colonic temperature. Mean arterial pressure increased until a subcutaneous temperature of ~42^{o}C was reached, then decreased until death (due to hypotension) as exposure continued. Heart rate increased throughout the duration of exposure.*
Jauchem et al., 2000	*Rat, male*	*10 GHz*	*0 to 35 min (until death); 670 W/m^2, WBA-SAR of 12 W/kg*	*Whole body*	*Ipsilateral subcutaneous temperature increased to a greater extent and more quickly than colonic temperature. Mean arterial pressure increased until a subcutaneous temperature of ~42^{o}C was reached, then decreased until death (due to hypotension) as exposure continued. Heart rate increased throughout the duration of exposure.*
Jauchem et al., 2004	*Rat, male*	*35 GHz*	*0 to 65 min*	*Whole body*	*Co-treatment with H-1 (diphendramine) and H-2 (cimetidine) histamine receptor*

			(until death); 750 W/m^2, WBA-SAR of 13 W/kg		*antagonists after sustained RFEMF exposure did not reverse hypotension. Pre-treatment with these antagonists reduced initial mean arterial pressure prior to RFEMF exposure and delayed the drop in mean arterial pressure after RFEMF exposure but did not alter survival time.*
Jauchem et al., 2016	*Rat, male*	*35 GHz*	*0 to 45 min (until death); 750 W/m^2, WBA-SAR of 13 W/kg*	*Whole body*	*Ipsilateral subcutaneous temperature increased to a greater extent and more quickly than colonic temperature. Mean arterial pressure increased until a subcutaneous temperature of ~42^{o}C was reached, then decreased until death (due to hypotension) as exposure continued. Heart rate increased throughout the duration of exposure.*
Kalns et al., 2000	*Rat, male*	*35 GHz*	*0 to 60 min; 750 W/m^2, WBA-SAR of 13 W/kg*	*Whole body*	*Short duration exposure to RFEMF, where colonic temperatures were increased but circulatory shock had not yet occurred, caused an accumulation of 3-NT in lung, liver and plasma. AT RFEMF exposure durations capable of inducing circulatory shock, 3-NT levels returned to baseline in these tissues with the exception of blood leukocytes. The authors concluded that RFEMF heating caused oxidative stress in many organs but prolonged exposure either cleared nitro adducts or they were no longer produced after shock ensued.*
Millenbaugh et al., 2006	*Rat, male*	*35 or 94 GHz*	*0 to 90 min (until death); 750-900 W/m^2*	*Whole body*	*Ipsilateral subcutaneous and skin temperatures increased faster than colonic temperature, with 94 GHz causing a larger skin surface and subcutaneous temperature increase than 35 GHz RFEMF. Heart rate increased throughout the duration of the exposures. Hemodynamic collapse was primarily related to colonic temperature, however elevated skin and subcutaneous temperatures could cause a hemodynamic collapse at lower colonic temperatures once a certain colonic temperature threshold has been reached.*
Ryan et al., 1996	*Rat, male*	*35 GHz*	*0 to 46 min; 750 W/m^2*	*Whole body*	*Co-treatment with L-NAME (a nitric oxide synthase inhibitor) when RFEMF exposure caused mean arterial pressure to drop to 75 mmHg caused a slight increase in MAP but did not alter survival time. The authors concluded that nitric oxide does not appear to be responsible for the hypotensive response.*
Ryan et al., 1997a	*Rat, male*	*35 GHz*	*0 to 55 min; 750 W/m^2,*	*Whole body*	*No differences were observed in superficial or colonic temperatures, heart rate, mean*

			WBA-SAR of 13.0 W/kg		*arterial pressure or survival time among young, middle-aged or older rats.*
Ryan et al., 1997b	*Rat, male*	*35 GHz*	*0 to 40 min; 750 W/m^2*	*Whole body*	*Pre-treatment for 14 days with L-NAME (a nitric oxide synthase inhibitor) caused a greater initial increase in mean arterial pressure (MAP) and decreased the time for a drop in MAP to 75 mmHg, but did not alter survival time. The authors concluded that nitric oxide does not appear to be responsible for the hypotensive response.*
Ryan et al., 1997c	*Rat, male*	*35 GHz*	*0 to 55 min; 750 W/m^2*	*Whole body*	*Co-treatment of RFEMF exposed rats with a nitric oxide donor (SNAP), either before RFEMF exposure or after mean arterial pressure from RFEMF exposure dropped to 75 mmHg, had no effect on mean arterial pressure changes or survival. The authors concluded that exogenous nitric oxide does not affect hypotension induced by RFEMF exposure.*
Ryan et al., 2002	*Rat, male*	*35 GHz*	*0 to 55 min; 750 W/m^2, WBA-SAR of 13.0 W/kg*	*Whole body*	*Co-treatment of RFEMF exposed rats with a platelet-activating factor antagonist (WEB 2086), either before exposure or after mean arterial pressure from RFEMF exposure dropped to 75 mmHg, had no effect on survival time or RFEMF-induced temperature or mean arterial pressure changes. The authors concluded that platelet-activating factor does not mediate the hypotension induced by RFEMF exposure.*
Sypniewska et al., 2010	*Rat, male*	*35 GHz*	*~46 min (until a colonic temperature of 41°C was reached); 750 W/m^2, WBA-SAR of 13.0 W/kg*	*Whole body*	*Differential expression (upregulation) of proteins associated with inflammation, oxidative stress and energy metabolism was observed in macrophages cultured with plasma from RFEMF and environmental heat (EH)-exposed animals. The authors concluded that both EH and RFEMF, at levels which cause a colonic temperature increase of 41-42°C, can induce the release of macrophage-activating mediators into the plasma of rats.*
Zavgorodny et al., 2000	*Rat*	*42.25 GHz*	*15 min, 500 W/m^2*	*Ear, nose or knee joint*	*Heart rate and blood pressure were reported to decline after 3-5 days exposure to RFEMF in spontaneously hypertensive rats.*

Risk-of-bias assessment of mammalian studies on skin temperature changes and cardiovascular effects

Table 4.5: Summary of risk-of-bias judgements (low, probably low, probably high, high) for each risk of bias item for each included mammalian study on cardiovascular responses to RFEMF in the 6 to 300 GHz frequency range.

Source	Study design	Blinding	Attrition/exclusion	Exposure assessment	Selective reporting	Conflict of interest	Other	Overall study Risk of Bias
Frei et al., 1989								
Frei et al., 1992								
Frei et al., 1995								
Jauchem et al., 1997								
Jauchem et al., 1999								
Jauchem et al., 2000								
Jauchem et al., 2004								
Jauchem et al., 2016								
Kalns et al., 2000								
Millenbaugh et al., 2006								
Ryan et al., 1996								
Ryan et al., 1997a								
Ryan et al., 1997b								
Ryan et al., 1997c								
Ryan et al., 2002								
Sypniewska et al., 2010								
Zavgorodny et al., 2000								
Overall Risk of Bias by domain								

Risk of bias categories: low risk (green), probably low risk (yellow), probably high risk (orange), high risk (red).

Most mammalian studies on cardiovascular endpoints have been conducted using anesthetized male rats where the relationship between skin and colonic temperature, heart rate and mean arterial pressure were assessed. From these studies, death resulting from severe hypotension was identified as an adverse health outcome. Since tissue temperature elevation below the heat-pain threshold (~42-43°C in humans, see section 4.2) is not considered an adverse health outcome, only RFEMF-induced hypotension was assessed for Quality and Strength of Evidence for an association between RFEMF exposure and the occurrence of this adverse health effect.

Quality and Strength of Evidence for hypotensive effects from millimeter-wave RFEMF exposure
The initial Quality of Evidence rating for mammalian experimental studies was established as "High". Most relevant studies on this endpoint did not randomly allocate animals among treatment groups or employ concealment during exposure. None of these studies incorporated blinding into their experimental protocol, however this was of minor concern as direct tissue temperature, heart rate and blood pressure endpoints are direct measurements that are not particularly susceptible to bias from a lack of blinding. While all studies reported dosimetric information, in most cases such information was lacking in detail with respect to heterogeneity of exposure across the animal. For these reasons, the Risk of Bias for this endpoint was rated as "Probably Low", resulting in a downgrade by one level in the Quality of Evidence. The Quality of Evidence was further downgraded by one level for Indirectness as the exposure levels required to elicit these effects are far above existing human exposure limits and are unlikely to be experienced by humans. No other downgrades were implemented for Inconsistency or Imprecision. The overall Quality of Evidence for an association between millimeter-wave RFEMF exposure and hypotensive cardiovascular response was therefore rated as "Low". The Strength of Evidence for an association between millimeter-wave RFEMF exposure and a hypotensive cardiovascular response was rated as "Sufficient" due to the highly consistent responses observed across studies.

The effects of RFEMF-induced hyperthermia and heat-stroke appear to share the same mechanisms as environmental heat and/or exercise induced cardiorespiratory effects, with colonic temperatures acting as the primary driver for systemic cardiovascular responses (Adair and Black, 2003). However, the distribution of tissue heating from RFEMF is dependent upon the carrier frequency and physiological responses can be somewhat altered by differences in the distribution of temperature elevation and peripheral blood diffusion. There is compelling evidence that intense RFEMF exposure results in both localized and systemic tissue heating, resulting in eventual hemodynamic collapse if exposures are prolonged. Such exposures, conducted on anesthetized rats, observed animal death from hypotension when colonic temperatures reached 41-42^{o}C but localized tissue temperatures often far exceeded the tissue damage (see section 4.2) and heat pain thresholds (see section 4.2). No evidence of adverse cardiorespiratory responses was reported in existing studies for either colonic or superficial (skin, subcutaneous) temperature elevations that remained below 1^{o}C.

Table 4.6: Summary of findings, quality of evidence, and strength of evidence for mammalian studies assessing hemodynamic collapse in response to millimeter-wave RFEMF exposure.

Factor	**Rating**	**Basis**
Risk of Bias across Studies	-1	Most studies utilized a small number of animals and lacked procedures for randomized allocation or exposure group concealment. Blinding was typically not employed but endpoints consisted of direct temperature and blood pressure measurements. No statistics were applied.

Indirectness	-1	Mammalian data are empirically recognized as direct evidence of human health data, though temperature responses may differ by frequency, intensity and distribution. The exposure levels required to elicit these effects are far above existing Canadian and international exposure limits and are considered unlikely to be experienced in normal living and working environments.
Inconsistency	0	Heart rate and mean arterial pressure change in relation to colonic temperature were consistent across studies.
Imprecision	0	Temperature and cardiovascular changes were consistent across studies. Responses may be more exaggerated in anesthetized animals. Most studies have been conducted by one group.
Overall Quality of Evidence	Low	"High" + (-2) = "Low"
Summary of findings from qualitative analysis	N/A	A consistent exposure-response relationship was observed across studies.
Overall Strength of Evidence	Sufficient	While all relevant RFEMF studies were conducted by one group, the results were remarkably consistent. These results are biologically plausible and consistent with complementary hyperthermia research.

Hypoalgesic (pain suppression) effects

A series of studies by Ziskin et al. have investigated the ability of millimeter-wave RFEMF to activate peripheral neuroreceptors and induce a hypoalgesia (pain suppression) response. Rojavin and Ziskin (1997) anesthetized mice with either ketamine or chloral hydrate, then exposed the noses of mice to 61.22 GHz RFEMF for 15 min at a power density of 150 W/m^2. The nose of mice was chosen as the exposure tissue as it is highly innervated with peripheral nerves and exposure to RFEMF only caused a 1.6^oC peak temperature elevation in the nose at the end of the exposure period. The authors observed that treatment with RFEMF caused a 50% increase in duration (~15 s) of anaesthesia for both anesthetics. When pre-treated with naloxone (an opioid receptor antagonist), the RFEMF-induced enhanced duration of anesthesia was abolished leading the authors to conclude that RFEMF exposure either caused the release of endogenous endorphins or it enhanced the opioid signalling pathways. In a related study, Rojavin et al. (1998) administered a pruritic (itching) agent to the back of mice before exposure of the noses of mice to 61.22 GHz RFEMF, then scratching activity was monitored for 90 min post-exposure. The authors reported that RFEMF exposure caused a reduction in scratching, and thus the pruritic response. When naloxone was administered prior to RFEMF exposure, an increase in scratching was observed in the RFEMF-treated mice relative to sham and placebo-controls, leading the authors to conclude once again that RFEMF exposure may have released endogenous opioids to induce an antipruritic response.

Radzievsky et al. (2000) further assessed RFEMF-induced hypoalgesia using the cold-water tail flick test as a model of experimental pain. In this study the authors exposed either the nose, the glabrous skin of the right footpad or the hairy skin (non-glabrous) of the mid-back of restrained mice to sham or 61.22 GHz RFEMF for 15 min at 150 W/m^2, then measured the response time for the animal to flick its tail when immersed in cold-water. The authors found that RFEMF exposure to the nose or footpad caused significantly greater hypoalgesic responses, when assessed immediately after exposure, than did RFEMF exposure to the back or sham exposure, possibly due to their higher level of innervation. Radzievsky et al. (2001) later demonstrated that sciatic nerve transection abolished the hypoalgesic response of RFEMF exposure to the footpad, providing further evidence of the involvement of peripheral neuroreceptors in the hypoalgesic response from RFEMF exposure. Radzievsky et al. (2004a) examined if the hypoalgesic effects of RFEMF exposure on the chronic non-neuropathic type of pain that is mimicked by the cold-water tail flick test also extend towards acute and chronic neuropathic pain. The authors exposed the nose of mice to 61.22 GHz RFEMF for 15 min at a power density of 133 W/m^2 (which caused a maximum temperature elevation in the nose of 1^{o}C), then assessed acute pain using the hot-water tail flick test, chronic non-neuropathic pain using the cold-water tail flick test and chronic neuropathic pain using chronic constriction injury to the sciatic nerve. The authors reported that RFEMF caused the greatest hypoalgesic response on chronic non-neuropathic pain, but was less effective for acute pain and largely ineffective for neuropathic pain. Irradiation of the nose area with an infra-red laser to cause the same maximum temperature increase did not induce a hypoalgesic response leading the authors to conclude that the response was not solely driven by thermal influences. Finally, Radzievsky et al. (2008) assessed the hypoalgesic response to other millimeter-wave frequencies. The authors exposed the noses of mice to either sham or 42.25, 53.57, 56.22, 61.22 or 66.22 GHz RFEMF for 15 min at a power density of 133 W/m^2, then assessed the hypoalgesic response using the cold-water tail flick test (for chronic non-neuropathic pain) and the wire surface test (for chronic neuropathic pain). The authors reported that 61.22 GHz treatment induced the largest hypoalgesic response (~2-fold delay in response time) for chronic non-neuropathic pain relative to other frequencies which ranged from ~1.33-1.6-fold. The hypoalgesic effect of 61.22 GHz on chronic neuropathic pain was modest (~1.5 fold) and delayed (1-10 days after exposure). Pre-treatment with selective δ- and κ-opioid receptor antagonists partially reversed the hypoalgesia induced by RFEMF.

Table 4.7: Summary of mammalian study characteristics on hypoalgesic endpoints.

Source	***Species***	***Frequency***	***Exposure duration and intensity***	***Tissue exposed***	***Findings***
Radzievsky et al., 2000	*Mouse, male*	*61.22 GHz*	*15 min; 150 W/m^2*	*Nose, footpad or mid-back*	*Greater hypoalgesia was observed following exposure to the nose or footpad, relative to the mid-back. The authors speculated that this was due to a greater degree of innervation in the nose and footpad.*

Radzievsky et al., 2001	*Mouse, male*	*61.22 GHz*	*15 min; 150 W/m²*	*Footpad*	*RFEMF exposure increased the latency time for tail flick when immersed in cold water. Transection of the sciatic nerve which caused deafferentation of the peripheral nerves in the footpad abolished this effect. The response was similar, but slightly reduced, when the contralateral foot was exposed.*
Radzievsky et al., 2004a	*Mouse, male*	*61.22 GHz*	*15 min; 133 W/m²*	*Nose*	*A single RFEMF exposure to the nose, associated with a 1°C temperature increase, was found to suppress chronic non-neuropathic pain but was less effective at suppressing acute pain and had no effect on chronic neuropathic pain. Local heating of the nose by laser irradiation did not produce similar hypoalgesic effects.*
Radzievsky et al., 2008	*Mouse, male*	*42.25, 53.57, 56.22, 61.22 or 66.22 GHz*	*15 min; 133 W/m²*	*Nose*	*Maximum hypoalgesic effect was observed at a frequency of 61.22 GHz. Pre-treatment of mice with κ- and δ-opioid receptor antagonists suppressed RFEMF-induced hypoalgesia.*
Rojavin and Ziskin, 1997	*Mouse, male*	*61.22 GHz*	*15 min; 150 W/m²*	*Nose*	*RFEMF exposure increased the length of time for mice to recover from either ketamine- or chloral hydrate-induced anaesthesia. Pre-treatment with naloxone abolished this effect. The authors concluded that RFEMF exposure either releases endogenous endorphins or enhances the activity of the opioid signalling pathway.*
Rojavin et al., 1998	*Mouse, male*	*61.22 GHz*	*15 min; 150 W/m²*	*Nose*	*RFEMF exposure caused a reduction in scratching behaviour in mice injected with a pruritogenic agent. Pre-treatment of RFEMF-exposed animals with (-)-naloxone (1 mg/kg, s.c.) caused a reduction in the anti-pruritogenic effect.*

Risk-of-bias assessment for mammalian studies on hypoalgesic effects

Table 4.8: Summary of risk-of-bias judgements (low, probably low, probably high, high) for each risk of bias item for each of the included mammalian studies on hypoalgesic responses to RFEMF in the 6 to 300 GHz frequency range.

Source	Study design	Blinding	Attrition/exclusion	Exposure assessment	Selective reporting	Conflict of interest	Other	Overall study Risk of Bias
Radzievsky et al., 2000								
Radzievsky et al., 2001								
Radzievsky et al., 2004a								
Radzievsky et al., 2008								
Rojavin and Ziskin, 1997								
Rojavin et al., 1998								
Overall Risk of Bias by domain								

Risk of bias categories: low risk (green), probably low risk (yellow), probably high risk (orange), high risk (red).

Most mammalian studies on hypoalgesia have been conducted in male mice where randomized allocation and concealment during exposure was not implemented. Most studies incorporated blinding into their experimental protocol for endpoint analysis and target tissue temperature was measured or monitored. All mammalian studies were conducted by one laboratory and reported that exposure of highly innervated superficial tissue to 61.22 GHz RFEMF for 15 min at a power density of 133-150 W/m^2 could induce a modest hypoalgesic response that appeared to be associated with either the release of endogenous opioids or activation of the opioid signaling pathway. These effects did not appear to be temperature-induced as temperature elevations in the exposed tissues did not exceed 1.0-1.6^{o}C. On the contrary, one clinical study assessed millimeter-wave-induced hypoalgesic responses in humans but found no evidence to support a hypoalgesic response in blinded subjects (Partyla et al., 2017). Since these findings did not demonstrate an adverse health effect from exposure to RFEMF, this endpoint was not assessed for Quality and Strength of Evidence.

Immune system effects

Several studies have assessed the ability of millimeter-wave RFEMF to affect a variety of immune-system related endpoints in a variety of animal models. Liddle et al. (1980) exposed *S. pneumoniae* infected female mice to 9 GHz pulsed RFEMF for 2 h/day for 5 days at a power density of 100 W/m^2, then assessed hematology and differential blood cell counts, circulating antibody titres and survival time. No changes were observed in hematology or blood counts but circulating antibody titres were found to be statistically higher (5%) in the RFEMF exposed animals and the survival time was slightly increased (although mortality at 10-days post exposure was not significantly different). In a follow up study using the same protocol but at a power density of 10 W/m^2, no significant differences were observed for any endpoint (Liddle et al., 1986).

Logani et al. (2002b) investigated the ability of 42.2 GHz RFEMF to modulate the immune system of male mice challenged with the chemotherapeutic agent, cyclophosphamide (CPA). Compared to vehicle-controls, treatment of mice with CPA (200 mg/kg, i.p.) caused a rapid decline in both blood leukocytes and bone marrow cell counts. Pre-treatment of restrained mice with whole-body RFEMF exposure for 30 min/day for 3 days at a power density of 310 W/m^2 prior to CPA-administration provided no protection from CPA-induced leukopenia and did not alter delayed-type hypersensitivity response in mouse skin. Logani et al. (2002a) exposed the backs of hairless female mice to 42.2 GHz RFEMF for 30 min/day, 5 days /week for 3 weeks at 310 W/m^2 either before or after co-treatment with CPA, then examined blood catalase activity to determine whether RFEMF may exert immunomodulatory effects by modulating antioxidant defense. The authors reported that treatment with RFEMF either before or after CPA exposure had no effect on blood catalase activity.

Novoselova et al. (1999) assessed the ability of millimeter-wave RFEMF to modulate the immune response by assessing pro-inflammatory cytokine (TNF-α) production in splenic T-cells and mitogenic activity in peritoneal macrophages after a 5 h exposure to 8.15-18 GHz broad band RFEMF. The authors observed increased TNF-α production in both peritoneal macrophages and splenic T-cells and increased mitogenic activity of T-cells. Co-treatment with lipid-soluble antioxidants further enhanced this response leading the authors to conclude that low level millimeter-wave RFEMF stimulated the immune system. In a series of follow-up studies, Makar et al. (2003, 2005, 2006) investigated the impact of 42.2 GHz RFEMF exposure on splenic leukocytes in CPA-treated mice. In these studies, mice were treated with CPA, which caused profound suppression of splenic $CD4^+$ T-cell proliferative capacity (in vitro), and an increase in splenic NK cell activation but reduced NK cell cytolytic activity. Co-treatment with 42.2 GHz RFEMF to the nose of mice at 310 W/m^2 for 30 min/day for 3 days caused an amelioration of CPA-induced suppression of splenic $CD4^+$ T-cell proliferative capacity, a further augmentation of splenic NK cell activation and a recovery of splenic NK cell cytolytic activity (Makar et al. 2003; 2005). The authors also examined the ability of 61.22 GHz RFEMF (30 min/day for 3 days at 310 W/m^2) to modulate the immune response of splenic macrophages and T cells after co-treatment with CPA. The authors reported that RFEMF exposure caused increased TNF-a production in splenic macrophages, increased IFN-δ production in splenocytes and enhanced proliferative capacity of T-cells after treatment with CPA. The authors concluded that RFEMF exposure caused an increased recovery process of the immune system after CPA treatment (Makar et al., 2006).

Radzievsky et al. (2004b) inoculated male mice with B16 melanoma cells, then administered 61 GHz RFEMF at 13.3 W/m^2 to the nose for 15 min daily for 5 days while animals were restrained, starting on day 1, 5 or 10 after inoculation. The authors noted no changes in tumor growth when RFEMF was initiated at day 0, reduced tumor growth when RFEMF was started on day 5 and increased tumor growth rate when RFEMF was started on day 10 after inoculation. The 5-day protocol was repeated several times and the results were consistent. Pre-treatment with naloxone was observed to inhibit this effect. The authors speculated that RFEMF interacts to induce a central-mediated immune response that involves opioid receptors that may interfere with tumor growth. In a similar study, Gapeyev et al. (2019) inoculated male mice subcutaneously into the right thigh with solid Ehrlich carcinoma cells and then irradiated them post-inoculation with 42.2 GHz RFEMF at 1.0 W/m^2 for 20 min/day for 5 days. The authors reported that RFEMF

exposure decreased tumor volume by ~50% and restored thymic fatty acid concentrations close to pre-inoculation values. Co-treatment of tumor-bearing animals with RFEMF and n-3 fatty acid was observed to improve thymus weight. The authors speculated that RFEMF was able to modulate thymic fatty acid composition, which in turn affected the immune system and ultimately the rate of tumor growth.

As extremely high frequency (EHF) RFEMF has often been used in Eastern European medicine for therapeutic purposes, a series of studies by Gapeyev and colleagues sought to understand potential mechanisms behind such treatments. Lushnikov et al. (2004) used zymosan-induced footpaw edema as a model of acute inflammation to study the immunomodulatory effects of millimeter-wave RFEMF exposure. The authors of this study measured hindpaw edema and neutrophil activity in hindpaw exudate after zymosan treatment and co-treatment with 42 GHz RFEMF at 1 W/m^2 for 20 min either 1 h before or after zymosan treatment. The authors observed that hindpaw edema and exudate neutrophil activity were decreased if animals were treated with RFEMF after zymosan administration. Pre-treatment with RFEMF before zymosan challenge did not modify the response. The authors concluded that RFEMF treatment had an anti-inflammatory effect by mediating the activity of neutrophils. Gapeyev et al. (2008) followed up on this work by examining the immunomodulatory response of 37.5 to 70 GHz RFEMF for 0 to 120 min at a power density of 0.1 or 1.0 W/m^2. Local zymosan-induced footpaw edema and skin temperature in mice was reduced by up to 20% at frequencies of 42.2, 51.8, and 65 GHz with the optimal exposure time of 20 min at a power density of 1 W/m^2. The authors also reported that a H1-receptor antagonist (clemastine) abolished the RFEMF-induced amelioration of zymosan-induced footpad edema and a cyclooxygenase inhibitor (sodium diclofenac) in conjunction with RFEMF exposure caused a further decrease in edema. The authors concluded that “arachidonic acid metabolites and histamine are involved in realization of anti-inflammatory effects of low-intensity EHF EMR”. In a follow-up study, Gapeyev et al. (2009) reported that 42.2 to 42.6 GHz RFEMF at 1 to 7 W/m^2 could cause a 19% reduction in zymosan-induced footpad edema and these responses were not modulation dependent. At less effective carrier frequencies of 43.0 and 61.22 GHz, modulation with 0.07 to 0.1 Hz or 20 to 30 Hz could improve the effectiveness of RFEMF amelioration of zymosan-induced footpad edema to a similar level as that of 42.2 GHz RFEMF.

In a related study, Gapeyev et al. (2011) assessed the role of fatty acids in the anti-inflammatory response from 42.2 GHz RFEMF exposure in normal mice and mice injected intra-peritoneally with zymosan to induce peritoneal inflammation. The authors reported that 42.2 GHz RFEMF whole-body exposure for 20 min at 1 W/m^2 increased the levels of polyunsaturated fatty acids (PUFA) in thymic cells from both normal mice and mice with peritoneal inflammation, and decreased monounsaturated fatty acid (MUFA) levels in thymic cells in mice with peritoneal inflammation (though the effect size was quite small). The authors speculated that PUFA metabolites may be acting as lipid messengers that mediate the anti-inflammatory response to RFEMF exposure. Gapeyev et al. (2013) investigated whether RFEMF treatment may have anti-tumor properties through an anti-inflammatory effect on fatty acids. Normal mice or mice injected with Erlich solid carcinoma cells were exposed to 42.2 GHz RFEMF for 20 min/day for 5 days at a power density of 1 W/m^2, then starting 5 days after injection of tumor cells, the fatty acid content of liver, thymus and tumor tissue was assessed. The authors reported, contrary to Gapeyev et al (2011), that RFEMF exposure of normal mice caused an increase in MUFA and a decrease in PUFA in the liver and thymus. In the thymus and in tumor tissue of tumor-bearing animals, RFEMF exposure caused a decrease in PUFA and a decrease

in MUFA. While the effect sizes were rather large in normal mice, they were quite small in tumor-treated animals. Gapeyev et al. (2015) also investigated the ability of RFEMF to alleviate ionizing radiation (IR)-induced changes to the thymus, which are believed to result from the formation of reactive oxygen species (ROS) following IR exposure. In this study, the authors exposed mice to 4 Gy IR alone or 4 Gy combined with exposure to 42.2 GHz RFEMF for 20 min at 1 W/m^2, then assessed the fatty acid content within thymus at various times after exposure. The authors reported that, relative to sham controls, IR caused a short-term increase in fatty acid content in mouse thymus at 4-5 h post-exposure, followed by a long-term decline at 10-30 days' post–exposure. Co-treatment with RFEMF either before or after IR exposure prevented changes to the total fatty acid content of thymus induced by IR exposure but did not appear to affect the relative MUFA or PUFA composition after IR exposure. The authors speculated that RFEMF exposure may have helped restore the thymus by modulating fatty acid levels.

Novoselova et al. (2017) investigated the ability of 8.15 – 18 GHz broad spectrum RFEMF at a very low power density of 0.016 W/m^2 for 1 h to modulate the immune response of mice to toluene inhalation. The authors assessed the cytokine profile and activation of signal transduction pathways in spleen lymphocytes after exposure to toluene inhalation either with or without co-exposure to RFEMF. The authors reported that toluene-inhalation alone activated the NF-κB, SAPK/JNK, IFR-3, p38 MAPK and TLR4 pathways in mouse splenocytes and increased HSP72, IL-1, IL-6 and TNF-α in blood plasma. Exposure to RFEMF alone caused increased levels of IL-6, TNF-α and IFN-δ in blood plasma and activation of the NF-κB, p38 MAPK and TLR4 pathways in splenic lymphocytes. When mice were pre-exposed to RFEMF before toluene-inhalation, the activation levels of plasma cytokines and most signal transduction pathways were closer to the sham values. It is unclear if RFEMF exposure caused an adaptive response or provided a protective response when combined with toluene-exposure. The authors concluded that "…exposure to low-intensity RFEMF exposure may recover immune parameters in mice undergoing inhalation exposure to low-level toluene via mechanisms involving cell signalling".

Table 4.9: Summary of mammalian study characteristics on immune system endpoints.

Source	***Species***	***Frequency***	***Exposure duration and intensity***	***Tissue exposed***	***Findings***
Gapeyev et al., 2008	*Mouse, male*	*37.5 to 70 GHz*	*0 to 120 min; 0.1 to 1.0 W/m^2*	*Whole body*	*Zymosan-induced edema and skin temperature in hindpaw were reduced if animals were co-exposed to RFEMF. Co-treatment with diclofenac, a cyclooxygenase inhibitor, caused an additive decrease in edema whereas co-treatment with the H1 histamine antagonist, clemastine, abolished the RFEMF-induced decrease in edema.*
Gapeyev et al., 2009	*Mouse, male*	*42.2, 43.0 or 61.22 GHz*	*20 min; 1 to 7 W/m^2*	*Whole body*	*Zymosan-induced edema in hindpaw was reduced if animals were co-exposed to RFEMF.*

Gapeyev et al., 2011	*Mouse, male*	*42.2 GHz*	*20 min; 1 W/m²*	*Whole body*	*Thymic cells of normal mice had increased polyunsaturated fatty acids after RFEMF exposure. Mice with zymosan-induced peritoneal inflammation had increased polyunsaturated fatty acids and decreased monounsaturated fatty acids after RFEMF exposure.*
Gapeyev et al., 2013	*Mouse, male*	*42.2 GHz*	*20 min/day for 5 days; 1.0 W/m²*	*Whole body*	*Monounsaturated fatty acid content was increased and polyunsaturated fatty acid content was decreased in all tissues examined in RFEMF-treated normal mice.*
Gapeyev et al., 2015	*Mouse, male*	*42.2 GHz*	*20 min; 1.0 W/m²*	*Whole body*	*X-irradiation caused increased fatty acid content in thymus at 4-5 h post-exposure, but decreased thymic fatty acid content at 10 and 30 days' post-exposure. X-irradiation caused increased polyunsaturated fatty acid content and decreased monounsaturated fatty acid content in thymus at 1 and 10-days post exposure. RFEMF exposure either before or after X-irradiation prevented changes to the total fatty acid content of thymus after X-irradiation.*
Gapeyev et al., 2019	*Mouse, male*	*42.2 GHz*	*20 min/day for 5 days, 1.0 W/m²*	*Whole body*	*Tumor growth was delayed and thymic fatty acid content was restored to pre-cancerous levels in animals inoculated with solid Ehrlich carcinoma cells. Combined treatment with RFEMF and oral n-3 polyunsaturated fatty acids restored thymus weight in tumor-bearing animals.*
Liddle et al., 1980	*Mouse, female*	*9 GHz, pulsed at ~1 kHz*	*2 h/day for 5 days; 100 W/m², WBA-SAR of ~4.7 W/kg*	*Whole body*	*No changes were found in hematology or differential blood counts. Antibody titre in S. pneumoniae injected mice exposed to RFEMF was slightly higher than sham control group.*
Liddle et al., 1986	*Mouse, female*	*9 GHz, pulsed at ~1 kHz*	*2 h/day for 5 days; 10 W/m², WBA-SAR of ~0.47 W/kg*	*Whole body*	*No changes were found in hematology or differential blood counts, antibody titre or survival for S. pneumoniae injected mice exposed to RFEMF.*

Logani et al., 2002a	*Mouse, female*	*42.2 GHz*	*30 min/day, 5 days/week for 3 weeks; 310 W/m^2, peak SAR of 622 W/kg*	*Mid-back*	*No changes in blood catalase activity were found in cyclophosphamide (CPA)-treated mice when exposed to RFEMF before or after CPA-treatment.*
Logani et al., 2002b	*Mouse, male*	*42.2 GHz*	*30 min/day for 3 days; 310 W/m^2, peak SAR of 622 W/kg*	*Nose*	*No changes were observed in cyclophosphamide (CPA)-induced leukopenia or bone marrow cellularity in response to RFEMF treatment. RFEMF exposure also had no effect on CPA-induced reduction in DTH reaction.*
Lushnikov et al., 2004	*Mouse, male*	*42 GHz*	*20 min, 1 W/m^2*	*Whole body*	*Zymosan-induced edema and activated neutrophils in hindpaw were reduced if animals were treated with RFEMF. Pre-treatment with RFEMF before zymosan challenge did not modify the response.*
Makar et al., 2003	*Mouse, male*	*42.2 GHz*	*30 min/day for 3 days; 310 W/m^2, peak SAR of 622 W/kg*	*Nose*	*RFEMF treatment (in vivo) increased anti-CD3 - induced splenic T-cell (CD4$^+$) proliferation (in vitro) after cyclophosphamide (CPA) treatment (in vivo). IFN-δ levels were increased 2-fold in T-cell cultures and peritoneal macrophages demonstrated increased TNF-α production in cultures prepared from animals co-treated with CPA and RFEMF. The authors suggested that RFEMF had immune stimulatory properties.*
Makar et al., 2005	*Mouse, male*	*42.2 GHz*	*30 min/day for 3 days; 310 W/m^2, peak SAR of 622 W/kg*	*Nose*	*Cyclophosphamide (CPA)-treatment caused increased splenic NK activation (CD69 expression), TNF-α production and decreased cytolytic activity in cell cultures at 2-7 days' post-treatment. Co-exposure to RFEMF caused an enhancement of NK activation and TNF-α production, but a recovery of CPA-induced suppression of cytolytic activity.*
Makar et al., 2006	*Mouse, male*	*61.22 GHz*	*30 min/day for 3 days; 310 W/m^2, peak SAR of 885 W/kg*	*Nose*	*Cyclophosphamide (CPA)-treatment caused decreased TNF-α production in cultured peritoneal macrophages, while exposure of CPA-treated mice with RFEMF restored TNF-α production. RFEMF exposure of CPA-treated mice caused increased splenic T-cell culture IFN-*

					δ production and anti-CD3-induced T-cell ($CD4^+$ and $CD8^+$) proliferation.
Novoselova et al., 1999	*Mouse, male*	*8.15 – 18 GHz (broad spectrum)*	*5 h; 0.01 W/m²*	*Whole body*	*TNF-α production was increased in peritoneal macrophages and splenic T-cells, while mitogenic activity was also increased in T-cells. Co-treatment with anti-oxidants further enhanced these responses.*
Novoselova et al., 2017	*Mouse, male*	*8.15 – 18 GHz (broad spectrum)*	*1 h; 0.016 W/m²*	*Whole body*	*Pro-inflammatory cytokine (TNF-α, IL-6) and IFN-δ levels increased in blood plasma, while activation of NF-κB, MAPK p38 and TLR4 pathways was observed in splenic lymphocytes exposed to RFEMF. The authors suggest that RFEMF exposure may improve the immune response to certain challenges (e.g. toluene exposure).*
Radzievsky et al., 2004b	*Mouse, male*	*61.22 GHz*	*15 min/day for 5 days; 133 W/m²*	*Nose*	*Exposure to RFEMF for 5 days, starting 5 days after injection of B16 melanoma cells subcutaneously into the flank of mice, caused a suppression in tumor growth. Pre-treatment with naloxone, a non-selective opioid receptor antagonist, abolished this effect.*

Risk-of-bias assessment for mammalian studies on immune system effects

Table 4.10: Summary of risk-of-bias judgements (low, probably low, probably high, high) for each risk of bias item for each of the included mammalian studies on immune system-related responses to RFEMF in the 6 to 300 GHz frequency range.

Source	Study design	Blinding	Attrition/exclusion	Exposure assessment	Selective reporting	Conflict of interest	Other	Overall study Risk of Bias
Gapeyev et al., 2008								
Gapeyev et al., 2009								
Gapeyev et al., 2011								
Gapeyev et al., 2013								
Gapeyev et al., 2015								
Gapeyev et al., 2019								

Liddle et al., 1980								
Liddle et al., 1986								
Logani et al., 2002a								
Logani et al., 2002b								
Lushnikov et al., 2004								
Makar et al., 2003								
Makar et al., 2005								
Makar et al., 2006								
Novoselova et al., 1999								
Novoselova et al., 2017								
Radzievsky et al., 2004b								
Overall Risk of Bias by Domain								

Risk of bias categories: low risk (green), probably low risk (yellow), probably high risk (orange), high risk (red).

A number of studies have been conducted to evaluate the impact of millimeter-wave RFEMF on an assortment of endpoints related to the immune system. None of the studies published to date reported evidence of adverse health effects on the immune system. On the contrary, most studies reported some form of therapeutic effect from RFEMF exposure on the immune system. Since the studies on this topic assess such a diverse assortment of endpoints, it is problematic to assess the body of evidence as much of it is unrelated. However, for the purpose of evaluating the current state of the literature in this area, the Quality and Strength of Evidence related to all studies on all immune system-related endpoints was quantified (Table 4.11).

Quality and Strength of Evidence for immune system effects from millimeter-wave RFEMF exposure

The initial Quality of Evidence rating for mammalian experimental studies was established as “High”. Most relevant studies on this endpoint did not randomly allocate animals among treatment groups or employ concealment during exposure. Many of these studies did not incorporate blinding into their experimental protocols. Limited dosimetric information was provided for a number of studies and inferential statistics were either not applied or were improperly applied in many studies. For these reasons, the Risk of Bias for this endpoint was rated as “Probably High”, resulting in a downgrade by two levels in the Quality of Evidence. No other downgrades were implemented for Indirectness, Inconsistency or Imprecision. The overall Quality of Evidence for an association between millimeter-wave RFEMF exposure and adverse immune system effects was therefore rated as “Low”. The Strength of Evidence for an association between millimeter-wave RFEMF exposure and adverse immune system effects was rated as “Insufficient”. Additional high-quality studies are required to more fully elucidate the impacts of RFEMF exposure on the immune system.

Table 4.11: Summary of findings, quality of evidence, and strength of evidence for mammalian studies assessing immune system effects in response to millimeter-wave RFEMF exposure.

Factor	**Rating**	**Basis**

Risk of Bias across Studies	-2	Most studies lacked procedures for randomization of allocation into treatment groups and did not apply concealment of treatment group from researchers. Dosimetric information was often incomplete or lacking. Animal or target tissue temperatures were often not monitored in order to exclude a direct thermal effect on the measured endpoints.
Indirectness	0	Mammalian data are empirically recognized as direct evidence of human health data.
Inconsistency	0	It is difficult to judge consistency due to the diverse assortment of endpoints evaluated.
Imprecision	0	It is difficult to judge imprecision due to the limited number of studies on each endpoint.
Overall Quality of Evidence	Low	"High" + (-2) = "Low"
Summary of findings from qualitative analysis	N/A	Most endpoints and exposure conditions have only been assessed by one laboratory.
Overall Strength of Evidence	Insufficient	There are an insufficient number of studies conducted on each endpoint. Most of the studies report a potential therapeutic benefit from RFEMF exposure as opposed to an adverse health outcome. Some of the results seem biologically implausible due to the superficial nature of exposure from millimeter-wave RFEMF and the internal organ-based endpoints assessed.

Ocular effects

While most studies on the ocular effects of RFEMF have been conducted at frequencies below 6 GHz, it is well established that cataracts, corneal burns and retinal effects can occur when the temperature of ocular tissues exceeds 41^{o}C, (Elder et al., 2003). In one of the first experimental studies on ocular endpoints using millimeter wave RFEMF, Birenbaum et al. (1969) exposed anaesthetized rabbits to a range of frequencies from 0.8 to 70 GHz and a range of exposure times from 2 to 60 min (power density at the location of the eye was not reported). The lens tissue was then examined for evidence of pathological alterations (e.g. opacities or cataracts) either immediately or for several weeks after exposure. After conducting a large number of experiments over a period of several years, the authors identified a relationship between output power and exposure time for the occurrence of lens abnormalities. The authors also noted that there were no apparent differences between pulsed and continuous wave RFEMF. Hagan and Carpenter (1976) followed up on this work by exposing the eyes of anesthetized rabbits to 10 GHz continuous wave RFEMF for 30 min at power densities ranging from 3100 to 4400 W/m^2, then assessed the eyes of these animals by slit lamp microscopy and ophthalmoscopy. The authors observed lens opacities in 50% of rabbit

eyes after a single exposure to 10 GHz RFEMF at a power density of 3450 W/m^2. Extensive damage to the cornea and iris were also observed under such exposure scenarios. Temperatures in the vitreous humor and anterior chamber were measured and found to be increased by 6.0 and 11.5^{o}C after exposure, respectively. Rosenthal et al. (1976) exposed anesthetized male rabbits to 35 or 107 GHz RFEMF for 15-80 min, then examined the eyes of these animals immediately and at one-day post-exposure using slit lamp microscopy and electron microscopy. The authors reported that irradiation at 107 GHz was found to be more effective at inducing stromal damage to the cornea, however 35 GHz exposures produced more persistent effects, including epithelial cell damage. The power density used for exposure in this study was not reported, only device output power was reported.

McAfee et al. (1979) exposed trained, non-anesthetized Rhesus monkeys to 9.31 GHz RFEMF for 30-40 sessions (unknown session time) at a power density of 1500 W/m^2, then examined the eyes of these animals for up to 1-year post-exposure. The authors reported they found no evidence of altered ocular pathology from RFEMF exposure. In a follow-up study, McAfee et al. (1983) chronically exposed non-anesthetized (unrestrained) Rhesus monkeys to 9.31 GHz RFEMF for up to 15 min/day over several months at a power density of 1500 or 3000 W/m^2, then examined the eyes of these animals. Once again, the authors reported no ocular abnormalities as assessed by slit lamp microscopy and ophthalmoscopic examination. While the exposure time and intensity in this study seem consistent with other studies that found ocular lesions under these conditions, it must be noted that the exposures in this study were intermittent over a 25 min period (not continuous over a 15-30 min period). This could allow for cooling of ocular tissues between exposures. Furthermore, animals in this study were not anesthetized, resulting in a greater thermoregulatory capacity than in anesthetized animals in other studies. These factors may have avoided excessive temperature-induced tissue damage to ocular tissue in the current study.

Kues et al. (1999) exposed the eyes of anesthetized rabbits and rhesus monkeys to 60 GHz RFEMF for either 8h on one day or 4 h/day for 5 days at a power density of 100 W/m^2, then assessed ocular endpoints using slit-lamp microscopy and ocular tissue was examined histologically. The authors found no ocular changes in response to RFEMF exposure, which is not surprising as the peak temperature elevation from these RFEMF exposures only resulted in a ~0.7^{o}C temperature elevation above resting ocular temperatures which is far below the threshold temperature for thermal effects in the eye (See section 4.2). Chalfin et al. (2002) exposed the eyes of anesthetized Rhesus monkeys to 35 or 94 GHz pulsed (1 kHz) RFEMF at a high power density of 10 to 80 kW/m^2 for 1 to 5 s while monitoring corneal temperature, then assessed ocular effects using slit lamp microscopy, corneal topography and specular microscopy. The authors found 50% of animals experienced a corneal lesion at mean fluence of 7.5 J/cm2 at 35 GHz and 5.0 J/cm2 at 94 GHz. However, measurement of the corneal temperature after 94 GHz exposure at 10 kW/m^2 for 5 s indicated a 30^{o}C corneal temperature elevation, momentarily reaching ~60^{o}C.

Kojima et al. (2009) assessed ocular damage in rabbits after exposure to 60 GHz RFEMF at very high RFEMF intensity levels using three different antenna sources. The authors reported that irradiation for 6 min at ~19 kW/m^2 caused highly reproducible ocular effects including: ~54^{o}C corneal surface temperature, corneal edema, epithelial cell loss and iris dilation. The authors noted that ocular heating and tissue

damage were not restricted to the cornea but appeared to have travelled to the iris, possibly via circulating aqueous humor.

Sasaki et al. (2014) developed a millimeter-wave exposure system and modelled ocular temperature increases in the rabbit eye in response to 26.5 to 95 GHz RFEMF. To confirm their modelling results, the authors measured corneal apex and anterior lens temperature in anesthetized animals exposed to either 40 or 75 GHz RFEMF at 2000 W/m^2 and reported that maximum temperatures in the corneal apex were 9.9 and 13.2^{o}C while maximum temperatures in the anterior lens were 4.6 and 2.9^{o}C, respectively. Based upon their modelling results, the authors predicted that corneal temperatures could exceed 43^{o}C in the 26.5 to 95 GHz frequency range when the incident power density exceeds ~2000 W/m^2. In a follow-up study, Kojima et al. (2015) exposed the eye of anesthetized rabbits to 18 to 40 GHz RFEMF at a power density of 2000 W/m^2 and monitored the corresponding temperature change in the cornea, lens and vitreous humor. The authors found that ocular temperatures reached steady state values at approximately 3 min after exposure began with the maximum temperature increases (e.g. ~11^{o}C) occurring in the cornea at the higher frequencies (40 GHz). The authors noted that while the penetration depth of the RFEMF was insufficient to reach the lens or vitreous, heat transport resulted in increased temperatures in these tissues (although to a much lower extent). More recently, Kojima et al. (2018) examined the extent of tissue damage in the eyes of rabbits in response to 40, 75 and 95 GHz RFEMF exposure for 6 min at power densities between 100 to 6000 W/m^2. The authors observed ocular damage in 50% of rabbit eyes at 24 h post-exposure at power densities of 2060, 1430 and 1460 W/m^2 at 40, 75 and 95 GHz, respectively. These exposure levels corresponded to corneal surface temperatures of ~41- 43^{o}C. When exposure at 75 GHz was extended to 30 min, corneal epithelium damage was observed at 24 h post-exposure at a power density of 500 W/m^2 (corresponding to a corneal surface temperature of ~37.1 ± 0.8^{o}C). Exposure for 30 min to infrared radiation to similar cornea surface temperature (~37.8^{o}C) was also observed to cause temporary changes to the corneal epithelium, indicating that a prolonged ~5^{o}C increase in cornea surface temperature (from baseline) is sufficient to cause minor corneal epithelial damage.

Crouzier et al. (2014) evaluated the impact of 9.71 GHz RFEMF exposure on the cornea healing process in rabbits after LASIK keratotomy. At one month after surgery, non-anesthetized rabbits were exposed to 9.71 GHz RFEMF for 1 h/day, 3 days/week for 5 months at a power density of 50 W/m^2. The authors examined the rabbit eyes at the end of the exposure period and reported no clinical, histological or experimental changes in relation to the sham control group.

Table 4.12: Summary of mammalian study characteristics on ocular endpoints.

Source	***Species***	***Frequency***	***Exposure duration and intensity***	***Tissue exposed***	***Findings***
Birenbaum et al., 1969	*Rabbit*	*6.3 and 70 GHz*	*2-30 min; unknown intensity*	*Eye*	*Authors observed a relationship between average output power and time of exposure for the occurrence of lens abnormalities across a wide frequency range. No differences were*

					observed between pulsed and continuous wave exposures.
Chalfin et al., 2002	*Rhesus monkey, male and female (anesthetized)*	*35 and 94 GHz, pulsed at 1 kHz*	*1 to 5 s; 10000-80000 W/m^2*	*Eye*	*Threshold fluence for corneal lesions in 50% of subjects were 5 and 7.5 J/cm^2 for 35 and 94 GHz, respectively. At these doses, no effects were observed on corneal endothelial cells. Such exposures were associated with transient corneal temperature increases of up to 30^{o}C above corneal baseline temperature.*
Crouzier et al., 2014	*Rabbit, male*	*9.71 GHz, pulsed*	*1 h/day, 3 days/week for 3 months; 50 W/m^{2,} peak SAR in eye of 6.35 W/kg*	*Eye*	*No differences observed in healing cornea in response to RFEMF exposure.*
Hagan and Carpenter, 1976	*Rabbit*	*10 GHz*	*30 min; 3100 to 4400 W/m^2*	*Eye*	*Irradiation for 30 min at 3450 W/m^2 caused increased lens opacity (cataracts) in 50% of animals. Such exposures were associated with temperature in the vitreous body and anterior chamber of 6.0 and 11.5^{o}C, respectively.*
Kojima et al., 2009	*Rabbit, male (anesthetized)*	*60 GHz*	*6 min at 18980 W/m^2 or 30 min at 4750 W/m^2*	*Eye*	*Irradiation for 6 min at ~19 kW/m^2 caused corneal surface temperature to reach 54^{o}C and highly reproducible ocular damage. The authors noted that the heat was not restricted to the cornea but appeared to have travelled to the iris, possibly via circulating aqueous humor.*
Kojima et al., 2015	*Rabbit, male (anesthetized)*	*18, 22, 26.6, 35 or 40 GHz*	*3 min; 2000 W/m^2*	*Eye*	*Ocular temperatures reached a thermal balance after 3 min of exposure and displayed a frequency dependent response with the highest temperature increases in cornea, lens and vitreous humor occurring at 40 GHz (~11.0^{o}C, 3.9^{o}C and 2.0^{o}C, respectively) and the lowest at 18 GHz (~5.0^{o}C,1.5^{o}C and 0.4^{o}C, respectively). Thermal transport by aqueous humor convection may increase lens temperature more rapidly and to a greater extent than predicted.*
Kojima et al., 2018	*Rabbit, male*	*40, 75 or 95 GHz*	*6 or 30 min; 100 to 6000 W/m^2*	*Eye*	*Corneal damage was induced in 50% of rabbit eyes after 6 min exposure to RFEMF at power densities of 2060 W/m^2 for 40 GHz, 1430 W/m^2 for 75 GHz and 1460 W/m^2 for 95 GHz. Corneal temperatures at these power densities were in the range of 41-43^{o}C. Exposure for 30 min at*

					the same power density resulted in greater ocular damage.
Kues et al., 1999	*Rabbit* *Rhesus monkey*	*60 GHz*	*8 h or 4 h/day for 5 days; 100 W/m²*	*Eye*	*No changes were found in rabbit or primate eyes after either acute (8h) or repeated (4 h/day for 5 days) exposure to RFEMF.*
McAfee et al., 1979	*Rhesus monkey*	*9.31 GHz*	*30-40 sessions, time per session unknown ; 1500 W/m²*	*Eye*	*No changes in ocular pathology observed up to one year after 30-40 exposures to RFEMF.*
McAfee et al., 1983	*Rhesus monkey*	*9.31 GHz*	*Up to 15 min/day, total exposure time of 275 to 946 min; 1500 or 3000 W/m²*	*Eye*	*Daily chronic exposure (up to 15 min/day over a 25 min period) for several months resulted in no ocular abnormalities.*
Rosenthal et al., 1976	*Rabbit, male*	*35 or 107 GHz*	*15 to 80 min, unknown intensity*	*Eye*	*Irradiation at 107 GHz was found to be more effective at inducing stromal damage to the cornea, however 35 GHz produced more persistent effects, including epithelial cell damage. The exposure power densities in this study were not reported.*
Sasaki et al., 2014	*Rabbit*	*40 or 75 GHz*	*0 to 160 s; 2000 W/m²*	*Eye*	*Temperature elevation increased in the cornea with increasing frequency, reaching a maximum of 9.9°C and 13.2°C at 40 GHz and 75 GHz, respectively. Maximum temperature elevations of 4.6°C and 2.9°C were observed in the lens at 40 GHz and 75 GHz, respectively. Based upon measurement and modelling results, the authors concluded that an ocular temperature of 43°C could be exceeded at an incident power density of ~2000 W/m².*

Risk-of-bias assessment for mammalian studies on ocular effects

Table 4.13: Summary of risk-of-bias judgements (low, probably low, probably high, high) for each risk of bias item for each included mammalian study on ocular responses to RFEMF in the 6 to 300 GHz frequency range.

Source	Study design	Blinding	Attrition/exclusion	Exposure assessment	Selective reporting	Conflict of interest	Other	Overall study Risk of Bias
Birenbaum et al., 1969								
Chalfin et al., 2002								
Crouzier et al., 2014								
Hagan and Carpenter, 1976								
Kojima et al., 2009								
Kojima et al., 2015								
Kojima et al., 2018								
Kues et al., 1999								
McAfee et al., 1979								
McAfee et al., 1983								
Rosenthal et al., 1976								
Sasaki et al., 2014								
Overall Risk of Bias by domain								

Risk of bias categories: low risk (green), probably low risk (yellow), probably high risk (orange), high risk (red).

Most studies assessing the ocular effects of RFEMF have been conducted at frequencies below 6 GHz (Elder, 2003). These studies have identified lens opacities (and cataracts) and corneal tissue damage following high intensity exposure to RFEMF as possible adverse ocular health effects. Therefore, Quality and Strength of Evidence was assessed separately for each of these endpoints.

Quality and Strength of Evidence for corneal tissue damage from millimeter-wave RFEMF exposure

The initial Quality of Evidence rating for mammalian experimental studies was established as “High”. Among the animal studies examining corneal tissue damage in response to millimeter wave RFEMF exposure, most have limitations related to randomization of allocation related to the exposure groups and concealment of the identity of the exposure groups from the investigators (Chalfin et al., 2002; Kojima et al., 2009, 2018; Kues et al, 1999; McAfee et al., 1979, 1983; Rosenthal et al., 1976). More importantly, most studies assessing corneal tissue damage have not employed blinding for endpoint analysis. This is less important for studies that simply measured ocular temperatures, but it is more important for subjective assessment of corneal tissue damage. For these reasons, the Risk of Bias for this endpoint was rated as “Probably High”, resulting in a downgrade by two levels in the Quality of Evidence. The Quality of Evidence was further downgraded by one level for Indirectness as the exposure levels required to elicit these effects are far above existing human exposure limits and are unlikely to be experienced by humans. No other downgrades were implemented for Inconsistency or Imprecision. The overall Quality of Evidence for an association between millimeter-wave RFEMF exposure and adverse ocular effects was therefore rated as “Very Low”. Complementary research has demonstrated tissue damage from elevated ocular

temperatures (See section 4.2). Therefore, the Strength of Evidence for an association between millimeter-wave RFEMF exposure and corneal tissue damage was rated as “Sufficient”.

The currently available scientific literature reports that corneal tissue damage can occur in experimental animals following exposure to high intensity millimeter-wave RFEMF, but such damage appears to be associated with the elevation of ocular temperature. There is no evidence from existing millimeter-wave RFEMF studies of corneal tissue damage where ocular tissue temperatures were not markedly increased.

Table 4.14: Summary of findings, quality of evidence, and strength of evidence for mammalian studies assessing corneal tissue damage in response to millimeter-wave RFEMF exposure.

Factor	**Rating**	**Basis**
Risk of Bias across Studies	-1	Most studies lacked procedures for randomization of allocation into treatment groups and did not indicate concealment of treatment group from researchers. Blinding was not reported for endpoint analysis.
Indirectness	-1	Mammalian data are empirically recognized as direct evidence of human health data. The exposure levels required to elicit these effects are far above existing Canadian and international exposure limits and are considered unlikely to be experienced in normal living and working environments.
Inconsistency	0	It is difficult to judge consistency due to the limited number of studies conducted and the variations in exposure conditions (frequency, intensity, time) used across such studies.
Imprecision	0	It is difficult to judge imprecision due to the limited number of studies on each exposure condition.
Overall Quality of Evidence	Low	“High” + (-2) = “Low”
Summary of findings from qualitative analysis	N/A	There is evidence of a threshold response based upon corneal temperature that is consistent with non-RFEMF research.
Overall Strength of Evidence	Sufficient	While a limited number of studies have been conducted, the results are biologically plausible and consistent with complementary results assessing thermal impacts (See section 4.2) and RFEMF studies conducted at lower frequencies (Elder, 2003).

Quality and Strength of Evidence for cataractogenic effects from millimeter-wave RFEMF exposure

The initial Quality of Evidence rating for mammalian experimental studies was established as “High”. Among animal studies examining lens opacities or cataract induction in response to millimeter wave

RFEMF exposure (Birenbaum et al., 1969; Hagan and Carpenter, 1976; Kues et al., 1999; McAfee et al., 1979, 1983), most have limitations related to randomization of allocation related to the exposure groups and concealment of the identity of the exposure groups from the investigators. More importantly, most studies assessing lens opacities and cataractogenesis have not employed blinding for endpoint analysis. This is less important for studies that simply measured ocular temperatures, but more important for subjective assessment. Limited dosimetric information was provided for a number of studies and inferential statistics were either not applied or were improperly applied in many studies. For these reasons, the Risk of Bias for this endpoint was rated as "Probably High", resulting in a downgrade by two levels in the Quality of Evidence. The Quality of Evidence was further downgraded by one level for Indirectness as the exposure levels required to elicit these effects are far above existing human exposure limits and are unlikely to be experienced by humans. No other downgrades were implemented for Inconsistency or Imprecision. The overall Quality of Evidence for an association between millimeter-wave RFEMF exposure and cataractogenesis was therefore rated as "Very Low". Complementary research has demonstrated cataract induction from exposure of experimental animals at frequencies below 6 GHz, when temperature in the lens reached 41^{o}C (Elder, 2003). Therefore, the Strength of Evidence for an association between supra-thermal millimeter-wave RFEMF exposures and corneal tissue damage was rated as "Sufficient". There is no evidence from existing millimeter-wave RFEMF studies of cataract formation when ocular tissue temperatures did not reach 41^{o}C.

Table 4.15: Summary of findings, quality of evidence, and strength of evidence for mammalian studies assessing lens opacities (cataracts) in response to millimeter-wave RFEMF exposure.

Factor	**Rating**	**Basis**
Risk of Bias across Studies	-2	Relevant studies lacked procedures for randomization of allocation into treatment groups and did not indicate concealment of treatment group from researchers. Blinding was not reported for endpoint analysis.
Indirectness	-1	Mammalian data are empirically recognized as direct evidence of human health data. The exposure levels required to elicit these effects are far above existing Canadian and international exposure limits and are considered unlikely to be experienced in normal living and working environments.
Inconsistency	0	It is difficult to judge consistency due to the limited number of relevant publications.
Imprecision	0	It is difficult to judge imprecision due to the limited number of relevant papers and the lack of statistics within such studies.
Overall Quality of Evidence	Very Low	"High" + (-3) = "Very Low"

Summary of findings from qualitative analysis	N/A	
Overall Strength of Evidence	Sufficient	While a limited number of studies have been conducted, the results are biologically plausible and consistent with complementary results assessing thermal impacts and RFEMF studies conducted at lower frequencies (Elder, 2003).

Reproductive system effects

Most animal studies on possible adverse reproductive outcomes of RFEMF have been conducted at frequencies below 6 GHz (Jauchem et al., 2008). Eight studies were identified that assessed reproductive system outcomes from exposure to RFEMF in the 6 to 300 GHz frequency range. Jensh et al. (1984a) exposed pregnant Wistar rats to whole-body 6 GHz RFEMF at a power density of 350 W/m^2 for 8 h/day throughout pregnancy, then examined maternal body and organ weights, litter size, number of resorptions and blood chemistry as well as fetal body weight and number of abnormalities. The authors reported that exposure at this level produced no measurable colonic temperature changes. Under these exposure conditions, the authors found no changes in litter size, number of resorptions or frequency of fetal abnormalities but fetuses from RFEMF-exposed dams displayed lower fetal weight than those of the sham-exposed group. The authors speculated that the difference in fetal weight may be due to "… a generalized compensated heat-stress reaction". In subsequent analysis using the same exposure conditions, Jensh et al. (1984b) evaluated post-natal neurophysiologic changes, development and reproductive outcomes in F1a offspring and teratogenic analysis was conducted in F1b and F2 fetuses (e.g. the dams that gave birth to F1a litters were re-bred to create F1b fetuses, F1a offspring were bred to create F2 fetuses). The authors reported that "…F1b term fetal weight; F1a eye opening, post-natal growth to 5th week, water T-maze and open-field test results; and several organ/body ratios" were significantly different between control and irradiated groups. Furthermore, F2 litter size and resorption rates were affected by pre-natal exposure of the F1a adults. The authors indicated that it appeared these effects manifested through maternal exposure and it was possible that these observations were due to a compensated maternal thermal stress response as the exposure level in this study may have induced thermoregulatory compensation. Furthermore, the authors indicated that localized microthermal effects which do not manifest as a total body hyperthermic response may also be an important consideration.

Two studies assessed the impact of *in utero* millimeter-wave RFEMF exposure on offspring development. Sharma et al. (2017) exposed pregnant mice to 10 GHz RFEMF for 2 h/day for 8 or 20 days during pregnancy at a power density of 2.5 W/m^2, then assessed litter size and offspring development and a variety of endpoints in the developing mouse brain. The authors reported no changes in litter size or crown-rump length but observed a significant reduction in average body weight and brain weight in the RFEMF exposed mice. Analysis of brain tissue demonstrated increased lipid peroxidation and decreased glutathione levels. Histological analysis of the cerebellum found a decreased thickness of the granule cell layer and fewer Purkinje cells in the RFEMF exposed pups. The authors noted that larger effects were observed in animals

that were exposed for a longer neonatal duration period. Zhang et al. (2015) exposed pregnant mice to 9.417 GHz RFEMF for 12 h/day from day 3.5 to 18 of gestation at a reported SAR of 2 W/kg, then assessed offspring cognitive dysfunction using a variety of behavioural tests. The authors found increased anxiety-like behaviour and decreased depression—related behaviour at 5 weeks of age in the RFEMF exposed mouse pups. The authors also reported that learning memory was reduced in male offspring.

A series of studies by Kumar et al. (2011, 2012, 2013) assessed the impact of chronic millimeter-wave RFEMF exposure on a number of oxidative stress and DNA damage biomarkers in rat sperm. Kumar et al. (2011) reported an increased level of ROS and decreased histone kinase activity in sperm. The authors also observed an increased percentage of apoptotic sperm and a decreased percentage of spermatozoa in G2/M phase of the cell cycle. Kumar et al. (2012) reported increased malondialdehyde levels (a biomarker of lipid peroxidation), increased creatine kinase activity and decreased melatonin levels in sperm. Analysis of complete blood counts found red blood cell counts and total hemoglobin levels were lower in RFEMF exposed rats. Total leukocyte, platelet and neutrophil concentrations were also observed to be lower in RFEMF-treated rats. Kumar et al. (2013) assessed DNA damage in rat sperm after chronic RFEMF exposure and found increased levels of DNA damage using the alkaline comet assay. Consistent with this finding, the authors also found increased caspase-3 staining in sperm from RFEMF exposed rats, a biomarker of apoptosis. Histological analysis of the testes found decreased diameter of the seminiferous tubules and decreased testes weight, while analysis of blood found decreased testosterone levels. Kesari et al. (2010) observed similar results in rats chronically exposed (2 h/day for 45 days) to 50 GHz RFEMF at 0.0086 W/m^2. The authors observed decreased activity of superoxide dismutase (SOD), glutathione peroxidase (GPx) and histone kinase in sperm, but an increase in catalase (CAT) activity. The authors also reported an increased number of apoptotic cells in sperm and a decreased number of G2/M cells in spermatozoa. The authors speculate that RFEMF exposure may increase reactive oxygen species in sperm and have negative consequences on male fertility.

Table 4.16: Summary of mammalian study characteristics on reproduction and development endpoints.

Source	***Species***	***Frequency***	***Exposure duration and intensity***	***Tissue exposed***	***Findings***
Jensh et al., 1984a	*Rat, female*	*6 GHz*	*8 h/day for 22 days throughout pregnancy; 350 W/m^2, WBA-SAR of 7.28 W/kg*	*Whole body*	*Fetal weight was reduced in the RFEMF exposed group. No changes were observed for fetal resorptions or maternal body/organ weights, litter size, hematocrit, hemoglobin or leukocyte count. Monocyte concentration was lower in irradiated rats.*
Jensh et al., 1984b	*Rat, male and female*	*6 GHz*	*8 h/day for 22 days throughout pregnancy;*	*Whole body*	*Maternal weight gain (during pregnancy) and fetal body weights were lower in RFEMF exposed rats. Some differences were observed in organ weights and behavioural indices*

			350 W/m^2, WBA-SAR of 7.28 W/kg		*among offspring exposed neonatally. The number of resorptions in F1a offspring was higher in irradiated animals than in sham exposed animals.*
Kesari et al., 2010	*Rat, male*	*50 GHz*	*2 h/day for 45 days; 0.0086 W/m^2*	*Whole body*	*Decreased antioxidant enzyme activity, increased apoptosis, decreased histone kinase activity in sperm. The authors speculate that RFEMF exposure may increase reactive oxygen species in sperm.*
Kumar et al., 2011	*Rat, male*	*10 GHz*	*2 h/day for 45 days; 2.1 W/m^2*	*Whole body*	*Increased reactive oxygen species and apoptosis, decreased histone kinase and percentage of G2/M cells in sperm.*
Kumar et al., 2012	*Rat, male*	*10 GHz*	*2 h/day for 45 days; 2.1 W/m^2*	*Whole body*	*Increased malondialdehyde levels and creatine kinase activity, decreased melatonin levels in sperm. Hemoglobin, red blood cell and leukocyte counts were lower in the RFEMF exposed rats.*
Kumar et al., 2013	*Rat, male*	*10 GHz*	*2 h/day for 45 days; 2.1 W/m^2*	*Whole body*	*Increased caspase-3 activity and DNA damage were observed in sperm. Histological analysis of seminiferous vesicles showed decreased lumen diameter, testes weight and the presence of apoptotic bodies. Analysis of blood found decreased testosterone.*
Sharma et al., 2017b	*Mouse, female*	*10 GHz*	*2 h/day for 8 or 20 days during pregnancy; 2.5 W/m^2*	*Whole body*	*Decreased body and brain weight in RFEMF exposed offspring. Increased lipid peroxidation and decreased glutathione in brain tissue. Decreased granule cell layer thickness and lower number of Purkinje cells in cerebellum.*
Zhang et al., 2015	*Mouse, female*	*9.417 GHz*	*12 h/day from gestational day 3.5 to 18; SAR = 2.0 W/kg*	*Whole body*	*Increased anxiety-like behaviour and decreased depression-related behaviour in offspring. Decreased learning memory in male offspring.*

Risk-of-bias assessment for mammalian studies on reproduction system effects

Table 4.17: Summary of risk-of-bias judgements (low, probably low, probably high, high) for each risk of bias item for each included mammalian study on reproduction system responses to RFEMF in the 6 to 300 GHz frequency range.

Source	Study design	Blinding	Attrition/exclusion	Exposure assessment	Selective reporting	Conflict of interest	Other	Overall study Risk of Bias
Jensh et al., 1984a								
Jensh et al., 1984b								
Kesari et al., 2010								
Kumar et al., 2011								
Kumar et al., 2012								
Kumar et al., 2013								
Sharma et al., 2017b								
Zhang et al., 2015								
Overall Risk of Bias by domain								

Risk of bias categories: low risk (green), probably low risk (yellow), probably high risk (orange), high risk (red).

In summary, four studies examined adverse pregnancy outcomes in animals exposed to millimeter-wave RFEMF (Jensh 1984a, 1984b; Sharma et al., 2017b; Zhang et al., 2015), and four studies assessed impacts on sperm (male fertility) (Kesari et al., 2010; Kumar et al., 2010, 2011, 2012). Each of these potential adverse health outcomes were assessed separately for Quality and Strength of Evidence.

Quality and Strength of Evidence for adverse pregnancy outcomes from millimeter-wave RFEMF exposure

The initial Quality of Evidence rating for mammalian experimental studies was established as “High”. Two studies assessed potential teratogenic effects of millimeter-wave RFEMF (Jensh et al., 1984a, 1984b) and two studies assessed potential developmental effects from maternal exposure to millimeter-wave RFEMF (Sharma et al., 2017b; Zhang et al., 2015). The studies by Jensh et al. reported no changes in rate of resorptions or fetal abnormalities but did observe that fetal weight was decreased from maternal RFEMF exposure during gestation at exposure levels that did not appreciably change maternal core body temperature. These studies did not randomly allocate animals into exposure groups and there was no indication of either concealment of exposure group or blinding during endpoint analysis. An absence of blinding was considered a critical confounder for these studies due to the subjective nature of the endpoint analysis. These studies also lacked methodological details related to endpoint analysis. The studies by Sharma et al. (2017b) and Zhang et al. (2015) reported decreased fetal brain and body weight and increased anxiety–like behaviour in offspring. However, these studies lacked blinding for endpoint analysis and provided insufficient dosimetric information. For these reasons, the Risk of Bias for the adverse pregnancy outcomes endpoint was rated as “Probably High”, resulting in a downgrade by two levels in the Quality of Evidence. No other downgrades were implemented for Indirectness, Inconsistency or Imprecision. The overall Quality of Evidence for an association between millimeter-wave RFEMF exposure and adverse pregnancy outcomes was therefore rated as “Low”. Complementary research has

demonstrated that maternal hyperthermia in experimental animals can result in an increased rate of resorptions and malformations (see section 4.2). Therefore, the Strength of Evidence for an association between millimeter-wave RFEMF exposure and adverse pregnancy outcomes was rated as "Sufficient", if RFEMF exposure is sufficiently intense to result in maternal or fetal hyperthermia. Although the temperature where heat becomes teratogenic is species specific, the increase in temperature required to lead to deleterious outcomes seems to be conserved at 2-2.5^{o}C above normal maternal core body temperature with a threshold duration at this increased temperature of approximately 1 h (Graham et al., 1998).

Table 4.18: Summary of findings, quality of evidence, and strength of evidence for mammalian studies assessing effects on adverse pregnancy outcomes in response to millimeter-wave RFEMF exposure.

Factor	**Rating**	**Basis**
Risk of Bias across Studies	-2	Studies lacked procedures for randomization of allocation into treatment groups and did not indicate concealment of treatment group from researchers. Blinding was not reported for endpoint analysis.
Indirectness	0	Mammalian data are empirically recognized as direct evidence of human health data.
Inconsistency	0	It is difficult to judge consistency due to the limited number of relevant papers.
Imprecision	0	It is difficult to judge imprecision due to the limited number of studies on these endpoints.
Overall Quality of Evidence	Low	"High" + (-2) = "Low"
Summary of findings from qualitative analysis	N/A	Teratogenic effects from millimeter wave RFEMF have only been assessed by one laboratory.
Overall Strength of Evidence	Sufficient	While a limited number of studies have been conducted, the results are biologically plausible. Complementary evidence from hyperthermia research has demonstrated teratogenic effects from hyperthermia (Section 4.2).

Quality and Strength of Evidence for effects on male fertility from millimeter-wave RFEMF exposure

The initial Quality of Evidence rating for mammalian experimental studies was established as "High". All studies on potential effects of millimeter-wave RFEMF on male fertility were conducted by the same group (Kesari et al., 2010; Kumar et al., 2011, 2012, 2013). These studies did not randomly allocate animals into exposure groups and there was no indication of either concealment of exposure group or blinding during endpoint analysis. An absence of blinding was considered a critical confounder for these studies due to

the subjective nature of the endpoint analysis. These studies provided insufficient information on sham control conditions and limited dosimetric information was provided for these studies. Inferential statistics were either not applied or were improperly applied in many studies. For these reasons, the Risk of Bias for this endpoint was rated as “Probably High”, resulting in a downgrade by two levels in the Quality of Evidence. No other downgrades were implemented for Indirectness, Inconsistency or Imprecision. The overall Quality of Evidence for an association between millimeter-wave RFEMF exposure and male infertility was therefore rated as “Low”. Complementary research has demonstrated that sustained or repeated temperature elevation (~1-2^{o}C) of the testes in human and mammalian models can result in reversible alterations in normal sperm function (See section 4.2). Therefore, the Strength of Evidence for an association between millimeter-wave RFEMF exposure and male infertility was rated as “Sufficient”, if exposure to RFEMF is sufficiently intense to cause hyperthermia or increase testes temperature by 1-2^{o}C.

Table 4.19: Summary of findings, quality of evidence, and strength of evidence for mammalian studies assessing effects on male fertility in response to millimeter-wave RFEMF exposure.

Factor	**Rating**	**Basis**
Risk of Bias across Studies	-2	Most studies lacked procedures for randomization of allocation into treatment groups and did not indicate concealment of treatment group from researchers. Blinding was not reported for endpoint analysis.
Indirectness	0	Mammalian data are empirically recognized as direct evidence of human health data.
Inconsistency	0	It is difficult to judge consistency due to the diverse assortment of endpoints evaluated.
Imprecision	0	It is difficult to judge imprecision due to the limited number of studies on each endpoint.
Overall Quality of Evidence	Low	“High” + (-2) = “Low”
Summary of findings from qualitative analysis	N/A	Most endpoints and exposure conditions have only been assessed by one laboratory.
Overall Strength of Evidence	Sufficient	While a limited number of studies have been conducted, the results are biologically plausible and consistent with complementary results assessing the impact of hyperthermia on male infertility (Section 4.2).

Cancer and genotoxic effects

One study was identified that assessed the effect of exposure of millimeter-wave RFEMF on cancer in animals. Mason et al. (2001) exposed 7,12-dimethylbenz[a]anthracene (DMBA) treated SENCAR mice to whole body 94 GHz RFEMF for either 10 s at 10,000 W/m^2 or repeated exposure twice/week for 12 weeks for 10 s at 3330 W/m^2, then assessed papilloma development to assess whether millimeter-wave RFEMF exposure can act as a promoter or co-promoter. The RFEMF exposures, while short, were reported to be capable of causing up to a ~5 to 15^{o}C temperature elevation to the skin, depending on the exposure regime. The authors reported no changes in the incidence or multiplicity of papilloma development under either exposure regime when assessed either as a promoter or as a co-promoter with 12-*O*-tetradecanoylphorbol (TPA).

Vijayalaxmi et al. (2004) assessed the genotoxic potential of millimeter-wave RFEMF. The authors exposed the nose of BALB/c mice to 42 GHz RFEMF for 30 min/day for 3 days at a power density of 315 W/m^2, then assessed the incidence of micronuclei (indicative of clastogenic or aneugenic activity) in peripheral blood and bone marrow cells as well as the % of polychromatic (immature) erythrocytes in blood and bone marrow cells. The authors measured temperature in the nose after exposure and found a ~1^{o}C temperature increase. The authors reported no changes in the incidence of micronuclei or immature erythrocytes in peripheral blood or bone marrow after RFEMF exposure alone or in combination with cyclophosphamide (CPA) when compared to the relevant control groups.

Kesari et al. (2009) exposed male rats to 50 GHz for 2 h/day for 45 days at a power density of 0.0086 W/m^2, then assessed DNA damage and a variety of other endpoints in the brain of these animals. The authors reported decreased superoxide dismutase, glutathione peroxidase and protein kinase C activity and increased catalase activity in the brains of RFEMF exposed animals. The authors also reported increased damage as assessed by the neutral comet assay, indicating an increased level of DNA double-strand breaks. In a similar study by the same group, Kumar et al. (2010) exposed male rats for 2 h/day for 45 days to 50 GHz at a power density of 0.0086 W/m^2 or 10 GHz at a power density of 2.1 W/m^2, then assessed DNA damage, reactive oxygen species and antioxidant levels in the blood and serum. The authors reported an increased level of reactive oxygen species and catalase activity and decreased superoxide dismutase and glutathione peroxidase activity in the blood and serum in RFEMF exposed animals. The authors also reported a lower ratio of immature to mature erythrocytes (%polychromatic erythrocytes/normochromatic erythrocytes) in RFEMF exposed animals, but they did not report data on micronuclei incidence despite this being part of the study design. In a second follow-up study, Kumar et al. (2013) exposed animals to 10 GHz RFEMF for 2 h/day for 45 days at a power density of 2.1 W/m^2 and reported an increased incidence of micronuclei in immature erythrocytes (polychromatic erythrocytes) but found no evidence of chromosomal aberrations in leukocytes.

Table 4.21: Summary of mammalian study characteristics on cancer and genotoxicity endpoints.

Source	***Species***	***Frequency***	***Exposure duration and intensity***	***Tissue exposed***	***Findings***

Kesari et al., 2009	*Rat, male*	*50 GHz*	*2 h/day for 45 days; 0.0086 W/m²*	*Whole body*	*Decreased superoxide dismutase, glutathione peroxidase and protein kinase C activity, and increased DNA double-strand breaks and catalase activity in the brains of RFEMF exposed animals.*
Kumar et al., 2010	*Rat, male*	*10 or 50 GHz*	*2 h/day for 45 days; 0.0086 W/m² at 50 GHz or 2.1 W/m² at 10 GHz*	*Whole body*	*Increased level of reactive oxygen species and catalase activity and decreased superoxide dismutase and glutathione peroxidase activity in the blood and serum in RFEMF exposed animals. The authors also reported a lower ratio of immature to mature erythrocytes.*
Kumar et al., 2013	*Rat, male*	*10 GHz*	*2 h/day for 45 days; 2.1 W/m²*	*Whole body*	*Analysis of blood found increased micronuclei in immature erythrocytes but no chromosomal aberrations in leukocytes.*
Mason et al., 2001	*Mouse, female*	*94 GHz*	*10 s (single exposure) or 10s/day, 2 days/week for 12 weeks (repeated exposure); 10000 W/m² (single exposure) or 3330 W/m² (repeated exposure)*	*Whole body*	*No changes were evident in the incidence or multiplicity of papilloma development or other skin endpoints in response to RFEMF treatment.*
Vijayalaxmi et al., 2004	*Mouse, male*	*42.2 GHz*	*30 min/day for 3 days; 315 W/m²*	*Nose*	*No changes were observed in the incidence of micronuclei in polychromatic erythrocytes in either peripheral blood or bone marrow.*

Risk-of-bias assessment for mammalian studies on cancer and genotoxic effects

Table 4.22: Summary of risk-of-bias judgements (low, probably low, probably high, high) for each risk of bias item for each included mammalian study on cancer and genotoxicity assessment in response to RFEMF exposure in the 6 to 300 GHz frequency range.

Source	Study design	Blinding	Attrition/exclusion	Exposure assessment	Selective reporting	Conflict of interest	Other	Overall study Risk of Bias
Kesari et al., 2009								
Kumar et al., 2010								
Kumar et al., 2013								
Mason et al., 2001								
Vijayalaxmi et al., 2004								
Overall Risk of Bias by domain								

Risk of bias categories: low risk (green), probably low risk (yellow), probably high risk (orange), high risk (red).

Only one study has assessed the ability of chronic millimeter wave RFEMF exposure to alter skin cancer promotion and/or co-promotion in the SENCAR mouse DMBA/TPA model of skin carcinogenesis (Mason et al., 2001). This study found no effect on tumor promotion or co-promotion. Four studies assessed genotoxicity/clastogenicity of millimeter-wave RFEMF exposure in either the brain or blood of rats and mice after short-term (3 days) or prolonged exposure (up to 45 days) (Kesari et al., 2009; Kumar et al., 2010, 2013; Vijayalaxmi et al., 2004). It would be inappropriate to include the single animal cancer study with the genotoxicity, therefore only the Quality and Strength of Evidence related to genotoxicity-related endpoints was assessed (Table 28).

Quality and Strength of Evidence for genotoxic effects from millimeter-wave RFEMF exposure

The initial Quality of Evidence rating for mammalian experimental studies was established as “High”. Most relevant studies provided no indication of either randomization of allocation of animals into treatment group or concealment of exposure group identity from the investigators. Two studies lacked blinding for endpoint analysis (Kumar et al., 2010, 2013). With the exception of the study by Vijayalaxmi et al., (2004), these studies provided insufficient dosimetric information. For these reasons, the Risk of Bias for this endpoint was rated as “Probably High”, resulting in a downgrade by two levels in the Quality of Evidence. No other downgrades were implemented for Indirectness, Inconsistency or Imprecision. The overall Quality of Evidence for an association between millimeter-wave RFEMF exposure and genotoxic effects was therefore rated as “Low”. While a limited number of studies have been conducted using millimeter-wave RFEMF, the results are considered biologically plausible as complementary studies on hyperthermia have indicated that exposure of cells in culture to increased temperature may increase DNA instability or interfere with DNA synthesis or repair. However, given the paucity of data examining the effects of hyperthermia on cancer and genotoxicity in human and mammalian models, the Strength of Evidence was rated as “Insufficient”.

Table 4.23: Summary of findings, quality of evidence, and strength of evidence for mammalian studies assessing effects on cancer and genotoxicity-related endpoints in response to millimeter-wave RFEMF exposure.

Factor	Rating	Basis
Risk of Bias across Studies	-2	Most studies lacked procedures for randomization of allocation into treatment groups and did not indicate concealment of treatment group from researchers. Dosimetry details were often lacking or insufficient.
Indirectness	0	Mammalian data are empirically recognized as direct evidence of human health data.
Inconsistency	0	It is difficult to judge consistency due to the diverse assortment of exposure conditions and endpoints evaluated.
Imprecision	0	It is difficult to judge imprecision due to the limited number of studies on each endpoint.
Overall Quality of Evidence	Low	"High" + (-2) = "Low"
Summary of findings from qualitative analysis	N/A	Most endpoints and exposure conditions have only been assessed by one laboratory.
Overall Strength of Evidence	Insufficient	The ability of hyperthermia to affect DNA instability or interfere with DNA synthesis or repair is considered biologically plausible based upon cell culture studies, however a limited number of studies have assessed hyperthermia-induced genotoxicity and cancer induction in human and mammalian models.

Other health endpoints and outcomes

A number of studies were also identified that assessed a variety of biological effects or health outcomes that did not fit into the categories above. Three studies assessed gene expression changes in animals exposed to millimeter-wave RFEMF. Pyrpasopolou et al. (2004) exposed pregnant rats to 9.4 GHz pulsed (50 Hz) RFEMF for 24 h/day at a power density of 0.05 W/m^2 on either days 1-3 or 4-7 post-coitum, then assessed gene and protein expression of bone morphogenetic proteins (BMP) and receptors (BMPR) in newborn rat kidney. The authors reported changes in the expression level and localization of BMP-4, BMP-IA and BMPR-II in newborn rat kidney but did not observe any malformations in newborn kidney and the authors concluded that these alterations did not appear to affect renal organogenesis. Millenbaugh et al. (2008) exposed mice to whole body 35 GHz RFEMF at a power density of 750 W/m^2 for approximately 60 min (until a colonic temperature of 41-42^{o}C was achieved), then assessed gene expression and conducted histological analysis of the skin. The authors reported histological changes in the dermis including aggregation of neutrophils in vessels, degeneration of stromal cells and breakdown of collagen but no

changes were observed in the epidermis, adipose tissue or muscle. Gene expression changes associated with heat-shock proteins, transcription, protein folding, oxidative stress, immune response, and tissue matrix turnover were observed at 6 h post-exposure. At 24 h post-exposure, altered gene expression related to extracellular matrix structure and chemokine activity were observed. The authors considered the observed histological and gene expression changes to be due to thermally related stress and tissue injury. Habauzit et al. (2020) assessed gene expression in the skin of young and adult hairless rats after whole body exposure to 94 GHz for 3 h/day, 3 days/week for 5 months at a power density of 100 W/m^2. In these experiments, skin temperature increased by approximately 1^{o}C in adult rats and 0.5^{o}C in young rats, but there was no measurable colonic temperature increase following RFEMF exposure. When analysis was conducted without Benjamini-Hochberg (BH)-correction, 14 differentially expressed genes were observed in adult rats and 4 were observed in young rats. There were no common genes expressed between the adult and young rats in response to RFEMF, making it likely that the identified genes were false-positive responses The authors found no differentially expressed genes when using a 1.5-fold change filter when applying BH-correction for multiple-comparisons testing.

Furman et al. (2020) exposed the skin on the flank of mice to pulses (5-10 μs) of 101 GHz RFEMF at a power density of 3 MW/m^2, then assessed changes in body weight, skin histology, locomotor activity, anxiety and blood hematology. Under these exposure conditions, skin temperature from RFEMF exposure did not change by more than 0.1^{o}C. The authors reported they found no changes to any endpoints studied. Xie et al. (2011) studied stress responses in rats irradiated with 35 GHz RFEMF for 30 s at a power density of 5000 to 75000 W/m^2 where the skin temperature rapidly increased from baseline by ~6 to 60^{o}C. Changes to EEG activity, indicative of a stress response, were only observed when skin temperature changes exceeded the rat heat-pain threshold (~43^{o}C). The authors concluded that: “The skin temperature increase produced by millimeter wave irradiation is the principle reason for stress reactions and skin injuries.” Alekseev et al. (2010) examined the ability of millimeter wave RFEMF to modulate the murine sural nerve in the hindpaw using electrophysiological approaches in an effort to understand how RFEMF interacts with receptors in the peripheral nervous system. The authors irradiated the receptive field of the mouse hindpaw with 42.2 5 GHz RFEMF at power densities ranging from 0 to 2200 W/m^2 for 100 s to 10 min and found that the spontaneous firing rate of the sural nerve decreased with exposures above 450 W/m^2 which were associated with temperature increases of ~1.5^{o}C. The authors speculated that cold-sensitive nerve fibres may be responsive to RFEMF exposure (e.g. heating) as stimulation with radiant heat caused a similar response.

Kolosova et al. (1996) assessed the ability of millimeter wave treatment to modulate the rate of recovery from sciatic nerve transection in rats. In this study, rats were exposed to 54 GHz RFEMF for 10 min/day every third day for 7 to 20 days at a power density of 40 W/m^2 delivered to the thigh area, then sciatic nerve regrowth and conduction velocity were assessed. The authors reported increased nerve regrowth and conduction velocity were evident at 20-days post-transection in the RFEMF exposed rats’ relative to the sham control group. In a follow-up study, Kolosova et al. (1998) used a similar sciatic nerve transection model and exposed the thigh skin of rats to 53.57 GHz for 10 min/day every third day for 2 weeks at a power density of 40 W/m^2. The authors measured total action potentials in regenerating nerve fibres at 5 months post-lesioning and found a 25-30% increase in the amplitude and conduction velocity among

animals treated with RFEMF. It is unclear if local tissue heating or a direct effect of RFEMF are responsible for these observations. Another study regarding the potential therapeutic benefits of RFEMF exposure on healing was conducted by Xia et al. (2012). In this study, the anterior cruciate ligament of rabbits was surgically transected, then at 6-weeks post-transection the knees of these animals were exposed to 37.5 GHz RFEMF for 20 or 40 min/day, 5 days/week for 2 weeks at a power density of 100 W/m^2. At the end of the RFEMF exposure period (8-weeks post-transection), the authors observed that the 'Mankin' score, chondrocyte apoptosis and the expression of caspase-3 and MMP-13 were significantly reduced in the animals exposed to RFEMF for 40 min/day. Similar, non-significant, trends were observed in animals exposed to RFEMF for 20 min/day. The authors concluded that RFEMF treatment provided a therapeutic benefit for osteoarthritis cartilage structure repair.

Shanin et al. (2005) used painful electrical stimulation (e.g. stress) to induce changes in splenic NK cytotoxic activity and c-*Fos* alterations in the hypothalamus, then assessed the ability of exposure to 42.2 GHz RFEMF to the knee or neck skin to modulate these stress-induced responses. The authors reported that RFEMF exposure (two 40 min exposures at an unknown intensity) prevented the suppression of splenic NK cytotoxic activity by electrical stimulation. RFEMF exposure was also reported to reduce the number of c-*Fos* positive cells within the hypothalamus. However, RFEMF exposure alone was able to increase the number of c-*Fos* positive cells in the hypothalamus compared to control groups, indicating that RFEMF exposure to the skin may have itself led to the stress response. Novikova et al. (2008) also assessed the ability of millimeter wave RFEMF to modulate c-*Fos* expression in the hypothalamus of experimental animals. The authors used movement restriction for 40 min as a stressor, which induced c-*Fos* expression in the anterior hypothalamic nucleus and the lateral hypothalamic area. Exposure of movement restricted rats (2 x 40 min) with 42.2 GHz RFEMF (unknown intensity) was found to enhance the number of c-*Fos* positive cells within the hypothalamus and such cells were found in all regions of the hypothalamus. It is unclear if this effect was due to RFEMF alone, due to the 80 min of movement restriction or due to a combination of factors which may have also included heat stress. de Seze et al. (2020) exposed male rats to 10 GHz RFEMF (1 ns pulse duration,100 pulses per second) for 10 s every 5 min for 1 hour at an instantaneous peak power density of 20 GW/m^2, then assessed a variety of behavioural endpoints and GFAP expression in the brain. The authors reported no significant differences in any of the behavioural tests conducted, but noted increased brain GFAP immunostaining at 7-day post-exposure but not at 2-days post-exposure.

Paulraj and Behari (2012a) exposed young rats to 9.9 GHz RFEMF for 2 h/day for 35 days at a power density of 1.25 W/m^2, then assessed enzyme activity and calcium ion efflux in brain tissue. The authors reported that calcium ion efflux was increased, ornithine decarboxylase activity was increased and protein kinase C activity was decreased in brain tissue of RFEMF exposed animals. In a similar study, Paulraj and Behari (2012b) exposed young rats to 16.5 GHz RFEMF for 2 h/day for 35 days at a power density of 10 W/m^2, then assessed protein kinase C activity and glial cell proliferation in the whole brain or hippocampus. The authors reported decreased protein kinase C activity and increased glial cell proliferation in RFEMF exposed animals.

Sharma et al. (2013) exposed mice to 10 GHz RFEMF for 2 h/day for 30 days at a power density of 2.5 W/m^2, then assessed spatial memory and learning using the Morris water maze and assessed brain protein concentration in RFEMF versus sham exposed animals. The authors reported an increased latency for mice in the RFEMF group to reach the target, possibly indicating decreased spatial learning and memory. Brain protein content was also reported to be lower in the RFEMF treatment group. In a similar study, Sharma et al. (2017) exposed young mice to 10 GHz RFEMF for 2 h/day for 15 days at a power density of 2.5 W/m^2, then assessed body and brain weight, brain tissue lipid peroxidation and antioxidant capacity either immediately or at 6 weeks' post-exposure and escape latency using the Morris water maze. The authors reported decreased brain and body weight, increased brain lipid peroxidation and catalase activity, decreased brain glutathione and superoxide dismutase activity, decreased brain protein concentration and increased escape latency in the RFEMF treatment group at both time points. The authors also reported histological changes in the brain. Unfortunately, there was no indication of blinding for any of the endpoints assessed in this study, limiting the strength of these observations.

Deghoyan et al. (2012) exposed the heads of restrained rats to 90-160 GHz broad spectrum RFEMF for up to 10 min at a crudely estimated peak $SAR_{0.5g}$ of 1.49 W/kg, then assessed skin and brain tissue dehydration. The authors reported decreased skin, cortex, subcortex and cerebellum hydration after RFEMF exposure with the greatest effect occurring after only 1 min exposure. The authors speculated that RFEMF may have induced structural change to water in the head skin which led to unknown messengers that modulated brain tissue hydration levels.

Minasyan et al. (2007) assessed the ability of millimeter wave RFEMF to modulate the activity of neurons in the supraoptic nucleus of the hypothalamus. Anesthetized rats were exposed to 42.2 GHz RFEMF for 40 min at a power density of 1.9 W/m^2, then neuronal spike activity was assessed. The authors reported RFEMF exposure altered the duration of interspike intervals and changed the regularity of spiking frequency. Sivachenko et al. (2016) measured spinal trigeminal nucleus neuronal discharges after treatment of the nose of anesthetized rats with 40 GHz RFEMF (unknown intensity) for three 10 minute episodes (with 10 min intervals between). The authors reported that RFEMF exposure of the receptive field of the spinal trigeminal nucleus inhibited spontaneous discharges and activity. The authors speculated that the use of millimeter wave RFEMF may be beneficial in clinical practice for treating migraine by reducing spinal trigeminal nucleus excitability.

Olchowik and Maj (2000) exposed the head of rats to 53.57 GHz RFEMF for 20 min day (10 days on, 10 days off) for 60 days at a power density of either 10 or 100 W/m^2, either before or after corticosterone treatment (20mg/kg for 60 days), then assessed δ-glutamyl transpeptidase activity in the livers of these animals. The authors reported that 53.57 GHz REFEMF exposure at a power density of 100 W/m^2, either before or after hydrocortisone treatment, suppressed the induction of δ-glutamyl transpeptidase activity in the liver by hydrocortisone. Olchowik (2001) assessed the ability of 54 GHz RFEMF exposure to modulate the regeneration of bone tissue. Rats were treated with hydrocortisone (20 mg/kg/day for 70 days) to reduce bone density and were co-exposed to sham or 54 GHz RFEMF for 20 min/day 70 days (14 days on, 14 days off) at a power density of 40 W/m^2. When bone density was assessed, animals in the RFEMF treatment group were observed to have slightly higher values compared to the cage control than the

sham/hydrocortisone group however the effect size was very small. The relevance of these findings towards adverse health outcomes is not apparent.

Since previous studies by Ziskin and colleagues had reported millimeter-wave RFEMF exposure induced opioid-like hypoalgesia in mice and that such effects could be suppressed by opioid antagonists, Radzievsky et al. (2002) assessed gastrointestinal transit in mice as opioids are known to cause gastrointestinal disturbance. The authors exposed the noses of mice to 61.22 GHz RFEMF for 15 min at 150 W/m^2, then assessed small intestine and colonic transit using the charcoal meal test. The authors reported no evidence of suppression of gastrointestinal motility in RFEMF exposed animals.

Ray and Behari (1990) exposed young rats to 7.5 GHz RFEMF for 3 h/day for 60 days at a power density of 6 W/m^2, then assessed physiological endpoints such as food intake, body and organ weights and hematological endpoints. The authors reported that RFEMF exposed animals had a lower food intake, lower body weight and organ weights but increased concentration of blood leukocytes. The authors speculated that RFEMF exposure caused a non-specific stress response.

Rotkovska et al. (1993) exposed mice to 34 GHz RFEMF for 17 h/day, 5 days/week for 2 weeks at a power density of 0.2 W/kg, then assessed hematology and organ cellularity. The authors reported increased spleen weight, increased bone marrow granulocyte and macrophage progenitor cell concentration and decreased total blood lymphocyte concentration in RFEMF exposed animals. Considering the number of blood and organ counts assessed, the authors concluded that "…none of the parameters tested was affected to an extent that would indicate the start of a pathological process or the risk of damage to genetic material".

Sisodia et al. (2013) exposed mice to 10 GHz RFEMF for 2 h/day for 30 consecutive days at a power density of 2.5 W/m^2, then assessed blood for hematological and biochemical changes after RFEMF treatment alone or when combined with a fruit extract. The authors reported alterations in most hematological and biochemical parameters measured in the RFEMF group with the most profound changes being increased platelet concentration, decreased RBC concentration, a decreased percentage of monocytes among leukocytes and decreased acid phosphatase. Pre-treatment with a fruit extract was reported to cause recovery of most of these parameters towards values observed in the sham control group. All observed values were within the normal physiological range. The significance of these observations is unclear.

Van Eeghem et al. (2017) exposed mice for 24 h/day for 6 days to 10 GHz RFEMF (2 Hz or 8 Hz modulated) at an estimated WBA-SAR of 0.3 W/kg, then assessed behaviour and brain neurotransmitter levels either immediately after the exposure period or at 4-weeks post-exposure. The authors reported that locomotor activity, as assessed by the open field test, was reduced in animals exposed to 2 Hz modulated RFEMF, but not 8 Hz modulated RFEMF immediately after exposure but these effects did not persist at 4 weeks' post-exposure. No effects were observed on the rota-rod test, on spatial working memory or anxiety/depression-like behavior. Analysis of brain neurochemical levels found no changes in dopamine, DOPAC, DOPAC/dopamine turnover or cortical glutamate concentration.

Table 4.24: Summary of mammalian study characteristics on other health and mechanistic endpoints.

Source	***Species***	***Frequency***	***Exposure duration and intensity***	***Tissue exposed***	***Findings***
Alekseev et al., 2010	*Mouse, male)*	*42.25 GHz, continuous and 1 kHz pulsed*	*100 s to 10 min; 0-2200 W/m^2*	*Hindpaw*	*At exposures of 450 W/m^2 or above, where a hindpaw skin temperature increase of 1.5^{o}C was observed, firing rate of the sural nerve was reduced by up to 44%. No effects were observed from exposures up to 10 min at exposure levels of up to 300 W/m^2. A similar decrease in sural nerve firing rate was invoked by radiant heating of the hindpaw leading the authors to conclude that this effect was mediated by hindpaw skin heating.*
Deghoyan et al., 2012	*Rat, male*	*90 to 160 GHz broad spectrum, 4 Hz-modulated*	*1, 5 or 10 min; unknown power density, peak SAR(0.5g) ≈1.49 W/kg*	*Head*	*Decreased brain tissue (cortex, subcortex, cerebellum) and head skin hydration were observed at 1 to 10 min after exposure.*
De Seze et al., 2020	*Rat, male*	*10 GHz, pulsed*	*10 s, every 5 min for 1 h; 20 GW/m^2*	*Whole body*	*No effects were observed on behaviour. Increased GFAP expression was observed in rat brain at 7 days post-exposure, but not at 2 days post-exposure.*
Furman et al., 2020	*Mouse, female*	*101 GHz, pulsed at 0.25 Hz*	*0-100 pulses (5-10 µs pulse width); 3 MW/m^2*	*Rear thigh*	*No changes were reported for any endpoint.*
Habauzit et al., 2020	*Rat, male*	*94 GHz*	*3 h/day, 3 days/week for 5 months; 100 W/m^2*	*Whole body*	*No changes in gene expression were observed in skin tissue. Skin temperature increased by 1.0^{o}C in adult rats and 0.5^{o}C in young rats, whereas colonic temperature did not change appreciably.*
Kolosova et al., 1996	*Rat, male*	*54 GHz*	*10 min/day, every third day for 7 or 20 days; 40 W/m^2*	*Femoral skin*	*Sciatic nerve regeneration and nerve conduction velocity were increased in RFEMF-treated animals.*

Kolosova et al., 1998	*Rat, male*	*53.57 GHz*	*10 min/day every third day for 2 weeks; 40 W/m^2*	*Thigh skin*	*At 5 months post-transection, sciatic nerve conduction velocity and amplitude were increased by 25-30% in RFEMF-treated animals.*
Millenbaugh et al., 2008	*Rat, male*	*35 GHz*	*~60 min (until a 41-42^{o}C colonic temperature was reached); 750 W/m^2*	*Whole body*	*After ~60 min RFEMF exposure, skin and colonic temperatures reached ~42^{o}C. At 3-6 h post-exposure, degeneration and necrosis of dermal stromal cells, dilation of blood vessels, leukocyte aggregation and collagen breakdown were evident. No changes were evident in the epidermis, muscle or adipose tissues. Expression of genes for heat shock proteins, transcription regulation, oxidative stress, immune response and tissue matrix turnover were altered at 6-24 h post-exposure due to thermally-related stress and injury.*
Minasyan et al., 2007	*Rat*	*42.2 GHz and 50.3 GHz*	*40 min; 1.9 W/m^2 at 42.2 GHz or 4.8 W/m^2 at 50.3 GHz*	*Whole body*	*RFEMF exposure altered the duration of interspike intervals and changed the proportion of neurons with irregular spiking frequency.*
Novikova et al., 2008	*Rat, male*	*42.2 GHz*	*40 min; unknown intensity*	*Knee or neck skin*	*Movement restriction (40 min) acted as a stressor which induced c-Fos expression in the anterior hypothalamic nucleus and the lateral hypothalamic area. RFEMF exposure of movement restricted rats (2 x 40 min, unknown intensity) was found to enhance the number of c-Fos positive cells and such cells were found in all regions of the hypothalamus.*
Olchowik and Maj, 2000	*Rat, female*	*53.57 GHz*	*20 min day (10 days on, 10 days off) for 60 days; 10 or 100 W/m^2*	*Head*	*RFEMF exposure at a power density of 100 W/m^2, either before or after hydrocortisone treatment, suppressed the induction of δ-glutamyl transpeptidase activity in liver.*
Olchowik, 2001	*Rat, female*	*54 GHz*	*20 min/day (14 days on, 14 days off) for 84 days; 40 W/m^2*	*Head*	*RFEMF exposure was reported to ameliorate hydrocortisone-induced bone density loss.*

Paulraj and Behari, 2012a	*Rat, male*	*9.9 GHz, 1 kHz modulated*	*2 h/day for 35 days; 1.25 W/m^2*	*Whole body*	*Increased calcium ion efflux and ornithine decarboxylase activity, decreased protein kinase C activity in developing rat brain after chronic exposure.*
Paulraj and Behari, 2012b	*Rat, male*	*16.5 GHz*	*2 h/day for 35 days; 10 W/m^2*	*Whole body*	*Decreased protein kinase C activity and increased glial cell numbers in developing rat brain after chronic exposure.*
Pyrpasopoulou et al., 2004	*Rat, female*	*9.35 GHz, pulsed at 50 Hz*	*24 h/day for either Days 1-3 or 4-7 post-coitum; 0.05 W/m^2*	*Whole body*	*Increased transcript expression of BMP-4 and BMPR-IA and decreased expression of BMPR-II in newborn kidneys. Immunohistochemistry showed altered protein expression and localization in the newborn kidney. These changes did not appear to affect renal development.*
Radzievsky et al., 2002	*Mouse, male*	*61.22 GHz*	*15 min; 150 W/m^2*	*Nose*	*No evidence of suppression of gastrointestinal motility in RFEMF exposed animals.*
Ray and Behari, 1990	*Rat, male and female*	*7.5 GHz, 1 kHz modulated*	*3 h/day for 60 days; 6 W/m^2*	*Whole body*	*RFEMF exposed animals had a lower food intake, lower body and organ weights but an increased concentration of blood leukocytes.*
Rotkovska et al., 1993	*Mouse*	*34 GHz*	*17 h/day, 5 days/week for 2 weeks; 0.2 W/m^2*	*Whole body*	*Increased spleen weight, increased bone marrow granulocyte and macrophage progenitor cell concentration and decreased total blood lymphocyte concentration in RFEMF exposed animals.*
Shanin et al., 2005	*Rat, male*	*42.2 GHz*	*Two 40 min exposure periods with a 40 min break in between; unknown intensity*	*Knee or neck skin*	*RFEMF exposure ameliorated the suppression of splenic NK cytotoxic activity and reduced the number of c-Fos positive cells within the hypothalamus induced by painful electrical stimulation (e.g. pain stress). RFEMF exposure alone was able to increase the number of c-Fos positive cells in the hypothalamus, indicating that RFEMF exposure itself may have led to a stress response.*
Sharma et al., 2014	*Mouse, male*	*10 GHz*	*2 h/day for 30 days; 2.5 W/m^2*	*Whole body*	*Decreased concentration of protein in brain and increased latency in Morris water maze test, indicating possible effects on spatial memory and learning.*
Sharma et al., 2017a	*Mouse, male and female*	*10 GHz*	*2 h/day for 15 days; 2.5 W/m^2*	*Whole body*	*Decreased brain and body weight, increased lipid peroxidation and decreased antioxidant capacity, decreased brain protein concentration and increased latency in Morris water maze indicating possible effects on spatial learning and memory.*
Sisodia et al., 2013	*Mouse, male*	*8-12 GHz*	*2 h/day for 30 days; 2.5 W/m^2*	*Whole body*	*RFEMF exposure caused alterations in hematological and biochemical parameters, with the most profound*

					changes being increased platelet concentration, decreased RBC concentration, a decreased percentage of monocytes among leukocytes and decreased acid phosphatase.
Sivachenko et al., 2016	*Rat, male*	*40 GHz, 10 Hz modulation*	*Three 10 min exposures with a 10 min interval; unknown intensity*	*Nose*	*RFEMF exposure of the receptive field of the spinal trigeminal nucleus inhibited spontaneous discharges and activity.*
Van Eeghem et al., 2017	*Mouse, male*	*10 GHz, 2 or 8 Hz amplitude-modulated*	*24 h/day for 6 days; estimated WBA-SAR of 0.3 W/kg*	*Whole body*	*Decreased locomotor activity immediately after exposure to 2 Hz modulated RFEMF, no effects after 8 Hz modulated RFEMF exposure.*
Xie et al., 2011	*Rat, male*	*35 GHz, pulsed at 0.5 or 1.0 kHz*	*30 s; 5000 to 75000 W/m²*	*Whole body*	*Stress reactions measured using EEG were evident shortly (1-2 s) after irradiation at 7.5kW/m². The corresponding skin temperature rise where EEG changes began to occur was ~ 44-50°C, at a level above the skin pain threshold (~43°C). As the irradiation intensity decreased, EEG stress changes occurred at a greater latency time, were less intense and the time required to induce a similar skin temperature was increased. The authors concluded that the EEG stress response was mediated by the skin temperature increase induced by RFEMF.*
Xia et al., 2012	*Rabbit, male and female*	*37.5 GHz*	*20 or 40 min/day, 5 days/week for 2 weeks; 100 W/m²*	*Knee*	*Mankin score, chondrocyte apoptosis and the expression of caspase-3 and MMP-13 were significantly reduced in the animals exposed to RFEMF for 40 min/day.*

Risk-of-bias assessment for mammalian studies on other effects and mechanistic endpoints

Table 4.25: Summary of risk-of-bias judgements (low, probably low, probably high, high) for each risk of bias item for each included mammalian study assessing other effects and mechanistic endpoints in response to RFEMF exposure in the 6 to 300 GHz frequency range.

Source	Study design	Blinding	Attrition/exclusion	Exposure assessment	Selective reporting	Conflict of interest	Other	Overall study Risk of Bias
Alekseev et al., 2010								
Deghoyan et al., 2012								
de Seze et al., 2020								
Furman et al., 2020								
Habauzit et al., 2020								
Kolosova et al., 1996								
Kolosova et al., 1998								
Millenbaugh et al., 2008								
Minasyan et al., 2007								
Novikova et al., 2008								
Olchowik and Maj, 2000								
Olchowik, 2001								
Paulraj and Behari, 2012a								
Paulraj and Behari, 2012b								
Pyrpasopolou et al., 2004								
Radzievsky et al., 2002								
Ray and Behari, 1990								
Rotkovska et al., 1993								
Shanin et al., 2005								
Sharma et al., 2014								
Sharma et al., 2017a								
Sisodia et al., 2013								
Sivachenko et al., 2016								
Van Eeghem et al., 2017								
Xie et al., 2011								
Xia et al., 2012								

Risk of bias categories: low risk (green), probably low risk (yellow), probably high risk (orange), high risk (red).

In summary, a number of animal studies have assessed a diverse assortment of mechanistic or physiological outcomes in response to millimeter-wave RFEMF exposure. Nearly all such studies lacked randomization for allocation into exposure groups, concealment during exposure and blinding for endpoint analysis. Since these studies evaluated different frequencies, intensities, exposure durations and endpoints it is not appropriate to develop an overall risk of bias that encompasses all such studies. These studies will not be considered further due to the lack of a direct linkage to any adverse health outcome.

Summary of evidence from human and mammalian studies

While there are a limited number of studies on most adverse health outcomes from exposure to millimeter-wave RFEMF, complementary research from hyperthermia-based studies provides sufficient evidence that RFEMF exposure may exert a number of adverse health outcomes through a temperature-induced mechanism. It is known that absorption of RFEMF energy can lead to elevated tissue or core body temperatures if the rate of energy absorption exceeds the body or tissues thermoregulatory capacity to dissipate such heat (see section 4.4). Based upon the available evidence, it can be concluded that there is sufficient evidence that millimeter-wave RFEMF exposure could lead to both a heat-pain sensation and tissue damage if exposures are sufficiently intense. While the occurrence of heat-pain is threshold dependent and can be perceived immediately once the threshold is achieved (~42-43^{o}C), tissue damage from temperatures exceeding ~43^{o}C is time-dependent (e.g. time above a certain temperature threshold) with different tissues exhibiting different sensitivities (see section 4.2). In most instances a heat-pain sensation, which can trigger a rapid reflexive avoidance response, will occur before the onset of tissue damage thus providing inherent protection against thermal tissue damage. As the tissue temperature increases above 43^{o}C, the time difference between the perception of heat pain and the occurrence of tissue damage decreases. In a worst-case scenario, tissue damage may occur instantaneously and simultaneously with the heat pain sensation (e.g. such as touching a hot object). For this reason, in order to avoid adverse health outcomes, it is imperative that the rate of RFEMF energy absorption is maintained at a level where either no appreciable tissue/body temperature elevation occurs or at a rate whereby an avoidance response is possible.

There is also evidence from rodent studies that whole-body millimeter-wave RFEMF exposure may exert a hypotensive response that may lead to death if exposure is sustained. It is important to note that such effects were observed in anesthetized rats where thermoregulation and hemodynamic stability are likely compromised due to the anesthetic, but more importantly resulted in skin and subcutaneous temperatures that exceeded the heat-pain threshold. Thus, in a non-anesthetized person or animal, heat-pain would be perceived and the person/animal would seek to avoid the exposure. Furthermore, since skin/subcutaneous temperature increases precede increases in core body temperature by several minutes, it is inconceivable that such an effect would occur in a human as: a) there are no realistic scenarios where such exposures would occur, and b) a person would not tolerate the heat-pain sensation and would seek shelter from the exposure prior to the occurrence of a hypotensive response. Ensuring the avoidance of a heat-pain sensation in humans from millimeter-wave RFEMF exposure would mitigate the occurrence of such an effect.

Evidence from complimentary research suggests that core body temperature elevations below the temperature threshold for the heat-pain sensation from millimeter-wave RFEMF most likely also has the ability to exert teratogenic effects and effects on male fertility (e.g. sperm quality) (see section 4.2). It is well established that hyperthermia during pregnancy can induce birth defects in experimental animals. Whole-body heating by intense millimeter-wave RFEMF, where maternal core temperature during pregnancy is increased to ≥39^{o}C, will likely exert teratogenic effects. It is unlikely that a core body temperature of 39^{o}C could be exceeded by whole-body millimeter-wave RFEMF exposure without first exceeding the heat-pain threshold (43^{o}C) in some superficial tissue since millimeter wave RFEMF are

primarily absorbed in the skin. Regardless, there is a need to avoid whole-body temperature elevation from millimeter-wave RFEMF to avoid possible teratogenic effects on the fetus.

Complimentary research has also demonstrated that elevation of testes temperature by as little as 1°C may exert reversible changes to sperm quality that may impact male fertility (see section 4.2). It is unclear if localized exposure of the scrotum to millimeter-wave RFEMF is capable of increasing testes temperature without first exceeding the heat-pain threshold (42-43°C) in scrotal skin. Since most millimeter-wave RFEMF energy will be deposited in the skin of the scrotum and due to the considerable thermoregulatory capacity of the skin to dissipate heat (See section 4.4), it is more likely that core body temperature would need to be increased to exert a 1°C temperature change within the testes.

There is insufficient evidence to support conclusions regarding the ability of millimeter-wave RFEMF (or complimentary research) to induce adverse health effects on the immune system and limited evidence to support an increased risk of cancer. A summary of the Quality and Strength of Evidence for adverse health effects from millimeter-wave RFEMF is depicted in Table 4.26.

Table 4.26: Summary of evidence for potential adverse health outcomes in human and mammalian studies in response to millimeter-wave RFEMF exposure. The occurrence of such effects considers complimentary research, including possible temperature-induced effects from RFEMF exposure.

Adverse Health Outcome	**Evidence stream**	**Quality of Evidence (from millimeter-wave RFEMF studies)[a]**	**Strength of Evidence (from RFEMF studies and complementary hyperthermia research)[b]**
Pain sensation	Human	Low	**Sufficient**
Cardiovascular (hypotensive collapse)	Mammalian	Low	**Sufficient**
Immune system	Mammalian	Low	Insufficient
Tissue damage (corneal)	Mammalian	Very Low	**Sufficient**
Cataractogenesis	Mammalian	Very Low	**Sufficient**
Reproduction (adverse pregnancy outcomes)	Mammalian	Low	**Sufficient**
Reproduction (male fertility)	Mammalian	Low	**Sufficient**
Cancer/Genotoxicity	Mammalian	Low	Insufficient

[a]Quality of Evidence ratings: High, Moderate, Low or Very low

[b]Strength of Evidence ratings: Sufficient, Limited, Insufficient or Evidence of no health effect.

Since the occurrence of potential adverse health effects from millimeter-wave RFEMF is highly dependent upon the site of exposure (localized or whole-body) and temperature (either threshold or relative), a summary of relevant exposure conditions is depicted in Table 4.27. It is evident from Table 4.27 that both whole-body and localized temperature must be considered for the avoidance of potential adverse health

effects. As such, both whole-body and localized human exposure limits must be developed for the avoidance of potential adverse health effects from millimeter-wave RFEMF.

Whole-body exposure limits have already been established in Safety Code 6 (2015), ICNIRP (2020) and IEEE (2019) at a power density limit of 10-20 W/m^2. The core body temperature increase associated with whole-body exposure to millimeter wave RFEMF at these limits has not been assessed in any known study. However, a study exposing human subjects (half-body exposure) to long wave infrared radiation at a power density of 1260 W/m^2 for approximately 40 min caused a 1^{o}C core body temperature increase (Brockow et al., 2007). ICNIRP (2020) have reported that this exposure translates to a whole-body SAR of approximately 18 W/kg which is far above the whole-body average SAR of 4 W/kg (or power density of ~500 W/m^2) for RFEMF that is conservatively estimated to be associated with a 1^{o}C core body temperature increase at frequencies between 6 to 300 GHz RFEMF (ICNIRP, 2020). Since Canadian and international exposure limits are set at 50-fold lower than the power density/whole body average SAR required to elicit an estimated 1^{o}C temperature increase, the core body temperature increase from exposure to millimeter wave RFEMF at the maximum allowable Canadian/International limits are likely to be less than 0.1^{o}C. Therefore, cardiovascular and reproductive effects are unlikely to occur from millimeter-wave RFEMF due to the large safety margins applied in the exposure limits, realistic exposure scenarios and the relative temperature increases expected to occur at the maximum allowable exposure level.

Safety Code 6 (2015) does not currently specify recommended human exposure limits for localized exposure to millimeter-wave RFEMF. At present, the whole-body exposure limits in Safety Code 6 (2015) are considered to also apply for localized exposures. However, the health effects associated with localized exposure to millimeter wave RFEMF are different than those upon which the whole-body exposure limits are based. Reliance upon whole-body based exposure limits for localized exposure, while protective due to the large safety margins applied, are not scientifically linked to the primary adverse health outcome (avoidance of heat-pain sensation and thermal tissue damage). Based upon an assessment of the currently available scientific literature, it is evident that localized human exposure limits for millimeter-wave RFEMF should be based upon the avoidance of a heat-pain sensation and tissue damage (skin and cornea) in superficial tissues.

Table 4.27: Exposure conditions relevant to occurrence of hazards from millimeter wave RFEMF.

Adverse Health Outcome	**Route of Exposure**	**Tissue**	**Thermal threshold or relative temperature increase (^{o}C)**	**Comments**
Pain sensation	Localized or whole body	Skin, Cornea	42-43^{o}C	Such effects may occur instantaneously if localized skin temperature reaches the threshold temperature for activation of pain receptors in the skin or cornea (See section 4.2).

Tissue damage	Localized or whole body	Skin, Cornea	43°C	Such effects may occur in skin or corneal tissue if a temperature of 43°C is achieved and maintained for a sufficient period of time (See section 4.2).
Cardiovascular (hemodynamic collapse)	Whole body	Whole body	41-42°C	Such effects may occur when colonic (core) body temperatures reach the threshold temperature and are sustained. However, heat pain in superficial tissues would be experienced prior to achieving such a core body temperature increase.
Reproduction (Male fertility)	Whole body	Testes	35-36°C (~1-2°C above normal testes temperature)	Reversible effects on male fertility (sperm function) may occur if testes temperatures increase 1-2°C above normal testes temperature.
Reproduction (adverse pregnancy outcomes)	Whole body	Embryo/ Fetus	39°C (~2°C above normal core body temperature)	The increase in temperature required to lead to deleterious outcomes seems to be conserved at ~2-2.5°C above normal maternal core body temperature with a threshold duration at this increased temperature of approximately 1 h. Such effects may occur when colonic (core) body temperatures reach the threshold temperature and are sustained. However, heat pain in superficial tissues would be experienced prior to achieving such a core body temperature increase.

4.2 Threshold of temperature-related adverse health effects

Thermal tissue damage

It is well established that excessive localized heating can result in tissue damage. Thermal thresholds for tissue damage are governed by the tissue temperature as well as the duration of the exposure at this temperature, and shift when either of these variables change (Dewhirst et al., 2003a). As such, the absolute temperature of a tissue (along with exposure duration), and not its change in temperature, is the most appropriate measure for estimating damage. Thermal stress of a tissue depends on many variables including its physiological characteristics and metabolic activity, age, sex and health status, as well as the ambient environmental conditions and the insulative capacity of overlying clothing. It is important to note that different tissues have varying sensitivities to heat, and that this sensitivity depends on where the tissues are found in the body as well as their ability to thermoregulate and mitigate thermal damage In order to compare thermal damage of tissues, a thermal isoeffect dose (TID) is used. The TID model

translates the different time-temperature histories of a tissue to a single number of minutes at a specific temperature. Cumulative equivalent minutes at 43°C (CEM 43°C) was developed (Sapareto and Dewey, 1984) to standardize the concept of thermal dose across tissues and exposure times, thus permitting the comparison of specific effects using a single common unit. The CEM 43°C method quantifies thermal exposure by taking the number of cumulative minutes at 43°C required to cause an equivalent effect, thereby enabling comparisons of thermal sensitivities between tissues (Figure 1). The cumulative equivalent minutes at 43°C can be calculated as follows:

$$\mathrm{CEM43^{\circ}C} = \sum_{i=1}^{n} t_i \cdot R^{(43-T_i)}$$

where t_i is the i^{th} time interval of exposure, R is a multiplication factor that takes into account the time needed to achieve an isoeffect when the temperature changes by 1°C either above or below the breakpoint of the Arrhenius plot and T is the average temperature during the time interval *t*. This method takes into account the time at each temperature and the value is summed to give a final CEM 43°C value that characterizes the history of the exposure of the tissue (Dewhirst et al., 2003b; Dewey, 2009; van Rhoon et al., 2013).

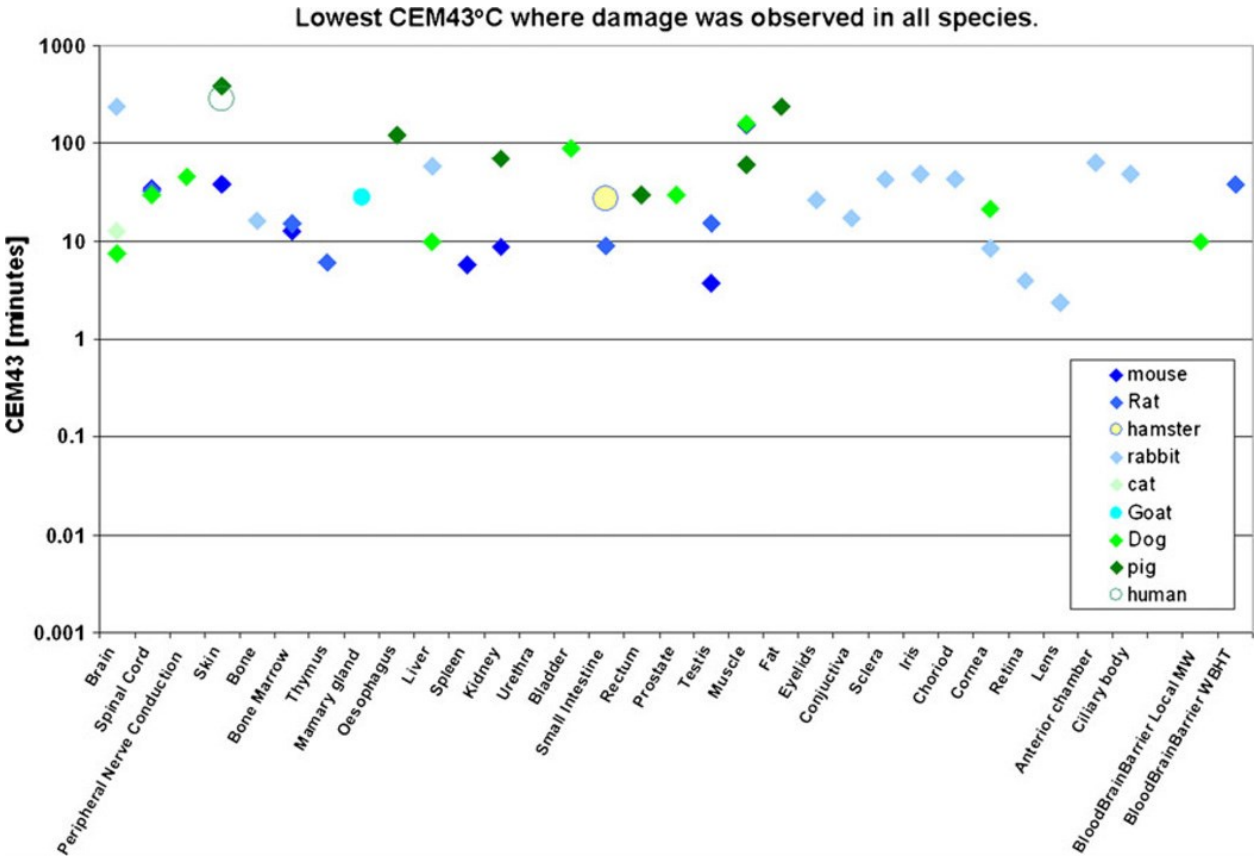

Figure 4.2: Lowest CEM 43°C for tissue damage for all tissues and all species.

(Source: van Rhoon et al., 2013)

Superficial tissues have a higher heat tolerance than deeper tissues and are by nature more resistant to fluctuating temperatures. Excessive superficial heating will usually result in the perception of pain before the occurrence of thermal tissue damage. This implies that the pain threshold sensation in skin is significantly lower than the threshold for thermal damage (Dewhirst et al., 2003a). Therefore, when looking to protect against the detrimental effects of hyperthermia due to RF exposure, it is both prudent and protective to choose a conservative threshold temperature responsible for pain perception, as this occurs at a much lower temperature than the hyperthermic tissue damage threshold (Stoll and Greene, 1959).

Thermal pain sensation:

Thermal pain receptors are located in human skin, muscle, bone, joints, viscera and the cornea. There are three classes of nerve receptors which respond to noxious stimuli: mechanical, mechanothermal and polymodal nociceptors. These free nerve endings, which are part of the peripheral nervous system, are responsible for the transmission of a pain signal from the point where the receptor is noxiously activated to the CNS, where the pain signal is received. There are 2 types of nerve fibres that detect thermal pain and transmit signals to the CNS: myelinated Aδ fibres and unmyelinated C fibres. The Aδ fibres transmit fast/sharp pain signals to the CNS, while the C fibres transmit slower (e.g. burning sensation) signals with a more delayed response.

Skin thickness varies across the body, ranging from 0.5 mm on the eyelids to approximately 4 mm on the bottom of the feet. Although most of the nerve tissue that supplies the skin is found in the dermis, the epidermis of the skin contains specialized sensory neurons termed nociceptors, which respond when a stimulus is sufficient to potentially cause tissue damage or when tissues are damaged and release inflammatory mediators. The heat-pain threshold (HPT) in skin can vary across the body, ranging from 42^{o}C on the chest to almost 45^{o}C in the foot (Defrin et al., 2006; Hagander et al., 2000). These changes have been attributed to their distance from the CNS, where proximity to it results in a shorter reaction time and as distance from the CNS increases so does the reaction time to the painful stimulus. When reaction time is eliminated from the HPT determination, noxious heat is felt at a uniform temperature of approximately 42-43^{o}C, regardless of the location on the body (Defrin et al., 2006). Therefore, pain results when a critical tissue (or receptor) temperature is reached and not when there is a change in temperature (Cook, 1952).

Pain receptors in the skin can be subject to habituation, where multiple exposures will decrease the behavioural response, resulting in an increase in the HPT (Agostinho et al., 2009). Consequently, when assessing the literature, it is important that the HPT not be averaged over many consecutive measurements, but rather averaged over many individuals. Although females generally display a lower tolerance to heat pain than males, no difference in HPT values exist based on sex in various body parts (Tracy et al., 2018; Racine et al., 2012). Thermal nociceptors in the skin have a trigger threshold of >42^{o}C (Voets, 2014; Vriens, 2014; Dubin and Patapoutian, 2010; Zhu and Lu, 2010; Basbaum, 2009; Defrin et al., 2006; Defrin et al., 2002; Van Hees et al., 1981).

The cornea is an approximately 0.5 mm thick covering of the eye, exposed to the external environment. The cornea is the most densely innervated tissue of the human body and contains the same Aδ- and C-nerve fibres that are found in the skin (Belmonte et al., 2004). The epidermis, the outermost layer of the cornea, contains these free nerve endings which are responsible for thermal pain perception, much like the epidermis of the skin discussed above. The thermal nociceptors responding to noxious heat in the cornea are polymodal and can also be activated by mechanical energy (pressure), chemical irritants and endogenous products resulting from inflammation due to tissue injury. These polymodal pain receptors have been shown to discharge impulses at a frequency that is roughly proportional to the intensity of the stimulus applied and can be sensitized by repeated noxious heat and inflammatory stimuli, making them more sensitive to repeated noxious exposures (Belmonte and Giraldez, 1981; Gallar et al., 1993; Acosta et al., 2001). The nociceptors responsible for responding to potentially noxious heat in the cornea have been found to be triggered around 42-43^{o}C (Tominaga and Caterina, 2004; Mergler et al., 2014; Belmonte et al., 2017).

Peripheral neuropathy is a general term that identifies a series of disorders that result from damage to the peripheral nervous system. Certain conditions such as diabetes, trauma, infections, auto-immune diseases and exposure to toxins such as chemotherapeutic agents as well as rare hereditary cases can result in peripheral neuropathy, but oftentimes its origin is unknown. This condition is hallmarked by the disruption of normal signalling between the central nervous system and the rest of the body either through a loss of signal, inappropriate signalling or errors in signalling which can lead to tingling, numbness, pain and extreme sensitivity to touch. Peripheral neuropathy is characterized by a general increased sensitivity to pain (Jensen and Finnerup, 2014; Oudejans et al., 2017) and it is exhibited through allodynia or hyperalgesia which are important indicators of neuropathic pain representing altered pain responses. Allodynia is defined as pain in response to a non-nociceptive stimulus (Loeser and Treede, 2008), and occurs through the lowering of the nociceptor threshold via sensitization of the peripheral nervous system ((Ochoa et al., 2005; Viana, 2018). Individuals with allodynia may perceive a noxious heat response at temperatures lower than the normal HPT due to a sensitization of the nerve endings. Hyperalgesia on the other hand is defined as a feeling of increased pain from a normally noxious stimulus (Huang et al., 2006), resulting from a stronger nociceptor response which occurs through a stronger nerve response once the HPT is reached. This hypersensitivity is typical of systemic inflammatory disorders and neuropathic pain conditions. Due to nociceptor sensitization, these responses can also be triggered in normal individuals following injury and ensure adequate tissue protection from repeated insults (i.e.: sunburn, physical trauma) through avoidance by creating a painful stimulus. However, in situations of chronic neuropathic pain, allodynia and hyperalgesia occur even in the absence of a noxious stimulus. Small fiber neuropathy (SFN), a hallmark of diabetes, specifically affects Aδ- and C-nerve fibres of the peripheral nervous system in the skin which are responsible for the control of the noxious heat pain response. Individuals suffering from SFN experience acute pain which begins in the extremities but can also affect the face and torso as it develops, rendering these areas extremely sensitive to temperature changes. Thermal allodynia occurs when the peripheral nerves are damaged through disease, such as chronically high blood sugar in diabetes. Generally, SFN is an acquired condition (exposure to chemotherapeutic drugs, infectious diseases, immune disorders) although some cases have proven to be genetic in origin (Themistocleous et al., 2014; Sène,

2018). Allodynia and hyperalgesia may elicit pain or increased pain from normally non-noxious stimuli, however these conditions do not increase the HPT, which remains at the normal range or below (Oudejans et al., 2017), allowing affected individuals to appropriately sense a noxious heat stimulus and initiate an avoidance response for the prevention of tissue damage.

Hyperthermia-induced teratogenicity

Human growth and development *in utero* are highly susceptible to heat stress. There are numerous key processes during embryonic and fetal development, such as cellular proliferation, organ differentiation, migration and apoptosis, that require tightly controlled conditions which are extremely vulnerable to elevated heat. The body of evidence for animal effects is large and irrefutably leads to the conclusion that an increase in maternal core body temperature during critically important moments in embryonic and fetal development results in adverse birth outcomes ranging from developmental defects and reduced growth to neural tube defects and death (Edwards et al., 2003; Graham et al., 1998; Edwards et al., 1995).

Mammalian prenatal development is divided into three main stages: the germinal stage, where the fertilized egg divides and travels to the uterus for implantation in the uterine wall; the embryonic stage, where cellular differentiation occurs and results in the generation of the majority of organs, including the basic components of the nervous system; and the fetal stage, characterized by brain development and organ growth. Early exposure to thermal insult can result in failure of the blastocyst to implant. Pre-implantation loss occurs early in gestation (within the first two weeks following fertilization) and may preclude the knowledge of pregnancy. Excessive heat exposure during the embryonic stage of development can have serious deleterious effects due to the sensitivity of the organogenesis processes. Embryonic organ differentiation has increased sensitivity windows where exposure can affect development and lead to a variety of congenital defects. The type of congenital malformation produced by an exposure depends on which organ is most vulnerable at the time of the teratogenic exposure. Hyperthermia during pregnancy has been shown to cause a wide range of deleterious effects in all species studied, including humans, where the outcome of the exposure depends not only on the thermal dose but also, the stage of development when the exposure occurred.

The fetus is fully dependent on the mother for thermoregulatory control (Ziskin and Morrissey, 2011), and therefore maternal core body temperature has a direct and important effect on embryonic/fetal temperature. The embryonic thermal dose is defined as not only the elevation above normal maternal core body temperature, but also the duration of the exposure to this elevated temperature and the sensitivity of the specific organ generation process being exposed (Edwards et al., 2003). Heat damage to embryos occurs via apoptosis and other forms of cell death in organs at critical growth stages with rapid cell proliferation resulting in either congenital or fatal defects, where the development of the central nervous system shows a high degree of susceptibility (Edwards et al., 2003).

Although the teratogenic effects of heat have been extensively studied in rodents, the literature in the study of human outcomes is sparse in comparison. Extrapolating the experimental findings in the literature to humans as an absolute temperature on a specific gestational day is difficult since both core body temperature and timing of organogenesis are species specific characteristics. Rodent core body

temperatures can range from 36°C in mice and rats to 39.5°C in guinea pigs, which is either at, or approaching the teratogenic temperature level in humans. Gestational periods also differ across species, but the critical feature to keep in mind is the timing of organ development (Table 4.28). Although the temperature where heat becomes teratogenic is species specific, the increase in temperature required to lead to deleterious outcomes seems to be conserved at 2-2.5°C above normal maternal core body temperature with a threshold duration at this increased temperature of approximately 1h (Graham et al., 1998). As the temperature increases, the duration of exposure that causes teratogenic effects shortens (Shiota, 1988).

TABLE 4.28: Experimental hyperthermia findings compared with observations in exposed humans.

	Mouse	**Rat**	**Hamster**	**Guinea Pig**	**Human**
Core body temperature (°C)	**36.5-38**	**36-38.5**	**36.1-38.9**	**39-40**	**36.1-37.2**
Major developmental periods (post-fertilization)					
Pre-implantation	0-5 days	0-7 days	0-5 days	0-8 days	0-8 days
Organogenesis	6-13	8-15	6-12	9-25	9-60
Foetal	14-19.5	16-21.5	13-16.5	26-68	61-270
Total length of gestation	**20 days**	**21–22 days**	**17 days**	**68 days**	**38 weeks**
Congenital observations					
Exencephaly/encephalocele	7–8 days	9 days	7–8 days	13–14 days	3–4 weeks
Vertebral kyphosis/scoliosis	8	9		13–14	
Microphthalmia	7–9	9		14–18	4–7
Maxillary/mandibular hypoplasia		9–10			4–7
Facial clefts	8	9	9–10		4–7
Microcephaly with seizures				20–30	4–7
Microcephaly with arthrogryposis				39–46	8–18
Microcephaly	12–15	13–14		53–60	18–26
Cardiac defects		9.5		13–14	5–6
Talipes			9–10	18–25	7–20
Hypodactyly	9	12–14		18–25	7–15
Exomphalos		9		20–23	6–10
Moebius syndrome		14–16			7–20
Arthrogryposis			9–10	30–46	7–20

Adapted from Graham et al. (1998) and Edwards et al. (2003).

Hyperthermia-induced male infertility

Spermatogenesis is the process of sperm cell development. There are three stages of spermatogenesis which occurs within the seminiferous tubules of the testes, the proliferative phase (spermatocytogenesis),

the meiotic phase (spermatidogenesis) and the maturation phase (spermiogenesis). Spermatogenesis is known to be highly susceptible to disruption by a variety of chemical exposures, but also by elevated testicular temperatures (Sharpe et al., 2010; Wu et al., 2015). Although all tissues are vulnerable to thermal injury, the process of spermatogenesis within testes is unique in that this process is disrupted if testes temperature is not maintained several degrees below normal core body temperature. Under normothermal conditions, sperm production and storage are maximized at cooler temperatures and, in healthy men, optimal testicular temperature is maintained 3-4°C lower than core body temperature (~34°C). Several thermoregulatory processes are required to maintain a lower testicular temperature, such as the exchange of heat with the environment through the thin, uninsulated skin of the scrotum, evaporative cooling of sweat from the surface of the skin, temperature-activated muscular relaxation or contraction resulting in the ability to either conserve or dissipate heat by changing the distance of the testes from the body and optimized vascularization, which works to remove heat through counter-current blood flow (for reviews see Durairajanayagam, 2015; Mieusset and Bujan, 1995; Setchell, 1998).

There are several external factors that affect the testes temperature and could impact sperm quality if the exposure were of sufficient duration. Normal daily lifestyle activities such as sauna exposure (Garolla et al., 2013), having a sedentary occupation (Hjollund et al., 2000; Hjollund et al., 2002a,2002b), spending extended time in a vehicle (Bujan et al., 2000) or an individual's choice of clothing (Rock and Robinson, 1965; Robinson et al., 1968) can result in an increased testes temperature which can have a detrimental impact on spermatogenesis. A study by Wang and colleagues (2007) looked at the effect of repeated elevated scrotal temperature (43°C, 30 min/day, 6 days) exposures in healthy men on the suppression of spermatogenesis. They observed a significant decrease in sperm concentration one week following the repeated exposure with the maximum decrease being reached 4 weeks following the exposure with full recovery occurring at the 10-week mark. In this study, the authors observed transient changes in both sperm motility and morphology. Heat induced declines in sperm count are considered a reversible effect and full recovery from the thermal insult is attained following a recovery period if no other thermal insult is experienced (Ivell, 2007).

The intricate thermoregulatory controls required to maintain an optimal temperature for spermatogenesis may not be able to withstand significant thermal increases. A 1-2°C rise in the temperature of the testes (to 35-36°C) can lead to disruption of spermatogenesis, resulting in a reduction in sperm production and motility as well as an increase in the presence of morphological defects (Boni, 2019; Jung and Schuppe, 2007; Setchell, 1998).

4.3 Normothermal temperature range of skin and cornea (Type 1 tissues)

Normothermal values for Type 1 tissues (skin and cornea) typically range between 31°C to 37°C (Table 4.29) in humans. Normal corneal temperature in humans is maintained around 33-34°C but can increase to 36°C in hot environments, where a plateau is achieved (Kessel et al., 2010; Geiser et al., 2004). Fabiani et al. (2016) observed differences in corneal temperature depending on the location of the measurement,

where the temporal side was always cooler than the nasal side, resulting in the calculation of an average corneal temperature. They also noticed a 0.5°C increase in corneal temperatures following a prolonged period with closed eyelids, where the average temperature approached 37°C. This increase in temperature correlated with a lack of evaporation of the tear film, which acts to decrease the eye temperature much like sweating for the skin.

Skin temperature not only varies with ambient temperature, it also varies depending on its location across the body. Skin temperature on the fingertips and toes can be as low as 22°C and reach 34-35°C on the forearm (Table 4.29). In contrast, heat-pain thresholds in the cornea and the skin are highly conserved and occur at a tissue temperature of 42-43°C (Zhu and Lu, 2010; Defrin, 2006).

Table 4.29: Normothermal temperatures of human tissues (Type 1)

Reference	**Location**	**Temperature, tissue (°C)**	**Temperature, ambient (°C)**
Montgomery and Williams, 1976	Forehead skin	33.7	23
John et al., 2018	Forehead skin	33.7	22
Montgomery and Williams, 1976	Chest skin	33.0	23
John et al., 2018	Chest skin	33.2	22
Montgomery and Williams, 1976	Extremities skin (upper arm, forearm, thigh, calf)	31.1 – 32.6	23
Cook, 1952	Extremities skin (fingertip, forearm)	23.5 – 36.5	20
Zaproudina et al., 2008	Skin (29 sites from toe to forehead)	22.1 – 34.1	23-24
Straume et al., 2005	Pinna skin	33.9 – 34.1	23.6
Kessel et al., 2010	Cornea	33 – 35	22 - 43
Dixon and Blackwood, 1991	Cornea	33.7	N/A
Geiser et al., 2004	Cornea	32.7 36.2	20 40
Fabiani et al., 2016	Cornea	36.3	25

4.4 Thermoregulatory processes

Thermoregulation is controlled by the hypothalamus in the brain. Information on both core and cutaneous temperatures is transmitted to the CNS, which responds by initiating the dissipation of heat when the temperature is sensed to be above the normal threshold. In the skin, heat dissipation to the environment occurs via cutaneous vasodilation and sweating. In hyperthermic situations, blood flow dissipates heat to the environment via the cutaneous microcirculation and is considered the tissue's most important physiological parameter in response to a thermal challenge (Patterson and Strang, 1979) where almost all of the circulation is dedicated to this purpose (Petrofsky, 2017). The vasculature of the skin consists of a microcirculatory network of vessels organized horizontally through the dermal layer of the skin in two

distinct plexuses. These interconnected networks of microvessels control the transport and exchange of heat with the environment and they are also responsible for other important physiological parameters such as respiratory gas exchange and nutrient delivery while continuously protecting from external stressors. The superficial horizontal vascular plexus establishes a thermal gradient between the skin and the surrounding environment where ultimately, heat loss occurs through thermoregulatory control. Cutaneous vasodilation is governed by a combination of neural reflexes and local tissue factors (Pergola et al. 1993; Taylor et al. 1984). During heat stress, cutaneous vasodilation is regulated by two distinct sympathetic neural pathways, an adrenergic vasoconstrictor system and an active cholinergic vasodilator system (Kellogg et al. 1995). Local skin temperature also has an important influence on the overall magnitude of the cutaneous vasodilator response during whole-body heating (Johnson et al., 1986b: Taylor et al. 1984).

Under normothermal conditions, the rate of blood flow to the skin remains around a value equivalent to approximately 5% of cardiac output, which is about 250-500 mL/min, and this results in the dissipation of heat close to resting metabolic heat production (Johnson *et al*., 1986a). An increase in body temperature through heat stress, results in the initiation of active heat loss through the evaporation of sweat, but also via active cutaneous vasodilation. During severe hyperthermia, the rate of blood flow to the skin can increase to levels reaching around 60% of cardiac output during a hyperthermic event, which has been estimated to be approximately 8 L/min (Koroxenidis, 1961; Rowell et al., 1974). Under these circumstances of increased cardiac output, visceral blood circulation is reduced through vessel constriction and it is redirected to the skin to dissipate heat to the environment and, along with sweat evaporation which cools the increased blood flow present in the microvasculature, temperature is decreased (Charkoudian, 2003).

Normal resting cutaneous blood flow rates vary both spatially (Table 4.30) and temporally (Tenland et al., 1983) as well as with age (Petrofsky, 2017). It is important to note that over a certain span of environmental conditions, thermal equilibrium is maintained exclusively through the modulation of cutaneous vasomotor tone (vasoconstriction/vasodilation), outside of which, active shivering and sweating responses are required to prevent hypothermia and hyperthermia, respectively. This can be accomplished because small changes in skin blood flow result in large differences in heat dissipation. This range is termed the neutral or vasomotor zone, and accounts for the range of normal blood flow rates. In the absence of a thermal challenge, vasomotor tone is highly conserved in both the very young (Young, 1962) and the aged (Gorgy, 1973). When skin is heated locally, considerable cutaneous vasodilation results in the heated area, where a prolonged local temperature of 42^{o}C leads to maximal dilation of the cutaneous microvasculature (Johnson *et al*., 1986b). During rapid, non-painful, local skin heating this response is biphasic and is characterized by an initial rapid vasodilator peak, which occurs via thermally sensitive nerve endings in the skin that instantly sense warming at temperatures between 29 – 40^{o}C (Stephens et al., 2001), followed by a slower, sustained plateau phase (approximately 10-30 minutes) that is primarily nitric oxide-dependent (Kellogg et al., 1999; Minson et al., 1985). Conversely, during a local noxious heating stimulus the initial vasodilator peak response is absent and a sustained plateau is rapidly achieved, which relies heavily on intact sympathetic and sensory nerve responses (Magerl and Treede, 1996; Carter and Hodges, 2011).

Modified blood flow capacity can impede an individual's ability to properly regulate both local and whole-body temperatures. Women experience changing reproductive hormone levels (pregnancy, menstrual cycle, menopause) throughout their life and this leads to an altered threshold for vasodilation in the skin, where increases in circulating progesterone and estrogen levels result in a delayed onset threshold (by 0.5°C) where cutaneous vasodilation occurs. This change affects initiation of active cutaneous vasodilation, but ultimately the magnitude of blood flow to the skin remains unchanged (Stephenson and Kolka, 1985). Infants, who do not have a fully developed thermoregulatory system (Knobel et al., 2009), are susceptible to changes in temperature, but cutaneous blood flow measurements showed a marked increase following local heating (Wu et al., 1974) indicating that an active response to heat stress is present. Individuals with diabetes may exhibit reduced blood flow to the limbs compared to healthy control individuals when exposed to localized cutaneous heating to 42-44°C (Colberg et al., 2003; Fuchs et al., 2017; Sokolnicki et al. 2007) or during whole body heating (Sokolnicki et al., 2009; Wick et al., 2006). These impairments in active vasodilation during local and whole-body heat stress could lead to thermal injury in this population.

Table 4.30: Resting blood flow (perfusion) rates in human skin.

Reference	**Tissue**	**Perfusion Rate**	**Ambient temperature (°C)**	**Measurement method**
Hertzman and Randall, 1948	Face	7.2 mL/100 g/min	25-27	Photoelectric plethysmograph
Sejrsen, 1969	Leg	5.7 mL/100 g/min	19-22	^{133}Xe clearance
Daly et al., 2006	Arm	14.6 mL/100 g/min	N/A	^{133}Xe clearance
Wu et al., 1974	Arm (infant)	4.4 mL/100 g/min	N/A	electrocapacitance plethysmograph
LeRoy et al., 1971	Hand	16.4 mL/100 g/min	17.5 - 18	^{133}Xe clearance
Chimoskey et al., 1972	Hand	5 mL/100 g/min 27 mL/100 g/min	18 29	^{133}Xe clearance

4.5 Conclusions

ICNIRP (2020) has developed recommended human exposure limits for localized exposure to RFEMF in the 6 to 300 GHz frequency range based upon established adverse health effects. These recommendations are based upon several assumptions and conclusions, including: a) the first adverse health effects to manifest as millimeter-wave RFEMF exposure intensity increases are a heat-pain sensation and thermal tissue damage in skin and cornea (Type 1 tissues), b) an absolute temperature threshold of 41°C for Type 1 tissues (the OAHET) provides a conservative estimate of the minimum temperature where adverse health effects may occur; and c) that the normothermal temperature of Type 1 tissues does not exceed 33-36 °C, which is at least 5°C below the OAHET. To assess whether these assumptions and conclusions are supported by the available scientific evidence, Health Canada has conducted a systematic analysis to identify adverse health outcomes from millimeter-wave RFEMF. This review also considered complementary research on hyperthermia, thermoregulation, and resting tissue temperatures and blood flow. This analysis has allowed Health Canada to develop evidence-based conclusions regarding the scientific validity of ICNIRP's approach to establishing recommended human exposure limits for localized exposure to millimeter-wave RFEMF.

a) Based upon a systematic review approach, Health Canada has identified two adverse health outcomes that are relevant to localized exposure to millimeter-wave RFEMF. These are a heat-pain sensation, which demonstrates an absolute threshold temperature of ~42-43°C, and tissue damage which can occur when skin or cornea are heated and maintained for a period of time at temperatures at or above 43°C. Other adverse health effects are theoretically possible if localized exposure to millimeter wave RFEMF heats the core body temperature by more than 1°C, however such effects are unlikely to occur from millimeter-wave RFEMF without first exceeding the heat-pain sensation temperature threshold in Type 1 tissues as most energy will be deposited in superficial tissues. Furthermore, existing whole-body exposure limits in Canadian and International exposure guidelines are sufficiently restrictive by limiting the increase in temperature to core body heating to less than 0.1°C. Therefore, Health Canada is in agreement with ICNIRP that the primary adverse health effects to be avoided as millimeter-wave RFEMF intensity increases are a heat-pain sensation and thermal tissue damage to Type 1 tissues (skin/cornea).

b) Based upon an analysis of millimeter-wave RFEMF studies and complementary research evidence on temperature thresholds for the occurrence of heat-pain sensation and thermal tissue damage (Section 4.2), Health Canada concludes that the ICNIRP OAHET of 41°C is a conservative estimate of the minimum temperature where adverse health effects may occur.

c) Based upon an analysis of complementary evidence of resting (normothermal) Type 1 tissue temperatures, Health Canada considers the normothermal temperature of skin and cornea to range between 33-36°C. Therefore, Health Canada considers the ICNIRP OAHET value of 41°C to be at least 5°C above normothermal Type 1 tissue temperatures. When a 10-fold safety margin is

applied for the uncontrolled environment, the estimated skin temperature increase in Type 1 tissues at the maximal allowable limits is estimated to be ~0.5°C.

In conclusion, Health Canada considers the ICNIRP OAHET value of 41°C to be a conservative estimate of the possible threshold of adverse health effects from localized exposure of Type 1 tissues to millimeter-wave RFEMF and considers the OAHET to be at least 5°C higher than normothermal Type 1 tissue temperatures. With the application of 10-fold and 2-fold safety margins in the ICNIRP (2020) exposure limits for the uncontrolled and controlled environments, this results in an approximate target temperature increase at the maximum allowable exposure limits of 0.5°C and 2.5°C, respectively. These temperature increases are well below the threshold for all known adverse health effects from millimeter-wave RFEMF. It is important to note that modest temperature increases (1-2°C) to Type 1 tissues are routinely experienced in our daily lives from a variety of other heat sources. Small deviations from the target tissue temperature elevations (e.g. up to 50%) under unique/exotic exposures scenarios will still maintain Type 1 tissue temperature elevations below the threshold for adverse effects.

Finally, it is important to point out that the absence of scientific evidence of harm does not guarantee that unidentified adverse health effects are not possible, especially when a limited number of studies have been conducted on the potential health impacts of millimeter wave RFEMF. Health Canada will continue to monitor the science to identify possible emerging adverse health effects from such exposures and will take appropriate action to revise Canada's recommended human exposure limits if new information emerges that indicates these limits must be revised.

4.6 References

Acosta MC, Belmonte C, Gallar J. Sensory experiences in humans and single-unit activity in cats evoked by polymodal stimulation of the cornea. J Physiol. 2001 Jul 15; 534(Pt. 2):511-25.

Adair ER, Black DR. Thermoregulatory responses to RF energy absorption. Bioelectromagnetics. 2003; Suppl 6:S17-38.

Agostinho CM, Scherens A, Richter H, Schaub C, Rolke R, Treede RD, Maier C. Habituation and short-term repeatability of thermal testing in healthy human subjects and patients with chronic non-neuropathic pain. Eur J Pain. 2009 Sep; 13(8):779-85.

Alekseev SI, Ziskin MC. Local heating of human skin by millimeter waves: a kinetics study. Bioelectromagnetics. 2003 Dec; 24(8):571-81.

Alekseev SI, Radzievsky AA, Szabo I, Ziskin MC. Local heating of human skin by millimeter waves: effect of blood flow. Bioelectromagnetics. 2005 Sep;26(6):489-501.

Alekseev SI, Gordiienko OV, Radzievsky AA, Ziskin MC. Millimeter wave effects on electrical responses of the sural nerve in vivo. Bioelectromagnetics. 2010 Apr;31(3):180-90.

Basbaum AI, Bautista DM, Scherrer G, Julius D. Cellular and molecular mechanisms of pain. Cell. 2009 Oct 16;139(2):267-84.

Belmonte C, Giraldez F. Responses of cat corneal sensory receptors to mechanical and thermal stimulation. J Physiol. 1981 Dec; 321: 355-68.

Belmonte C, Acosta MC, Gallar J. Neural basis of sensation in intact and injured corneas. Exp Eye Res. 2004 Mar; 78(3):513-25.

Belmonte C, Nichols JJ, Cox SM, Brock JA, Begley CG, Bereiter DA, Dartt DA, Galor A, Hamrah P, Ivanusic JJ, Jacobs DS, McNamara NA, Rosenblatt MI, Stapleton F, Wolffsohn JS. TFOS DEWS II pain and sensation report. Ocul Surf. 2017 Jul; 15(3):404-437.

Birenbaum L, Kaplan IT, Metlay W, Rosenthal SW, Schmidt H, Zaret MM. Effect of microwaves on the rabbit eye. J Microwave Power 1969 4:232–243.

Blackie CA, McMonnies CW, Korb DR. Warm compresses and the risks of elevated corneal temperature with massage. Cornea. 2013 Jul;32(7):e146-9.

Blick DW, Adair ER, Hurt WD, Sherry CJ, Walters TJ, Merritt JH. Thresholds of microwave-evoked warmth sensations in human skin. Bioelectromagnetics. 1997;18(6):403-9.

Boni R. Heat stress, a serious threat to reproductive function in animals and humans. Mol Reprod Dev. 2019 Oct;86(10):1307-1323.

Brockow T, Wagner A, Franke A, Offenbächer M, Resch KL. A randomized controlled trial on the effectiveness of mild water-filtered near infrared whole-body hyperthermia as an adjunct to a standard multimodal rehabilitation in the treatment of fibromyalgia. Clin J Pain. 2007 Jan;23(1):67-75.

Bujan L, Daudin M, Charlet JP, Thonneau P, Mieusset R. Increase in scrotal temperature in car drivers. Hum Reprod. 2000 Jun;15(6):1355-7.

Carter SJ, Hodges GJ. Sensory and sympathetic nerve contributions to the cutaneous vasodilator response from a noxious heat stimulus. Exp Physiol. 2011;96(11):1208-1217.

Chalfin S, D'Andrea JA, Comeau PD, Belt ME, Hatcher DJ. Millimeter wave absorption in the nonhuman primate eye at 35 GHz and 94 GHz. Health Phys. 2002 Jul;83(1):83-90.

Charkoudian N. Skin blood flow in adult human thermoregulation: how it works, when it does not, and why. Mayo Clin Proc. 2003 May;78(5):603-12.

Chimoskey JE. Skin blood flow by ^{133}Xe disappearance validated by venous occlusion plethysmography. J Appl Physiol. 1972;32(3):432-435.

Colberg SR, Parson HK, Holton DR, Nunnold T, Vinik AI. Cutaneous blood flow in type 2 diabetic individuals after an acute bout of maximal exercise. Diabetes Care. 2003 Jun;26(6):1883-8.

Cook HF. The pain threshold for microwave and infra-red radiations. J Physiol. 1952 Sep;118(1):1-11.

Crouzier D, Dabouis V, Gentilhomme E, Vignal R, Bourbon F, Fauvelle F, Debouzy JC. Chronic Electromagnetic Exposure at Occupational Safety Level Does Not Affect the Metabolic Profile nor Cornea Healing after LASIK Surgery J Ophthalmol 2014: 762364-1-762364-11.

Daly CH, Chimoskey JE, Holloway GA, Kennedy D. The effect of pressure loading on the blood flow rate in human skin. J Tissue Viability. 2006;16(4):17-21.

Defrin R, Ohry A, Blumen N, Urca G. Sensory determinants of thermal pain. Brain. 2002 Mar; 125 (Pt 3): 501-10.

Defrin R, Shachal-Shiffer M, Hadgadg M, Peretz C. Quantitative somatosensory testing of warm and heat-pain thresholds: the effect of body region and testing method. Clin J Pain. 2006 Feb;22(2):130-6.

Deghoyan A, Heqimyan A, Nikoghosyan A, Dadasyan E, Ayrapetyan S. Cell bathing medium as a target for non thermal effect of millimeter waves. Electromagn Biol Med. 2012 Jun;31(2):132-42.

de Seze R, Poutriquet C, Gamez C, Maillot-Maréchal E, Robidel F, Lecomte A, Fonta C. Repeated exposure to nanosecond high power pulsed microwaves increases cancer incidence in rat. PLoS One. 2020 Apr 8;15(4):e0226858.

Dewey WC. Arrhenius relationships from the molecule and cell to the clinic. Int J Hyperthermia. 2009 Feb;25(1):3-20.

Dewhirst MW, Viglianti BL, Lora-Michiels M, Hoopes PJ, Hanson M. Thermal dose requirement for tissue effect: experimental and clinical findings. Proc SPIE Int Soc Opt Eng. 2003a Jun 2;4954:37.

Dewhirst MW, Viglianti BL, Lora-Michiels M, Hanson M, Hoopes PJ. Basic principles of thermal dosimetry and thermal thresholds for tissue damage from hyperthermia. Int J Hyperthermia. 2003b May-Jun;19(3):267-94.

Dixon JM, Blackwood L. Thermal variations of the human eye. Trans Am Ophthalmol Soc. 1991;89:183-90; discussion 190-3.

Dubin AE, Patapoutian A. Nociceptors: the sensors of the pain pathway. J Clin Invest. 2010 Nov;120(11):3760-72.

Durairajanayagam D, Agarwal A, Ong C. Causes, effects and molecular mechanisms of testicular heat stress. Reprod Biomed Online. 2015 Jan;30(1):14-27.

Edwards MJ, Shiota K, Smith MS, Walsh DA. Hyperthermia and birth defects. Reprod Toxicol. 1995 Sep-Oct;9(5):411-25.

Edwards MJ, Saunders RD, Shiota K. Effects of heat on embryos and foetuses. Int J Hyperthermia. 2003 May-Jun;19(3):295-324.

Elder JA. Ocular effects of radiofrequency energy. Bioelectromagnetics. 2003;Suppl 6:S148-61.

Fabiani C, Li Voti R, Rusciano D, Mutolo MG, Pescosolido N. Relationship between Corneal Temperature and Intraocular Pressure in Healthy Individuals: A Clinical Thermographic Analysis. J Ophthalmol. 2016;2016:3076031.

Frei M, Jauchem J, Heinmets F. Physiological effects of 2.8 GHz radio-frequency radiation: a comparison of pulsed and continuous-wave radiation. J Microw Power Electromagn Energy. 1988;23(2):85-93.

Frei MR, Jauchem JR, Heinmets F. Thermoregulatory responses of rats exposed to 9.3-GHz radiofrequency radiation. Radiat Environ Biophys. 1989;28(1):67-77.

Frei MR, Jauchem JR. Thermoregulatory responses of rats exposed to 9.3-GHz microwaves: a comparison of E and H orientation. Physiol Chem Phys Med NMR. 1992;24(1):1-10.

Frei MR, Ryan KL, Berger RE, Jauchem JR. Sustained 35-GHz radiofrequency irradiation induces circulatory failure. Shock. 1995 Oct;4(4):289-93.

Fuchs D, Dupon PP, Schaap LA, Draijer R. The association between diabetes and dermal microvascular dysfunction non-invasively assessed by laser Doppler with local thermal hyperemia: a systematic review with meta-analysis. Cardiovasc Diabetol. 2017;16(1):11.

Furman O, Komoshvili K, Levitan J, Yahalom A, Marks H, Borodin D, Liberman-Aronov S. The Lack of Toxic Effect of High-Power Short-Pulse 101 GHz Millimeter Waves on Healthy Mice. Bioelectromagnetics 2020 Apr;41(3):188-199.

Gallar J, Pozo MA, Tuckett RP, Belmonte C. Response of sensory units with unmyelinated fibres to mechanical, thermal and chemical stimulation of the cat's cornea. J Physiol. 1993 Aug;468:609-22.

Gapeyev AB, Mikhailik EN, Chemeris NK. Anti-inflammatory effects of low-intensity extremely high-frequency electromagnetic radiation: frequency and power dependence. Bioelectromagnetics. 2008 Apr;29(3):197-206.

Gapeyev AB, Mikhailik EN, Chemeris NK. Features of anti-inflammatory effects of modulated extremely high-frequency electromagnetic radiation. Bioelectromagnetics. 2009 Sep;30(6):454-61.

Gapeyev AB, Kulagina TP, Aripovsky AV, Chemeris NK. The role of fatty acids in anti-inflammatory effects of low-intensity extremely high-frequency electromagnetic radiation. Bioelectromagnetics. 2011 Jul;32(5):388-95.

Gapeyev AB, Kulagina TP, Aripovsky AV. Exposure of Tumor-Bearing Mice to Extremely High-Frequency Electromagnetic Radiation Modifies the Composition of Fatty Acids in Thymocytes and Tumor Tissue. Int J Radiat Biol. 2013 Aug;89(8):602-10.

Gapeyev AB, Aripovsky AV, Kulagina TP. Modifying effects of low-intensity extremely high-frequency electromagnetic radiation on content and composition of fatty acids in thymus of mice exposed to X-rays. Int J Radiat Biol. 2015 Mar;91(3):277-85.

Gapeyev AB, Aripovsky AV, Kulagina TP. Fatty Acid Content and Tumor Growth Changes in Mice After Exposure to Extremely High-Frequency Electromagnetic Radiation and Consumption of N-3 Fatty Acids. Nutr Cancer. 2019 Apr 16:1-10.

Garolla A, Torino M, Sartini B, Cosci I, Patassini C, Carraro U, Foresta C. Seminal and molecular evidence that sauna exposure affects human spermatogenesis. Hum Reprod. 2013 Apr;28(4):877-85.

Geiser MH, Bonvin M, Quibel O. Corneal and retinal temperatures under various ambient conditions: a model and experimental approach. Klin Monbl Augenheilkd. 2004 May;221(5):311-4.

Gorgy AN, David SB, Friedman SA. Vasomotor tone in the aged. Arch Neurol. 1973 Dec;29(6):439-40.

Graham JM Jr, Edwards MJ, Edwards MJ. Teratogen update: gestational effects of maternal hyperthermia due to febrile illnesses and resultant patterns of defects in humans. Teratology. 1998 Nov;58(5):209-21.

Gustrau F, Bahr A. W-band investigation of material parameters, SAR distribution, and thermal response in human tissue. IEEE Transactions on Microwave Theory and Techniques (2002) 50(10): 2393 – 2400.

Habauzit D, Nugue G, Bourbon F, Martin C, Del Vecchio F, Maunoir-Regimbal S, Poyot T, Valente M, Jaoui R, Crouzier D, Le Dréan Y, Debouzy JC. Evaluation of the Effect of Chronic 94 GHz Exposure on Gene Expression in the Skin of Hairless Rats In Vivo. Radiat Res. 2020 Apr;193(4):351-358.

Hagan GJ, Carpenter RL. 1976. Relative cataractogenic potencies of two microwave frequencies (2.45 and 10 GHz). In: Johnson CC, Shore ML, editors. Biological effects of electromagnetic waves. Vol. 1. Rockville, MD: HEW Publication (FDA) 77-8010. pp 143–155

Hagander LG, Midani HA, Kuskowski MA, Parry GJ. Quantitative sensory testing: effect of site and skin temperature on thermal thresholds. Clin Neurophysiol. 2000 Jan;111(1):17-22.

Health Canada. Safety Code 6. Limits of Human Exposure to Radiofrequency Electromagnetic Energy in the Frequency Range from 3 kHz to 300 GHz. 2015.

Hendler E, Hardy JD. Infrared and microwave effects on skin heating and temperature sensation. IRE Trans Med Electron. 1960 Jul;ME-7:143-52.

Hertzman AB, Randall WC. Regional differences in the basal and maximal rates of blood flow in the skin. J Appl Physiol. 1948;1(3):234-241.

Hjollund NH, Bonde JP, Jensen TK, Olsen J. Diurnal scrotal skin temperature and semen quality. The Danish First Pregnancy Planner Study Team. Int J Androl. 2000 Oct;23(5):309-18.

Hjollund NH, Storgaard L, Ernst E, Bonde JP, Olsen J. Impact of diurnal scrotal temperature on semen quality. Reprod Toxicol. 2002a May-Jun;16(3):215-21.

Hjollund NH, Storgaard L, Ernst E, Bonde JP, Olsen J. The relation between daily activities and scrotal temperature. Reprod Toxicol. 2002b May-Jun;16(3):209-14.

Huang J, Zhang X, McNaughton PA. Inflammatory pain: the cellular basis of heat hyperalgesia. Curr Neuropharmacol. 2006 Jul;4(3):197-206.

ICNIRP. Guidelines for limiting exposure to time-varying electric, magnetic and electromagnetic fields (up to 300 GHz). Health Phys 1998. 74:494-522;1998.

ICNIRP, Guidelines for limiting exposure to electromagnetic fields (100 kHz to 300 GHz). Health Phys. 2020 May;118(5):483-524.

IEEE C95.1-2019 - IEEE Standard for Safety Levels with Respect to Human Exposure to Electric, Magnetic, and Electromagnetic Fields, 0 Hz to 300 GHz. Institute of Electronics and Electrical Engineers, 2019.

Ivell R. Lifestyle impact and the biology of the human scrotum. Reprod Biol Endocrinol. 2007 Apr 20; 5:15.

Jauchem JR, Ryan KL, Lovelace JD, Frei MR. Effects of esmolol on 35 GHz microwave-induced lethal heat stress. J Auton Pharmacol. 1997 Jun;17(3):165-73.

Jauchem JR, Ryan KL, Frei MR. Cardiovascular and thermal responses in rats during 94 GHz irradiation. Bioelectromagnetics. 1999;20(4):264-7.

Jauchem JR, Ryan KL, Frei MR. Cardiovascular and thermal effects of microwave irradiation at 1 and/or 10 GHz in anesthetized rats. Bioelectromagnetics. 2000 Apr;21(3):159-66.

Jauchem JR, Ryan KL, Tehrany MR. Effects of histamine receptor blockade on cardiovascular changes induced by 35 GHz radio frequency radiation heating. Auton Autacoid Pharmacol. 2004 Jan;24(1):17-28.

Jauchem JR. Effects of low-level radio-frequency (3kHz to 300GHz) energy on human cardiovascular, reproductive, immune, and other systems: a review of the recent literature. Int J Hyg Environ Health. 2008 Mar;211(1-2):1-29.

Jauchem JR, Ryan KL, Walters TJ. Pathophysiological alterations induced by sustained 35-GHz radio-frequency energy heating. J Basic Clin Physiol Pharmacol. 2016 Jan;27(1):79-89.

Jensen TS, Finnerup NB. Allodynia and hyperalgesia in neuropathic pain: clinical manifestations and mechanisms. Lancet Neurol. 2014 Sep;13(9):924-35.

Jensh RP. Studies of the teratogenic potential of exposure of rats to 6000-MHz microwave radiation. I. Morphologic analysis at term. Radiat Res. 1984a Feb;97(2):272-81.

Jensh RP. Studies of the teratogenic potential of exposure of rats to 6000-MHz microwave radiation. II. Postnatal psychophysiologic evaluations. Radiat Res. 1984b Feb;97(2):282-301.

John RT, Henricson J, Junker J, Jonson CO, Nilsson GE, Wilhelms D, Anderson CD. A cool response-The influence of ambient temperature on capillary refill time. J Biophotonics. 2018 Jun;11(6):e201700371.

Johnson JM, Brengelmann GL, Hales JR, Vanhoutte PM, Wenger CB. Regulation of the cutaneous circulation. Fed Proc. 1986a Dec;45(13):2841-50.

Johnson JM, O'Leary DS, Taylor WF, Kosiba W. Effect of local warming on forearm reactive hyperaemia. Clin Physiol. 1986b Aug;6(4):337-46.

Jung A, Schuppe HC. Influence of genital heat stress on semen quality in humans. Andrologia. 2007 Dec;39(6):203-15.

Kalns J, Ryan KL, Mason PA, Bruno JG, Gooden R, Kiel JL. Oxidative stress precedes circulatory failure induced by 35-GHz microwave heating. Shock. 2000 Jan;13(1):52-9.

Kellogg DL Jr, Pérgola PE, Piest KL, et al. Cutaneous active vasodilation in humans is mediated by cholinergic nerve cotransmission. Circ Res. 1995;77(6):1222-1228.

Kellogg DL Jr, Liu Y, Kosiba IF, O'Donnell D. Role of nitric oxide in the vascular effects of local warming of the skin in humans. J Appl Physiol (1985). 1999 Apr;86(4):1185-90.

Kesari KK, Behari J. Fifty-gigahertz microwave exposure effect of radiations on rat brain. Appl Biochem Biotechnol. 2009 Jul;158(1):126-39.

Kesari KK, Behari J. Microwave exposure affecting reproductive system in male rats. Appl Biochem Biotechnol. 2010 Sep;162(2):416-28.

Kessel L, Johnson L, Arvidsson H, Larsen M. The relationship between body and ambient temperature and corneal temperature. Invest Ophthalmol Vis Sci. 2010 Dec;51(12):6593-7.

Knobel RB, Holditch-Davis D, Schwartz TA, Wimmer JE Jr. Extremely low birth weight preterm infants lack vasomotor response in relationship to cold body temperatures at birth. J Perinatol. 2009 Dec;29(12):814-21.

Kojima M., Suzuki Y., Tsai CY. et al. Characteristics of ocular temperature elevations after exposure to quasi- and millimeter waves (18-40 GHz) J Infrared Milli Terahz Waves (2015) 36: 390.

Kojima M, Yukihisa S, Masao T, Kanako W, Soichi W, Maya M, Tasaki T, Sasaki H. Ocular Effects of Exposure to 40, 75, and 95 GHz Millimeter Waves. Journal of Infrared, Millimeter, 440 and Terahertz Waves, 2018 39(9):912–925

Kolosova LI, Akoev GN, Avelev VD, Riabchikova OV, Babu KS. Effect of low-intensity millimeter wave electromagnetic radiation on regeneration of the sciatic nerve in rats. Bioelectromagnetics. 1996;17(1):44-7.

Kolosova LI, Akoev GN, Ryabchikova OV, Avelev VD. Effect of low-intensity millimeter-range electromagnetic irradiation on the recovery of function in lesioned sciatic nerves in rats. Neurosci Behav Physiol. 1998 Jan-Feb;28(1):26-30.

Koroxenidis GT, Shepherd JT, Marshall RJ. Cardiovascular response to acute heat stress. J Appl Physiol. 1961 Sep;16:869-72.

Kues HA, D'Anna SA, Osiander R, Green WR, Monahan JC. Absence of ocular effects after either single or repeated exposure to 10 mW/cm(2) from a 60 GHz CW source. Bioelectromagnetics. 1999 Dec;20(8):463-73.

Kumar S, Kesari KK, Behari J. Evaluation of genotoxic effects in male Wistar rats following microwave exposure. Indian J Exp Biol. 2010 Jun;48(6):586-92.

Kumar S, Kesari KK, Behari J. Influence of microwave exposure on fertility of male rats. Fertil Steril. 2011 Mar 15;95(4):1500-2.

Kumar S, Behari J, Sisodia R. Impact of microwave at X-band in the aetiology of male infertility. Electromagn Biol Med. 2012 Sep;31(3):223-32.

Kumar S, Behari J, Sisodia R. Influence of electromagnetic fields on reproductive system of male rats. Int J Radiat Biol. 2013 Mar;89(3):147-54.

LeRoy EC, Downey JA, Cannon PJ. Skin capillary blood flow in scleroderma. J Clin Invest. 1971;50(4):930-939.

Liddle CG, Putnam JP, Ail JS, Lewis JY, Bell B, West MW, Lewter OH. Alteration of circulating antibody response of mice exposed to 9-GHz pulsed microwaves Bioelectromagnetics. 1980;1(4):397-404.

Liddle CG, Putnam JP, Lewter OH, West M, Morrow G. Circulating antibody response of mice exposed to 9-GHz pulsed microwave radiation. Bioelectromagnetics. 1986;7(1):91-4.

Loeser JD, Treede RD. The Kyoto protocol of IASP Basic Pain Terminology. Pain. 2008 Jul 31;137(3):473-7.

Logani MK, Agelan A, Ziskin MC. Effect of millimeter wave radiation on catalase activity. Electromagnetic Biology and Medicine. 2002a. 21(3): 303-308.

Logani MK, Anga A, Szabo I, Agelan A, Irizarry AR, Ziskin MC. Effect of millimeter waves on cyclophosphamide induced suppression of the immune system. Bioelectromagnetics. 2002b Dec;23(8):614-21.

Lushnikov KV, Shumilina YV, Yakushina VS, Gapeyev AB, Sadovnikov VB, Chemeris NK. Effects of low-intensity ultrahigh frequency electromagnetic radiation on inflammatory processes. Bull Exp Biol Med. 2004 Apr;137(4):364-6.

Magerl W, Treede RD. Heat-evoked vasodilatation in human hairy skin: axon reflexes due to low-level activity of nociceptive afferents. J Physiol. 1996;497 (Pt 3)(Pt 3):837-848.

Makar V, Logani M, Szabo I, Ziskin M. Effect of millimeter waves on cyclophosphamide induced suppression of T cell functions. Bioelectromagnetics.2003 Jul;24(5):356-65.

Makar VR, Logani MK, Bhanushali A, Kataoka M, Ziskin MC. Effect of millimeter waves on natural killer cell activation. Bioelectromagnetics. 2005 Jan;26(1):10-9.

Makar VR, Logani MK, Bhanushali A, Alekseev SI, Ziskin MC. Effect of cyclophosphamide and 61.22 GHz millimeter waves on T-cell, B-cell, and macrophage functions. Bioelectromagnetics. 2006 Sep;27(6):458-66.

Mason PA, Walters TJ, DiGiovanni J, Beason CW, Jauchem JR, Dick EJ Jr, Mahajan K, Dusch SJ, Shields BA, Merritt JH, Murphy MR, Ryan KL. Lack of effect of 94 GHz radio frequency radiation exposure in an animal model of skin carcinogenesis. Carcinogenesis. 2001 Oct;22(10):1701-8.

McAfee RD, Longacre A Jr, Bishop RR, Elder ST, May JG, Holland MG, Gordon R. Absence of ocular pathology after repeated exposure of unanesthetized monkeys to 9.3-GHz microwaves. J Microw Power. 1979 Mar;14(1):41-4.

McAfee RD, Ortiz-Lugo R, Bishop R, Gordon R. Absence of deleterious effects of chronic microwave radiation on the eyes of rhesus monkeys. Ophthalmology. 1983 Oct;90(10):1243-5.

Mieusset R, Bujan L. Testicular heating and its possible contributions to male infertility: a review. Int J Androl. 1995 Aug;18(4):169-84.

Mergler S, Valtink M, Takayoshi S, Okada Y, Miyajima M, Saika S, Reinach PS. Temperature-sensitive transient receptor potential channels in corneal tissue layers and cells. Ophthalmic Res. 2014;52(3):151-9.

Millenbaugh NJ, Kiel JL, Ryan KL, Blystone RV, Kalns JE, Brott BJ, Cerna CZ, Lawrence WS, Soza LL, Mason PA. Comparison of blood pressure and thermal responses in rats exposed to millimeter wave energy or environmental heat. Shock. 2006 Jun;25(6):625-32.

Millenbaugh NJ, Roth C, Sypniewska R, Chan V, Eggers JS, Kiel JL, Blystone RV, Mason PA. Gene expression changes in the skin of rats induced by prolonged 35 GHz millimeter-wave exposure. Radiat Res. 2008 Mar;169(3):288-300.

Minasyan SM, Grigoryan GY, Saakyan SG, Akhumyan AA, Kalantaryan VP. Effects of the action of microwave-frequency electromagnetic radiation on the spike activity of neurons in the supraoptic nucleus of the hypothalamus in rats. Neurosci Behav Physiol. 2007 Feb;37(2):175-80.

Minson CT, Berry LT, Joyner MJ. Nitric oxide and neurally mediated regulation of skin blood flow during local heating. J Appl Physiol (1985). 2001;91(4):1619-1626.

Montgomery LD, Williams BA. Effect of ambient temperature on the thermal profile of the human forearm, hand, and fingers. Ann Biomed Eng. 1976 Sep;4(3):209-19.

Nelson DA, Walters TJ, Ryan KL, Emerton KB, Hurt WD, Ziriax JM, Johnson LR, Mason PA. Inter-species extrapolation of skin heating resulting from millimeter wave irradiation: modeling and experimental results. Health Phys. 2003 May;84(5):608-15.

Novikova NS, Perekrest SV, Rogers VJ, Korneva EA. Morphometric analysis of hypothalamic cells showing c-Fos proteins after movement restriction and EHF-irradiation. Pathophysiology. 2008 Jun;15(1):19-24.

Novoselova EG, Glushkova OV, Khrenov MO, Novoselova TV, Lunin SM, Fesenko EE. Extremely low-level microwaves attenuate immune imbalance induced by inhalation exposure to low-level toluene in mice. Int J Radiat Biol. 2017 May;93(5):535-543.

Novoselova EG, Glushkova OV, Khrenov MO, Novoselova TV, Lunin SM, Fesenko EE. Extremely low-level microwaves attenuate immune imbalance induced by inhalation exposure to low-level toluene in mice. Int J Radiat Biol. 2017 May;93(5):535-543.

Ochoa JL, Campero M, Serra J, Bostock H. Hyperexcitable polymodal and insensitive nociceptors in painful human neuropathy. Muscle Nerve. 2005 Oct;32(4):459-72.

Olchowik G, Maj JG. Inhibitory action of microwave radiation on gamma-glutamyl transpeptidase activity in liver of rats treated with hydrocortisone. Folia Histochem Cytobiol. 2000;38(4):189-91.

Olchowik G. Influence of hydrocortisone and microwave radiation on the mechanical characteristics of rat bone tissue. Cytobios. 2001;105(410):147-52.

Oudejans LC, Niesters M, Brines M, Dahan A, van Velzen M. Quantification of small fiber pathology in patients with sarcoidosis and chronic pain using cornea confocal microscopy and skin biopsies. J Pain Res. 2017;10:2057-2065.

Partyla T, Hacker H, Edinger H, Leutzow B, Lange J, Usichenko T. Remote Effects of Electromagnetic Millimeter Waves on Experimentally Induced Cold Pain: A Double-Blinded Crossover Investigation in Healthy Volunteers. Anesth Analg. 2017 Mar;124(3):980-985.

Paulraj R, Behari J. Biochemical changes in rat brain exposed to low intensity 9.9 GHz microwave radiation. Cell Biochem Biophys. 2012a May;63(1):97-102.

Paulraj R, Behari J. Enzymatic alterations in developing rat brain cells exposed to a low-intensity 16.5 GHz microwave radiation. Electromagn Biol Med. 2012b Sep;31(3):233-42.

Patterson J, Strang R. The role of blood flow in hyperthermia. Int J Radiat Oncol Biol Phys. 1979 Feb;5(2):235-41.

Pérgola PE, Kellogg DL Jr, Johnson JM, Kosiba WA, Solomon DE. Role of sympathetic nerves in the vascular effects of local temperature in human forearm skin. Am J Physiol. 1993;265(3 Pt 2):H785-H792.

Petrofsky JS. (2017) Control of Skin Blood Flow. In: Farage M., Miller K., Maibach H. (eds) Textbook of Aging Skin. Pp: 1091-1104. Springer, Berlin, Heidelberg

Pyrpasopoulou A, Kotoula V, Cheva A, Hytiroglou P, Nikolakaki E, Magras IN, Xenos TD, Tsiboukis TD, Karkavelas G. Bone morphogenetic protein expression in newborn rat kidneys after prenatal exposure to radiofrequency radiation. Bioelectromagnetics. 2004 Apr;25(3):216-27.

Racine M, Tousignant-Laflamme Y, Kloda LA, Dion D, Dupuis G, Choinière M. A systematic literature review of 10 years of research on sex/gender and experimental pain perception - part 1: are there really differences between women and men? Pain. 2012 Mar;153(3):602-18.

Radzievsky AA, Rojavin MA, Cowan A, Ziskin MC. Suppression of pain sensation caused by millimeter waves: a double-blinded, cross-over, prospective human volunteer study. Anesth Analg. 1999 Apr;88(4):836-40.

Radzievsky AA, Rojavin MA, Cowan A, Alekseev SI, Ziskin MC. Hypoalgesic effect of millimeter waves in mice: dependence on the site of exposure. Life Sci. 2000 Apr 14;66(21):2101-11.

Radzievsky AA, Rojavin MA, Cowan A, Alekseev SI, Radzievsky AA Jr, Ziskin MC. Peripheral neural system involvement in hypoalgesic effect of electromagnetic millimeter waves. Life Sci. 2001 Jan 26;68(10):1143-51.

Radzievsky AA, Cowan A, Byrd C, Radzievsky AA, Ziskin MC. Single millimeter wave treatment does not impair gastrointestinal transit in mice. Life Sci. 2002 Aug 30;71(15):1763-70.

Radzievsky AA, Gordiienko O, Cowan A, Alekseev S, Ziskin M. Millimeter-Wave-Induced Hypoalgesia in Mice: Dependence on Type of Experimental Pain. 2004a. Plasma Science, IEEE Transactions on. 32. 1634 - 1643.

Radzievsky AA, Gordiienko OV, Szabo I, Alekseev SI, Ziskin MC. Millimeter wave-induced suppression of B16 F10 melanoma growth in mice: involvement of endogenous opioids. Bioelectromagnetics. 2004b Sep;25(6):466-73.

Radzievsky AA, Gordiienko OV, Alekseev S, Szabo I, Cowan A, Ziskin MC. Electromagnetic millimeter wave induced hypoalgesia: frequency dependence and involvement of endogenous opioids. Bioelectromagnetics. 2008 May;29(4):284-95.

Ray S, Behari J. Physiological changes in rats after exposure to low levels of microwaves. Radiat Res. 1990 Aug;123(2):199-202.

Robinson D, Rock J, Menkin MF. Control of human spermatogenesis by induced changes of intrascrotal temperature. JAMA. 1968 Apr 22;204(4):290-7.

Rock J, Robinson D. Effect of induced intrascrotal hyperthermia on testicular function in man. Am J Obstet Gynecol. 1965 Nov 15;93(6):793-801.

Rojavin MA, Cowan A, Radzievsky AA, Ziskin MC. Antipruritic effect of millimeter waves in mice: evidence for opioid involvement. Life Sci. 1998;63(18):PL251-7.

Rojavin MA, Ziskin MC. Electromagnetic millimeter waves increase the duration of anaesthesia caused by ketamine and chloral hydrate in mice. Int J Radiat Biol. 1997 Oct;72(4):475-80.

Rooney AA, Cooper GS, Jahnke GD, Lam J, Morgan RL, Boyles AL, Ratcliffe JM, Kraft AD, Schünemann HJ, Schwingl P, Walker TD, Thayer KA, Lunn RM. How credible are the study results? Evaluating and applying internal validity tools to literature-based assessments of environmental health hazards. Environ Int. 2016 92-93:617-29.

Rosenthal SW, Birenbaum L, Kaplan IT, Metlay W, Snyder WZ, Zaret MM. 1976. Effects of 35 and 107 GHz CW microwaves on the rabbit eye. In: Johnson CC, Shore ML, editors. Biological effects of electromagnetic waves. Vol. 1. Rockville, MD: HEW Publication (FDA) 77-8010. pp 110–128.

Rotkovská D, Moc J, Kautská J, Bartonícková A, Keprtová J, Hofer M. Evaluation of the biological effects of police radar RAMER 7F. Environ Health Perspect. 1993 Jun;101(2):134-6.

Rowell LB. Human cardiovascular adjustments to exercise and thermal stress. Physiol Rev. 1974;54(1):75-159.

Ryan KL, Frei MR, Berger RE, Jauchem JR. Does nitric oxide mediate circulatory failure induced by 35-GHz microwave heating? Shock. 1996 Jul;6(1):71-6.

Ryan KL, Walters TJ, Tehrany MR, Lovelace JD, Jauchem JR. Age does not affect thermal and cardiorespiratory responses to microwave heating in calorically restricted rats. Shock. 1997a Jul;8(1):55-60.

Ryan KL, Frei MR, Jauchem JR. Circulatory failure induced by 35 GHz microwave heating: effects of chronic nitric oxide synthesis inhibition. Shock. 1997b Jan;7(1):70-6.

Ryan KL, Lovelace JD, Frei MR, Jauchem JR. Administration of a nitric oxide donor does not affect hypotension induced by 35-GHz microwave heating. Methods Find Exp Clin Pharmacol. 1997c Sep;19(7):455-64.

Ryan KL, Jauchem JR, Tehrany MR, Boyle HL. Platelet-activating factor does not mediate circulatory failure induced by 35-GHz microwave heating. Methods Find Exp Clin Pharmacol. 2002 Jun;24(5):279-86.

Sapareto SA, Dewey WC. Thermal dose determination in cancer therapy. Int J Radiat Oncol Biol Phys. 1984 Jun;10(6):787-800.

Sasaki K, Sakai T, Nagaoka T, Wake K, Watanabe S, Kojima M, Hasanova N, Sasaki H, Sasaki K, Suzuki Y, Taki M, Kamimura Y, Hirata A, Shirai H. Dosimetry Using a Localized Exposure System in the Millimeter-Wave Band for in vivo Studies on Ocular Effects. IEEE Transactions on Microwave Theory and Techniques. 2014. 62(7): 1554-1564.

Scientific Committee on Emerging and Newly Identified Health Risks. 2015. Potential health effects of exposure to electromagnetic fields (EMF). European Commission.

Sejrsen P. Blood flow in cutaneous tissue in man studied by washout of radioactive xenon. Circ Res. 1969;25(2):215-229.

Sène D. Small fiber neuropathy: Diagnosis, causes, and treatment. Joint Bone Spine. 2018 Oct;85(5):553-559.

Setchell BP. The Parkes Lecture. Heat and the testis. J Reprod Fertil. 1998 Nov;114(2):179-94

Shanin SN, Rybakina EG, Novikova NN, Kozinets IA, Rogers VJ, Korneva EA. Natural killer cell cytotoxic activity and c-Fos protein synthesis in rat hypothalamic cells after painful electric stimulation of the hind limbs and EHF irradiation of the skin. Med Sci Monit. 2005 Sep;11(9):BR309-15.

Sharma A, Sisodia R, Bhatnagar D, Saxena VK. Spatial memory and learning performance and its relationship to protein synthesis of Swiss albino mice exposed to 10 GHz microwaves. Int J Radiat Biol. 2014 Jan;90(1):29-35.

Sharma A, Kesari KK, Saxena VK, Sisodia R. The influence of prenatal 10 GHz microwave radiation exposure on a developing mice brain. Gen Physiol Biophys. 2017a Jan;36(1):41-51.

Sharma A, Kesari KK, Saxena VK, Sisodia R. Ten gigahertz microwave radiation impairs spatial memory, enzymes activity, and histopathology of developing mice brain. Mol Cell Biochem. 2017b Nov;435(1-2):1-13.

Sharpe RM. Environmental/lifestyle effects on spermatogenesis. Philos Trans R Soc Lond B Biol Sci. 2010 May 27;365(1546):1697-712.

Shiota K. Induction of neural tube defects and skeletal malformations in mice following brief hyperthermia in utero. Biol Neonate. 1988;53(2):86-97.

Sisodia R, Rifat F, Sharma A, Srivastava P, Sharma K. Effects of 10-GHz microwaves on hematological parameters in Swiss albino mice and their modulation by Prunus avium. J Environ Pathol Toxicol Oncol. 2013;32(3):205-17.

Sivachenko IB, Medvedev DS, Molodtsova ID, Panteleev SS, Sokolov AY, Lyubashina OA. Effects of Millimeter-Wave Electromagnetic Radiation on the Experimental Model of Migraine. Bull Exp Biol Med. 2016 Feb;160(4):425-8.

Sokolnicki LA, Roberts SK, Wilkins BW, Basu A, Charkoudian N. Contribution of nitric oxide to cutaneous microvascular dilation in individuals with type 2 diabetes mellitus. Am J Physiol Endocrinol Metab. 2007;292(1):E314-E318.

Sokolnicki LA, Strom NA, Roberts SK, Kingsley-Berg SA, Basu A, Charkoudian N. Skin blood flow and nitric oxide during body heating in type 2 diabetes mellitus. J Appl Physiol (1985). 2009;106(2):566-570.

Stephens DP, Charkoudian N, Benevento JM, Johnson JM, Saumet JL. The influence of topical capsaicin on the local thermal control of skin blood flow in humans. Am J Physiol Regul Integr Comp Physiol. 2001 Sep;281(3):R894-901.

Stephenson LA, Kolka MA. Menstrual cycle phase and time of day alter reference signal controlling arm blood flow and sweating. Am J Physiol. 1985 Aug;249(2 Pt 2):R186-91.

Stoll AM, Greene LC. Relationship between pain and tissue damage due to thermal radiation. J Appl Physiol. 1959 May;14(3):373-82.

Straume A, Oftedal G, Johnsson A. Skin temperature increase caused by a mobile phone: a methodological infrared camera study. Bioelectromagnetics. 2005 Sep;26(6):510-9.

SSM. SSM's Scientific Council on Electromagnetic Fields. Recent research on EMF and health risk—tenth report from SSM's Scientific Council on Electromagnetic Fields. Luxembourg: Publication 19; 2015.

SSM. SSM's Scientific Council on Electromagnetic Fields. Recent research on EMF and health risk—eleventh report from SSM's Scientific Council on Electromagnetic Fields. Stockholm: SSM; Publication 15; 2016.

SSM. SSM's Scientific Council on Electromagnetic Fields. Recent Research on EMF and health risk—twelfth report from SSM's Scientific Council on Electromagnetic Fields. Publication 09; 2018.

Sypniewska RK, Millenbaugh NJ, Kiel JL, Blystone RV, Ringham HN, Mason PA, Witzmann FA. Protein changes in macrophages induced by plasma from rats exposed to 35 GHz millimeter waves. Bioelectromagnetics. 2010 Dec;31(8):656-63.

Tenland T, Salerud EG, Nilsson GE, Oberg PA. Spatial and temporal variations in human skin blood flow. Int J Microcirc Clin Exp. 1983;2(2):81-90.

Themistocleous AC, Ramirez JD, Serra J, Bennett DL. The clinical approach to small fibre neuropathy and painful channelopathy. Pract Neurol. 2014 Dec;14(6):368-79.

Tominaga M, Caterina MJ. Thermosensation and pain. J Neurobiol. 2004 Oct;61(1):3-12.

Tracy LM, Koenig J, Georgiou-Karistianis N, Gibson SJ, Giummarra MJ. Heart rate variability is associated with thermal heat pain threshold in males, but not females. Int J Psychophysiol. 2018 Sep;131:37-43.

Van Eeghem V, El Arfani A, Anthoula A, Walrave L, Pourkazemi A, Bentea E, Demuyser T, Smolders I, Stiens J. Selective changes in locomotor activity in mice due to low-intensity microwaves amplitude modulated in the EEG spectral domain. Neuroscience. 2017 Sep 17;359:40-48.

Van Hees J, Gybels J. C nociceptor activity in human nerve during painful and non painful skin stimulation. J Neurol Neurosurg Psychiatry. 1981 Jul;44(7):600-7.

van Rhoon GC, Samaras T, Yarmolenko PS, Dewhirst MW, Neufeld E, Kuster N. CEM43°C thermal dose thresholds: a potential guide for magnetic resonance radiofrequency exposure levels? Eur Radiol. 2013 Aug;23(8):2215-27.

Viana F. Nociceptors: thermal allodynia and thermal pain. Handb Clin Neurol. 2018;156:103-119.

Vijayalaxmi, Logani MK, Bhanushali A, Ziskin MC, Prihoda TJ. Micronuclei in peripheral blood and bone marrow cells of mice exposed to 42 GHz electromagnetic millimeter waves. Radiat Res. 2004 Mar;161(3):341-5.

Voets T. TRP channels and thermosensation. Handb Exp Pharmacol. 2014;223:729-41.

Vriens J, Nilius B, Voets T. Peripheral thermosensation in mammals. Nat Rev Neurosci. 2014 Sep;15(9):573-89.

Walters TJ, Blick DW, Johnson LR, Adair ER, Foster KR. Heating and pain sensation produced in human skin by millimeter waves: comparison to a simple thermal model. Health Phys. 2000 Mar;78(3):259-67.

Walters TJ, Ryan KL, Nelson DA, Blick DW, Mason PA. Effects of blood flow on skin heating induced by millimeter wave irradiation in humans. Health Phys. 2004 Feb;86(2):115-20.

Wang C, Cui YG, Wang XH, Jia Y, Sinha Hikim A, Lue YH, Tong JS, Qian LX, Sha JH, Zhou ZM, Hull L, Leung A, Swerdloff RS. Transient scrotal hyperthermia and levonorgestrel enhance testosterone-induced spermatogenesis suppression in men through increased germ cell apoptosis. J Clin Endocrinol Metab. 2007 Aug;92(8):3292-304.

Wick DE, Roberts SK, Basu A, et al. Delayed threshold for active cutaneous vasodilation in patients with Type 2 diabetes mellitus. J Appl Physiol (1985). 2006;100(2):637-641.

World Health Organization. Radiofrequency fields; Public Consultation Document, released October 2014. Geneva: WHO; 2014.

Wu H, Hauser R, Krawetz SA *et al.* Environmental Susceptibility of the Sperm Epigenome During Windows of Male Germ Cell Development. Curr Envir Health Rpt **2,** 356–366 (2015).

Wu PY, Wong WH, Hodgman JE, Levan N. Changes in blood flow in the skin and muscle with phototherapy. Pediatr Res. 1974 Apr;8(4):257-62.

Xia L, Luo QL, Lin HD, Zhang JL, Guo H, He CQ. The effect of different treatment time of millimeter waves on chondrocyte apoptosis, caspase-3, caspase-8, and MMP-13 expression in rabbit surgically induced model of knee osteoarthritis. Rheumatol Int. 2012 Sep;32(9):2847-56.

Xie T, Pei J, Cui Y, Zhang J, Qi H, Chen S, Qiao D. EEG changes as heat stress reactions in rats irradiated by high intensity 35 GHz millimeter waves. Health Phys. 2011 Jun;100(6):632-40.

Young IM. Vasomotor tone in the skin blood vessels of the newborn infant. Clin Sci. 1962 Jun;22:325-32.

Zaproudina N, Varmavuo V, Airaksinen O, Närhi M. Reproducibility of infrared thermography measurements in healthy individuals. Physiol Meas. 2008;29(4):515-524.

Zavgorodny V, Murashev AN, Sadovnikov VB, Medvedev OS, Voronkov VN. Investigating the influence of electromagnetic radiation from millimeter ranges on the cardiovascular system in the hypertensive rat. Crit Rev Biomed Eng. 2000;28(5-6):83-8.

Zhang Y, Li Z, Gao Y, Zhang C. Effects of fetal microwave radiation exposure on offspring behavior in mice. J Radiat Res. 2015 Mar;56(2):261-8.

Zhu YJ, Lu TJ. A multi-scale view of skin thermal pain: from nociception to pain sensation. Philos Trans A Math Phys Eng Sci. 2010 Feb 13;368(1912):521-59.

Ziskin MC, Morrissey J. Thermal thresholds for teratogenicity, reproduction, and development. Int J Hyperthermia. 2011;27(4):374-87.

5.0 Evaluation of ICNIRP (2020) Local Exposure Basic Restrictions (> 6 GHz) Using the Approximate Gaussian Beam Model

LIST OF ACRONYMS

1D – one dimensional
3D – three dimensional
AED – absorbed energy density
APD – absorbed power density
BHTE – bioheat transfer equation (after Pennes, 1948)
BR – basic restriction
CW – continuous wave
DF – duty factor
EM – electromagnetic
FD – finite difference
FDTD – finite difference, time domain (referring to a method of computational electrodynamics)
FWHM – full width at half maximum
HPBD – half-power projected beam diameter
ICNIRP – International Committee on Non-Ionizing Radiation Protection
MC– Monte Carlo
OAHE – operational adverse health effect
OBR – operational basic restriction
SAR – specific absorption rate
SAT – sub-cutaneous adipose tissue
SS – steady state
TOT – total ON time
TR – temperature rise (referring to the spatial peak value usually on the surface of the skin)

TABLE OF SYMBOLS

ΔT_{3D}	spatial peak, surface TR for a narrow beam (computed from 3D BHTE)
ΔT_{1D}	surface TR for a wide beam (computed from 1D BHTE)
$FWHM$	full width at half-maximum of the transverse SAR distribution (spot size)
$HPBD$	half-power projected beam diameter of external power density (beam diameter)
$R_{1\text{-}eff}$	effective diffusion length
S_{ab}	absorbed power density (APD)
$S_{ab\text{-}5}$	absorbed power density that produces 5 ^{o}C maximum TR in type 1 tissue
$S_{ab,1cm\text{-}5}$	APD, spatially averaged over 1 cm^2, that produces 5 ^{o}C maximum TR in type 1 tissue
$S_{ab,4cm\text{-}5}$	APD, spatially averaged over 4 cm^2, that produces 5 ^{o}C maximum TR in type 1 tissue
$S_{ab,o}$	spatial peak APD of a narrow beam
$S_{ab,o\text{-}5}$	spatial peak APD of a narrow beam that produces 5 ^{o}C TR in type 1 tissue
$S_{ab,pk}$	temporal peak APD (during the pulse ON)
$S_{ab,ave}$	time averaged APD (averaged over a 360 s reference period)
$S_{ab,\,OBR}$	absorbed power density operational basic restriction
S_{inc}	incident, unperturbed power density
$S_{inc,Xcm}$	incident, unperturbed power density, spatially averaged over X cm^2
U_{ab}	absorbed energy density or AED
$U_{ab\text{-}5}$	AED that produces 5 ^{o}C maximum TR in type 1 tissue
$U_{ab,1cm\text{-}5}$	AED, spatially averaged over 1 cm^2, that produces 5 ^{o}C maximum TR in type 1 tissue
$U_{ab,4cm\text{-}5}$	AED, spatially averaged over 4 cm^2, that produces 5 ^{o}C maximum TR in type 1 tissue
$U_{ab,o}$	spatial peak AED of a narrow beam
$U_{ab,o\text{-}5}$	spatial peak AED of a narrow beam that produces 5 ^{o}C TR in type 1 tissue
$U_{ab,OBR}$	absorbed energy density or AED operational basic restriction
t_d	exposure duration of a single isolated pulse or TOT for multiple pulses
t_{OFF}	inter-pulse period or time period that separates pulses
t_{ON}	pulse width
T_R	electromagnetic power or energy transmission coefficient across the air-tissue interface

5.1 Background: OAHET basic restrictions for 6 -300 GHz

The operational adverse health effect threshold (OAHET) basic restriction (shortened to operational basic restriction or OBR) is intended to be a lower bound of values of absorbed energy density (U_{ab}) or absorbed power density (S_{ab}) that produces a 5 °C maximum temperature-rise (TR) in type 1 human tissue (e.g. epidermal, dermal, SAT, muscle and bone) or 2 °C maximum temperature-rise in type 2 human tissue (e.g. brain, eye, testes and deeper tissues or organs that maintain the homeostatic temperature). For frequencies greater than 6 GHz, the OBRs implied in ICNIRP (2020) can be categorized by exposure duration, t_d, and by spatial averaging area (4 cm^2 and 1 cm^2) and are given in Table 5.1. In this report OBRs represent the OAHET basic restrictions used by ICNIRP in their 2020 exposure guidelines (ICNIRP, 2020), to derive the occupational and general public basic restrictions by application of 2-fold and 10-fold reduction factors, respectively.

Table 5.1 Operational basic restrictions based on an OAHET of 5 °C in Type 1 tissue.

exposure duration or TOT t_d s	spatial averaging area cm^2	frequency range GHz	$U_{ab,OBR}$ kJ/m^2	$S_{ab,\ OBR}$ W/m^2
< 360	4	6 - 300	$72\left[0.05+0.95\sqrt{t_d/360}\right]$ eqn (5.1)	NA
< 360	1	30 - 300	$144\left[0.025+0.975\sqrt{t_d/360}\right]$ eqn (5.2)	NA
≥ 360	4	6 - 300	NA	200
≥ 360	1	30 - 300	NA	400

5.2 Definitions

absorbed energy density (AED or U_{ab})

For an isolated single pulse, the absorbed energy density (AED) is given by $U_{ab} = S_{ab}\ t_{ON}$ where t_{ON} is the ON time of the pulse. If S_{ab} is time-dependent over the reference period, then the AED is given by integrating S_{ab} over time: $U_{ab} = \int_0^{\Delta t} S_{ab} dt$, where Δt is the reference period. This case is not considered in this evaluation.

absorbed power density (APD or S_{ab})

The fraction of the incident power density that is absorbed in the tissues. Absorbed power density (APD) is given by $S_{ab} = S_{inc}\ T_R$, where S_{inc} is the incident, unperturbed power density and T_R is the power transmission coefficient across the air-tissue interface.

beam diameter
The diameter of the external power density beam that would be projected on a surface representing the target tissue, but in the absence of the tissue. (The definition of beam diameter assumes no interaction between the EM wave and tissue.) It is quantified as the linear distance between the half-power intensity points in the projected beam and is termed the "Half-power Projected Beam Diameter" or *HPBD*.

continuous pulse train
A regularly spaced train of pulses occurring continuously over all time.

continuous wave (CW)
A constant amplitude electromagnetic (EM) exposure, occurring continuously over all time (or for practical reasons lasting more than the reference period).

exposure duration
The duration or "ON time" of a single isolated pulse or in the case of multiple pulses, the total ON time in the reference period.

isolated group of pulses
A group of pulses whose combined ON and OFF times are less than the reference period, occurring once over all time. Alternatively, a group of pulses can be considered isolated if by the time a follow-on group arrives, the TR due to the first group has returned to zero through the cooling mechanisms of heat diffusion and blood transport.

isolated single pulse
A pulse of duration or "ON time" less than the reference period, occurring once over all time. Alternatively, a single pulse can be considered isolated if by the time a follow-on pulse arrives, the TR due to the first pulse has returned to zero through the cooling mechanisms of heat diffusion and blood transport. This can take as short as 4.5 minutes for brief pulses of narrow beam diameters and up to 40 minutes for wide beams with pulse widths approaching the reference period (based on a 99% drop in TR).

pulse
A brief period (lasting less than the reference period) of constant-amplitude, electromagnetic (EM) exposure.

reference period
A time duration of exposure throughout which energy density (for pulsed exposures) and time-averaged power density (for CW exposures) limits apply. The reference period is 6 minutes for localized exposures in ICNIRP and for all exposures in Health Canada's Safety Code 6 (2015).

spatial averaging
The projected power density beam is assumed to have a circularly symmetric intensity distribution that is Gaussian with respect to the radial distance from the centre of the beam. For the purposes of this evaluation, this beam is spatially averaged over square areas of 4 cm^2, 1 cm^2 and 0 cm^2 (i.e. non spatially averaged). Appendix D.5 gives further details on the spatial averaging of these projected beams.

spot size

The size of the transverse SAR distribution (transverse to the axis of propagation of the EM wave) inside the tissue. It is quantified as the diameter at half-power intensity of the transverse SAR distribution and is termed the "Full Width at Half Maximum" or *FWHM*.

time averaging

For time dependent exposures of duration greater than the reference period, the APD is time averaged over the reference period (360 s) such that the APD is given by: $S_{ab} = T_R \left[\int_0^{360} S_{inc}\, dt\right] /360$ where the 360 s integration window is a rolling one (i.e. scanned over the waveform(s) to find the highest value) and T_R is the power transmission coefficient across the air/tissue interface. This evaluation only considers time-averaging in the case of continuous pulse trains.

total ON time (TOT)

The sum of the ON times of an isolated group of pulses or the sum of the ON times in a single reference period of a continuous pulse train.

5.3 Assessing ICNIRP's Basic Restrictions

Assessing the ICNIRP (2020) occupational and general public basic restrictions above 6 GHz consists of computing the AED or APD necessary to produce 5 °C TR in Type 1 human tissues (penetration depth for frequencies above 6 GHz is shallow enough to exclude Type 2 tissues from the analysis) and comparing them against the OBRs in Table 5.1. If those values are greater than their corresponding OBR, then the occupational and general public basic restrictions can be considered conservative, at least for the range of exposure conditions (i.e. frequencies and beam diameters or spot sizes) used in this assessment. This is possible due to the linearity of the governing relationship between TR and exposure and also due to the assumed absence of thermoregulatory effects, local or global (e.g. vasodilation). The model that is being used for this assessment includes the effect of heat diffusion, heat transport by blood perfusion and heat loss at the air-skin convective boundary but neglects the natural thermoregulatory effect of the human body such as sweat mechanisms and vasodilation.

Throughout the rest of this chapter, the symbols $S_{ab\text{-}5}$ and $U_{ab\text{-}5}$ will be used to denote values of APD and AED that produce 5 °C maximum TR in type 1 tissue at a given frequency, exposure duration and for a specific tissue composition and thickness configuration. These constitute the "evaluation metrics". The $S_{ab,OBR}$ and $U_{ab,OBR}$ are levels that are considered to represent a lower envelope of all possible values of $S_{ab\text{-}5}$ and $U_{ab\text{-}5}$ for any type of exposure condition and type 1 tissue configuration.

5.3.1 Exposure & thermal model:

Details of the exposure model used for this assessment can be found in (Gajda et al. 2019). It consists of a transverse electric and magnetic (TEM) electromagnetic beam illuminating a planar, multi-layer tissue at normal incidence. The beam is assumed to have far-field characteristics (i.e. a constant wave impedance

of ≈ 377 Ω) and its propagation through the multiple layers is assumed to correspond to that of a plane wave.

The external beam is assumed to be circularly symmetric about the propagation axis and is characterized by its half-power projected beam diameter (HPBD). This is the diameter of the unperturbed, incident power density pattern that would occur on the surface of the tissue at an intensity equal to one-half that of the centre of the beam. This parameter is used for spatial averaging the power density.

TR in the tissues is calculated using the dynamic Pennes Bio-Heat Transfer Equation (BHTE) with the SAR distribution in the multiple layers as the input energy term (see the Appendix D.1 for more details). The transverse width of the circularly symmetric SAR distribution (i.e. transverse to the propagation direction) is related to the HPBD and is an important parameter in determining the TR over time. It is characterized by its Full Width at Half Maximum (FWHM) and is referred to as the "spot size" to distinguish it from the "beam diameter" or HPBD of the external power density.

From information obtained from Finite Difference Time Domain (FDTD) simulations of electrically small sources (up to a half-wavelength) illuminating planar tissues, it was found that the FWHM is approximately 80% of the HPBD. For the purposes of calculating spatial averages throughout this report, a ratio of *FWHM/HPBD* = 0.80 was assumed.

For all BHTE solutions, a convective surface boundary condition with a heat loss coefficient of 10 $W/m^2/^oC$ was adopted (see Appendix D.1 for more details). This choice produces a realistic skin surface temperature of 31-33 ^oC (depending on the tissue configuration) at room temperatures (22^oC) in the absence of electromagnetic exposure.

The validity of the Pennes BHTE is extensively reviewed in the Appendix A of this report. Conditions for maximal electromagnetic energy absorption in terms of angle of incidence and polarization state of the incident wave are detailed in Appendix B. The conclusions contained in this appendix support the use of the normal incidence model as the worst case for maximizing the absorbed power in tissues for a given incident power density.

5.3.2 Tissue Models

Two tissue models and thermal/dielectric parameter databases were used depending on the frequency range. At the lower frequencies, 6-60 GHz, a 3-tissue configuration consisting of skin (combined epidermis and dermis), sub-cutaneous adipose tissue (SAT) and a bulk layer of muscle was used. It employed the thermal and dielectric parameters contained in Hasgall et al. 2018 and employed a fixed thickness configuration that produced a relatively high TR per absorbed power input while retaining realistic thicknesses of skin and SAT that occur in the human population (thicknesses are skin: 0.6 mm, SAT: 6 mm and muscle to 50mm).

At the higher range of frequencies, 60-200 GHz, a 4-tissue configuration consisting of separate layers of epidermis, dermis, SAT and a bulk layer of muscle was used. It employed the thermal and dielectric parameters in Sasaki et al. 2017 (see Appendix D.6 for more details). The fixed thicknesses of the layers were the same as used in Sasaki et al. (epidermis: 80 µm, dermis: 1.25 mm SAT: 14.3mm and muscle to a total of 50 mm), which were quoted to be the mean thicknesses for the abdomen. This configuration is not a worst-case one in the sense of maximizing 1D temperature rise as was done for the 3-tissue one, but was chosen for its traceability to the literature.

The choice of a 3 or 4-layer model and the parameter database depending on frequency was predicated on several factors. At 60 GHz and above, a 4 tissue model was used (i.e. the skin was split into epidermis and dermis) due to the smaller in-tissue wavelengths and consequent greater interactions with the thinner layers. The dielectric data in Hasgall et al. 2018 is from the Cole-Cole fitting of measured data (to approximately 20 GHz) and extrapolated beyond (Gabriel, 1996). This is in contrast to the Sasaki et al. 2017 dielectric data that was obtained from measurements to at least 100 GHz with some to 1000 GHz along with extrapolation for some tissues (see Appendix D.6 for details).

Amongst the thermal/physical parameters, differences between Hasgall and Sasaki perfusion rates are -10% (Hasgall is lower), 24% and 5% for skin/dermis, SAT and muscle, respectively (epidermis has zero perfusion in the Sasaki data). For the thermal conductivity, differences are -12%, -16% and -2% for the same tissues, respectively (epidermis and dermis are equal in Sasaki). Both databases have identical density and specific heat capacity for each tissue.

In order to qualitatively assess the degree of conservatism of the two fixed-thickness models, some calculations of the evaluation metrics were also made using statistical thickness models based on a Monte Carlo (MC) technique (Gajda et al. 2019). In the MC technique, random selections (within the known human population) of skin and SAT thickness (3-tissue) or epidermis, dermis and SAT (4-tissue) are used in solutions of the BHTE in order to compile statistics of TR. After a sufficient number of iterations, the 95th percentile TR is extracted to determine a reasonable estimate of the worst-case TR which can be compared to TRs obtained from the fixed thickness models. These sample calculations could only be carried out for wide beam exposures (described in more detail below) due to the long computation times necessary for narrow beam simulations.

5.3.3 Wide beams versus narrow beams

Two projected beams having the same spatial-peak power density but different HPBDs will produce different steady-state TRs (i.e. after a sufficiently long exposure). In general, the maximal surface TR increases for increasing HPBD (or FWHM). An example of the steady-state surface TR for a narrow beam (denoted as ΔT_{3D}), normalized to the TR of a plane wave (denoted as ΔT_{1D}) with the same spatial-peak power density, is shown plotted versus the spot size, FWHM, in Fig. 5.2. The general shape of the curve is the same for any multi-layer tissue model and is controlled by a parameter known as the effective diffusion length, $R_{1\text{-}eff}$ (Gajda et al. 2019). For any tissue configuration and frequency, it has been found that at a value of $FWHM \approx 10\ R_{1\text{-}eff}$, the narrow beam TR is approximately 95% of the one due to a plane wave.

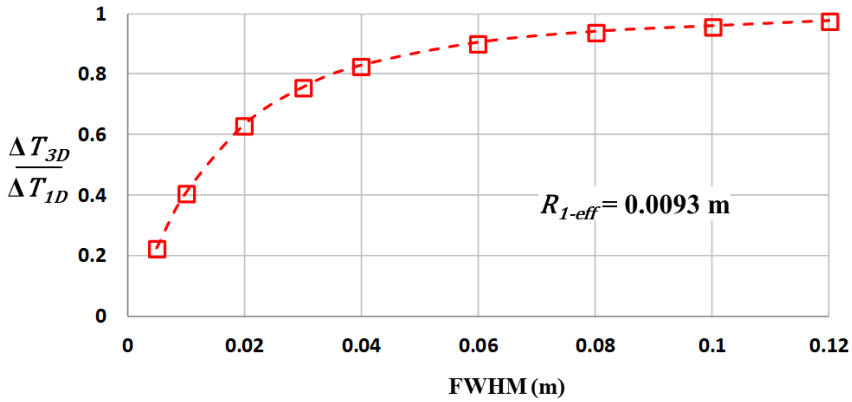

Fig. 5.2, Ratio of Steady State (SS), narrow-beam to wide-beam TR versus *FWHM* for a 4-tissue, fixed-thickness configuration (Sasaki database) at 120 GHz. For this configuration and frequency, the effective diffusion length ($R_{1\text{-}eff}$) is 9.3 mm.

Plane wave TR (ΔT_{1D}) is obtained from solution of the 1-dimensional (1D) form of the BHTE, which takes far less computation time than a solution of the 3-dimensional (3D) form required for ΔT_{3D} (i.e. for narrow beams). Thus, for a beam diameter that satisfies $FWHM \geq 10\ R_{1\text{-}eff}$, the maximal surface TR for any exposure duration is reasonably approximated by the solution of the 1D BHTE. Throughout the remainder of this report, beams diameters for which $FWHM \geq 10\ R_{1\text{-}eff}$ will be referred to as wide beams and solutions of the 1D BHTE will be used to determine their TR. Any beam whose spot size that does not satisfy this criterion will be referred to as a narrow beam and solutions of the 3D BHTE will be used to determine the surface TR, ΔT_{3D}.

5.3.4 Evaluation Metrics

Solutions of the 1D and 3D dynamic BHTEs are the TR distributions in the tissues at a time point, t_o, denoted as $\Delta T_{1D}(t_o, z)$ and $\Delta T_{3D}(t_o, r, z)$, respectively. For long exposure durations, and especially at lower frequencies where the power absorption is deeper, maximal TR actually occurs a short distance inside the tissues (<1mm for h = 10 W/m^2/^{o}C). However, the difference between these and surface TRs are small. In addition, TR is always greatest in the centre of the beam at r = 0. Thus, all TR results will be quoted as surface values in the centre of the beam and will be given abbreviated symbols such as for a single isolated pulse: $\Delta T_{1D} = \Delta T_{1D}(t_d,0)$ and $\Delta T_{3D} = \Delta T_{3D}(t_d,0,0)$, where t_d is the pulse width (or exposure duration).

Depending on the time-dependence of exposure, computed TRs are normalized to the AED and/or APD that produced them to generate the ratios: $\Delta T_{1D}/U_{ab,Xcm}$, $\Delta T_{1D}/S_{ab,Xcm}$, $\Delta T_{3D}/U_{ab,Xcm}$, and $\Delta T_{3D}/S_{ab,Xcm}$ (the subscript "*X*" can take on the symbols "4" or "1" to denote whether the spatial averaging is over 4 cm^2 or 1 cm^2 square areas, respectively).

The evaluation metrics, i.e. the AED or the APD that produces 5 ^{o}C surface TR, are calculated for the 1D case using:

$$U_{ab,Xcm-5} = \frac{5}{\left(\Delta T_{1D} \middle/ U_{ab,Xcm}\right)} \qquad or \qquad S_{ab,Xcm-5} = \frac{5}{\left(\Delta T_{1D} \middle/ S_{ab,Xcm}\right)} \tag{5.3}$$

with similar formulae used for the 3D case.

The evaluation metrics can be compared directly to the corresponding OBRs in Table 5.1 to assess the conservativeness of the ICNIRP BRs. Alternatively, ratios of $U_{ab,Xcm-5}$ and $S_{ab,Xcm-5}$ to their respective OBR can be formed. If the ratio is greater than unity, then the evaluation metric is greater than the respective OBR and the latter can be considered conservative with respect to the specific exposure conditions (e.g. frequency, exposure duration, beam diameter, tissue model, etc.) under consideration.

5.3.5 Spatial averaging considerations

Wide beams

Effective diffusion lengths ($R_{1\text{-}eff}$) for frequencies of 10-80 GHz range from 0.011 m to 0.008 m (Gajda et al. 2019) and generally decrease with frequency. Therefore, spot sizes satisfying the wide-beam criterion would have FWHMs ranging from 0.10 to 0.08 m with associated HPBDs being commensurately larger. When spatially averaged over 4 cm^2 or 1 cm^2, the spatially averaged power density of such beams would be approximately equal to the spatial-peak value in the centre of the beam. Thus, in all subsequent wide beam evaluations, both spatially averaged values (i.e. 4 cm^2 and 1 cm^2) are equal to the value of plane wave power density used in the 1D BHTE solver and the distinction between 4 cm^2 averaged and 1 cm^2 averaged values will be dropped (i.e. $U_{ab\text{-}5} = U_{ab,4cm\text{-}5} = U_{ab,1cm\text{-}5}$).

For the purposes of testing the conservatism of the OBRs, computed $U_{ab\text{-}5}$ and $S_{ab\text{-}5}$ data is only compared to the lowest OBRs (i.e. eqn 5.1 for $U_{ab\text{-}5}$ and 200 W/m^2 for $S_{ab\text{-}5}$) since these two levels form the most stringent requirements for wide beams.

Narrow beams

Spatial averages were computed over square areas of 4 cm^2 and 1 cm^2. Appendix D.5 has more information on how spatial averaging is carried out. Since different averaging areas produce different spatially averaged values of $U_{ab,Xcm\text{-}5}$ and $S_{ab,Xcm\text{-}5}$, comparison to both sets of OBRs are made.

Appendix C has information on the range and limits of possible spot sizes and beam diameters for several practical antenna types. Based on this appendix, it was found that minimum SAR spot size to consider for frequencies below 30 GHz is (FWHM = 0.010 m) and for frequencies above and equal to 30 GHz is (FWHM = 0.005 m).

5.4 Single isolated pulse and CW

This section begins with the presentation of simulated results at selected frequencies for a single isolated pulse and CW exposures for the purposes of illustrating the TR behaviour of the tissue models and assessing their degree of conservatism (evaluations of scenarios which present the worst-case TR). This is followed by the OBR test results over a wide range of exposure durations, frequencies and beam sizes.

5.4.1 Wide beams

Sample calculations were performed at 10, 30 and 60 GHz using the fixed 3-tissue model and 80-200 GHz using the 4-tissue one. For any MC-based calculations, thickness distributions (log-normal) for skin and SAT found in (Gajda et al. 2019) were used for generating random thicknesses. For the 4-tissue model, a uniform thickness distribution of epidermis with minimum and maximum boundaries of 70 and 110 µm, respectively, was adopted. The sample of dermal thickness was obtained by using the distribution for skin thicknesses found in (Gajda et al. 2019) to generate a random thickness sample for epidermis + dermis. This was followed by subtracting the random thickness for epidermis generated previously to obtain the sample for dermis alone.

5.4.1.1 Sample results: 3-tissue model

Fig. 5.3 shows results from the 1D solver for the fixed, 3-tissue model at 10, 30 and 60 GHz for an exposure (pulse) duration of 1 s and a fixed incident power density. In the figure, the absolute spatial peak temperature at the surface of skin is plotted during the 1 s heating (pulse ON) phase and then for an additional 0.5 s of cooling after the exposure has ceased.

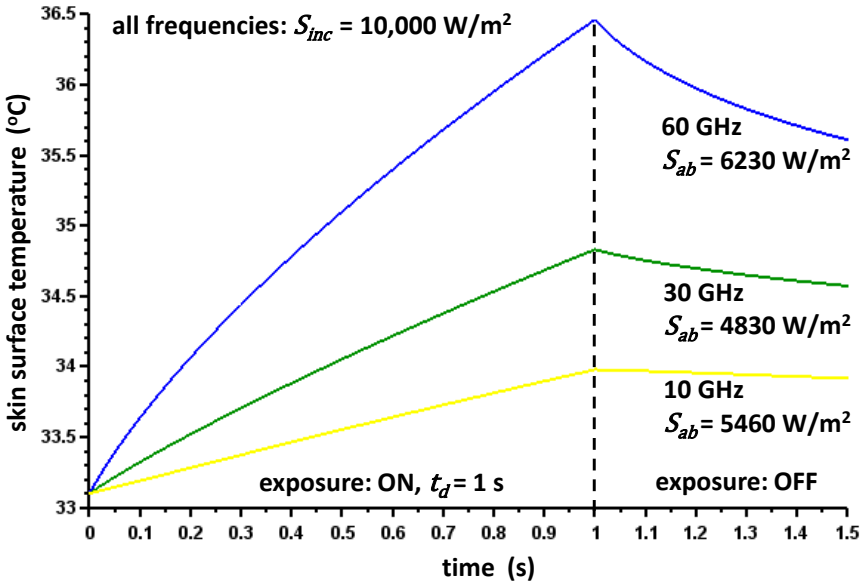

Fig. 5.3, Surface temperature versus time (under convective boundary conditions) for skin: 0.6 mm and SAT: 6 mm at 10, 30 and 60 GHz for an incident power density S_{inc} = 10,000 W/m^2. The 1s exposure duration yields net TR of ΔT_{1D} = 0.9 °C (10 GHz), 1.7 °C (30 GHz) and 3.4 °C (60 GHz).

The TR at 60 GHz is about 2 times higher than that at 30 GHz, as is the TR at 30 GHz compared to 10 GHz. This is not entirely due to changes in transmission coefficient as it is seen that the APD, S_{ab}, is not closely correlated to the TR. It has more to do with the penetration depth of the absorbed power, which becomes progressively more superficial as frequency increases. This results in a successively higher SAR over a thinner layer of tissue, producing higher surface TR as the frequency increases.

Figure 5.4 gives results of calculations of $U_{ab\text{-}5}$, the AED required to give a 5 ^{o}C skin surface TR, versus the exposure duration for both fixed-thickness and MC calculations. For the MC results, the 95th percentile value of $\Delta T_{1D}/U_{ab}$ was extracted from its distribution and the $U_{ab\text{-}5}$ calculated from it. This makes the resulting statistic of $U_{ab\text{-}5}$ actually at the 5th percentile, however, in the graphs it is denoted as the 95th percentile in keeping with its relationship to TR.

The shapes of the curves in Fig. 5.4 show the effects of diffusion and perfusion (heat removal by blood flow) as the exposure duration increases. At very short durations, there is insufficient time for either diffusion or perfusion to remove heat from the skin surface. (Effects of diffusion are negligible for durations under approximately 1s and hundreds of seconds are required for perfusion or blood flow to remove significant amounts of heat. These are referred to as "characteristic" times throughout the remainder of this report.) Thus, the AED required to produce 5 ^{o}C is initially small. As exposure duration further increases, diffusion begins to take place and the required AED increases. At still longer durations, perfusion begins to contribute to the removal of heat and a steady state is approached whereby the rate of heat energy removal begins to equal the rate of electromagnetic energy absorbed. In this regime, the rate of absorption of electromagnetic energy determines the surface TR and not the total energy absorbed.

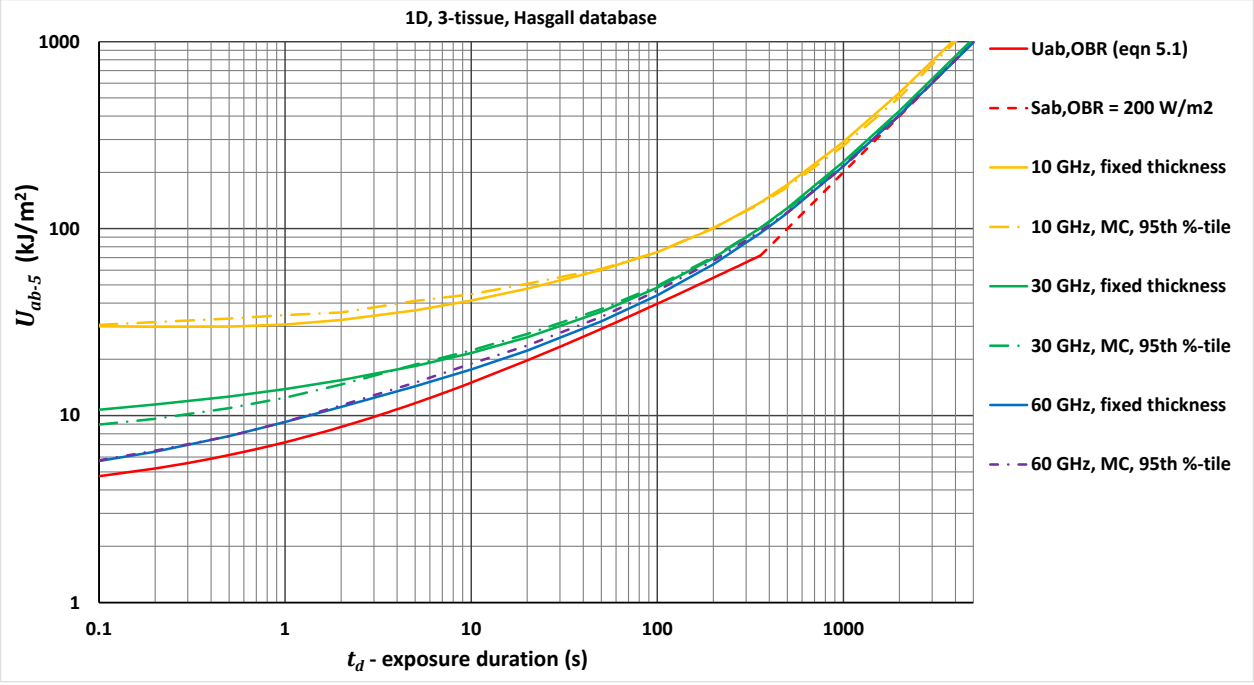

Fig. 5.4, $U_{ab\text{-}5}$ versus single pulse exposure duration for the 3-tissue configuration (Hasgall database, fixed thickness and MC) for wide beams at 10, 30 and 60 GHz. Also plotted are the OBRs of eqn (1.1) for t_d <360 s (solid red line) and the AED curve equivalent to 200 W/m^2 (dashed red line).

In terms of the conservatism of the fixed thickness 3-tissue model, it is seen that their curves and the corresponding ones for the 95th percentile MC calculation are close in value over the whole range of exposure durations. This lends confidence that the 3-tissue fixed-thickness model can be representative of a worst-case model.

With the data presented over a wide dynamic range (as in Fig. 5.4), it becomes difficult to compare the evaluation metrics with the OBRs when the two are close. Figs. 5.5 and 5.6 show the wide-beam metrics (i.e. $U_{ab\text{-}5}$ and $S_{ab\text{-}5}$) normalized to the OBRs versus exposure duration, allowing the degree of conservatism in the OBRs to be seen more clearly.

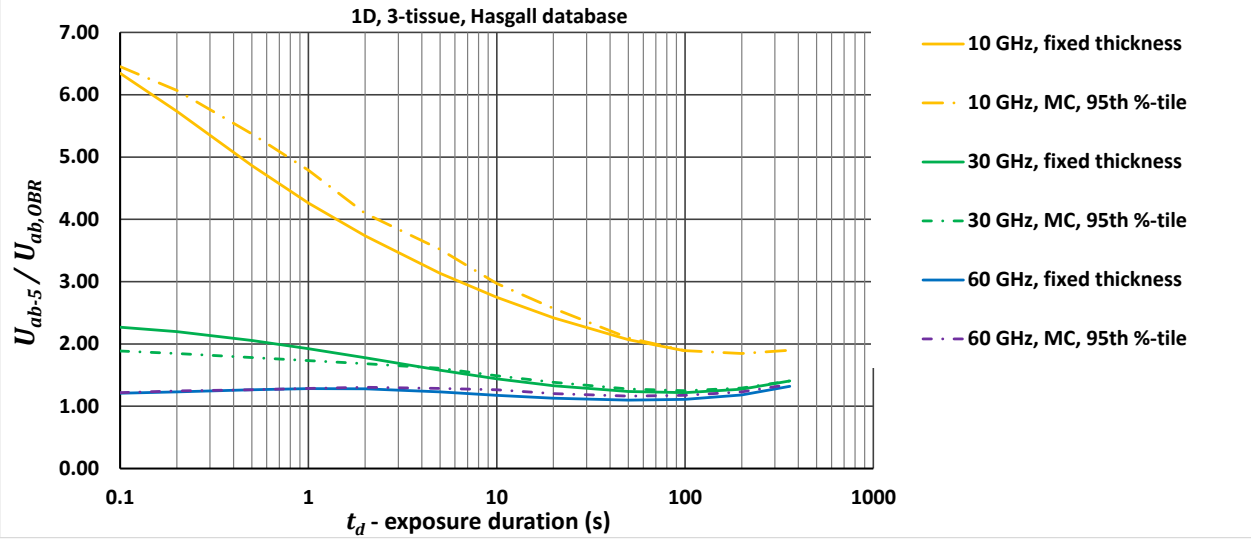

Fig. 5.5, Ratios of wide-beam $U_{ab\text{-}5}/U_{ab,OBR}$ versus single-pulse exposure duration for 3-tissue models (Hasgall database) of fixed thickness and MC.

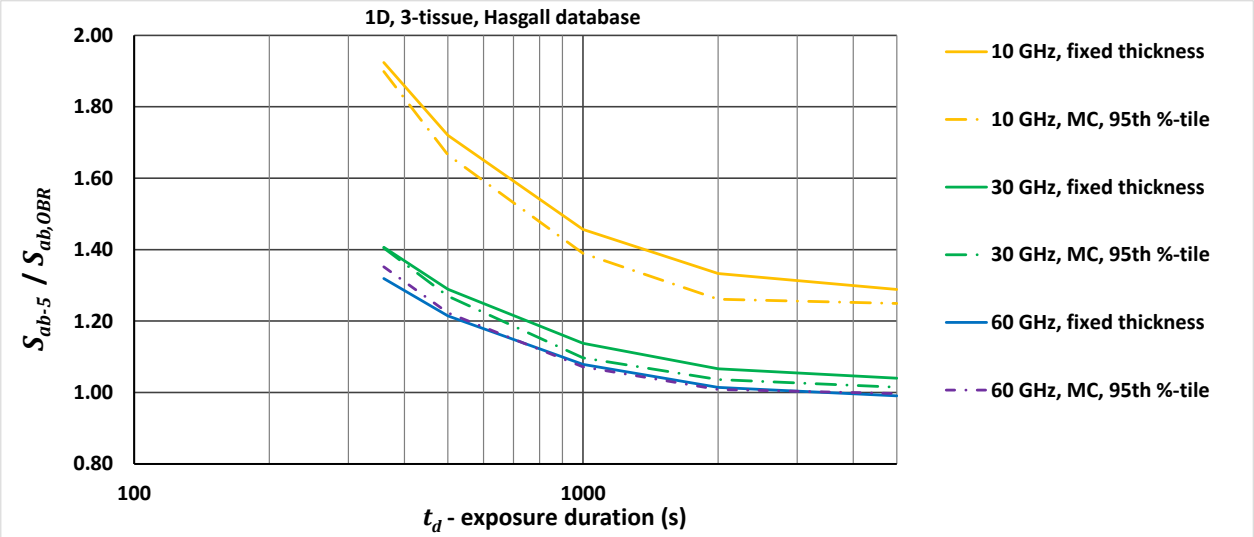

Fig. 5.6, Ratios of wide-beam $S_{ab\text{-}5}/S_{ab,OBR}$ for 3-tissue models (fixed thickness and MC, Hasgall database) versus exposure duration for $t_d \geq 360$s.

5.4.1.2 Sample results: 4-tissue model

The results of the wide-beam calculations for the 4-tissue model using the Sasaki database are shown in Figs. 5.7 and 5.8. In Fig. 5.7 ($t_d < 360$ s). The value of $U_{ab\text{-}5}$ calculated using a short-duration approximation (see Appendix D.2 for details) was assigned at $t_d = 0.001$ s. The full 1D FD solver was used for exposure durations of $t_d = 0.05$ s and higher.

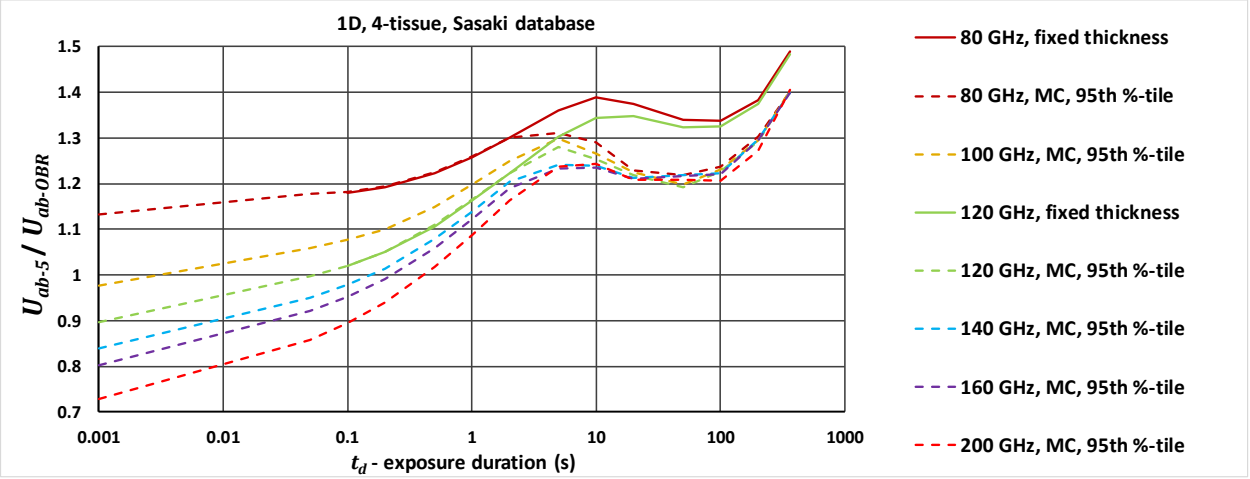

Fig. 5.7, Ratios $U_{ab\text{-}5}/U_{ab,OBR}$ for wide-beams incident on 4-tissue models (Sasaki database) versus single-pulse exposure duration.

In Fig. 5.7, the fixed-thickness results appear to be identical to the MC results at exposure durations shorter than approximately 1-2 s. Once the exposure duration becomes longer than the characteristic diffusion time (1 -2 s), the two sets of results begin to diverge. For very short durations, the thickness and

composition of tissues behind the outermost layer of epidermis plays little role in the resulting surface temperature rise for this model.

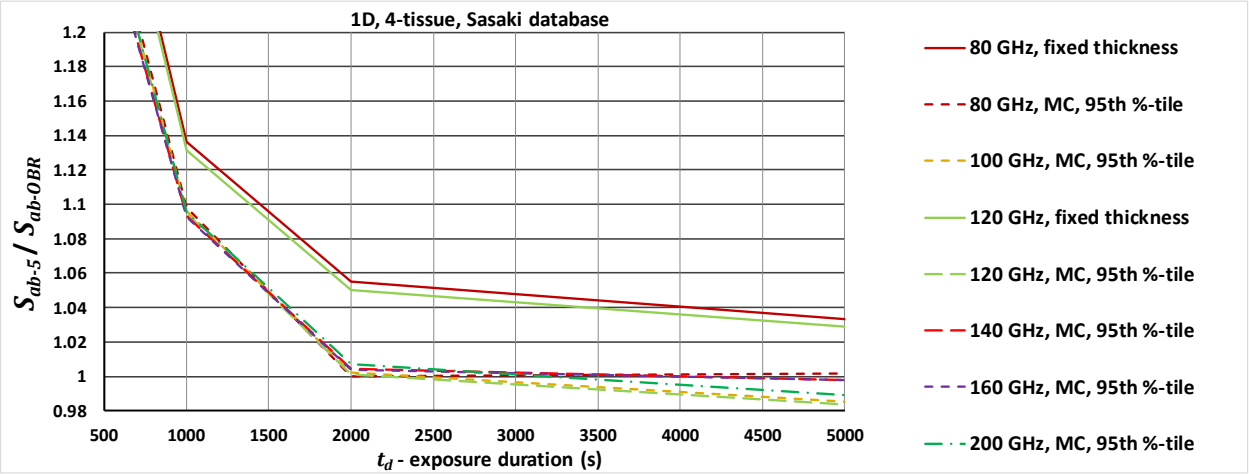

Fig. 5.8, Ratios $S_{ab\text{-}5}/S_{ab,OBR}$ for wide-beams incident on 4-tissue models (Sasaki database) versus exposure duration for $t_d \geq 360$ s.

In terms of the conservatism of the fixed-thickness, 4-tissue model, it is seen that it consistently produces slightly higher ratios of $U_{ab\text{-}5}/U_{ab,OBR}$ and $S_{ab\text{-}5}/S_{ab,OBR}$ than the corresponding 95th percentile MC one. This would suggest that the chosen thicknesses are not strictly the worst case, however, the degree of difference is relatively small. As will be seen in the general results section, these subtle differences are significantly smaller than the large degrees of non-conservatism found in the OBRs for narrow beams at higher frequencies.

5.4.2 Narrow beams

To help understand the behaviour of narrow beams with short exposure duration, the spatial peak TR on the surface, normalized to the spatial-peak AED, $U_{ab,o}$ (i.e. not spatially averaged), is plotted versus the single-pulse exposure duration in Fig. 5.9. For brief exposure durations, diffusion has no time to remove heat away from the centre of the beam resulting in the spatial peak TR of a narrow beam being identical in magnitude to that of a wide beam (for the same spatial-peak AED).

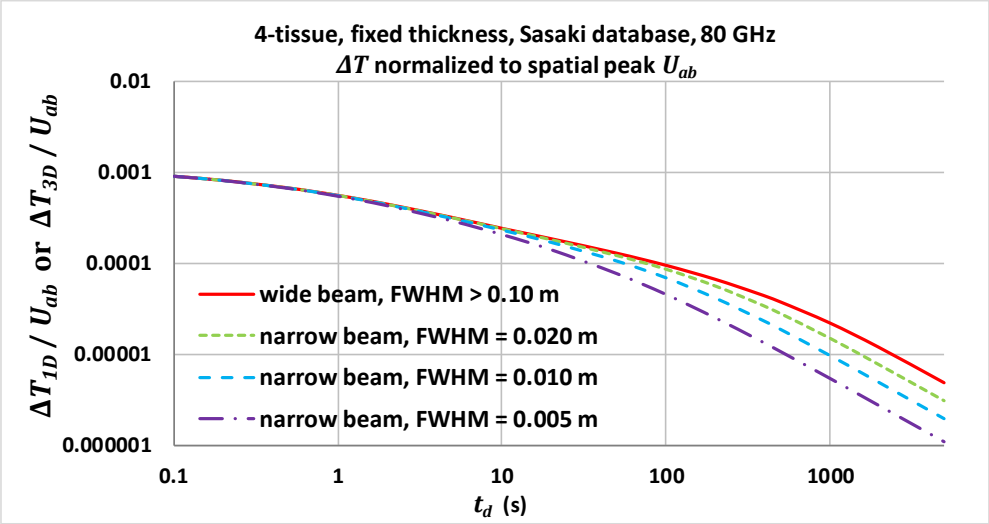

Fig. 5.9, TR normalized to the spatial-peak AED, $U_{ab,o}$, versus single-pulse exposure duration for the fixed-thickness, 4-tissue configuration (Sasaki database) at 80 GHz.

The results in Fig. 5.9 show that for exposure durations up to the characteristic diffusion time (1 – 2 s), the effects of diffusion are negligible and the spatial-peak TR is independent of beam diameter for fixed spatial-peak AED. The same TR data, when normalized to the spatially averaged AED (over 4 cm^2), $U_{ab,4cm}$, is shown in Fig. 5.10. (Beam diameters given by: *HPBD = HPBW/0.8* were assumed for spatial averaging of the external beam.) This data clearly shows the effect of using the spatially averaged AED when computing the normalized TR. Small beam diameters result in exaggeratedly large normalized TRs at the lower end of the exposure duration range.

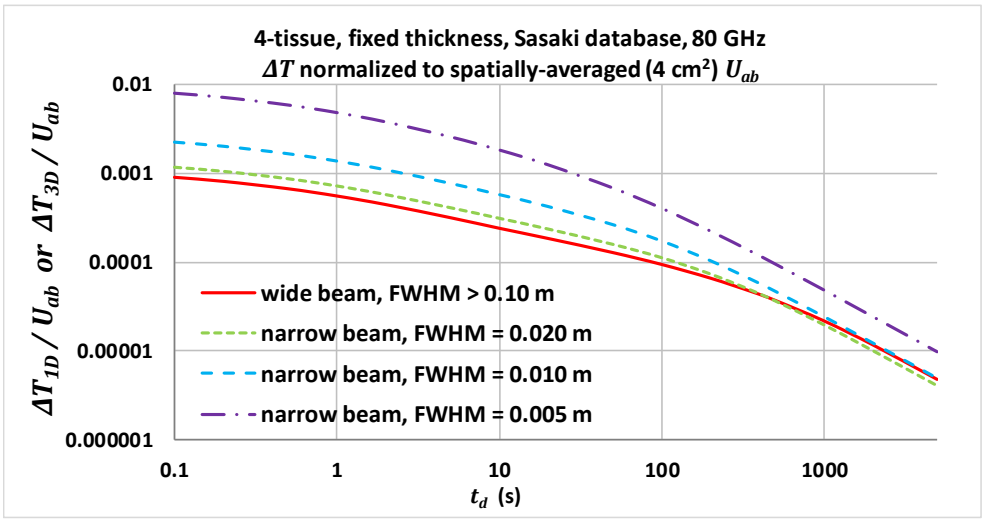

Fig. 5.10, TR normalized to the spatially averaged AED (over 4 cm^2) versus single-pulse exposure duration for the same fixed-thickness, 4-tissue model (Sasaki database) at 80 GHz as in Fig. 5.9.

Fig. 5.11 shows the data in Fig. 5.10 converted to the evaluation metric, $U_{ab,4cm\text{-}5}$, and then normalized to the OBR of eqn (5.1). The OBR is seen to be non-conservative for small beam diameters and short exposure

durations. This non-conservativeness, however, is due to the requirement for spatial averaging as it can be seen from Fig 5.9 that all beam diameters produce identical TRs for the same spatial-peak AED at the shorter durations.

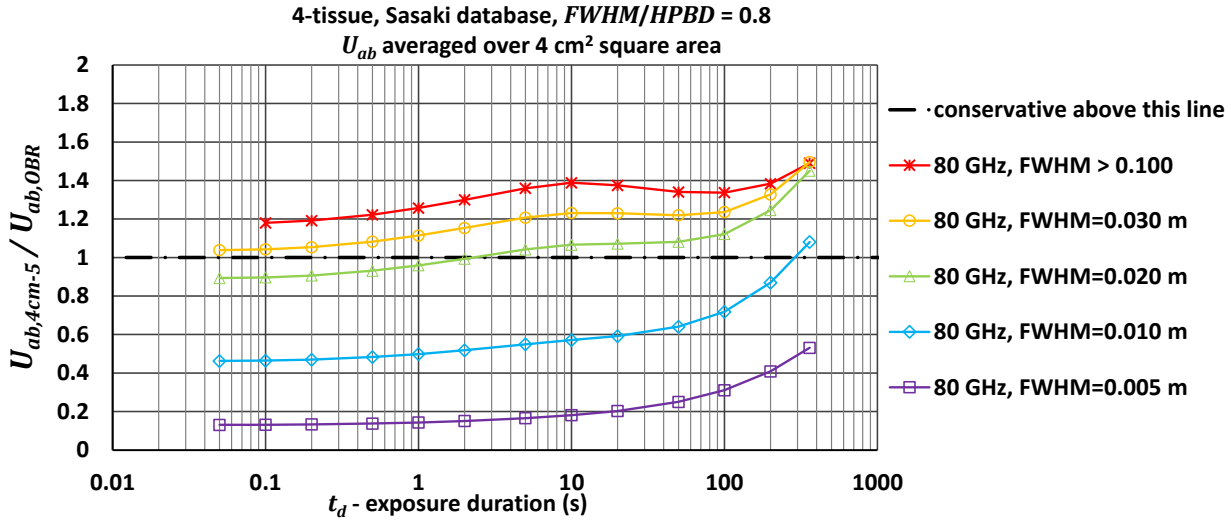

Fig. 5.11, Ratio of evaluation metric-to-OBR: $U_{ab,4cm\text{-}5}/U_{ab,OBR}$ for a 4-tissue, fixed-thickness model (Sasaki database) versus single-pulse exposure duration for different values of FWHM (same TR data as in Figs. 5.9 and 5.10).

5.4.3 General results, single isolated pulse & CW

Calculations were performed at 6, 10, 20, 30 and 60 GHz using the fixed thickness, 3-tissue model and 60, 80, 120, 160 and 200 GHz using the 4-tissue model. Results are presented in color-coded tables in the subsequent figures. These tables present the evaluation metric normalized to their corresponding OBR for a range of spot sizes and single-pulse exposure durations (t_d). The longest exposure duration of 5000 s in the tables is equivalent to a CW exposure since that duration is greater than the longest time required to reach steady state for any beam diameter and frequency.

For all considered narrow beam SAR spot sizes (*FWHM* = 0.005, 0.010, 0.020 and 0.030 m), a beam diameter of *HPBD* = *FWHM/0.8* was assumed in the calculation of spatially averaged U_{ab} or S_{ab}. Table entries with a blue-coloured background indicate that the OBR is conservative for that set of exposure parameters. A green, yellow or red-coloured background indicates a non-conservative OBR according to the scale in Table 5.3.

Table 5.3, Colour code for evaluation table entries.

Range of ratio: $U_{ab,Xcm\text{-}5}/U_{ab,OBR}$ or $S_{ab,Xcm\text{-}5}/S_{ab,OBR}$	Colour	TR for an exposure at the OBR	TR for an exposure at the general public limit	TR for an exposure at the occupational limit
ratio ≥ 1.0	Blue	$\Delta T \leq 5$ °C	$\Delta T \leq 0.5$ °C	$\Delta T \leq 2.5$ °C
0.50 ≤ ratio < 1.0	Green	5 °C < $\Delta T \leq 10$ °C	0.5 °C < $\Delta T \leq 1.0$ °C	2.5 °C < $\Delta T \leq 5.0$ °C
0.25 ≤ ratio < 0.50	Yellow	10 °C < $\Delta T \leq 20$ °C	1.0 °C < $\Delta T \leq 2.0$ °C	5.0 °C < $\Delta T \leq 10$ °C
ratio < 0.25	Red	20 °C < ΔT	2.0 °C < ΔT	10 °C < ΔT

5.4.3.1 Spatial averaging area: 4 cm^2:

$$U_{ab,OBR} = 72\left[0.05 + 0.95\sqrt{t_d/360}\right] \quad (kJ/m^2) \quad , \quad S_{ab,OBR} = 200 \quad (W/m^2)$$

averaging area: 4 cm^2

6 GHz, 3-tiss. Hasgall data

FWHM:	0.01	0.02	0.03	0.10
td (s)	ratio-U_{ab}			
0.05	5.7	11.0	12.8	14.4
0.1	5.2	10.1	11.8	13.2
0.2	4.7	9.1	10.5	11.8
0.5	3.9	7.5	8.8	9.8
1	3.4	6.5	7.5	8.4
2	2.9	5.5	6.4	7.2
5	2.4	4.5	5.2	5.8
10	2.0	3.7	4.3	4.8
20	1.7	3.1	3.6	4.0
50	1.5	2.6	2.9	3.1
100	1.5	2.3	2.5	2.7
200	1.7	2.3	2.4	2.5
	ratio-S_{ab}			
360	2.0	2.5	2.6	2.5
500	1.9	2.3	2.3	2.2
1000	1.8	2.1	2.0	1.8
2000	1.8	2.0	1.9	1.6
5000	1.8	2.0	1.9	1.5

10 GHz, 3-tiss. Hasgall data

FWHM:	0.01	0.02	0.03	0.10
td (s)	ratio-U_{ab}			
0.05	2.7	5.2	6.0	6.8
0.1	2.5	4.8	5.6	6.3
0.2	2.2	4.3	5.0	5.7
0.5	1.9	3.7	4.3	4.8
1	1.7	3.2	3.8	4.2
2	1.5	2.8	3.3	3.7
5	1.3	2.4	2.8	3.1
10	1.1	2.1	2.4	2.7
20	1.0	1.9	2.2	2.4
50	1.0	1.7	1.9	2.1
100	1.0	1.6	1.7	1.9
200	1.2	1.7	1.8	1.8
	ratio-S_{ab}			
360	1.4	1.9	1.9	1.9
500	1.4	1.7	1.8	1.7
1000	1.3	1.6	1.6	1.4
2000	1.3	1.6	1.5	1.3
5000	1.3	1.6	1.5	1.3

20 GHz, 3-tiss. Hasgall data

FWHM:	0.01	0.02	0.03	0.10
td (s)	ratio-U_{ab}			
0.05	1.6	3.0	3.5	3.9
0.1	1.5	2.8	3.3	3.7
0.2	1.4	2.6	3.0	3.4
0.5	1.2	2.3	2.6	2.9
1	1.0	2.0	2.3	2.6
2	0.9	1.8	2.1	2.3
5	0.8	1.5	1.7	2.0
10	0.7	1.3	1.6	1.7
20	0.7	1.2	1.4	1.6
50	0.7	1.1	1.3	1.4
100	0.7	1.1	1.2	1.3
200	0.9	1.2	1.3	1.4
	ratio-S_{ab}			
360	1.1	1.4	1.5	1.5
500	1.0	1.4	1.4	1.4
1000	1.0	1.3	1.3	1.2
2000	1.0	1.3	1.2	1.1
5000	1.0	1.3	1.2	1.1

30 GHz, 3-tiss. Hasgall data

FWHM:	0.005	0.01	0.02	0.03	0.1
td (s)	ratio-U_{ab}				
0.05	0.3	0.9	1.8	2.0	2.3
0.1	0.3	0.9	1.7	2.0	2.2
0.2	0.2	0.9	1.7	1.9	2.2
0.5	0.2	0.8	1.6	1.8	2.0
1	0.2	0.8	1.5	1.7	1.9
2	0.2	0.7	1.4	1.6	1.8
5	0.2	0.6	1.2	1.4	1.6
10	0.2	0.6	1.1	1.3	1.4
20	0.2	0.6	1.0	1.2	1.3
50	0.2	0.6	1.0	1.1	1.2
100	0.3	0.6	1.0	1.1	1.2
200	0.4	0.8	1.1	1.2	1.3
	ratio-S_{ab}				
360	0.5	1.0	1.3	1.4	1.4
500	0.5	0.9	1.3	1.3	1.3
1000	0.5	0.9	1.2	1.2	1.1
2000	0.5	0.9	1.2	1.2	1.1
5000	0.5	0.9	1.2	1.2	1.0

Fig. 5.12, Tables of $U_{ab,4cm\text{-}5}/U_{ab,OBR}$ and $S_{ab,4cm\text{-}5}/S_{ab,OBR}$ for a 3-tissue, fixed-thickness model (Hasgall database) at 6, 10, 20 and 30 GHz versus single-pulse exposure duration and *FWHM*.

averaging area: 4 cm^2

60 GHz, 3-tiss. Hasgall data					
FWHM:	0.005	0.01	0.02	0.03	0.10
td (s)	ratio-U_{ab}				
0.05	0.1	0.5	0.9	1.0	1.2
0.1	0.1	0.5	0.9	1.1	1.2
0.2	0.1	0.5	0.9	1.1	1.2
0.5	0.1	0.5	1.0	1.1	1.3
1	0.1	0.5	1.0	1.1	1.3
2	0.1	0.5	1.0	1.1	1.3
5	0.1	0.5	0.9	1.1	1.2
10	0.2	0.5	0.9	1.0	1.2
20	0.2	0.5	0.9	1.0	1.1
50	0.2	0.5	0.9	1.0	1.1
100	0.2	0.6	0.9	1.0	1.1
200	0.3	0.7	1.0	1.1	1.2
	ratio-S_{ab}				
360	0.4	0.9	1.2	1.3	1.3
500	0.4	0.9	1.2	1.2	1.2
1000	0.4	0.8	1.1	1.1	1.1
2000	0.4	0.8	1.1	1.1	1.0
5000	0.4	0.8	1.1	1.1	1.0

60 GHz, 4-tiss. Sasaki data					
FWHM:	0.005	0.01	0.02	0.03	0.10
td (s)	ratio-U_{ab}				
0.05	0.2	0.5	1.0	1.2	1.4
0.1	0.2	0.5	1.0	1.2	1.3
0.2	0.2	0.5	1.0	1.2	1.3
0.5	0.2	0.5	1.0	1.2	1.3
1	0.2	0.5	1.0	1.2	1.4
2	0.2	0.6	1.1	1.2	1.4
5	0.2	0.6	1.1	1.3	1.4
10	0.2	0.6	1.1	1.3	1.4
20	0.2	0.6	1.1	1.3	1.4
50	0.3	0.7	1.1	1.2	1.3
100	0.3	0.7	1.1	1.3	1.3
200	0.4	0.9	1.3	1.3	1.4
	ratio-S_{ab}				
360	0.5	1.1	1.5	1.5	1.5
500	0.5	1.1	1.4	1.4	1.3
1000	0.5	1.0	1.3	1.3	1.1
2000	0.5	1.0	1.3	1.2	1.0
5000	0.5	1.0	1.2	1.2	1.0

80 GHz, 4-tiss. Sasaki data					
FWHM:	0.005	0.01	0.02	0.03	0.10
td (s)	ratio-U_{ab}				
0.05	0.1	0.5	0.9	1.0	1.2
0.1	0.1	0.5	0.9	1.0	1.2
0.2	0.1	0.5	0.9	1.1	1.2
0.5	0.1	0.5	0.9	1.1	1.2
1	0.1	0.5	1.0	1.1	1.2
2	0.2	0.5	1.0	1.2	1.3
5	0.2	0.5	1.0	1.2	1.3
10	0.2	0.6	1.1	1.2	1.4
20	0.2	0.6	1.1	1.2	1.4
50	0.3	0.6	1.1	1.2	1.3
100	0.3	0.7	1.1	1.2	1.3
200	0.4	0.9	1.2	1.3	1.4
	ratio-S_{ab}				
360	0.5	1.1	1.5	1.5	1.5
500	0.5	1.0	1.4	1.4	1.3
1000	0.5	1.0	1.3	1.3	1.1
2000	0.5	1.0	1.2	1.2	1.0
5000	0.5	1.0	1.2	1.2	1.0

Fig. 5.13, Tables of $U_{ab,4cm\text{-}5}/U_{ab,OBR}$ and $S_{ab,4cm\text{-}5}/S_{ab,OBR}$ for a fixed-thickness, 3-tissue model (Hasgall database) at 60 GHz and a fixed thickness, 4-tissue model (Sasaki database) at 60 and 80 GHz versus single-pulse exposure duration and *FWHM*.

averaging area: 4 cm^2

120 GHz, 4-tiss. Sasaki data					
FWHM:	0.005	0.01	0.02	0.03	0.10
td (s)	ratio-U_{ab}				
0.05	0.1	0.4	0.8	0.9	1.0
0.1	0.1	0.4	0.8	0.9	1.0
0.2	0.1	0.4	0.8	0.9	1.0
0.5	0.1	0.4	0.8	1.0	1.1
1	0.1	0.5	0.9	1.0	1.1
2	0.1	0.5	0.9	1.1	1.2
5	0.2	0.5	1.0	1.2	1.3
10	0.2	0.6	1.0	1.2	1.3
20	0.2	0.6	1.1	1.2	1.3
50	0.2	0.6	1.1	1.2	1.3
100	0.3	0.7	1.1	1.2	1.3
200	0.4	0.9	1.2	1.3	1.4
	ratio-S_{ab}				
360	0.5	1.1	1.4	1.5	1.5
500	0.5	1.0	1.4	1.4	1.3
1000	0.5	1.0	1.3	1.2	1.1
2000	0.5	1.0	1.2	1.2	1.0
5000	0.5	1.0	1.2	1.2	1.0

160 GHz, 4-tiss. Sasaki data					
FWHM:	0.005	0.01	0.02	0.03	0.10
td (s)	ratio-U_{ab}				
0.05	0.1	0.4	0.7	0.8	0.9
0.1	0.1	0.4	0.7	0.8	0.9
0.2	0.1	0.4	0.8	0.9	1.0
0.5	0.1	0.4	0.8	0.9	1.0
1	0.1	0.4	0.9	1.0	1.1
2	0.1	0.5	0.9	1.1	1.2
5	0.2	0.5	1.0	1.1	1.3
10	0.2	0.5	1.0	1.2	1.3
20	0.2	0.6	1.0	1.2	1.3
50	0.2	0.6	1.1	1.2	1.3
100	0.3	0.7	1.1	1.2	1.3
200	0.4	0.9	1.2	1.3	1.4
	ratio-S_{ab}				
360	0.5	1.1	1.4	1.5	1.5
500	0.5	1.0	1.4	1.4	1.3
1000	0.5	1.0	1.3	1.2	1.1
2000	0.5	1.0	1.2	1.2	1.0
5000	0.5	1.0	1.2	1.2	1.0

200 GHz, 4-tiss. Sasaki data					
FWHM:	0.005	0.01	0.02	0.03	0.10
td (s)	ratio-U_{ab}				
0.05	0.1	0.3	0.7	0.8	0.8
0.1	0.1	0.4	0.7	0.8	0.9
0.2	0.1	0.4	0.7	0.8	0.9
0.5	0.1	0.4	0.8	0.9	1.0
1	0.1	0.4	0.8	1.0	1.1
2	0.1	0.5	0.9	1.0	1.1
5	0.2	0.5	1.0	1.1	1.2
10	0.2	0.5	1.0	1.2	1.3
20	0.2	0.6	1.0	1.2	1.3
50	0.2	0.6	1.1	1.2	1.3
100	0.3	0.7	1.1	1.2	1.3
200	0.4	0.9	1.2	1.3	1.4
	ratio-S_{ab}				
360	0.5	1.1	1.4	1.5	1.5
500	0.5	1.0	1.3	1.4	1.3
1000	0.5	1.0	1.3	1.2	1.1
2000	0.5	1.0	1.2	1.2	1.0
5000	0.5	1.0	1.2	1.2	1.0

Fig. 5.14, Tables of $U_{ab,4cm\text{-}5}/U_{ab,OBR}$ and $S_{ab,4cm\text{-}5}/S_{ab,OBR}$ for a fixed thickness, 4-tissue model (Sasaki database) at 120, 160 and 200 GHz versus single-pulse exposure duration and *FWHM*.

5.4.3.2 Spatial averaging area: 1 cm^2:

$$U_{ab,OBR} = 144\left[0.025 + 0.975\sqrt{t_d/360}\right] \quad (kJ/m^2) \quad , \quad S_{ab,OBR} = 400 \quad (W/m^2)$$

averaging area: 1 cm^2

6 GHz, 3-tiss. Hasgall data

FWHM:	0.01	0.02	0.03	0.10
td (s)	ratio-U_{ab}			
0.05	9.3	11.4	11.8	12.2
0.1	8.1	9.9	10.3	10.6
0.2	6.8	8.4	8.7	9.0
0.5	5.3	6.4	6.7	6.9
1	4.3	5.2	5.4	5.6
2	3.4	4.2	4.4	4.5
5	2.6	3.2	3.3	3.4
10	2.2	2.6	2.6	2.7
20	1.8	2.1	2.1	2.2
50	1.5	1.6	1.6	1.7
100	1.5	1.5	1.4	1.4
200	1.6	1.4	1.4	1.3
	ratio-S_{ab}			
360	1.9	1.6	1.4	1.3
500	1.8	1.4	1.3	1.1
1000	1.7	1.3	1.1	0.9
2000	1.7	1.3	1.1	0.8
5000	1.7	1.2	1.1	0.8

10 GHz, 3-tiss. Hasgall data

FWHM:	0.01	0.02	0.03	0.10
td (s)	ratio-U_{ab}			
0.05	4.4	5.4	5.6	5.7
0.1	3.8	4.7	4.9	5.0
0.2	3.3	4.0	4.2	4.3
0.5	2.6	3.2	3.3	3.4
1	2.1	2.6	2.7	2.8
2	1.8	2.2	2.2	2.3
5	1.4	1.7	1.8	1.8
10	1.2	1.4	1.5	1.5
20	1.1	1.2	1.3	1.3
50	1.0	1.1	1.1	1.1
100	1.0	1.0	1.0	1.0
200	1.1	1.0	1.0	0.9
	ratio-S_{ab}			
360	1.4	1.1	1.1	1.0
500	1.3	1.1	1.0	0.9
1000	1.3	1.0	0.9	0.7
2000	1.3	1.0	0.8	0.7
5000	1.3	1.0	0.8	0.6

20 GHz, 3-tiss. Hasgall data

FWHM:	0.01	0.02	0.03	0.10
td (s)	ratio-U_{ab}			
0.05	2.5	3.1	3.2	3.3
0.1	2.3	2.8	2.9	3.0
0.2	2.0	2.4	2.5	2.6
0.5	1.6	1.9	2.0	2.1
1	1.3	1.6	1.7	1.7
2	1.1	1.3	1.4	1.4
5	0.9	1.1	1.1	1.1
10	0.8	0.9	0.9	1.0
20	0.7	0.8	0.8	0.8
50	0.7	0.7	0.7	0.7
100	0.7	0.7	0.7	0.7
200	0.8	0.8	0.7	0.7
	ratio-S_{ab}			
360	1.0	0.9	0.8	0.8
500	1.0	0.8	0.8	0.7
1000	1.0	0.8	0.7	0.6
2000	1.0	0.8	0.7	0.6
5000	1.0	0.8	0.7	0.5

30 GHz, 3-tiss. Hasgall data

FWHM:	0.005	0.01	0.02	0.03	0.1
td (s)	ratio-U_{ab}				
0.05	0.8	1.5	1.8	1.9	1.9
0.1	0.7	1.4	1.7	1.8	1.8
0.2	0.7	1.3	1.5	1.6	1.7
0.5	0.6	1.1	1.3	1.4	1.4
1	0.5	1.0	1.2	1.2	1.3
2	0.5	0.8	1.0	1.1	1.1
5	0.4	0.7	0.9	0.9	0.9
10	0.4	0.6	0.8	0.8	0.8
20	0.4	0.6	0.7	0.7	0.7
50	0.4	0.6	0.6	0.6	0.6
100	0.5	0.6	0.6	0.6	0.6
200	0.6	0.8	0.7	0.7	0.6
	ratio-S_{ab}				
360	0.8	0.9	0.8	0.8	0.7
500	0.8	0.9	0.8	0.7	0.6
1000	0.8	0.9	0.7	0.7	0.6
2000	0.8	0.9	0.7	0.6	0.5
5000	0.8	0.9	0.7	0.6	0.5

Fig. 5.15, Tables of $U_{ab,1cm\text{-}5}/U_{ab,OBR}$ and $S_{ab,1cm\text{-}5}/S_{ab,OBR}$ for a 3-tissue, fixed-thickness model (Hasgall database) at 6, 10, 20 and 30 GHz versus single-pulse exposure duration and *FWHM*.

averaging area: 1 cm^2

60 GHz, 3-tiss. Hasgall data

FWHM:	0.005	0.01	0.02	0.03	0.10
td (s)	ratio-U_{ab}				
0.05	0.4	0.8	0.9	1.0	1.0
0.1	0.4	0.7	0.9	0.9	1.0
0.2	0.4	0.7	0.9	0.9	0.9
0.5	0.3	0.7	0.8	0.9	0.9
1	0.3	0.6	0.8	0.8	0.8
2	0.3	0.6	0.7	0.8	0.8
5	0.3	0.6	0.7	0.7	0.7
10	0.3	0.5	0.6	0.6	0.7
20	0.3	0.5	0.6	0.6	0.6
50	0.4	0.5	0.6	0.6	0.6
100	0.4	0.6	0.6	0.6	0.6
200	0.6	0.7	0.6	0.6	0.6
	ratio-S_{ab}				
360	0.7	0.9	0.8	0.7	0.7
500	0.7	0.8	0.7	0.7	0.6
1000	0.7	0.8	0.7	0.6	0.5
2000	0.7	0.8	0.7	0.6	0.5
5000	0.7	0.8	0.7	0.6	0.5

60 GHz, 4-tiss. Sasaki data

FWHM:	0.005	0.01	0.02	0.03	0.10
td (s)	ratio-U_{ab}				
0.05	0.5	0.9	1.1	1.1	1.2
0.1	0.4	0.8	1.0	1.1	1.1
0.2	0.4	0.8	1.0	1.0	1.0
0.5	0.4	0.7	0.9	0.9	0.9
1	0.4	0.7	0.8	0.9	0.9
2	0.4	0.7	0.8	0.8	0.9
5	0.4	0.6	0.8	0.8	0.8
10	0.4	0.6	0.8	0.8	0.8
20	0.4	0.6	0.7	0.7	0.8
50	0.5	0.7	0.7	0.7	0.7
100	0.6	0.7	0.7	0.7	0.7
200	0.7	0.9	0.8	0.7	0.7
	ratio-S_{ab}				
360	1.0	1.1	0.9	0.8	0.7
500	0.9	1.0	0.8	0.8	0.7
1000	0.9	1.0	0.8	0.7	0.6
2000	0.9	1.0	0.8	0.7	0.5
5000	0.9	1.0	0.8	0.7	0.5

80 GHz, 4-tiss. Sasaki data

FWHM:	0.005	0.01	0.02	0.03	0.10
td (s)	ratio-U_{ab}				
0.05	0.4	0.7	0.9	1.0	1.0
0.1	0.4	0.7	0.9	0.9	0.9
0.2	0.4	0.7	0.8	0.9	0.9
0.5	0.3	0.6	0.8	0.8	0.8
1	0.3	0.6	0.8	0.8	0.8
2	0.3	0.6	0.8	0.8	0.8
5	0.3	0.6	0.7	0.8	0.8
10	0.4	0.6	0.7	0.8	0.8
20	0.4	0.6	0.7	0.7	0.7
50	0.5	0.6	0.7	0.7	0.7
100	0.6	0.7	0.7	0.7	0.7
200	0.7	0.8	0.8	0.7	0.7
	ratio-S_{ab}				
360	0.9	1.0	0.9	0.8	0.7
500	0.9	1.0	0.8	0.8	0.7
1000	0.9	1.0	0.8	0.7	0.6
2000	0.9	1.0	0.8	0.7	0.5
5000	0.9	1.0	0.8	0.7	0.5

Fig. 5.16, Tables of $U_{ab,1cm\text{-}5}/U_{ab,OBR}$ and $S_{ab,1cm\text{-}5}/S_{ab,OBR}$ for a fixed-thickness, 3-tissue model (Hasgall database) at 60 GHz and a fixed thickness, 4-tissue model (Sasaki database) at 60 and 80 GHz versus single-pulse exposure duration and *FWHM*.

averaging area: 1 cm^2

120 GHz, 4-tiss. Sasaki data

FWHM:	0.005	0.01	0.02	0.03	0.10
td (s)	ratio-U_{ab}				
0.05	0.3	0.6	0.8	0.8	0.8
0.1	0.3	0.6	0.8	0.8	0.8
0.2	0.3	0.6	0.7	0.8	0.8
0.5	0.3	0.6	0.7	0.8	0.8
1	0.3	0.6	0.7	0.7	0.8
2	0.3	0.6	0.7	0.7	0.8
5	0.3	0.6	0.7	0.7	0.8
10	0.3	0.6	0.7	0.7	0.7
20	0.4	0.6	0.7	0.7	0.7
50	0.5	0.6	0.7	0.7	0.7
100	0.6	0.7	0.7	0.7	0.7
200	0.7	0.8	0.8	0.7	0.7
	ratio-S_{ab}				
360	0.9	1.0	0.9	0.8	0.7
500	0.9	1.0	0.8	0.8	0.7
1000	0.9	1.0	0.8	0.7	0.6
2000	0.9	1.0	0.8	0.7	0.5
5000	0.9	1.0	0.8	0.7	0.5

160 GHz, 4-tiss. Sasaki data

FWHM:	0.005	0.01	0.02	0.03	0.10
td (s)	ratio-U_{ab}				
0.05	0.3	0.6	0.7	0.8	0.8
0.1	0.3	0.6	0.7	0.7	0.8
0.2	0.3	0.6	0.7	0.7	0.7
0.5	0.3	0.6	0.7	0.7	0.7
1	0.3	0.6	0.7	0.7	0.7
2	0.3	0.6	0.7	0.7	0.7
5	0.3	0.6	0.7	0.7	0.7
10	0.3	0.6	0.7	0.7	0.7
20	0.4	0.6	0.7	0.7	0.7
50	0.4	0.6	0.7	0.7	0.7
100	0.5	0.7	0.7	0.7	0.7
200	0.7	0.8	0.8	0.7	0.7
	ratio-S_{ab}				
360	0.9	1.0	0.9	0.8	0.7
500	0.9	1.0	0.8	0.8	0.7
1000	0.9	1.0	0.8	0.7	0.6
2000	0.9	1.0	0.8	0.7	0.5
5000	0.9	1.0	0.8	0.7	0.5

200 GHz, 4-tiss. Sasaki data

FWHM:	0.005	0.01	0.02	0.03	0.10
td (s)	ratio-U_{ab}				
0.05	0.3	0.5	0.7	0.7	0.7
0.1	0.3	0.5	0.7	0.7	0.7
0.2	0.3	0.5	0.7	0.7	0.7
0.5	0.3	0.5	0.7	0.7	0.7
1	0.3	0.5	0.7	0.7	0.7
2	0.3	0.6	0.7	0.7	0.7
5	0.3	0.6	0.7	0.7	0.7
10	0.3	0.6	0.7	0.7	0.7
20	0.4	0.6	0.7	0.7	0.7
50	0.4	0.6	0.7	0.7	0.7
100	0.5	0.7	0.7	0.7	0.7
200	0.7	0.8	0.8	0.7	0.7
	ratio-S_{ab}				
360	0.9	1.0	0.9	0.8	0.7
500	0.9	1.0	0.8	0.8	0.7
1000	0.9	1.0	0.8	0.7	0.6
2000	0.9	0.9	0.8	0.7	0.5
5000	0.9	0.9	0.8	0.7	0.5

Fig. 5.17, Tables of $U_{ab,1cm\text{-}5}/U_{ab,OBR}$ and $S_{ab,1cm\text{-}5}/S_{ab,OBR}$ for a fixed thickness, 4-tissue model (Sasaki database) at 120, 160 and 200 GHz versus single-pulse exposure duration and *FWHM*.

5.4.3.3 Discussion – single pulse exposures and ICNIRP OBRs

In Figs. 5.12 to 5.17, it is seen that the OBRs are increasingly non-conservative as the beam diameter or spot size decreases. This is especially pronounced for the 4 cm^2-averaged data at frequencies above 30 GHz. For AED (exposure durations < 360 s), it can generally be stated (with some exceptions) that the degree of non-conservatism increases as the beam diameter decreases and the exposure duration diminishes. This is due to the effect illustrated in the example of Figs. 5.9 and 5.10, whereby the TR was found to be independent of beam diameter for durations shorter than a few seconds. The effect of spatial averaging a narrow beam at short durations is that it produces an artificially low net energy density that does not reflect its actual potential to produce TR.

The APD OBRs do not appear to suffer from the same non-conservatism as the AED OBRs, especially for the $S_{ab,OBR}$ = 200 W/m^2 limit. The greater conservatism of this limit over the limit which is averaged over 1cm^2 (400 W/m^2) raises the question of the necessity of the latter.

5.4.4 Isolated groups of pulses

An example of the TR response from an isolated group of pulses is shown in Fig. 5.18 for a wide-beam exposing the fixed thickness, 3-tissue model at 30 GHz. The pulse width is t_{ON} = 1s and pulse heights have an APD of 7200 W/m^2, resulting in an AED of 7.2 kJ/m^2 for each pulse and a total AED of 28.8 kJ/m^2 for the group. The TR dynamics exhibit alternate periods of heating during the pulse ON periods then cooling over the pulse OFF periods.

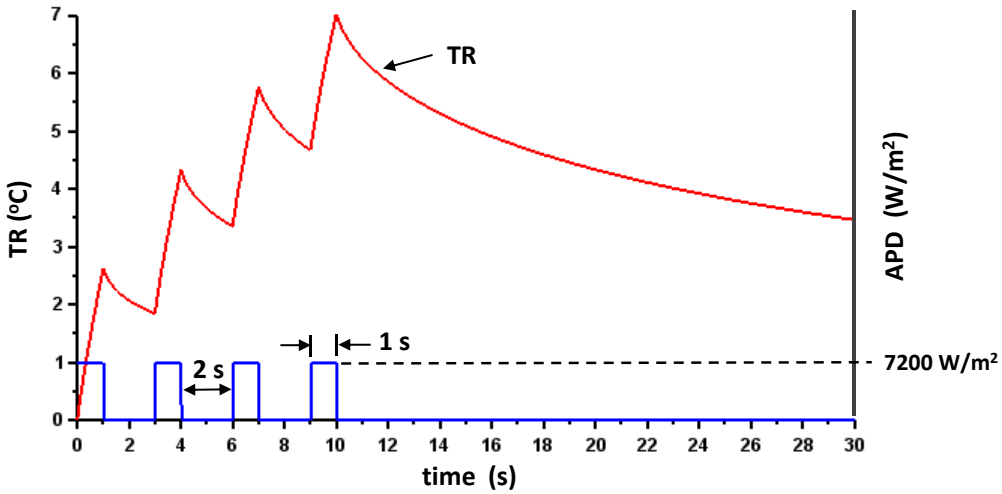

Fig. 5.18, TR versus time for a wide-beam, 4-pulse group incident on the fixed thickness, 3-tissue model at 30 GHz.

The first pulse produces a TR of 2.5 °C while the resulting TR after the fourth pulse is 7 °C. The initial rate of cooling is much slower than the heating rate and results in the buildup of TR after the end of the group.

5.4.4.1 Exposure duration of an isolated group of pulses

The AED basic restrictions for an isolated group of pulses are, in principle, the same as for a single isolated pulse and are given by eqns (5.1) or (5.2). However, it is not immediately obvious what to use as the exposure duration, t_d, in the calculation. Table 3 - Note 5 of the ICNIRP 2020 guideline states: "*Exposure from any pulse, group of pulses, or subgroup of pulses in a train, as well as from the summation of exposures (including non-pulsed EMF), delivered in t_d seconds, must not exceed these levels*" where the levels referred to are the occupational and general public limits derivable from the OBRs in Table 5.1.

If the statement in Table 3 - Note 5 is written as a condition, it would take the form (e.g. for the 4 cm^2 spatially averaged case):

$$\int_{t_o}^{t_o+\Delta t} S_{ab,4cm}(t)dt \leq 72\left[0.05 + 0.95\sqrt{\Delta t/360}\right] \tag{5.4}$$

where the left-hand side is a 4cm^2-averaged AED found by integrating $S_{ab,4cm}(t)$ over any possible time interval, Δt, ranging from 0 s to the reference period, 360 s, and starting at an arbitrary time, t_o. In principle, this condition would be evaluated for all values of Δt that would include single pulses, pairs of adjacent pulses and their inter-pulse periods and all other possible combinations of sub-groups in the group (including the whole group). Since all combinations must meet the condition of eqn (5.4), the lowest pulse

height (in terms of $S_{ab,4cm}$) found amongst the different combinations defines the maximum allowable APD by the ICNIRP (2020) Note 5.

Appendix D.7 provides examples of the implementation of this procedure for evenly spaced, 2-pulse, 3-pulse and *N*-pulse groups. As seen in the appendix, carrying out this procedure requires significant computation time, even for a small number of pulses in a group. In addition to calculating maximum allowable pulse heights for the groups, TRs calculated for the fixed-thickness, 3-tissue model at 30 and 60 GHz are given. The outcome of these examples is that the resulting worst-case TRs of the group could be up to 50 % higher than the TRs obtained for an exposure of a single isolated pulse with both the group and the single pulse being at their maximum allowable pulse heights.

Such increases in TR, by the implementation of the Note 5 procedure, are undesirable for exposure conditions where the margin of conservatism of the OBRs are already small for a single isolated pulse. An alternative and conservative approach is to define the exposure duration for isolated groups of pulses to include only the ON times of pulses or periods of non-zero exposure. This will be given the term "Total ON Time" (TOT).

This approach for defining the exposure duration is preferable as it can be argued that if the AED OBR is conservative for a single isolated pulse of width t_d, then it will be even more conservative if t_d is divided into 2 or more sub-periods (pulse widths) because of the cooling that takes place in the intervening inter-pulse periods. This is illustrated in Fig. 5.19 where the TRs (same tissue model, frequency and beam size of Fig. 5.18) are calculated for different 2-pulse groups having constant pulse height and AED (only the inter-pulse periods are varied).

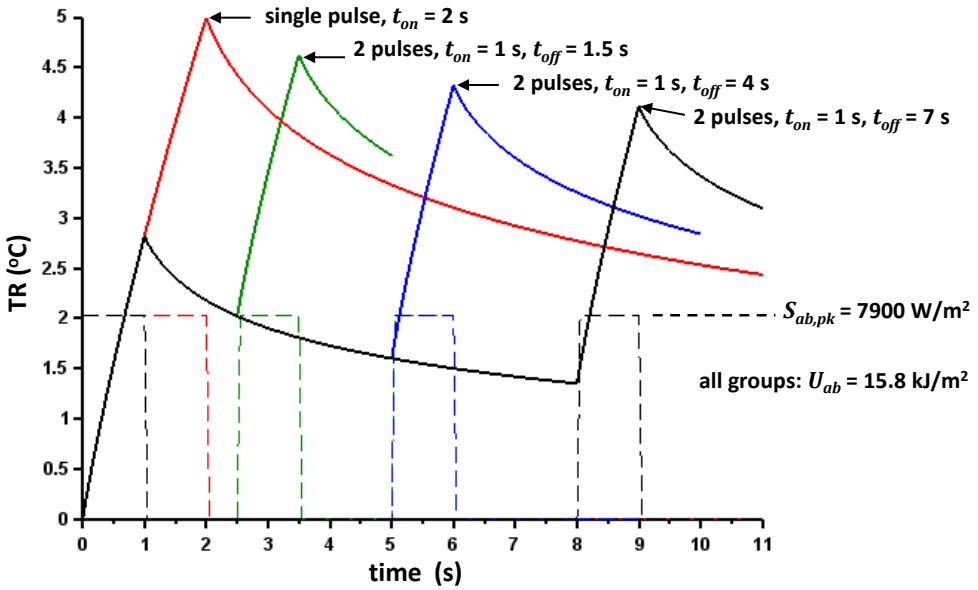

Fig. **5.19**, TR versus time for wide-beam exposures on a 3-tissue, fixed thickness (Hasgall database) configuration at 30 GHz. All pulse groups have the same TOT of 2 s and net AED.

As Fig. 5.19 illustrates, the worst-case TR occurs when all of the EM energy is contained in a single pulse. This has important implications when considering continuous pulse trains and the conditions that maximize their worst-case TRs.

Since, under this new definition of the exposure duration (i.e. t_d = TOT), an isolated single pulse produces higher TR than isolated groups of pulses of the same total AED, there is no need to test the conservatism of the AED OBRs for the latter. As such, the comparison results in Section 5.4.3 stand as the worst case for isolated exposures.

5.5 Continuous Pulse Trains

5.5.1 TR response to pulsed exposure

Continuous trains of pulses represent an exposure condition that has both a transient and a SS component. In the SS, pulse trains produce TR oscillations super-imposed on a constant TR. Pulse trains with very low duty factor (or high peak-to-average ratio) can produce high peak TR in the SS (depending on pulse width) while others produce relatively small TR oscillation. For the former, AED limits are necessary for restricting these high peak TRs.

An example of an oscillatory TR response is shown in Fig. 5.20. The tissue is exposed to a wide-beam at 30 GHz where the spatial peak (and temporal peak) APD is adjusted to produce 5 ^{o}C TR after the 5th pulse (a minimum of 5 pulses are necessary to reach within 95% of the SS peak TR). The pulse train has a 1s pulse ON time and a 59 s pulse OFF time and a period of 60 s.

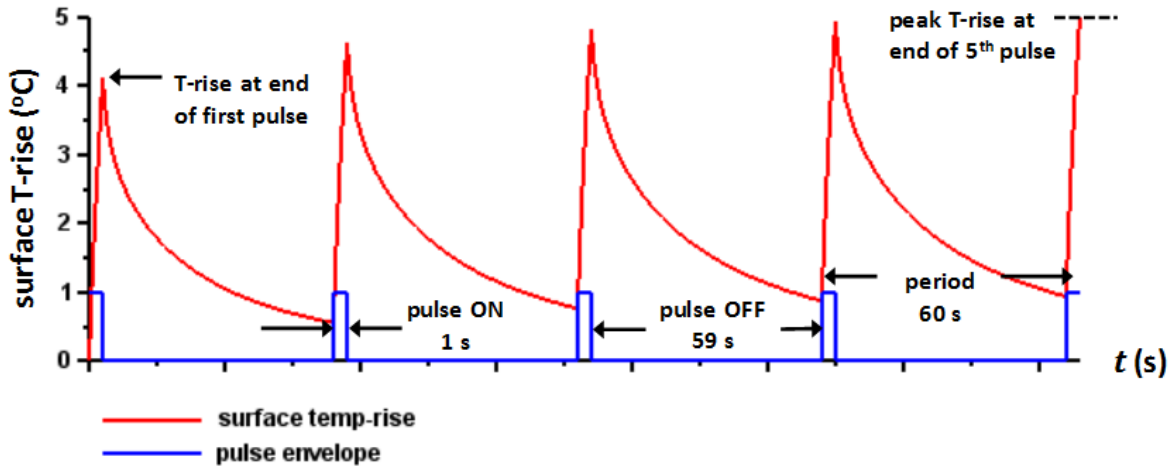

Fig. 5.20, TR response of a 3-tissue model (skin: 0.6 mm, SAT: 6 mm, muscle: 43 mm) to a continuous pulse train of 1 s pulse width and 60 s period, wide beam at 30 GHz.

In the example, the TR oscillations consist of a 1s rise in temperature (heating during the pulse) followed by a 59 s temperature drop (cooling period). The temperature response to a continuous train of pulsed RF is influenced by the following:

1. In the electromagnetic model, RF power deposition is greatest at the surface and decays with depth in the tissues. Similarly, for the thermal model, temperature elevation is generally greatest at the surface and also decreases with depth (recall that the term "TR" refers to the temperature rise at the surface). (Note also that in the absence of RF exposure, absolute temperature is lower at the surface and increases with depth, e.g. skin surface temperatures are normally around 32-33 ^{o}C while the temperature of deep tissue is close to 37 ^{o}C.)
2. During a pulse, the rate of TR in the tissue is dependent on the temporal peak APD, spot size of the beam (FWHM) and by the thermal and physical properties of the tissue. For very short pulses, where diffusion and perfusion have insufficient time to remove heat, the rate of TR is almost linear.
3. During the cooling period (pulse OFF), the rate of surface cooling is determined by the thermal/ physical properties of the tissue and the amount of heat energy that has been transported into the deeper tissues during the preceding pulses.

For the first few TR periods in Fig 5.20, the rate of TR increase is largely determined by the peak APD and spot size. The rate of drop is primarily determined by the natural rate of cooling since little build-up of heat in the tissues has occurred. This can be seen better in Fig. 5.21 where during the early phase of exposure to a 50 % duty cycle pulse train, the rate of temperature-drop is slower than the rate of temperature-rise.

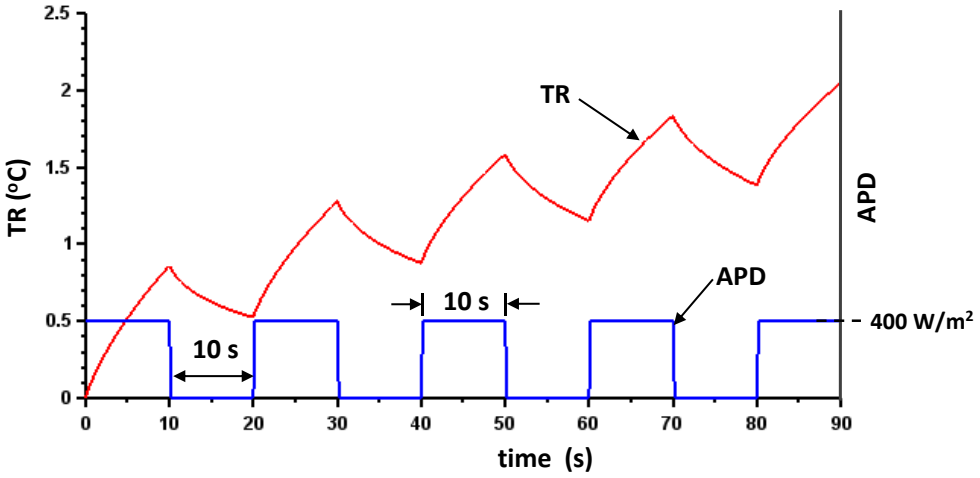

Fig. 5.21, TR response after the application of a 50 % duty factor pulse train (wide beam) at 30 GHz to the 3-tissue model. The time averaged APD is set to the OBR of 200 W/m^2.

The lower initial rate of cooling means that the temperature does not return to its starting value at the beginning of the next pulse. Early in the process, each successive pulse leads to a higher resulting TR than the previous one due to the slower rate of cooling as compared to the rate of heating.

As the process continues, the rate of cooling gradually increases while the rate of heating decreases because heat diffusion and heat transport by blood perfusion increases with the higher temperature gradient and TR respectively. This eventually leads to a steady state where the rate of cooling and heating are equal and there is no additional increase in the peak TR from one pulse to another. As a result, a steady-state TR oscillation is formed that is superimposed on a constant TR. This is shown in Fig. 5.22 for the same exposure conditions as Fig. 5.21, but at a much later time in the process.

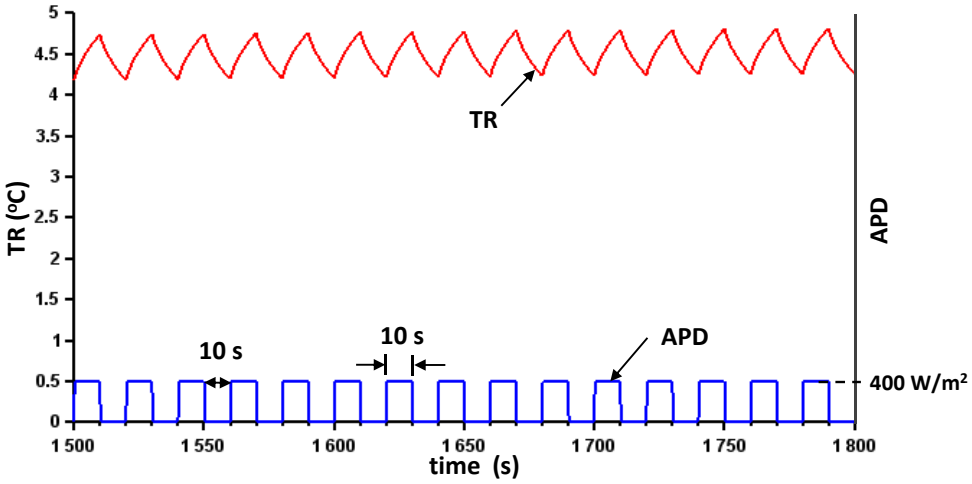

Fig. 5.22, SS TR response due to a 50 % duty factor pulse train (wide beam) at 30 GHz applied to the 3-tissue model.

5.5.1.1 Time-averaged TR

The TR responses of pulsed (50% Duty Factor) and CW exposures (both wide beam) on the 3-tissue model at 30 GHz is shown in Fig. 5.23. Both exposures have the same time averaged APD of 200 W/m^2 as prescribed by the OBR for a 4 cm^2 spatial average.

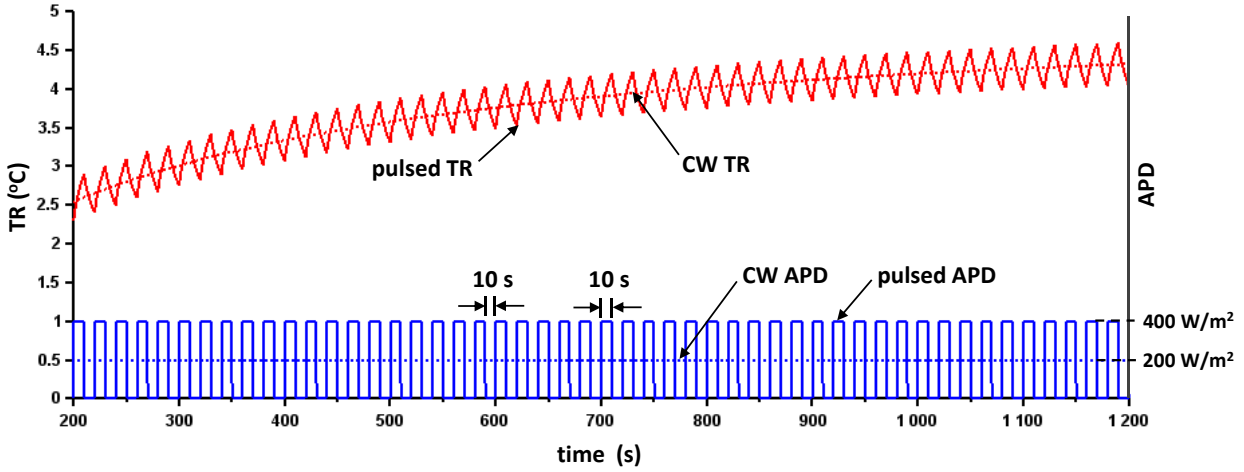

Fig. 5.23, TR response from a 50 % DF pulse train and CW at 30 GHz on the 3-tissue model (both wide beam). Both exposures are of the same time averaged APD of 200 W/m^2.

In Fig. 5.23, the time-averaged TR (averaged over 1 cycle) of the pulsed response increases with time identically to the TR due to a "step" application of CW. (In formal terms, the TR responses in Fig. 5.23 can be referred to as "step" responses where the "step" refers to the Heaviside unit step function, $H(t)$. Therefore, for the CW response, the time-dependent function of SAR is given by $SAR(t, r, z) = H(t)\, SAR(r, z)$.)

If the time-averaged TR of the pulsed response (averaged over a period) is compared to the response of a CW exposure at an APD value equal to the time-averaged pulsed exposure, it is seen that both have the same rise times and TR values once the SS is reached. It can be shown that the SS, time-averaged TR of the pulsed response is always equal to the CW SS TR for equal time-averaged APDs. (This statement would also apply to time averaged SARs since SAR and APD are linearly related.)

5.5.4 General results – Continuous pulse trains

For isolated groups of pulses with AEDs equal to the OBR (using the TOT as the exposure duration), the highest transient TRs are realized when the energy was confined to a single pulse in a reference period. For continuous pulse trains, this same conclusion holds if the exposure duration in the AED OBR is also taken to be the TOT in any 6-minute reference period. Verification of this is given in Appendix D.3, which also highlights the pulse widths and spacings that result in significant TR oscillation relative to the time-averaged TR (i.e. trains with high peak-to-average power).

The 3-tissue, model (Hasgall database) was used for frequencies of 6-60 GHz while the 4-tissue model (Sasaki database) was used for frequencies of 60 – 200 GHz. At all frequencies, spot sizes of FWHM = 1, 2, 3 cm were used in the 3D BHTE solutions while for wide beams (i.e. $FWHM > 10$ cm), the 1D BHTE was used. In addition, at 30 GHz and above, computations for a spot-size of $FWHM = 0.5$ cm were also carried out. For the purpose of narrow-beam spatial averaging, beam diameters given by $HPBD = FWHM/0.8$ were assumed for all cases.

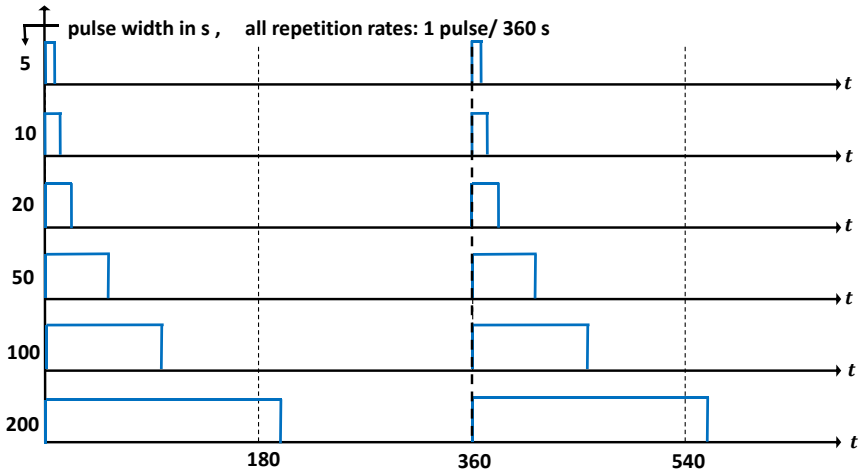

Fig. 5.24, Examples of the first two periods of some of the continuous pulse trains used for testing the ICNIRP (2020) AED and APD OBRs.

The computed SS TRs considered in the assessment of continuous pulse trains were the temporal peak values occurring after 5 pulses, which was determined to approximate the SS value (see Appendix D.3 for more details). TRs were normalized to the spatially-averaged values of total AED in 360 s and the time-averaged, APD (averaged over 360 s) to produce the ratios: $\Delta T/U_{ab,Xcm}$ and $\Delta T/S_{ab,Xcm}$, where the subscript "*X*" can take on the symbols "4" or "1" to denote whether the power and energy densities were spatially averaged over 4 cm^2 or 1 cm^2 square areas, respectively.

The evaluation metrics, i.e. the total AED in 360s or the time-averaged APD that produces 5 °C temporal-peak, TR, were calculated using eqn (5.3) (repeated below):

$$U_{ab,Xcm-5} = \frac{5}{\left(\Delta T / U_{ab,Xcm}\right)} \qquad or \qquad S_{ab,Xcm-5} = \frac{5}{\left(\Delta T / S_{ab,Xcm}\right)} \tag{5.3}$$

The metrics in eqn (5.3) were compared to their corresponding OBRs in Table 5.1 by forming the ratios of $U_{ab,Xcm-5}$ and $S_{ab,Xcm-5}$ to their respective OBR. Ratios greater than unity signify that the OBR is conservative with respect to the specific exposure conditions (e.g. frequency, exposure duration, spot size, tissue model, etc.) that gave rise to the evaluation metric. Results for both metrics, $U_{ab,Xcm-5}$ and $S_{ab,Xcm-5}$, are given since continuous pulse trains produce both a peak and time average TR.

The results are presented in the form of colour-coded tables according to the scheme in Table 5.3 (repeated below for convenience).

Table 5. 3, Colour code for evaluation table entries.

Range of ratio: $U_{ab\text{-}5\text{-}x}/U_{ab,OBR}$ or $S_{ab\text{-}5\text{-}x}/S_{ab,OBR}$	colour	TR for an exposure at the OBR	TR for an exposure at the general public limit	TR for an exposure at the occupational limit
ratio ≥ 1.0	blue	$\Delta T \leq 5$ °C	$\Delta T \leq 0.5$ °C	$\Delta T \leq 2.5$ °C
0.50 ≤ ratio < 1.0	green	5 °C < $\Delta T \leq 10$ °C	0.5 °C < $\Delta T \leq 1.0$ °C	2.5 °C < $\Delta T \leq 5.0$ °C
0.25 ≤ ratio < 0.50	yellow	10 °C < $\Delta T \leq 20$ °C	1.0 °C < $\Delta T \leq 2.0$ °C	5.0 °C < $\Delta T \leq 10$ °C
ratio < 0.25	red	20 °C < ΔT	2.0 °C < ΔT	10 °C < ΔT

5.5.3.1 Results - 4 cm² spatial average:

$$U_{ab,OBR} = 72\left[0.05 + 0.95\sqrt{t_d/360}\right] \quad (kJ/m^2) \quad , \quad S_{ab,OBR} = 200 \quad (W/m^2)$$

6 GHz, 3-tiss. Hasgall data

	ratio-U_{ab}				ratio-S_{ab}			
FWHM:	0.01	0.02	0.03	0.10	0.01	0.02	0.03	0.10
td (s)								
0.05	5.5	10.1	11.2	11.6	0.3	0.6	0.7	0.7
0.1	5.1	9.2	10.3	10.6	0.3	0.6	0.7	0.7
0.2	4.5	8.2	9.2	9.4	0.3	0.6	0.7	0.7
0.5	3.8	6.8	7.6	7.8	0.3	0.6	0.6	0.7
1	3.2	5.9	6.5	6.7	0.3	0.6	0.7	0.7
2	2.8	5.0	5.5	5.6	0.3	0.6	0.7	0.7
5	2.3	4.0	4.4	4.5	0.4	0.6	0.7	0.7
10	1.9	3.3	3.7	3.7	0.4	0.7	0.8	0.8
20	1.7	2.8	3.0	3.0	0.5	0.8	0.8	0.8
50	1.4	2.2	2.4	2.3	0.6	0.9	1.0	0.9
100	1.4	2.0	2.0	1.9	0.8	1.1	1.1	1.0
200	1.5	1.9	1.9	1.7	1.2	1.5	1.4	1.3

10 GHz, 3-tiss. Hasgall data

	ratio-U_{ab}				ratio-S_{ab}			
FWHM:	0.01	0.02	0.03	0.10	0.01	0.02	0.03	0.10
td (s)								
0.05	2.6	5.0	5.7	6.1	0.2	0.3	0.3	0.4
0.1	2.4	4.6	5.2	5.6	0.2	0.3	0.3	0.4
0.2	2.2	4.1	4.7	5.0	0.2	0.3	0.3	0.4
0.5	1.9	3.5	4.0	4.3	0.2	0.3	0.3	0.4
1	1.6	3.1	3.5	3.7	0.2	0.3	0.3	0.4
2	1.4	2.7	3.0	3.2	0.2	0.3	0.4	0.4
5	1.2	2.2	2.5	2.7	0.2	0.4	0.4	0.4
10	1.1	2.0	2.2	2.3	0.2	0.4	0.5	0.5
20	1.0	1.7	1.9	2.0	0.3	0.5	0.5	0.5
50	0.9	1.5	1.6	1.6	0.4	0.6	0.7	0.7
100	1.0	1.4	1.5	1.4	0.5	0.8	0.8	0.8
200	1.1	1.4	1.4	1.3	0.8	1.1	1.1	1.0

Fig. 5.25, Tables of $U_{ab,4cm\text{-}5}/U_{ab,OBR}$ (ratio- U_{ab}) and $S_{ab,4cm\text{-}5}/S_{ab,OBR}$ (ratio- S_{ab}) for a fixed thickness, 3-tissue model (Hasgall database) exposed to a continuous pulse train at 6 and 10 GHz versus exposure duration (i.e. TOT in the reference period) and FWHM.

20 GHz, 3-tiss. Hasgall data

	ratio-U_{ab}				ratio-S_{ab}			
FWHM:	0.01	0.02	0.03	0.10	0.01	0.02	0.03	0.10
td (s)								
0.05	1.5	2.9	3.4	3.7	0.1	0.2	0.2	0.2
0.1	1.4	2.7	3.2	3.4	0.1	0.2	0.2	0.2
0.2	1.3	2.5	2.9	3.2	0.1	0.2	0.2	0.2
0.5	1.2	2.2	2.5	2.7	0.1	0.2	0.2	0.2
1	1.0	1.9	2.2	2.4	0.1	0.2	0.2	0.2
2	0.9	1.7	1.9	2.1	0.1	0.2	0.2	0.3
5	0.8	1.4	1.6	1.8	0.1	0.2	0.3	0.3
10	0.7	1.3	1.4	1.5	0.1	0.3	0.3	0.3
20	0.7	1.2	1.3	1.4	0.2	0.3	0.4	0.4
50	0.6	1.1	1.2	1.2	0.3	0.4	0.5	0.5
100	0.7	1.0	1.1	1.1	0.4	0.6	0.6	0.6
200	0.8	1.1	1.1	1.1	0.6	0.8	0.9	0.8

30 GHz, 3-tiss. Hasgall data

	ratio-U_{ab}					ratio-S_{ab}				
FWHM:	0.005	0.01	0.02	0.03	0.1	0.005	0.01	0.02	0.03	0.1
td (s)										
0.05	0.3	0.9	1.7	2.0	2.2	0.0	0.1	0.1	0.1	0.1
0.1	0.3	0.9	1.7	1.9	2.1	0.0	0.1	0.1	0.1	0.1
0.2	0.2	0.9	1.6	1.9	2.1	0.0	0.1	0.1	0.1	0.1
0.5	0.2	0.8	1.5	1.8	1.9	0.0	0.1	0.1	0.1	0.2
1	0.2	0.8	1.4	1.6	1.8	0.0	0.1	0.1	0.2	0.2
2	0.2	0.7	1.3	1.5	1.6	0.0	0.1	0.2	0.2	0.2
5	0.2	0.6	1.2	1.3	1.4	0.0	0.1	0.2	0.2	0.2
10	0.2	0.6	1.1	1.2	1.3	0.0	0.1	0.2	0.3	0.3
20	0.2	0.6	1.0	1.1	1.2	0.1	0.2	0.3	0.3	0.3
50	0.2	0.6	0.9	1.0	1.1	0.1	0.2	0.4	0.4	0.4
100	0.3	0.6	0.9	1.0	1.0	0.2	0.3	0.5	0.6	0.6
200	0.4	0.7	1.0	1.0	1.0	0.3	0.6	0.8	0.8	0.8

Fig. 5.26, Tables of $U_{ab,4cm\text{-}5}/U_{ab,OBR}$ (ratio- U_{ab}) and $S_{ab,4cm\text{-}5}/S_{ab,OBR}$ (ratio- S_{ab}) for a fixed thickness, 3-tissue model (Hasgall database) exposed to a continuous pulse train at 20 and 30 GHz versus exposure duration (i.e. TOT in the reference period) and FWHM.

60 GHz, 3-tiss. Hasgall data

	ratio-U_{ab}					ratio-S_{ab}				
FWHM:	0.005	0.01	0.02	0.03	0.10	0.005	0.01	0.02	0.03	0.10
td (s)										
0.05	0.1	0.5	0.9	1.0	1.1	0.0	0.0	0.1	0.1	0.1
0.1	0.1	0.5	0.9	1.0	1.2	0.0	0.0	0.1	0.1	0.1
0.2	0.1	0.5	0.9	1.1	1.2	0.0	0.0	0.1	0.1	0.1
0.5	0.1	0.5	0.9	1.1	1.2	0.0	0.0	0.1	0.1	0.1
1	0.1	0.5	1.0	1.1	1.2	0.0	0.1	0.1	0.1	0.1
2	0.1	0.5	1.0	1.1	1.2	0.0	0.1	0.1	0.1	0.1
5	0.1	0.5	0.9	1.0	1.1	0.0	0.1	0.1	0.2	0.2
10	0.2	0.5	0.9	1.0	1.1	0.0	0.1	0.2	0.2	0.2
20	0.2	0.5	0.8	0.9	1.0	0.0	0.1	0.2	0.3	0.3
50	0.2	0.5	0.8	0.9	1.0	0.1	0.2	0.3	0.4	0.4
100	0.2	0.6	0.9	0.9	0.9	0.1	0.3	0.5	0.5	0.5
200	0.3	0.7	0.9	1.0	0.9	0.2	0.5	0.7	0.7	0.7

60 GHz, 4-tiss. Sasaki data

	ratio-U_{ab}					ratio-S_{ab}				
FWHM:	0.005	0.01	0.02	0.03	0.10	0.005	0.01	0.02	0.03	0.10
td (s)										
0.05	0.2	0.5	1.0	1.2	1.3	0.0	0.0	0.1	0.1	0.1
0.1	0.2	0.5	1.0	1.2	1.3	0.0	0.0	0.1	0.1	0.1
0.2	0.2	0.5	1.0	1.2	1.3	0.0	0.0	0.1	0.1	0.1
0.5	0.2	0.5	1.0	1.2	1.3	0.0	0.0	0.1	0.1	0.1
1	0.2	0.5	1.0	1.2	1.3	0.0	0.1	0.1	0.1	0.1
2	0.2	0.5	1.0	1.2	1.3	0.0	0.1	0.1	0.1	0.2
5	0.2	0.6	1.1	1.2	1.3	0.0	0.1	0.2	0.2	0.2
10	0.2	0.6	1.1	1.2	1.3	0.0	0.1	0.2	0.2	0.3
20	0.2	0.6	1.0	1.2	1.2	0.1	0.2	0.3	0.3	0.3
50	0.3	0.6	1.0	1.1	1.1	0.1	0.3	0.4	0.4	0.5
100	0.3	0.7	1.0	1.1	1.1	0.2	0.4	0.6	0.6	0.6
200	0.4	0.8	1.1	1.1	1.0	0.3	0.6	0.8	0.8	0.8

Fig. 5.27, Tables of $U_{ab,4cm\text{-}5}/U_{ab,OBR}$ (ratio- U_{ab}) and $S_{ab,4cm\text{-}5}/S_{ab,OBR}$ (ratio- S_{ab}) for a fixed thickness model (3-tissue, Hasgall database left, 4-tissue, Sasaki database right) exposed to a continuous pulse train at 60 GHz versus exposure duration (i.e. TOT in the reference period) and FWHM.

80 GHz, 4-tiss. Sasaki data

	ratio-U_{ab}					ratio-S_{ab}				
FWHM:	0.005	0.01	0.02	0.03	0.10	0.005	0.01	0.02	0.03	0.10
td (s)										
0.05	0.1	0.5	0.9	1.0	1.1	0.0	0.0	0.1	0.1	0.1
0.1	0.1	0.5	0.9	1.0	1.1	0.0	0.0	0.1	0.1	0.1
0.2	0.1	0.5	0.9	1.0	1.1	0.0	0.0	0.1	0.1	0.1
0.5	0.1	0.5	0.9	1.1	1.2	0.0	0.0	0.1	0.1	0.1
1	0.1	0.5	0.9	1.1	1.2	0.0	0.0	0.1	0.1	0.1
2	0.2	0.5	1.0	1.1	1.2	0.0	0.1	0.1	0.1	0.1
5	0.2	0.5	1.0	1.1	1.2	0.0	0.1	0.2	0.2	0.2
10	0.2	0.6	1.0	1.2	1.2	0.0	0.1	0.2	0.2	0.3
20	0.2	0.6	1.0	1.1	1.2	0.1	0.2	0.3	0.3	0.3
50	0.2	0.6	1.0	1.1	1.1	0.1	0.3	0.4	0.4	0.4
100	0.3	0.7	1.0	1.1	1.0	0.2	0.4	0.6	0.6	0.6
200	0.4	0.8	1.1	1.1	1.0	0.3	0.6	0.8	0.8	0.8

120 GHz, 4-tiss. Sasaki data

	ratio-U_{ab}					ratio-S_{ab}				
FWHM:	0.005	0.01	0.02	0.03	0.10	0.005	0.01	0.02	0.03	0.10
td (s)										
0.05	0.1	0.4	0.8	0.9	1.0	0.0	0.0	0.0	0.1	0.1
0.1	0.1	0.4	0.8	0.9	1.0	0.0	0.0	0.1	0.1	0.1
0.2	0.1	0.4	0.8	0.9	1.0	0.0	0.0	0.1	0.1	0.1
0.5	0.1	0.4	0.8	1.0	1.1	0.0	0.0	0.1	0.1	0.1
1	0.1	0.5	0.9	1.0	1.1	0.0	0.0	0.1	0.1	0.1
2	0.1	0.5	0.9	1.0	1.1	0.0	0.1	0.1	0.1	0.1
5	0.2	0.5	1.0	1.1	1.2	0.0	0.1	0.2	0.2	0.2
10	0.2	0.5	1.0	1.1	1.2	0.0	0.1	0.2	0.2	0.2
20	0.2	0.6	1.0	1.1	1.2	0.1	0.2	0.3	0.3	0.3
50	0.2	0.6	1.0	1.1	1.1	0.1	0.2	0.4	0.4	0.4
100	0.3	0.7	1.0	1.1	1.0	0.2	0.4	0.6	0.6	0.6
200	0.4	0.8	1.1	1.1	1.0	0.3	0.6	0.8	0.8	0.8

Fig. 5.28, Tables of $U_{ab,4cm\text{-}5}/U_{ab,OBR}$ (ratio- U_{ab}) and $S_{ab,4cm\text{-}5}/S_{ab,OBR}$ (ratio- S_{ab}) for a fixed thickness, 4-tissue model (Sasaki database) exposed to a continuous pulse train at 80 and 120 GHz versus exposure duration (i.e. TOT in the reference period) and FWHM.

160 GHz, 4-tiss. Sasaki data

	ratio-U_{ab}					ratio-S_{ab}				
FWHM: / td (s)	0.005	0.01	0.02	0.03	0.10	0.005	0.01	0.02	0.03	0.10
0.05	0.1	0.4	0.7	0.8	0.9	0.0	0.0	0.0	0.0	0.1
0.1	0.1	0.4	0.7	0.8	0.9	0.0	0.0	0.0	0.1	0.1
0.2	0.1	0.4	0.7	0.9	1.0	0.0	0.0	0.1	0.1	0.1
0.5	0.1	0.4	0.8	0.9	1.0	0.0	0.0	0.1	0.1	0.1
1	0.1	0.4	0.8	1.0	1.1	0.0	0.0	0.1	0.1	0.1
2	0.1	0.5	0.9	1.0	1.1	0.0	0.1	0.1	0.1	0.1
5	0.2	0.5	0.9	1.1	1.2	0.0	0.1	0.2	0.2	0.2
10	0.2	0.5	1.0	1.1	1.2	0.0	0.1	0.2	0.2	0.2
20	0.2	0.6	1.0	1.1	1.2	0.1	0.2	0.3	0.3	0.3
50	0.2	0.6	1.0	1.1	1.1	0.1	0.2	0.4	0.4	0.4
100	0.3	0.7	1.0	1.1	1.0	0.2	0.4	0.6	0.6	0.6
200	0.4	0.8	1.1	1.1	1.0	0.3	0.6	0.8	0.8	0.8

200 GHz, 4-tiss. Sasaki data

	ratio-U_{ab}					ratio-S_{ab}				
FWHM: / td (s)	0.005	0.01	0.02	0.03	0.10	0.005	0.01	0.02	0.03	0.10
0.05	0.1	0.3	0.6	0.8	0.8	0.0	0.0	0.0	0.0	0.1
0.1	0.1	0.4	0.7	0.8	0.9	0.0	0.0	0.0	0.1	0.1
0.2	0.1	0.4	0.7	0.8	0.9	0.0	0.0	0.1	0.1	0.1
0.5	0.1	0.4	0.8	0.9	1.0	0.0	0.0	0.1	0.1	0.1
1	0.1	0.4	0.8	0.9	1.0	0.0	0.0	0.1	0.1	0.1
2	0.1	0.5	0.9	1.0	1.1	0.0	0.1	0.1	0.1	0.1
5	0.2	0.5	0.9	1.1	1.1	0.0	0.1	0.2	0.2	0.2
10	0.2	0.5	1.0	1.1	1.2	0.0	0.1	0.2	0.2	0.2
20	0.2	0.6	1.0	1.1	1.1	0.1	0.2	0.3	0.3	0.3
50	0.2	0.6	1.0	1.1	1.1	0.1	0.2	0.4	0.4	0.4
100	0.3	0.7	1.0	1.1	1.0	0.2	0.4	0.5	0.6	0.6
200	0.4	0.8	1.1	1.1	1.0	0.3	0.6	0.8	0.8	0.8

Fig. 5.29, Tables of $U_{ab,4cm\text{-}5}/U_{ab,OBR}$ (ratio- U_{ab}) and $S_{ab,4cm\text{-}5}/S_{ab,OBR}$ (ratio- S_{ab}) for a fixed thickness, 4-tissue model (Sasaki database) exposed to a continuous pulse train at 160 and 200 GHz versus exposure duration (i.e. TOT in the reference period) and FWHM.

5.5.3.2 Results - 1 cm² spatial average:

$$U_{ab,OBR} = 144\left[0.025 + 0.975\sqrt{t_d/360}\right] \quad (kJ/m^2) \quad , \quad S_{ab,OBR} = 400 \quad (W/m^2)$$

6 GHz, 3-tiss. Hasgall data

	ratio-U_{ab}				ratio-S_{ab}			
FWHM: / td (s)	0.01	0.02	0.03	0.10	0.01	0.02	0.03	0.10
0.05	8.9	10.4	10.3	9.8	0.3	0.4	0.4	0.4
0.1	7.8	9.0	9.0	8.5	0.3	0.4	0.4	0.4
0.2	6.6	7.6	7.6	7.2	0.3	0.4	0.4	0.3
0.5	5.1	5.8	5.8	5.5	0.3	0.4	0.4	0.3
1	4.1	4.7	4.7	4.4	0.3	0.4	0.4	0.3
2	3.3	3.8	3.8	3.5	0.3	0.4	0.4	0.3
5	2.5	2.8	2.8	2.6	0.4	0.4	0.4	0.4
10	2.1	2.3	2.2	2.1	0.4	0.4	0.4	0.4
20	1.7	1.8	1.8	1.6	0.4	0.5	0.5	0.4
50	1.5	1.4	1.3	1.2	0.6	0.6	0.5	0.5
100	1.4	1.2	1.1	1.0	0.7	0.7	0.6	0.5
200	1.5	1.2	1.1	0.9	1.1	0.9	0.8	0.6

10 GHz, 3-tiss. Hasgall data

	ratio-U_{ab}				ratio-S_{ab}			
FWHM: / td (s)	0.01	0.02	0.03	0.10	0.01	0.02	0.03	0.10
0.05	4.3	5.1	5.2	5.1	0.2	0.2	0.2	0.2
0.1	3.8	4.5	4.6	4.5	0.2	0.2	0.2	0.2
0.2	3.2	3.8	3.9	3.8	0.2	0.2	0.2	0.2
0.5	2.5	3.0	3.0	3.0	0.2	0.2	0.2	0.2
1	2.1	2.5	2.5	2.4	0.2	0.2	0.2	0.2
2	1.7	2.0	2.1	2.0	0.2	0.2	0.2	0.2
5	1.4	1.6	1.6	1.5	0.2	0.2	0.2	0.2
10	1.2	1.3	1.3	1.3	0.2	0.3	0.3	0.2
20	1.0	1.1	1.1	1.1	0.3	0.3	0.3	0.3
50	1.0	1.0	0.9	0.9	0.4	0.4	0.4	0.3
100	1.0	0.9	0.8	0.7	0.5	0.5	0.4	0.4
200	1.1	0.9	0.8	0.7	0.8	0.7	0.6	0.5

Fig. 5.30, Tables of $U_{ab,1cm\text{-}5}/U_{ab,OBR}$ (ratio- U_{ab}) and $S_{ab,1cm\text{-}5}/S_{ab,OBR}$ (ratio- S_{ab}) for a fixed thickness, 3-tissue model (Hasgall database) exposed to a continuous pulse train at 6 and 10 GHz versus exposure duration (i.e. TOT in the reference period) and FWHM.

20 GHz, 3-tiss. Hasgall data

	ratio-U_{ab}				ratio-S_{ab}			
FWHM:	0.01	0.02	0.03	0.10	0.01	0.02	0.03	0.10
td (s)								
0.05	2.5	3.0	3.1	3.1	0.1	0.1	0.1	0.1
0.1	2.2	2.7	2.8	2.8	0.1	0.1	0.1	0.1
0.2	1.9	2.3	2.4	2.4	0.1	0.1	0.1	0.1
0.5	1.6	1.9	1.9	1.9	0.1	0.1	0.1	0.1
1	1.3	1.6	1.6	1.6	0.1	0.1	0.1	0.1
2	1.1	1.3	1.3	1.3	0.1	0.1	0.1	0.1
5	0.9	1.0	1.0	1.0	0.1	0.1	0.1	0.1
10	0.8	0.9	0.9	0.9	0.1	0.2	0.2	0.2
20	0.7	0.8	0.8	0.7	0.2	0.2	0.2	0.2
50	0.7	0.7	0.7	0.6	0.3	0.3	0.3	0.2
100	0.7	0.6	0.6	0.6	0.4	0.3	0.3	0.3
200	0.8	0.7	0.6	0.5	0.6	0.5	0.5	0.4

30 GHz, 3-tiss. Hasgall data

	ratio-U_{ab}					ratio-S_{ab}				
FWHM:	0.005	0.01	0.02	0.03	0.1	0.005	0.01	0.02	0.03	0.1
td (s)										
0.05	0.8	1.5	1.8	1.8	1.8	0.0	0.1	0.1	0.1	0.1
0.1	0.7	1.4	1.7	1.7	1.7	0.0	0.1	0.1	0.1	0.1
0.2	0.7	1.2	1.5	1.6	1.6	0.0	0.1	0.1	0.1	0.1
0.5	0.6	1.1	1.3	1.3	1.4	0.0	0.1	0.1	0.1	0.1
1	0.5	1.0	1.1	1.2	1.2	0.0	0.1	0.1	0.1	0.1
2	0.4	0.8	1.0	1.0	1.0	0.0	0.1	0.1	0.1	0.1
5	0.4	0.7	0.8	0.8	0.8	0.1	0.1	0.1	0.1	0.1
10	0.4	0.6	0.7	0.7	0.7	0.1	0.1	0.1	0.1	0.1
20	0.4	0.6	0.6	0.7	0.6	0.1	0.1	0.2	0.2	0.2
50	0.4	0.6	0.6	0.6	0.6	0.2	0.2	0.2	0.2	0.2
100	0.5	0.6	0.6	0.6	0.5	0.3	0.3	0.3	0.3	0.3
200	0.6	0.7	0.6	0.6	0.5	0.5	0.5	0.5	0.4	0.4

Fig. 5.31, Tables of $U_{ab,1cm\text{-}5}/U_{ab,OBR}$ (ratio- U_{ab}) and $S_{ab,1cm\text{-}5}/S_{ab,OBR}$ (ratio- S_{ab}) for a fixed thickness, 3-tissue model (Hasgall database) exposed to a continuous pulse train at 20 and 30 GHz versus exposure duration (i.e. TOT in the reference period) and FWHM.

60 GHz, 3-tiss. Hasgall data

	ratio-U_{ab}					ratio-S_{ab}				
FWHM:	0.005	0.01	0.02	0.03	0.10	0.005	0.01	0.02	0.03	0.10
td (s)										
0.05	0.4	0.8	0.9	1.0	1.0	0.0	0.0	0.0	0.0	0.0
0.1	0.4	0.7	0.9	0.9	0.9	0.0	0.0	0.0	0.0	0.0
0.2	0.4	0.7	0.9	0.9	0.9	0.0	0.0	0.0	0.0	0.0
0.5	0.3	0.7	0.8	0.8	0.8	0.0	0.0	0.0	0.1	0.1
1	0.3	0.6	0.8	0.8	0.8	0.0	0.0	0.1	0.1	0.1
2	0.3	0.6	0.7	0.7	0.8	0.0	0.1	0.1	0.1	0.1
5	0.3	0.5	0.6	0.7	0.7	0.0	0.1	0.1	0.1	0.1
10	0.3	0.5	0.6	0.6	0.6	0.1	0.1	0.1	0.1	0.1
20	0.3	0.5	0.6	0.6	0.5	0.1	0.1	0.1	0.1	0.1
50	0.4	0.5	0.5	0.5	0.5	0.1	0.2	0.2	0.2	0.2
100	0.4	0.5	0.5	0.5	0.5	0.2	0.3	0.3	0.3	0.3
200	0.6	0.7	0.6	0.5	0.5	0.4	0.5	0.4	0.4	0.4

60 GHz, 4-tiss. Sasaki data

	ratio-U_{ab}					ratio-S_{ab}				
FWHM:	0.005	0.01	0.02	0.03	0.10	0.005	0.01	0.02	0.03	0.10
td (s)										
0.05	0.5	0.9	1.1	1.1	1.1	0.0	0.0	0.0	0.0	0.0
0.1	0.4	0.8	1.0	1.0	1.1	0.0	0.0	0.0	0.0	0.0
0.2	0.4	0.8	0.9	1.0	1.0	0.0	0.0	0.0	0.0	0.0
0.5	0.4	0.7	0.9	0.9	0.9	0.0	0.0	0.1	0.1	0.1
1	0.4	0.7	0.8	0.8	0.8	0.0	0.1	0.1	0.1	0.1
2	0.4	0.7	0.8	0.8	0.8	0.0	0.1	0.1	0.1	0.1
5	0.4	0.6	0.7	0.8	0.8	0.0	0.1	0.1	0.1	0.1
10	0.4	0.6	0.7	0.7	0.7	0.1	0.1	0.1	0.1	0.1
20	0.4	0.6	0.7	0.7	0.7	0.1	0.2	0.2	0.2	0.2
50	0.5	0.6	0.6	0.6	0.6	0.2	0.2	0.3	0.2	0.2
100	0.6	0.7	0.6	0.6	0.5	0.3	0.4	0.3	0.3	0.3
200	0.7	0.8	0.7	0.6	0.5	0.5	0.6	0.5	0.5	0.4

Fig. 5.32, Tables of $U_{ab,1cm\text{-}5}/U_{ab,OBR}$ (ratio- U_{ab}) and $S_{ab,1cm\text{-}5}/S_{ab,OBR}$ (ratio- S_{ab}) for a fixed thickness model (3-tissue, Hasgall database left, 4-tissue, Sasaki database right) exposed to a continuous pulse train at 60 GHz versus exposure duration (i.e. TOT in the reference period) and FWHM.

80 GHz, 4-tiss. Sasaki data

	ratio-U_{ab}					ratio-S_{ab}				
FWHM:	0.005	0.01	0.02	0.03	0.10	0.005	0.01	0.02	0.03	0.10
td (s)										
0.05	0.4	0.7	0.9	0.9	1.0	0.0	0.0	0.0	0.0	0.0
0.1	0.4	0.7	0.9	0.9	0.9	0.0	0.0	0.0	0.0	0.0
0.2	0.4	0.7	0.8	0.9	0.9	0.0	0.0	0.0	0.0	0.0
0.5	0.3	0.6	0.8	0.8	0.8	0.0	0.0	0.0	0.0	0.1
1	0.3	0.6	0.8	0.8	0.8	0.0	0.0	0.1	0.1	0.1
2	0.3	0.6	0.7	0.8	0.8	0.0	0.1	0.1	0.1	0.1
5	0.3	0.6	0.7	0.7	0.7	0.0	0.1	0.1	0.1	0.1
10	0.4	0.6	0.7	0.7	0.7	0.1	0.1	0.1	0.1	0.1
20	0.4	0.6	0.7	0.7	0.6	0.1	0.2	0.2	0.2	0.2
50	0.5	0.6	0.6	0.6	0.6	0.2	0.2	0.2	0.2	0.2
100	0.6	0.7	0.6	0.6	0.5	0.3	0.4	0.3	0.3	0.3
200	0.7	0.8	0.7	0.6	0.5	0.5	0.6	0.5	0.5	0.4

120 GHz, 4-tiss. Sasaki data

	ratio-U_{ab}					ratio-S_{ab}				
FWHM:	0.005	0.01	0.02	0.03	0.10	0.005	0.01	0.02	0.03	0.10
td (s)										
0.05	0.3	0.6	0.8	0.8	0.8	0.0	0.0	0.0	0.0	0.0
0.1	0.3	0.6	0.8	0.8	0.8	0.0	0.0	0.0	0.0	0.0
0.2	0.3	0.6	0.7	0.8	0.8	0.0	0.0	0.0	0.0	0.0
0.5	0.3	0.6	0.7	0.7	0.7	0.0	0.0	0.0	0.0	0.0
1	0.3	0.6	0.7	0.7	0.7	0.0	0.0	0.1	0.1	0.1
2	0.3	0.6	0.7	0.7	0.7	0.0	0.1	0.1	0.1	0.1
5	0.3	0.6	0.7	0.7	0.7	0.0	0.1	0.1	0.1	0.1
10	0.3	0.6	0.7	0.7	0.7	0.1	0.1	0.1	0.1	0.1
20	0.4	0.6	0.7	0.7	0.6	0.1	0.1	0.2	0.2	0.2
50	0.4	0.6	0.6	0.6	0.6	0.2	0.2	0.2	0.2	0.2
100	0.5	0.7	0.6	0.6	0.5	0.3	0.4	0.3	0.3	0.3
200	0.7	0.8	0.7	0.6	0.5	0.5	0.6	0.5	0.5	0.4

Fig. 5.33, Tables of $U_{ab,1cm\text{-}5}/U_{ab,OBR}$ (ratio- U_{ab}) and $S_{ab,1cm\text{-}5}/S_{ab,OBR}$ (ratio- S_{ab}) for a fixed thickness, 4-tissue model (Sasaki database) exposed to a continuous pulse train at 80 and 120 GHz versus exposure duration (i.e. TOT in the reference period) and FWHM.

160 GHz, 4-tiss. Sasaki data

FWHM: td (s)	ratio-U_{ab} 0.005	0.01	0.02	0.03	0.10	ratio-S_{ab} 0.005	0.01	0.02	0.03	0.10
0.05	0.3	0.6	0.7	0.7	0.8	0.0	0.0	0.0	0.0	0.0
0.1	0.3	0.6	0.7	0.7	0.7	0.0	0.0	0.0	0.0	0.0
0.2	0.3	0.6	0.7	0.7	0.7	0.0	0.0	0.0	0.0	0.0
0.5	0.3	0.6	0.7	0.7	0.7	0.0	0.0	0.0	0.0	0.0
1	0.3	0.6	0.7	0.7	0.7	0.0	0.0	0.1	0.1	0.1
2	0.3	0.6	0.7	0.7	0.7	0.0	0.1	0.1	0.1	0.1
5	0.3	0.6	0.7	0.7	0.7	0.0	0.1	0.1	0.1	0.1
10	0.3	0.6	0.7	0.7	0.7	0.1	0.1	0.1	0.1	0.1
20	0.4	0.6	0.6	0.7	0.6	0.1	0.1	0.2	0.2	0.2
50	0.4	0.6	0.6	0.6	0.6	0.2	0.2	0.2	0.2	0.2
100	0.5	0.7	0.6	0.6	0.5	0.3	0.4	0.3	0.3	0.3
200	0.7	0.8	0.7	0.6	0.5	0.5	0.6	0.5	0.5	0.4

200 GHz, 4-tiss. Sasaki data

FWHM: td (s)	ratio-U_{ab} 0.005	0.01	0.02	0.03	0.10	ratio-S_{ab} 0.005	0.01	0.02	0.03	0.10
0.05	0.3	0.5	0.7	0.7	0.7	0.0	0.0	0.0	0.0	0.0
0.1	0.3	0.5	0.7	0.7	0.7	0.0	0.0	0.0	0.0	0.0
0.2	0.3	0.5	0.7	0.7	0.7	0.0	0.0	0.0	0.0	0.0
0.5	0.3	0.5	0.7	0.7	0.7	0.0	0.0	0.0	0.0	0.0
1	0.3	0.5	0.7	0.7	0.7	0.0	0.0	0.0	0.1	0.1
2	0.3	0.5	0.7	0.7	0.7	0.0	0.1	0.1	0.1	0.1
5	0.3	0.6	0.7	0.7	0.7	0.0	0.1	0.1	0.1	0.1
10	0.3	0.6	0.7	0.7	0.7	0.1	0.1	0.1	0.1	0.1
20	0.4	0.6	0.6	0.6	0.6	0.1	0.1	0.2	0.2	0.2
50	0.4	0.6	0.6	0.6	0.6	0.2	0.2	0.2	0.2	0.2
100	0.5	0.7	0.6	0.6	0.5	0.3	0.4	0.3	0.3	0.3
200	0.7	0.8	0.7	0.6	0.5	0.5	0.6	0.5	0.5	0.4

Fig. 5.34, Tables of $U_{ab,1cm\text{-}5}/U_{ab,OBR}$ (ratio- U_{ab}) and $S_{ab,1cm\text{-}5}/S_{ab,OBR}$ (ratio- S_{ab}) for a fixed thickness, 4-tissue model (Sasaki database) exposed to a continuous pulse train at 160 and 200 GHz versus exposure duration (i.e. TOT in the reference period) and FWHM.

5.5.4 Discussion – continuously pulsed exposures and ICNIRP OBRs

AED OBRs

For frequencies up to 20 GHz, both the 4cm^2 and 1 cm^2-averaged AED OBRs are mostly conservative for all beam diameters or spot sizes. At 30 GHz and above, there is increasing non-conservatism as the spot size and exposure duration (pulse width) diminishes. This is especially pronounced for the smallest spot size above 30 GHz.

APD OBRs

The APD OBRs are almost completely non-conservative with the ratios decreasing with increasing frequency and decreasing spot size. This suggests that pulse heights of continuous pulse trains should be restricted by the AED limits, which it can be shown, to produce lower allowable pulse heights than the time-averaged APD limits.

5.6 References

Gabriel S, Lau RW, Gabriel C. The dielectric properties of biological tissues: III. parametric models for the dielectric spectrum of tissues. Phys Med Biol 41:2271-2293; 1996

Gajda GB, Lemay E, Paradis J, “Model of Steady-state Temperature Rise in Multilayer Tissues Due to Narrow-beam Millimeter-wave Radiofrequency Field Exposure.” Health Phys. Vol. 117, No. 3, September 2019. doi: 10.1097/HP.0000000000001036.

Hasgall PA, Di Gennaro F, Baumgartner C, Neufeld E, Gosselin MC, Payne D, Klingenböck A, Kuster N, “IT’IS Database for thermal and electromagnetic parameters of biological tissues,” Version 3.0, September 01st, 2018, DOI: 10.13099/VIP21000-03-0.

Pickwell E, Cole B E, Fitzgerald A J, Pepper M, Wallace V P, “In vivo study of human skin using pulsed terahertz radiation,” Phys. Med. Biol. 49, 1595–607, 2004

Sasaki K, Wake K, Watanabe S, “Measurement of the dielectric properties of the epidermis and dermis at frequencies from 0.5 GHz to 110 GHz.” Phys. Med. Biol. 59, 4739–4747, 2014

Sasaki K, Mizuno M, Wake K, Watanabe S, “Monte Carlo simulations of skin exposure to electromagnetic field from 10 GHz to 1 THz”, Phys. Med. Biol. 62 6993-7010, 2017

6.0 Recommendations regarding the use of the localized exposure limits for frequencies > 6 GHz

According to the evaluation of the ICNIRP guidelines (ICNIRP, 2020) in Section 5, it was found that the application of the limits applicable to localized EMF exposures above 6 GHz, could result in exceeding the OAHET (e.g. a 5^{o}C temperature increase in Type 1 tissues) for occupational exposures under certain exposure conditions. This conclusion is based on the approximate Gaussian planar model used in Section 5 which was published in Health Physics (Gajda et al., 2019).

Section 5 of this document explored in detail the level of conservativeness of the ICNIRP (2020) proposed basic restrictions without including the reduction factors and did not specifically address the related reference level. Nevertheless, it should be mentioned that this analysis is sufficient because; i) in the applied model there is a linear relationship between the exposure quantity and the related temperature increase which means that the level of conservativeness (dimensionless ratio) is not affected by the reduction factor and ii) the basic restrictions and the reference levels are only related by the transmission coefficient which have been studied separately in Appendix B. As can be seen in Appendix B, figures B.9 and B.10, the estimated 95th percentile transmission coefficients in the frequency range of 6 GHz to 300 GHz, based on our human tissue planar model, are smaller than the transmission coefficients used by ICNIRP except for 6 GHz. This means that, except for 6 GHz, the reference levels are even more conservative than what was assessed for the basic restrictions. For the special case of 6 GHz, the estimated 95th percentile transmission coefficient is only 10% higher than ICNIRP's value, but since the level of conservatism of the basic restrictions is quite high at 6 GHz (see figures 5.12 and 5.25) it is fair to conclude that the reference levels at 6 GHz are still conservative.

In an effort to maintain the maximal extent of international harmonization and ensure conservativeness in the safety margins for both occupational and general public exposures limits, the following recommendations are made.

For Basic Restrictions of localized exposures above 6 GHz, it is recommended to use:

- ICNIRP (2020) Guidelines, **Table 2**, for occupational and general public exposure scenarios, in the frequency range >6 GHz to 300 GHz, applicable to CW or quasi-CW exposures,) where:
    - **Note 5** of Table 2 shall be modified to: "Local S_{ab} is to be averaged over a square 4-cm^2 surface area of the body. Above 30 GHz, an additional constraint is imposed, such ***that the spatial peak*** exposure is restricted to two times that of the 4-cm^2 restriction."
- ICNIRP (2020) Guidelines, **Table 3**, for occupational and general public exposure scenarios, in the frequency range >6 GHz to 300 GHz, applicable to any pulse, group of pulses, or subgroup of pulses in a train, where:
    - **Note 4** of Table 3 shall be modified to: "Local U_{ab} is to be averaged over a square 4-cm^2 surface area of the body. Above 30 GHz, an additional constraint is imposed, such ***that***

the spatial peak exposure is restricted to $72[0.025+0.975(t/360)^{0.5}]$ kJ/m^2 for occupational and $14.4[0.025+0.975(t/360)^{0.5}]$ kJ/m^2 for general public exposure."

- **Note 5** of Table 3 shall be modified to: "Exposure from any pulse, group of pulses, or subgroup of pulses in a train, as well as from the summation of exposures (including non-pulsed EMF), delivered in *t* s, ***where t is the sum of all periods in which there is non-zero exposure***, must not exceed these levels." (i.e. all pulses are glued together within any 6-minute reference period).

For Reference Levels of localized exposures above 6 GHz, it is recommended to use:

- ICNIRP (2020) Guidelines, **Table 6**, for occupational and general public exposure scenarios, in the frequency range >6 GHz to 300 GHz, applicable to CW or quasi-CW exposures, where:
  - **Note 7** of Table 6 shall be modified to: "For frequencies of >30 GHz to 300 GHz, ***the spatial peak*** exposure must not exceed twice that of the square 4-cm^2 restrictions."
- ICNIRP (2020) Guidelines, **Table 7**, for occupational and general public exposure scenarios, in the frequency range >6 GHz to 300 GHz, applicable to any pulse, group of pulses, or subgroup of pulses in a train, where:
  - **Note 2** of Table 7 shall be modified to: "f_M is frequency in MHz; f_G is frequency in GHz; t is time interval in seconds, such that exposure from any pulse, group of pulses, or subgroup of pulses in a train, as well as from the summation of exposures (including non-pulsed EMF), delivered in *t* seconds, ***where t is the sum of all periods in which there is non-zero exposure***, must not exceed these levels." (i.e. all pulses are glued together within any 6-minute reference period).
  - **Note 7** of Table 7 shall be modified to: "For frequencies of >30GHz to 300 GHz, ***the spatial peak*** exposure must not exceed $275/f_G^{0.177}$ X $0.72[0.025+0.975(t/360)^{0.5}]$ kJ/m^2 for occupational and $55/f_G^{0.177}$ X $0.72[0.025+0.975(t/360)^{0.5}]$ kJ/m^2 for general public exposure."

The recommendations above can be reproduced in a simplified table format where the information in ICNIRP pertaining to frequencies below 6 GHz can be removed because it was not subject to this evaluation. The following tables have been generated for that purpose:

Table 6.1: Basic restrictions for local electromagnetic field exposure above 6 GHz up to 300 GHz

Exposure Scenario	Exposure Duration (t)	Local Absorbed Energy Density [kJ/m^2]	Local Absorbed Power Density [W/m^2]
Controlled Environment	0 sec < t < 360 sec	36 $[0.05+0.95(t/360)^{0.5}]$	NA
	t ≥ 6 min	NA	100
Uncontrolled Environment	0 sec < t < 360 sec	7.2 $[0.05+0.95(t/360)^{0.5}]$	NA
	t ≥ 6 min	NA	20

Notes:

1. "NA" signifies "not applicable" and does not need to be taken into account when determining compliance.
2. "t" is time in seconds, and restrictions must be satisfied for all values of t between >0 s and <360 s, regardless of the temporal characteristics of the exposure itself.
3. Local absorbed power density exposures are to be averaged over 6 min.

4. Local absorbed power density is to be averaged over a square 4-cm^2 surface area of the body. Above 30 GHz, an additional constraint is imposed, such that the spatial peak exposure is restricted to two times that of the 4-cm^2 restriction.
5. Local absorbed energy density is to be averaged over a square 4-cm^2 surface area of the body. Above 30 GHz, an additional constraint is imposed, such that the spatial peak exposure is restricted to $72[0.025+0.975(t/360)^{0.5}]$ kJ/m^2 for controlled environment and $14.4[0.025+0.975(t/360)^{0.5}]$ kJ/m^2 for uncontrolled environment exposure.
6. Exposure from any pulse, group of pulses, or subgroup of pulses in a train, as well as from the summation of exposures (including non-pulsed EMF), delivered in t s, where t is the sum of all periods in which there is non-zero exposure, must not exceed these levels.

Table 6.2: Reference Levels for local electromagnetic field exposure above 6 GHz up to 300 GHz

Exposure Scenario	Exposure Duration (t)	Local Incident Energy Density [kJ/m^2]	Local Incident Power Density [W/m^2]
Controlled Environment	0 sec < t < 360 sec	$275/f_G^{0.177}$ X $0.36[0.05+0.95(t/360)^{0.5}]$	NA
	t ≥ 6 min	NA	$275/f_G^{0.177}$
Uncontrolled Environment	0 sec < t < 360 sec	$55/f_G^{0.177}$ X $0.36[0.05+0.95(t/360)^{0.5}]$	NA
	t ≥ 6 min	NA	$55/f_G^{0.177}$

Notes:
1. "NA" signifies "not applicable" and does not need to be taken into account when determining compliance.
2. f_G is frequency in GHz; t is time interval in seconds, such that exposure from any pulse, group of pulses, or subgroup of pulses in a train, as well as from the summation of exposures (including non-pulsed EMF), delivered in t seconds, where t is the sum of all periods in which there is non-zero exposure, must not exceed these levels.
3. Incident energy density is to be calculated over time t,
4. Incident power density is to be averaged over 6 min.
5. For frequencies of >6 GHz to 300 GHz: (a) within the far-field zone, compliance is demonstrated if the incident power density, averaged over a square 4-cm^2 projected body surface space, does not exceed the above reference level values; plane-wave equivalent incident power density may be substituted for the incident power density; (b) within the radiative near-field zone, compliance is demonstrated if the incident power density, averaged over a square 4-cm^2 projected body surface space, does not exceed the above reference level values; and (c) within the reactive near-field zone reference levels cannot be used to determine compliance, and so basic restrictions must be assessed.
6. For frequencies of >6 GHz to 300GHz: (a) within the far-field or radiative near-field zone, compliance is demonstrated if the incident energy density, averaged over a square 4-cm^2 projected body surface space, does not exceed the above reference level values; (b) within the reactive near-field zone, reference levels cannot be used to determine compliance, and so basic restrictions must be assessed.
7. For frequencies of >30 GHz to 300 GHz, the spatial peak incident power density exposure must not exceed twice that of the square 4-cm^2 restrictions
8. For frequencies of >30GHz to 300 GHz, the spatial peak incident energy density exposure must not exceed $275/f_G^{0.177}$ X $0.72[0.025+0.975(t/360)^{0.5}]$ kJ/m^2 for controlled environment and $55/f_G^{0.177}$ X $0.72[0.025+0.975(t/360)^{0.5}]$ kJ/m^2 for uncontrolled environment exposure.

These recommendated localized exposures limits for frequencies above 6 GHz, adapted from the ICNIRP (2020) guidelines, are considered sufficiently conservative to offer protection against the all established RFEMF adverse health effects. In an effort to simplify the analysis of the impact of such recommendations,

the following tables have been generated where the estimated temperature increases have been tabulated using the adapted ICNIRP (2020) limits, when the reduction factors are applied for controlled and uncontrolled environments:

Estimated Temperature Rise at 6 GHz (uncontrolled)						**Estimated Temperature Rise** at 10 GHz (uncontrolled)						**Estimated Temperature Rise** at 20 GHz (uncontrolled)					
FWHM:	0.005	0.01	0.02	0.03	0.1	**FWHM:**	0.005	0.01	0.02	0.03	0.1	**FWHM:**	0.005	0.01	0.02	0.03	0.1
t [sec]	°C	°C	°C	°C	°C	t [sec]	°C	°C	°C	°C	°C	t [sec]	°C	°C	°C	°C	°C
0.05	-	0.09	0.05	0.04	0.04	0.05	-	0.19	0.10	0.09	0.08	0.05	-	0.32	0.17	0.15	0.14
0.1	-	0.10	0.05	0.05	0.05	0.1	-	0.20	0.11	0.10	0.09	0.1	-	0.35	0.18	0.16	0.15
0.2	-	0.11	0.06	0.05	0.05	0.2	-	0.23	0.12	0.11	0.10	0.2	-	0.37	0.20	0.17	0.16
0.5	-	0.13	0.07	0.07	0.06	0.5	-	0.27	0.14	0.13	0.12	0.5	-	0.43	0.23	0.20	0.18
1	-	0.15	0.09	0.08	0.08	1	-	0.30	0.16	0.14	0.14	1	-	0.49	0.26	0.23	0.21
2	-	0.18	0.10	0.09	0.09	2	-	0.35	0.19	0.17	0.16	2	-	0.55	0.29	0.26	0.24
5	-	0.22	0.13	0.11	0.11	5	-	0.41	0.22	0.20	0.19	5	-	0.64	0.35	0.31	0.28
10	-	0.26	0.15	0.14	0.14	10	-	0.45	0.25	0.23	0.22	10	-	0.71	0.39	0.35	0.32
20	-	0.30	0.18	0.17	0.17	20	-	0.50	0.29	0.26	0.25	20	-	0.76	0.43	0.39	0.37
50	-	0.35	0.23	0.21	0.22	50	-	0.53	0.33	0.31	0.31	50	-	0.77	0.48	0.43	0.42
100	-	0.36	0.25	0.25	0.26	100	-	0.52	0.36	0.34	0.35	100	-	0.72	0.48	0.45	0.46
200	-	0.33	0.26	0.26	0.30	200	-	0.46	0.35	0.35	0.38	200	-	0.62	0.45	0.44	0.47
CW	-	0.27	0.23	0.23	0.26	CW	-	0.37	0.30	0.30	0.33	CW	-	0.49	0.38	0.38	0.40

Fig. 6.1, Tables showing the impact of the recommendations in terms of maximum temperature increase estimates, for exposures in uncontrolled environment at 6 GHz, 10 GHz and 20 GHz.

Estimated Temperature Rise at 30 GHz (uncontrolled)						**Estimated Temperature Rise** at 60 GHz (uncontrolled)						**Estimated Temperature Rise** at 80 GHz (uncontrolled)					
FWHM:	0.005	0.01	0.02	0.03	0.1	**FWHM:**	0.005	0.01	0.02	0.03	0.1	**FWHM:**	0.005	0.01	0.02	0.03	0.1
t [sec]	°C	°C	°C	°C	°C	t [sec]	°C	°C	°C	°C	°C	t [sec]	°C	°C	°C	°C	°C
0.05	0.26	0.26	0.26	0.25	-	0.05	0.50	0.50	0.51	0.48	-	0.05	0.51	0.51	0.51	0.49	-
0.1	0.28	0.28	0.28	0.26	0.23	0.1	0.52	0.52	0.52	0.48	0.43	0.1	0.53	0.53	0.53	0.49	0.44
0.2	0.30	0.30	0.31	0.27	0.24	0.2	0.54	0.54	0.54	0.47	0.42	0.2	0.55	0.56	0.56	0.48	0.44
0.5	0.35	0.35	0.33	0.29	0.26	0.5	0.56	0.57	0.53	0.46	0.41	0.5	0.58	0.59	0.55	0.47	0.43
1	0.39	0.40	0.35	0.31	0.28	1	0.58	0.59	0.52	0.45	0.41	1	0.59	0.60	0.53	0.46	0.42
2	0.44	0.45	0.38	0.33	0.30	2	0.61	0.63	0.52	0.46	0.42	2	0.59	0.62	0.52	0.45	0.41
5	0.50	0.54	0.43	0.38	0.35	5	0.64	0.69	0.55	0.48	0.44	5	0.58	0.62	0.50	0.44	0.41
10	0.53	0.60	0.47	0.41	0.39	10	0.65	0.74	0.57	0.50	0.46	10	0.55	0.63	0.49	0.43	0.41
20	0.53	0.65	0.51	0.45	0.43	20	0.63	0.77	0.60	0.53	0.49	20	0.51	0.63	0.49	0.44	0.42
50	0.47	0.66	0.54	0.49	0.47	50	0.54	0.75	0.60	0.55	0.53	50	0.43	0.61	0.50	0.46	0.45
100	0.40	0.62	0.54	0.50	0.50	100	0.45	0.69	0.59	0.55	0.54	100	0.35	0.56	0.49	0.47	0.48
200	0.31	0.53	0.49	0.48	0.50	200	0.35	0.58	0.53	0.51	0.53	200	0.28	0.47	0.46	0.45	0.49
CW	0.24	0.42	0.41	0.40	0.43	CW	0.27	0.46	0.44	0.43	0.45	CW	0.21	0.38	0.38	0.38	0.42

Fig. 6.2, Tables showing the impact of the recommendations in terms of maximum temperature increase estimates, for exposures in uncontrolled environment at 30 GHz, 60 GHz and 80 GHz.

Estimated Temperature Rise at 120 GHz (uncontrolled)						**Estimated Temperature Rise** at 160 GHz (uncontrolled)						**Estimated Temperature Rise** at 200 GHz (uncontrolled)					
FWHM:	0.005	0.01	0.02	0.03	0.1	**FWHM:**	0.005	0.01	0.02	0.03	0.1	**FWHM:**	0.005	0.01	0.02	0.03	0.1
t [sec]	°C	°C	°C	°C	°C	t [sec]	°C	°C	°C	°C	°C	t [sec]	°C	°C	°C	°C	°C
0.05	0.60	0.60	0.60	0.57	-	0.05	0.64	0.65	0.65	0.62	0.55	0.05	0.69	0.69	0.70	0.66	0.60
0.1	0.61	0.61	0.62	0.56	0.50	0.1	0.66	0.66	0.66	0.60	0.54	0.1	0.70	0.70	0.70	0.64	0.58
0.2	0.63	0.63	0.63	0.55	0.49	0.2	0.66	0.67	0.67	0.58	0.52	0.2	0.70	0.71	0.71	0.61	0.55
0.5	0.64	0.65	0.60	0.52	0.47	0.5	0.67	0.68	0.63	0.54	0.49	0.5	0.70	0.71	0.66	0.57	0.52
1	0.64	0.65	0.57	0.50	0.46	1	0.66	0.68	0.60	0.52	0.47	1	0.69	0.70	0.61	0.53	0.49
2	0.63	0.66	0.55	0.48	0.44	2	0.65	0.67	0.56	0.49	0.45	2	0.67	0.69	0.58	0.50	0.46
5	0.60	0.65	0.52	0.45	0.42	5	0.62	0.66	0.53	0.46	0.43	5	0.63	0.67	0.54	0.47	0.44
10	0.57	0.65	0.50	0.45	0.42	10	0.58	0.66	0.51	0.45	0.42	10	0.59	0.66	0.52	0.46	0.43
20	0.53	0.64	0.50	0.45	0.43	20	0.53	0.65	0.51	0.45	0.43	20	0.54	0.66	0.51	0.46	0.44
50	0.44	0.62	0.51	0.46	0.46	50	0.44	0.62	0.51	0.47	0.46	50	0.45	0.62	0.51	0.47	0.46
100	0.36	0.56	0.50	0.47	0.48	100	0.36	0.57	0.50	0.47	0.48	100	0.37	0.57	0.50	0.47	0.48
200	0.28	0.48	0.46	0.45	0.49	200	0.28	0.48	0.46	0.45	0.49	200	0.28	0.48	0.46	0.46	0.49
CW	0.22	0.38	0.38	0.38	0.42	CW	0.22	0.39	0.38	0.39	0.42	CW	0.22	0.39	0.39	0.39	0.42

Fig. 6.3, Tables showing the impact of the recommendations in terms of maximum temperature increase estimates, for exposures in uncontrolled environment at 120 GHz, 160 GHz and 200 GHz.

Estimated Temperature Rise at 6 GHz (controlled)						**Estimated Temperature Rise** at 10 GHz (controlled)						**Estimated Temperature Rise** at 20 GHz (controlled)					
FWHM:	0.005	0.01	0.02	0.03	0.1	**FWHM:**	0.005	0.01	0.02	0.03	0.1	**FWHM:**	0.005	0.01	0.02	0.03	0.1
t [sec]	°C	°C	°C	°C	°C	t [sec]	°C	°C	°C	°C	°C	t [sec]	°C	°C	°C	°C	°C
0.05	-	0.45	0.25	0.22	0.22	0.05	-	0.95	0.50	0.44	0.41	0.05	-	1.62	0.86	0.75	0.68
0.1	-	0.49	0.27	0.24	0.24	0.1	-	1.02	0.55	0.48	0.45	0.1	-	1.73	0.91	0.79	0.73
0.2	-	0.55	0.30	0.27	0.26	0.2	-	1.13	0.61	0.53	0.50	0.2	-	1.87	0.99	0.86	0.79
0.5	-	0.66	0.37	0.33	0.32	0.5	-	1.33	0.71	0.63	0.59	0.5	-	2.16	1.15	1.00	0.92
1	-	0.77	0.43	0.38	0.38	1	-	1.52	0.82	0.72	0.68	1	-	2.44	1.30	1.13	1.04
2	-	0.90	0.50	0.45	0.44	2	-	1.73	0.93	0.83	0.78	2	-	2.75	1.47	1.29	1.19
5	-	1.11	0.63	0.57	0.56	5	-	2.03	1.12	0.99	0.94	5	-	3.20	1.74	1.53	1.42
10	-	1.30	0.75	0.68	0.68	10	-	2.27	1.27	1.14	1.09	10	-	3.54	1.96	1.73	1.62
20	-	1.51	0.90	0.83	0.84	20	-	2.48	1.44	1.31	1.27	20	-	3.79	2.17	1.94	1.84
50	-	1.73	1.13	1.06	1.10	50	-	2.64	1.66	1.54	1.54	50	-	3.85	2.38	2.17	2.11
100	-	1.78	1.27	1.23	1.31	100	-	2.58	1.78	1.69	1.75	100	-	3.62	2.42	2.27	2.28
200	-	1.64	1.30	1.31	1.48	200	-	2.29	1.75	1.73	1.88	200	-	3.09	2.27	2.21	2.33
CW	-	1.35	1.13	1.15	1.29	CW	-	1.86	1.49	1.50	1.64	CW	-	2.47	1.90	1.88	2.00

Fig. 6.4, Tables showing the impact of the recommendations in terms of maximum temperature increase estimates, for exposures in controlled environment at 6 GHz, 10 GHz and 20 GHz.

Estimated Temperature Rise at 30 GHz (controlled)						**Estimated Temperature Rise** at 60 GHz (controlled)						**Estimated Temperature Rise** at 80 GHz (controlled)					
FWHM:	0.005	0.01	0.02	0.03	0.1	**FWHM:**	0.005	0.01	0.02	0.03	0.1	**FWHM:**	0.005	0.01	0.02	0.03	0.1
t [sec]	°C	°C	°C	°C	°C	t [sec]	°C	°C	°C	°C	°C	t [sec]	°C	°C	°C	°C	°C
0.05	1.29	1.30	1.31	1.26	-	0.05	2.51	2.52	2.53	2.42	-	0.05	2.53	2.54	2.54	2.43	-
0.1	1.38	1.39	1.41	1.29	1.17	0.1	2.59	2.60	2.62	2.39	2.15	0.1	2.64	2.66	2.67	2.43	2.19
0.2	1.50	1.52	1.53	1.33	1.21	0.2	2.68	2.70	2.71	2.35	2.12	0.2	2.76	2.78	2.79	2.41	2.18
0.5	1.73	1.75	1.64	1.43	1.30	0.5	2.81	2.84	2.65	2.29	2.07	0.5	2.89	2.93	2.73	2.36	2.15
1	1.94	1.99	1.76	1.53	1.40	1	2.92	2.97	2.61	2.27	2.06	1	2.96	3.02	2.66	2.31	2.11
2	2.18	2.27	1.90	1.66	1.52	2	3.04	3.15	2.62	2.28	2.08	2	2.97	3.08	2.58	2.25	2.07
5	2.49	2.70	2.14	1.88	1.73	5	3.22	3.46	2.74	2.39	2.19	5	2.90	3.12	2.48	2.18	2.03
10	2.65	3.02	2.35	2.07	1.93	10	3.27	3.70	2.86	2.52	2.32	10	2.76	3.14	2.45	2.17	2.03
20	2.64	3.26	2.54	2.26	2.13	20	3.16	3.85	2.98	2.64	2.47	20	2.56	3.15	2.47	2.21	2.11
50	2.35	3.31	2.69	2.44	2.36	50	2.71	3.76	3.02	2.74	2.63	50	2.15	3.04	2.50	2.29	2.27
100	1.98	3.10	2.68	2.50	2.48	100	2.24	3.44	2.94	2.73	2.70	100	1.77	2.79	2.46	2.33	2.39
200	1.55	2.65	2.47	2.38	2.49	200	1.74	2.90	2.66	2.56	2.65	200	1.38	2.37	2.28	2.25	2.44
CW	1.19	2.12	2.05	2.01	2.13	CW	1.34	2.31	2.19	2.14	2.25	CW	1.07	1.91	1.90	1.91	2.09

Fig. 6.5, Tables showing the impact of the recommendations in terms of maximum temperature increase estimates, for exposures in controlled environment at 30 GHz, 60 GHz and 80 GHz.

Estimated Temperature Rise at 120 GHz (controlled)						**Estimated Temperature Rise** at 160 GHz (controlled)						**Estimated Temperature Rise** at 200 GHz (controlled)					
FWHM:	0.005	0.01	0.02	0.03	0.1	**FWHM:**	0.005	0.01	0.02	0.03	0.1	**FWHM:**	0.005	0.01	0.02	0.03	0.1
t [sec]	°C	°C	°C	°C	°C	t [sec]	°C	°C	°C	°C	°C	t [sec]	°C	°C	°C	°C	°C
0.05	2.98	2.99	3.00	2.86	-	0.05	3.22	3.23	3.24	3.09	2.77	0.05	3.46	3.47	3.48	3.32	2.98
0.1	3.06	3.07	3.08	2.80	2.52	0.1	3.28	3.29	3.30	3.00	2.70	0.1	3.49	3.50	3.52	3.20	2.88
0.2	3.13	3.15	3.16	2.73	2.47	0.2	3.32	3.35	3.35	2.90	2.62	0.2	3.50	3.53	3.54	3.05	2.76
0.5	3.19	3.23	3.00	2.60	2.37	0.5	3.35	3.39	3.15	2.72	2.47	0.5	3.48	3.53	3.28	2.84	2.58
1	3.20	3.27	2.87	2.49	2.28	1	3.32	3.39	2.98	2.59	2.36	1	3.43	3.50	3.07	2.67	2.44
2	3.16	3.28	2.74	2.38	2.19	2	3.26	3.37	2.82	2.45	2.25	2	3.34	3.45	2.88	2.51	2.31
5	3.02	3.25	2.58	2.27	2.11	5	3.09	3.32	2.63	2.31	2.15	5	3.14	3.37	2.68	2.35	2.18
10	2.85	3.23	2.52	2.23	2.09	10	2.90	3.28	2.56	2.26	2.12	10	2.94	3.32	2.59	2.28	2.15
20	2.63	3.22	2.51	2.25	2.15	20	2.66	3.25	2.54	2.27	2.17	20	2.69	3.28	2.56	2.29	2.19
50	2.19	3.08	2.53	2.32	2.30	50	2.21	3.10	2.55	2.33	2.31	50	2.23	3.12	2.56	2.35	2.32
100	1.80	2.82	2.48	2.35	2.40	100	1.82	2.84	2.50	2.36	2.41	100	1.83	2.86	2.51	2.37	2.42
200	1.40	2.40	2.29	2.26	2.45	200	1.41	2.41	2.30	2.27	2.46	200	1.42	2.42	2.31	2.28	2.46
CW	1.08	1.92	1.91	1.92	2.10	CW	1.09	1.93	1.92	1.93	2.11	CW	1.10	1.94	1.93	1.93	2.11

Fig. 6.6, Tables showing the impact of the recommendations in terms of maximum temperature increase estimates, for exposures in controlled environment at 120 GHz, 160 GHz and 200 GHz.

As can be seen from figures 6.1 to 6.6, the application of modified ICNIRP recommendations may lead to a maximum temperature increase of 0.77 °C for uncontrolled environment and 3.85 °C for controlled environment. Accepting ICNIRP's initial OAHET of 5°C temperature elevation for type 1 tissue (to prevent absolute skin temperature in excess of 41 °C) would mean that, based on our analysis and recommendations, there would be a reduction factor of at least 6.5 for localized exposures above 6 GHz in uncontrolled environment and a reduction factor of at least 1.3 for controlled environment.

Appendix A - Validity of PBHTE in computational dosimetry

Appendix A summary: A summary of the scientific evaluation of the Pennes Bio Heat Transfer Equation which is used in the approximate Gaussian model to estimate the temperature elevation in human tissue after the specific absorption rate (heat source) has been estimated using plane wave propagation solutions in plane layered human tissue model. Several scientific papers, including ICNIRP's workshop report on thresholds for thermal damage, were evaluated to conclude that the Pennes Bio Heat Transfer Equation, although not an exact model, can be used to provide temperature increase estimates with sufficient accuracy.

A.1 Review of the ICNIRP Thermal Workshop

There have been significant advances in computational dosimetry which can be a useful tool for estimating absorbed doses or dose rates and their related temperature increases in human tissues for various exposure conditions. However, since computational dosimetry is based on a biophysics model, the validity of its estimated doses and related temperature increases is dependent on i) the validity of the model itself (e.g. Pennes Bio Heat Transfer Equation - PBHTE), ii) the determined normal exposure conditions and iii) the variation in thermoregulatory capacity across sensitive groups in the population. The model that is mainly used to estimate temperature increases is the PBHTE (introduced in 1948) which has not changed much since its inception. There are still open questions regarding the amount of precision required for thermal and spatial averaging (ICNIRP, 2016). The model essentially includes a heat diffusion term with time-dependence, a heat source term that is directly related to SAR for RFEMF sources and a heat sink term that is associated with normal blood flow in human tissues. It should be noted that the blood perfusion factor (heat sink term) has a significant impact on steady-state temperature estimate and can increase significantly with temperature up to ten fold, likely due to vasodilation effects (ICNIRP, 2016).

Since this model is essentially a differential equation of time and space, it can be solved numerically for a variety of geometries (e.g. organ volumes) and boundary conditions (e.g. adiabatic or air convection effects) to take into account variation of thermal properties of tissues and ambient environmental conditions. The result of its solution is essentially a fine temperature elevation map in the tissues which can then be used to assess a combination of factors required to produce thermal damage. For exposures to RFEMF below 6 GHz, there are still some questions related to what size of averaging mass should be used for the assessment. For instance, it was mentioned that 10 g of tissue is consistent with the mass of a teste but that there was insufficient research to evaluate if temperatures within smaller volumes would be better predictor of harm (ICNIRP, 2016). Also, few studies have examined the effect of recurrent elevated temperature.

The exposure conditions (size of RF beam, angle of incidence, thickness of the tissues in the exposed area, exposure duration, etc.) can be difficult to determine and yet have a significant impact on the estimated temperature increases in the tissues. Since there is consensus that absolute temperature is a better indicator than temperature increase for assessing harm, knowledge of a variety of typical exposure scenarios should be evaluated to identify conservative environmental conditions. Those could then be

identified as normal exposure conditions which are needed in computational dosimetry to set the proper boundary conditions (e.g. insulation clothes vs air cooled skin scenarios).

The thermoregulation mechanisms in humans are generally considered efficient (when subjected to thermal stress) and there is evidence to indicate that it varies across sensitive groups in the population (e.g. elderly, children and possibly pregnant women). The main thermoregulatory mechanisms are autonomic responses which use vasodilation and sweat to lose heat and conversely use shivering to generate heat and vasoconstriction to restrict blood flow to the extremities (ICNIRP, 2016). According to the ICNIRP workshop document, those thermoregulatory responses are mainly driven by skin temperatures rather than whole body core temperature. Hirata has developed models that include both the vasodilation and sweating mechanism which have been validated by experimental measurements (ICNIRP, 2016).

In order to use a biophysics model to assess proposed limits to RFEMF exposure, one must also understand how thermal damage is assessed. Computational dosimetry can be used to estimate temperature increases as a function of time but there is still some uncertainty as to how these estimates relate to thermal damage. It was acknowledged during the workshop (ICNIRP, 2016) that absolute temperature over time is the most relevant metric for predicting thermal damage (not temperature change) which means that knowledge of initial organ temperature is essential when using computational methods. Since thermal damage depends on both absolute temperature and exposure time, the concept of thermal dose could be used to assess human tissue adverse health effects. The cumulative equivalent minutes at 43 ^{o}C metric, named CEM43, has been used for guidance in medical applications. However, while the concept of CEM43 seems to be accepted for evaluating thermal tissue damage, it is not clear if this concept has any bearing on absolute tissue temperatures below 41 ^{o}C, relevant to ICNIRP's RF exposure guidelines. In other words, some studies (Moritz 1947) have not reported tissue damage for skin temperatures below 43 ^{o}C (in the study, 44 ^{o}C exposures for at least 5 hours were required in order to observe hyperemia).

The workshop (ICNIRP, 2016) on thermal damage raised interesting points regarding the relationship between thermal damage and adverse health outcomes (or end points of interest). It was emphasized during the workshop that the relationship between temperature and harm is complex, particularly because of varying thresholds across tissue and organ types. For instance, one could assess thermal damage to tissues by focussing only on the amount of cell death (or burns) or could focus more holistically on the impact of temperature elevation on organ function or whole body responses (e.g. spermatogenesis in testes, metabolism changes, strain and heart rates, circadian cycle variation). Therefore, assessing thermal damage for localized or whole body exposures is complex and may require using different endpoints to identify adverse health outcome pathways for which consideration should be given to human repair mechanisms.

A.2 Scientific Evaluation of the Pennes BHTE and Computational Dosimetry

Computational dosimetry is an interdisciplinary approach that uses computer modeling to study the interaction between electromagnetic (EM) fields and human tissues in order to assess the effects of

exposure to EM radiation. Using biological data obtained from measurements performed directly on human tissues, such as the work of (Gabriel C. *et al.*, 1996), computational dosimetry describes the phenomena appertaining to physical electromagnetic propagation in tissues. Electromagnetic simulation platforms build their exposure models by employing the methods of applied mathematics, and users observe and analyze computational results with the help of various analysis tools. Computational dosimetry enables exploration of the cases where an experimental study is not possible, difficult or unethical to perform. It is effective in revealing causal relationships and gaining insight into the role of various factors pertaining to the model, such as the ability to vary physiological parameters, and is less expensive and time consuming than other research approaches such as randomized controlled trials or prospective cohort studies. The main disadvantage of simulation modeling is that a computer model may provide an inaccurate description of the reality, when the exposure environment complexity is not well represented in the model and could show a variance between members of the population, thus resulting in inaccurate assessments.

The validity of computational dosimetry is determined by the validity of its key components. The experimental anatomical and histological data available now have led to the creation of virtual human anatomical models (using MRI imagery) that have high accuracy and resolution, cover a substantial range of the population, are poseable, morphable, and are augmented with various details to perform functionalized computations (Kainz W. *et al.*, 2019). Advances in measurement techniques and instrumentation have allowed the accumulation of a wealth of information about various physical parameters of human tissues. For example, a comprehensive up-to-date database of thermal, electromagnetic, fluidic, acoustic and other properties of tissues is maintained by the IT'IS Foundation (Hasgall PA. *et al.*, 2018). However, a reliable knowledge of physical properties of human tissues is far from being complete, the major limitation being the fact that many data for human tissues have been estimated only from ex vivo and/or animal studies (Rossmann C. *et al.*, 2014). As well, methods for measuring the physical parameters of skin in vivo are subjected to many factors which influence tissue properties, such as temperature, state of vasodilation or vasoconstriction, age, gender and ethnic differences, and so on.

For the description of the EM field-tissue interactions, computational dosimetry invokes Maxwell's equations in conjunction with suitable numerical techniques. Maxwell's equations are known to correctly describe all classical EM phenomena, and have found practical applications in numerous scientific, engineering and industrial contexts - see (Kong JA., 1986) and the literature cited therein. For moderate-sized (roughly up to several material wavelengths) parts of the human body, direct numerical techniques such as finite difference time domain method (Taflove A. *et al.*, 2005), finite element method (Sadiku MN, 2001) or fast multipole method (Chew WC. *et al.*, 2001) can provide reliable results in acceptable computation time for such commonly employed dosimetric quantities as electric and magnetic field strengths, specific energy absorption rate (SAR), specific energy absorption (SA), transmitted power density, transmitted energy density, and induced currents. Larger models or models with fine features may be currently beyond our capacity to investigate numerically because they need a large number of computational resources (cells, voxels or unknowns, depending on the computational platform used)

required in order to accurately capture spatial behaviour of the EM field, and therefore may face memory and processor power limitations.

As discussed in the new guidelines proposed by (ICNIRP, 2020), the radiofrequency (RF) EM field can affect the body via three primary biological effects, namely nerve stimulation, membrane permeabilization, and temperature elevation. It is noted that a) the nerve stimulation is not known to occur in vivo at frequencies higher than 10 MHz, b) the ICNIRP guidelines inherently provide protection against membrane permeabilization whenever the restrictions designed to protect against thermally induced harm are observed. Naturally, the temperature elevation during irradiation by the EM fields emerges as an important metric for RF exposure.

A standard mathematical formulation for predicting the temperature distribution in the capillarized biological tissue is the classical Pennes Bio Heat Transfer Equation (PBHTE) (Pennes HH., 1948). Pennes' 1948 paper has been cited more than 5400 times according to Google Scholar. As stated in (Liu, 2006, p. 1), the PBHTE "has been commonly accepted as the best practical approach for modeling bio heat transfer due to its simplicity and validity". For example, it has been adopted in the heat transfer modules of such commercial software as Sim4Life from ZMT Zurich MedTech AG (www.zmt.swiss), COMSOL Multiphysics from COMSOL Inc. (www.comsol.com), and Xfdtd from Remcom (www.remcom.com). The PBHTE has been widely used by experts in the field for computational modelling studies. Underlying theoretical analyses of the relationship between the SAR and temperature elevation in a human body exposed to the far field RF radiation have been performed by such researchers as (Hirata A. *et al.*, 2006; Kanezaki A. *et al.*, 2010; Ziskin MC. *et al.*, 2018; Zilberti L. *et al.*, 2014; Li K. *et al.*, 2019).

Physically, the PBHTE is a continuum model that assumes the following micro-scale scenario: at any given point in the tissue, the arterial blood enters the capillary compartment at the body temperature; creating heat exchange equilibrium with the local tissue; and after the blood leaves the capillary bed, it enters the venous circulation at the local tissue temperature. The main criticism against the above physical picture is that it neglects the following aspects that might have an important effect (Crezee J. *et al.*, 1990): (i) the heat transfer coupled to the mass transport of blood; (ii) the actual temperature of the arterial blood entering the capillaries, (iii) cooling/heating of individual large vessels, (iv) the role of the venous system as a whole by assuming an infinite thermal equilibrium length of different venous vessels. For a detailed analysis, references, review of various extensions of, and alternatives to, the PBHTE, we refer to (Perl W, 1962; Charny CK, 1992; Gafiychuk V. *et al.*, 1999; Liu J, 2006; Huang WH *et al.*, 2015; Shrivastava D, 2018). A critical analysis of several alternative bio-heat transfer theories given in (Arkin H. *et al.*, 1994) emphasizes their inherent complexity and lack of experimental validation, the conclusion being that the best practical approach for modeling bio-heat transfer for medical applications is the Pennes model.

In Pennes' paper (Pennes HH., 1948), the BHTE was derived by interpreting the experimentally measured temperature distributions with the help of the heat flow theory. The temperature profile was obtained by pulling fine thermocouples through the forearms of nine unanesthetized subjects – a rather invasive procedure by today's standards (Nelson DA., 1998-Jul). In (Wissler EH, 1998) several potential flaws in Pennes' presentation and analysis of experimental data (such as errors in the processing of the measured

temperature distribution, use of incorrect tissue property values) were identified. Wissler's analysis demonstrates that those errors essentially cancel each other out, and after proper scaling Pennes' experimental results show quite good agreement with the Pennes model.

In (Baish JW. *Et al.*, 1986), an artificial physical model of a microwave heated perfused tissue was experimentally tested. The phantom consisted of an EM tissue-equivalent matrix permeated by a sparse array of parallel water-carrying tubes to simulate the cooling effects of the blood perfusion. The heat source was a ridged waveguide hyperthermia applicator operating at 915 MHz. A time-dependent 3D mathematical model was constructed using finite difference time domain method. It has been shown that the measured transient thermal behaviour of the model with a physically reasonable perfusion rate or with no perfusion at all is nearly identical to that predicted by the PBHTE.

In (Crezee J. *et al.*, 1990), the temperature distribution in a perfused tissue in the proximity of a large vessel was examined both experimentally and theoretically. The laboratory experiment was conducted on an isolated bovine kidney into which a plastic tube (outer diameter 2 mm) was inserted to simulate the vessel. The tissue was kept at room temperature; the fluid passing through the tube had a higher temperature than that of the surrounding tissue, and could be heated in a step-wise manner to study transient effects. The temperature profile was measured on the outside of the tube with the help of thin thermocouple wire sensors (outer diameter approximately 50 microns). Two alternative mathematical formulations, the PBHTE from (Pennes HH., 1948) and the effective thermal conductivity theory from (Weinbaum S. *et al.*, 1985), were used. The equations were written in cylindrical coordinates with no angular dependence; they were solved analytically in the steady state case, and by separation of variables in the time-dependent case. It was concluded that both in the steady state and transient situations the bio-heat equation from (Weinbaum S. *et al.*, 1985) fits with the experimental results better than the PBHTE. Incidentally, a further theoretical study in (Weinbaum S. *et al.*, 1997) has shown that the theory of (Weinbaum S. *et al.*, 1985) is essentially equivalent to a modified Pennes model whereby the perfusion coefficient is multiplied by a correction factor (which varies between 0.6 and 0.7 for most muscle tissues) to account for the difference between the inlet artery and venous return temperatures.

In (Nelson DA. *et al.*, 1998-Aug), the Pennes model was applied to simulating temperature fields in the human brain, with its dense capillary network, for a range of environment temperatures varying from mildly warm to extremely hot, and for various arterial temperatures (normothermic vs hyperthermic individuals). The geometry modelled was a hemisphere of cerebral tissue with overlaying layers of cerebrospinal fluid, skull and scalp. Boundary conditions at the surface of the head accounted for the external heat exchange by convection and evaporation. A steady state 2D mathematical model was solved via a finite difference approach. The results showed consistency with the experimental data reported in the literature, in particular those from (Stone JG. *et al.*, 1997) obtained via direct measurement in 39 normothermic patients who were undergoing partial temporal lobectomies.

Simple and efficient models for heating of tissues with microwave energy based on the PBHTE were developed in (Foster KR. *et al.*, 2016). Within the frames of these models, the distribution of the RF energy is due to a plane wave, or assumes the form of an irradiated circular disk with the uniform or Gaussian

pattern, and the values of physical parameters were taken from the literature with no further adjustment. As well, an extensive critical survey of available experimental data on microwave heating of tissues at 3 GHz and above (including the frequency spectrum 30 GHz-300 GHz corresponding to the millimetre wave range) was carried out, with a special focus on the data of (Hendler E. *et al.*, 1963; Alekseev SI. *et al.*, 2003; Walters TJ. *et al.*, 2004; Alekseev SI. *et al.*, 2005). The predictions of the modeling study were shown to be in excellent agreement with available data. The authors arrived at a conclusion that the experimental observations support the use of the PBHTE to aid in the development and evaluation of RF safety limits at frequencies above 3 GHz and for millimetre waves, particularly when the irradiated area of skin is small and when combined with more detailed numerical models.

Thus, a review of the literature reveals that the majority of experimental results lend validity to the PBHTE model. To summarize, "for many practical applications, the simplicity of the Pennes model is appropriate to the required accuracy and the level of detailed anatomic knowledge available" (Nelson DA., 1998-Jul).

A.3 References

Alekseev SI, Radzievsky AA, Szabo I, et al. Local heating of human skin by millimeter waves: effect of blood flow. Bioelectromagnetics. 2005 Sep;26(6):489-501. DOI: 10.1002/bem.20118

Alekseev SI, Ziskin MC. Local heating of human skin by millimeter waves: a kinetics study. Bioelectromagnetics. 2003 Dec;24(8):571-81. DOI: DOI: 10.1002/bem.10137

Arkin H, Xu LX, Holmes KR. Recent developments in modeling heat transfer in blood perfused tissues. IEEE Trans Biomed Eng. 1994 Feb;41(2):97-107. DOI:10.1109/10.284920

Baish JW, Foster KR, Ayyaswamy PS. Perfused phantom models of microwave irradiated tissue. J Biomech Eng. 1986 Aug;108(3):239-45. DOI: 10.1115/1.3138609

Charny CK. Mathematical models of bioheat transfer. In: Cho YI, editor. Advances in heat transfer. Vol. 22. New York: Academic Press; 1992. p. 19-155.

Chew WC, Jin JM, Michielssen E, et al. Fast and efficient algorithms in computational electromagnetics. Boston (MA): Artech House; 2001.

Crezee J, Lagendijk JJ. Experimental verification of bioheat transfer theories: measurement of temperature profiles around large artificial vessels in perfused tissue. Phys Med Biol. 1990 Jul;35(7):905-23. DOI:10.1088/0031-9155/35/7/007

Foster KR, Ziskin MC, Balzano Q. Thermal response of human skin to microwave energy: a critical review. Health Phys. 2016 Dec;111(6):528-541. DOI:10.1097/HP.0000000000000571

Gabriel C, Gabriel S, Corthout E. The dielectric properties of biological tissues: I. Literature survey. Phys Med Biol. 1996 Nov;41(11):2231-49. DOI:10.1088/0031-9155/41/11/001

Gabriel S, Lau RW, Gabriel C. The dielectric properties of biological tissues: II. Measurements in the frequency range 10 Hz to 20 GHz. Phys Med Biol. 1996 Nov;41(11):2251-69. DOI:10.1088/0031-9155/41/11/002

Gabriel S, Lau RW, Gabriel C. The dielectric properties of biological tissues: III. Parametric models for the dielectric spectrum of tissues. Phys Med Biol. 1996 Nov;41(11):2271-93. DOI:10.1088/0031-9155/41/11/003

Gafiychuk V, Lubashevsky I. Mathematical description of heat transfer in living tissue. Lviv (Ukraine): VNTL Publishers; 1999. [See also e-prints arXiv:adap-org/9911001 and arXiv:adap-org/9911002]

Hasgall PA, Di Gennaro F, Baumgartner C, Neufeld E, Lloyd B, Gosselin MC, Payne D, Klingenböck A, Kuster N, "IT'IS Database for thermal and electromagnetic parameters of biological tissues," Version 4.0, May 15, 2018, DOI: 10.13099/VIP21000-04-0. itis.swiss/database

Hendler E, Hardy JD, Murgatroyd D. Skin heating and temperature sensation produced by infrared and microwave irradiation. In: Hardy JD, editor. Temperature. Its measurement and control in science and industry. Vol. 3, part 3. Biology and medicine. New York: Reinhold Pub. Corp.; 1963. p. 211-30. (Herzfeld CM, editor-in-chief).

Hirata A, Asano T, Fujiwara O. FDTD analysis of human body-core temperature elevation due to RF far-field energy prescribed in the ICNIRP guidelines. Phys Med Biol. 2007 Aug 21;52(16):5013-23. DOI:10.1088/0031-9155/52/16/020

Huang WH, Horng TL. Bioheat transfer and thermal heating for tumor treatment. In: Becker SM, Kuznetsov AV, editors. Heat transfer and fluid flow in biological processes. Amsterdam (Netherlands): Elsevier, Academic Press; 2015. p. 1-42.

International Commission on Non-Ionizing Radiation Protection. Guidelines for limiting exposure to electromagnetic fields (100 kHz to 300 GHz). Health Phys 118(5):483-524; 2020.

International Commission on Non-Ionizing Radiation Protection (ICNIRP, 2016). Workshop Report. A closer look at the thresholds of thermal damage: Workshop report by an ICNIRP task group. Oberschleissheim (Germany): ICNIRP; Health Phys. Vol. 111, No.3:300-306; 2016

Kainz W, Neufeld E, Bolch WE, Graff CG, Kim CH, Kuster N, Lloyd B, Morrison T, Segars P, Yeom YS, Zankl M, Xu XG, Tsui BM . Advances in computational human phantoms and their applications in biomedical engineering - a topical review. IEEE Trans Radiat Plasma Med Sci. 2019 Jan;3(1):1-23. DOI:10.1109/TRPMS.2018.2883437

Kanezaki A, Hirata A, Watanabe S, Shirai H. Parameter variation effects on temperature elevation in a steady-state, one-dimensional thermal model for millimeter wave exposure of one- and three-layer human tissue. Phys Med Biol. 2010 Aug 21;55(16):4647-59. DOI:10.1088/0031-9155/55/16/003

Kong JA. Electromagnetic wave theory. New York: Wiley; 1986.

Moritz A.R. and Henriques, Studies of Thermal Injury II. The Relative Importance of Time and Surface Temperature in the Causation of Cutaneous Burns, Am J Pathol. 1947 Sep; 23(5): 695–720

Li K, Sasaki K, Watanabe S, Shirai H. Relationship between power density and surface temperature elevation for human skin exposure to electromagnetic waves with oblique incidence angle from 6 GHz to 1 THz. Phys Med Biol. 2019 Mar 14;64(6):065016. DOI:10.1088/1361-6560/ab057a

Liu J. Bioheat transfer model. In: Akay M, editor. Wiley encyclopedia of biomedical engineering. Vol. 1. Hoboken (NJ): Wiley-Interscience; 2006. DOI:10.1002/9780471740360.ebs0571

Nelson DA. Invited editorial on “Pennes' 1948 paper revisited”. J Appl Physiol (1985). 1998 Jul;85(1):2-3. DOI:10.1152/jappl.1998.85.1.2

Nelson DA, Nunneley SA. Brain temperature and limits on transcranial cooling in humans: quantitative modeling results. Eur J Appl Physiol. 1998 Aug;78(4):353-9. DOI:10.1007/s004210050431

Pennes HH. Analysis of tissue and arterial blood temperatures in the resting human forearm. J Appl Physiol. 1948 Aug;1(2):93-122. DOI:10.1152/jappl.1948.1.2.93

Perl W. Heat and matter distribution in body tissues and the determination of tissue blood flow by local clearance methods. J Theor Biol. 1962 May;2(3):201-35. DOI:10.1016/0022-5193(62)90025-5

Rossmann C, Haemmerich D. Review of temperature dependence of thermal properties, dielectric properties, and perfusion of biological tissues at hyperthermic and ablation temperatures. Crit Rev Biomed Eng. 2014;42(6):467-92. DOI:10.1615/CritRevBiomedEng.2015012486

Sadiku MN. Numerical techniques in electromagnetics. 2nd ed. Boca Raton (FL): CRC Press; 2001.

Shrivastava D. A generic thermal model for perfused tissues. In: Shrivastava D, editor. Theory and applications of heat transfer in humans. Vol. 1. Hoboken (NJ): Wiley; 2018. p. 3-13.

Stone JG, Goodman PR, Baker KZ, Baker CJ, Solomon RA. Direct intraoperative measurement of human brain temperature. Neurosurgery. 1997 Jul;41(1):20-4. DOI:10.1097/00006123-199707000-00007

Taflove A, Hagness SC. Computational electrodynamics: the finite-difference time-domain method. 3rd ed. Boston (MA): Artech House; 2005.

Walters TJ, Ryan KL, Nelson DA, Blick DW, Mason PA . Effects of blood flow on skin heating induced by millimeter wave irradiation in humans. Health Phys. 2004 Feb;86(2):115-20. DOI: 10.1097/00004032-200402000-00001

Weinbaum S, Jiji LM. A new simplified bioheat equation for the effect of blood flow on local average tissue temperature. J Biomech Eng. 1985 May;107(2):131-9. DOI: 10.1115/1.3138533

Weinbaum S, Xu LX, Zhu L, Ekpene A . A new fundamental bioheat equation for muscle tissue: Part I - Blood perfusion term. J Biomech Eng. 1997 Aug;119(3):278-88. DOI:10.1115/1.2796092

Wissler EH. Pennes' 1948 paper revisited. J Appl Physiol (1985). 1998 Jul;85(1):35-41. DOI:10.1152/jappl.1998.85.1.35.

Zilberti L, Arduino A, Bottauscio O, Chiampi M. Parametric analysis of transient skin heating induced by terahertz radiation. Bioelectromagnetics. 2014 Jul;35(5):314-23. DOI:10.1002/bem.21842

Ziskin MC, Alekseev SI, Foster KR, Balzano Q. Tissue models for RF exposure evaluation at frequencies above 6 GHz. Bioelectromagnetics. 2018 Apr;39(3):173-89. DOI:10.1002/bem.22110

Appendix B - Validity of the approximate unpolarised Gaussian model as an RF exposure model in computational dosimetry

Appendix B - summary: An analysis of the impact of angle of incidence and polarization states on the transmitted power density in a plane layered human tissue model (either 3-layer or 4-layer model) by using an electromagnetic field propagation model for an arbitrary plane wave. A variety of transmission (equivalent to absorption in this case because all the transmitted radiation is absorbed in human tissues) coefficients were calculated for a variety of grazing angles, frequencies and for 4 polarization states. It was found that the maximum transmission coefficient was always for normal incidence and, that for such angle of incidence, the polarization states did not affect the transmission coefficient value. This was done to confirm that the simplified approximate Gaussian model's assumptions were correct because the polarization of the electric field was assumed to be linear and the plane waves were normal to the planelayers of tissues. Furthermore, a Monte Carlo analysis of transmission coefficients was performed on both the 3-layer and 4-layer models to obtain the 95^{th} percentile value for frequencies between 6 GHz and 200 GHz and compared with ICNIRP's transmission coefficients which are used to link the reference levels (outside the body) to the basic restrictions (inside the body). Since our Monte Carlo analysis demonstrated that ICNIRP's transmission coefficient is always higher than our estimates, except at 6 GHz, it means that no further evaluation of the reference levels are needed. Essentially, this means that validating the Basic Restrictions is sufficient. In the case of 6 GHz, the estimated transmission coefficient using the Monte Carlo analysis was only 10% higher then what is used in ICNIRP, so this did not affect the final recommendation because at 6 GHz the basic restrictions were already very conservative.

An analysis was conducted of the scattering of plane electromagnetic waves by a plane-layered medium for the purpose of understanding the impact of basic physical parameters for RFEMF exposures in the human body. A model was developed to solve the electromagnetic field scattering problem for an arbitrary plane wave incident on a plane-layered model composed of N layers using a well known numerical-analytical recursive method. This method was used to solve Maxwell's Equations directly in each of those N-layers by assuming the planes are infinitely wide.

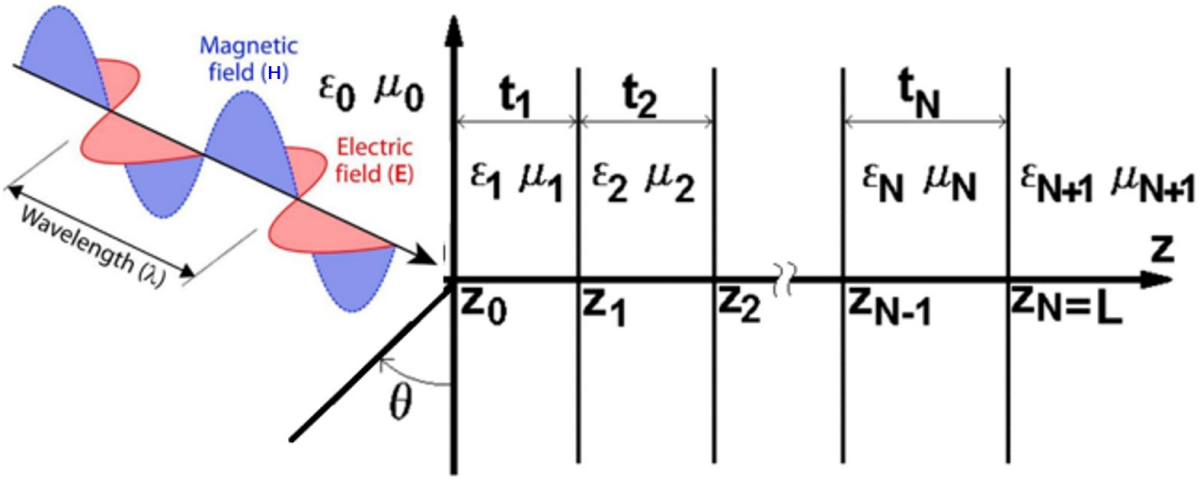

Figure B.1: Graphical representation of an arbitrary plane wave incident on plane-layered model.

In the above figure, the time-harmonic plane electromagnetic wave propagates at an arbitrary grazing angle θ. The orientation of the electric field vector E is also assumed to have a general form of elliptical polarization which means that this model can be used to solve the scattering problem for any plane electromagnetic wave.

The plane layers that compose the scattering media are defined by three parameters namely the complex permittivity "ε" (which allows the inclusion of the lossy component or conductivity), the complex permeability "μ" (typically only real values are applicable in human tissues) and the thickness "t" of the layer.

B.1 Assessment of the transmitted PD as function of Grazing Angle and polarization state

In an effort to help justify the use of the Approximate Unpolarised Gaussian Beam at Normal Incidence model described in (Section 5) for the evaluation of the conservativeness of the new ICNIRP guidelines, the arbitrary plane wave incident on a plane-layered model was used to evaluate the worst-case exposure condition (i.e. maximum transmission of energy in human tissues) in the far-field in terms of grazing angle and polarization state. Two human tissue coefficient sources were used to help generate data in the frequency range from 6 GHz up to 200 GHz. In our first 3-layer model example, which is composed of plane layers of three human tissue type (skin – SAT – muscle), the values of the relative permittivity and conductivity for those human tissues were taken from the IT'IS Foundation (Hasgall PA *et al.*,2018), as a function of frequency. The latter database can provide values of permittivity and conductivity between

10 Hz up to 100 GHz. As can be seen later in the document, another source of human tissue coefficient was used for frequencies between 60 GHz and 200 GHz from Sasaki K. *et al.*, 2014 and Sasaki K. *et al.*, 2017. In this example, the values of the skin and SAT thicknesses (1.66 mm and 6.524 mm, respectively) were chosen to be the geometric mean values for the log-normal tissue thickness distributions (see section B.2), and the muscle layer was assumed to be infinite with respect to the penetration depth of EMF above 6 GHz.

The recursive algorithm that was developed to solve the plane-layered scattering problem by numerical-analytical method was used to assess the transmitted power density in the previously mentioned three-layer human tissue model for 4 different polarization states (LH: Linear Horizontal, LV: Linear vertical, L45: Linear 45 degrees and CWC: Clockwise Circular) as a function of grazing angle and in the frequency range of 6 to 100 GHz. For simplicity, the incident plane wave power density was set to S_{inc} = 100 W/m^2.

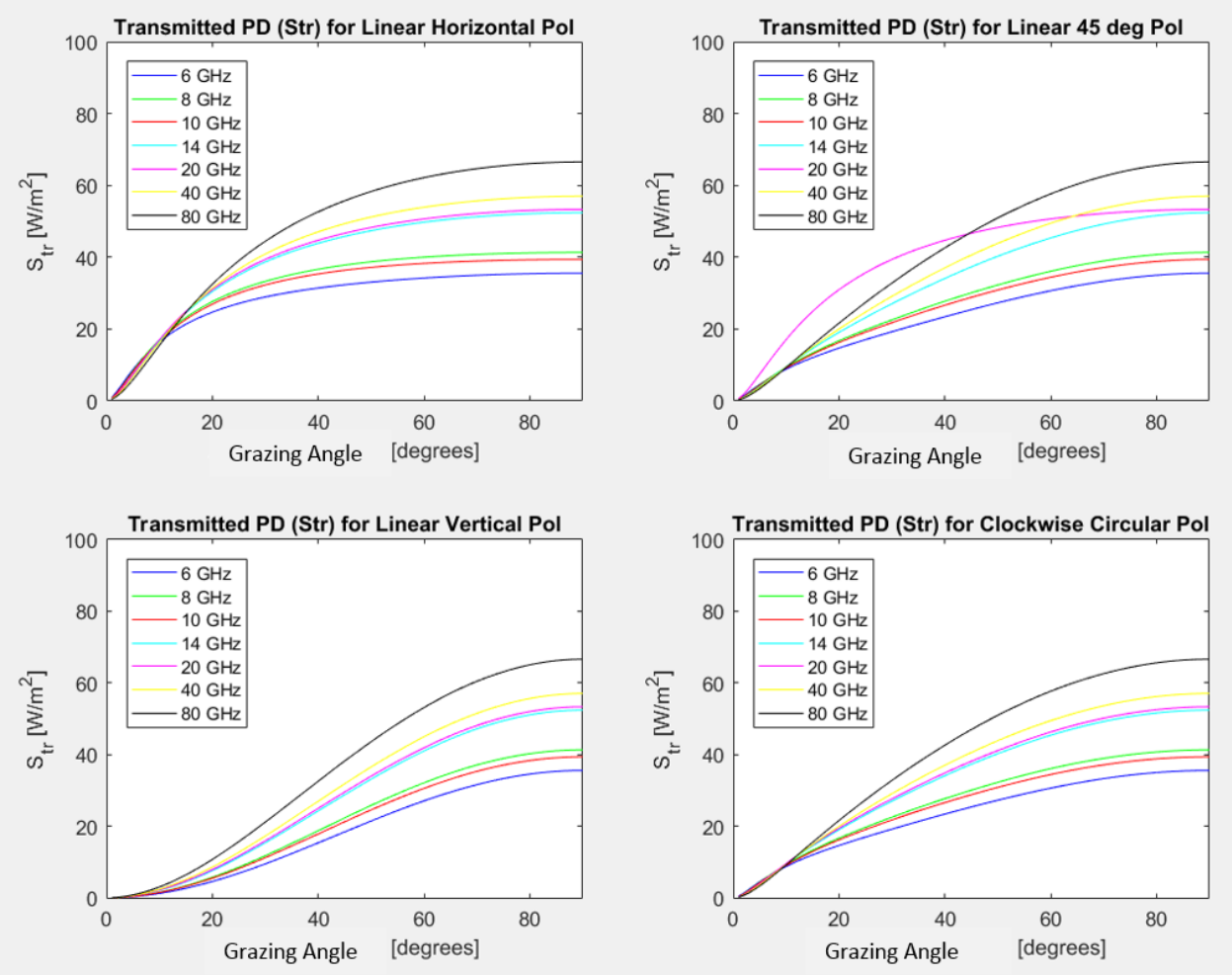

Figure B.2: Transmitted Power Density (S_{tr})curves for layers of Air = ∞ / Skin= 1.66 mm / SAT= 6.524 mm / Muscle= ∞, S_{inc} = 100 W/m^2 (2D slices of frequency)

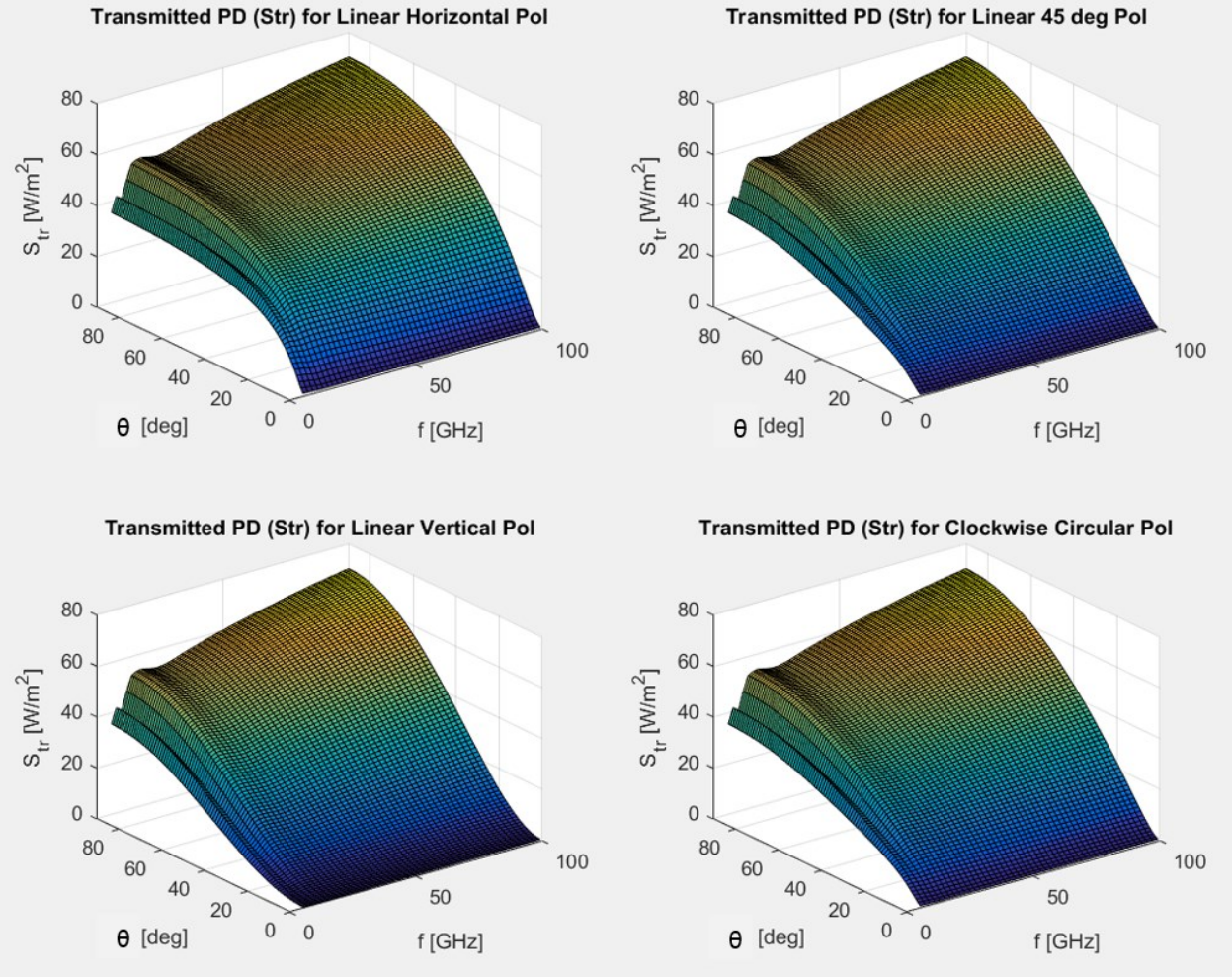

Figure B.3: Transmitted Power Density (S_{tr})curves for layers of Air = ∞ / Skin= 1.66 mm / SAT= 6.524 mm / Muscle= ∞, S_{inc} = 100 W/m^2 (3D surface plots)

As can be observed in both figures B.2 and B.3, for any frequencies and for any polarization state, the transmitted power density always monotonously increases as a function of the grazing angle to reach a peak at 90 degrees (or normal incidence). In figure B.2, one can more easily notice that the transmitted power density curves as a function of grazing angles are different depending on the polarization states. For instance, the magenta curve in the upper right quadrant of figure B.2 (Linear polarization at 45 degrees) representing the 20 GHz frequency shows a different behavior than the magenta curve in the upper left quadrant (Linear Horizontal polarization). However, for a given frequency, the curves on those four graphs (representing 4 polarization states) reach the same transmitted power density values at normal incidence. In other words, the polarization state of the electromagnetic plane wave does not matter at normal incidence which is what we intuitively expect. It should be mentioned that a few other combinations of human tissue thicknesses have been computed to verify if the transmitted power density is always maximal at normal incidence, and it remained true for the following combinations:

Skin Thickness [mm]	SAT Thickness [mm]	Observation
0. 5	2	Max transmission at normal incidence, worst-case transmission at 6 GHz (**see figure B.4**)
0.5	6.5	Max transmission at normal incidence
0.65	6.5	Max transmission at normal incidence
1	2	Max transmission at normal incidence
2	10	Max transmission at normal incidence
3	12	Max transmission at normal incidence
5	25	Max transmission at normal incidence

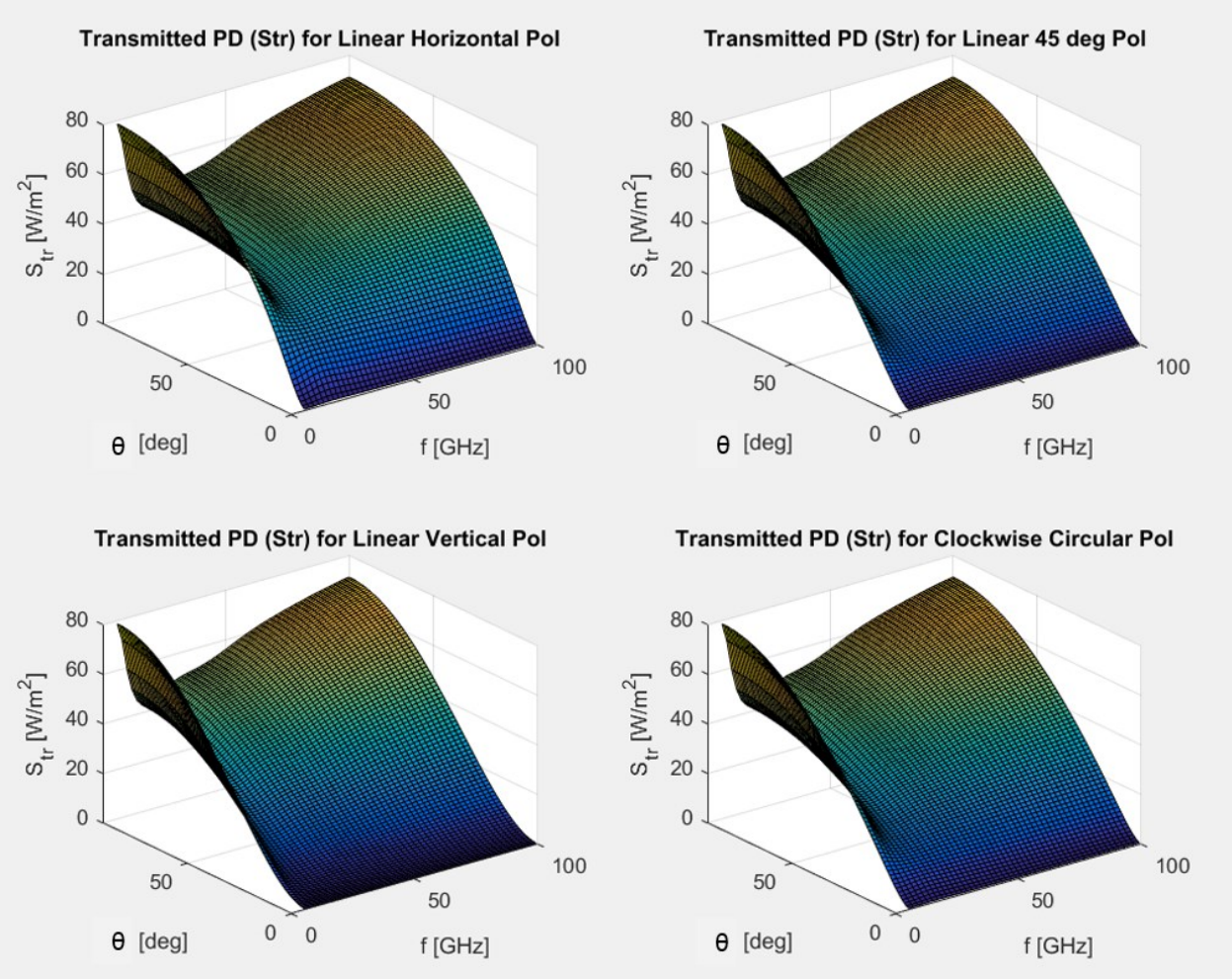

Figure B.4: Transmitted Power Density curves for layers of Air = ∞ / Skin= 0.5 mm / SAT= 2 mm / Muscle= ∞, S_{inc} = 100 W/m^2 (3D surface plots)

The previous model allowed the generation of transmitted power density values for the frequency range of 6 GHz to 100 GHz, however ICNIRP's guidance document is applicable to frequencies up to 300 GHz. Therefore, a second 4-layer model was used, composed of a stack of four human tissue type (Epidermis – Dermis – SAT – muscle), where the values of the relative permittivity and conductivity was taken from

(Sasaki K. *et al.*, 2014; Sasaki K. *et al.*, 2017). This database provides coefficient values between 60 GHz up to 200 GHz. The values of the human tissue thicknesses were chosen to be aligned with the example provided in Section 5 for the epidermis (~ 0.080 mm), the dermis (~ 1.25 mm) and SAT (~ 14.3 mm) and by assuming the muscle layer is infinite with respect to the penetration depth of the EMF above 6 GHz.

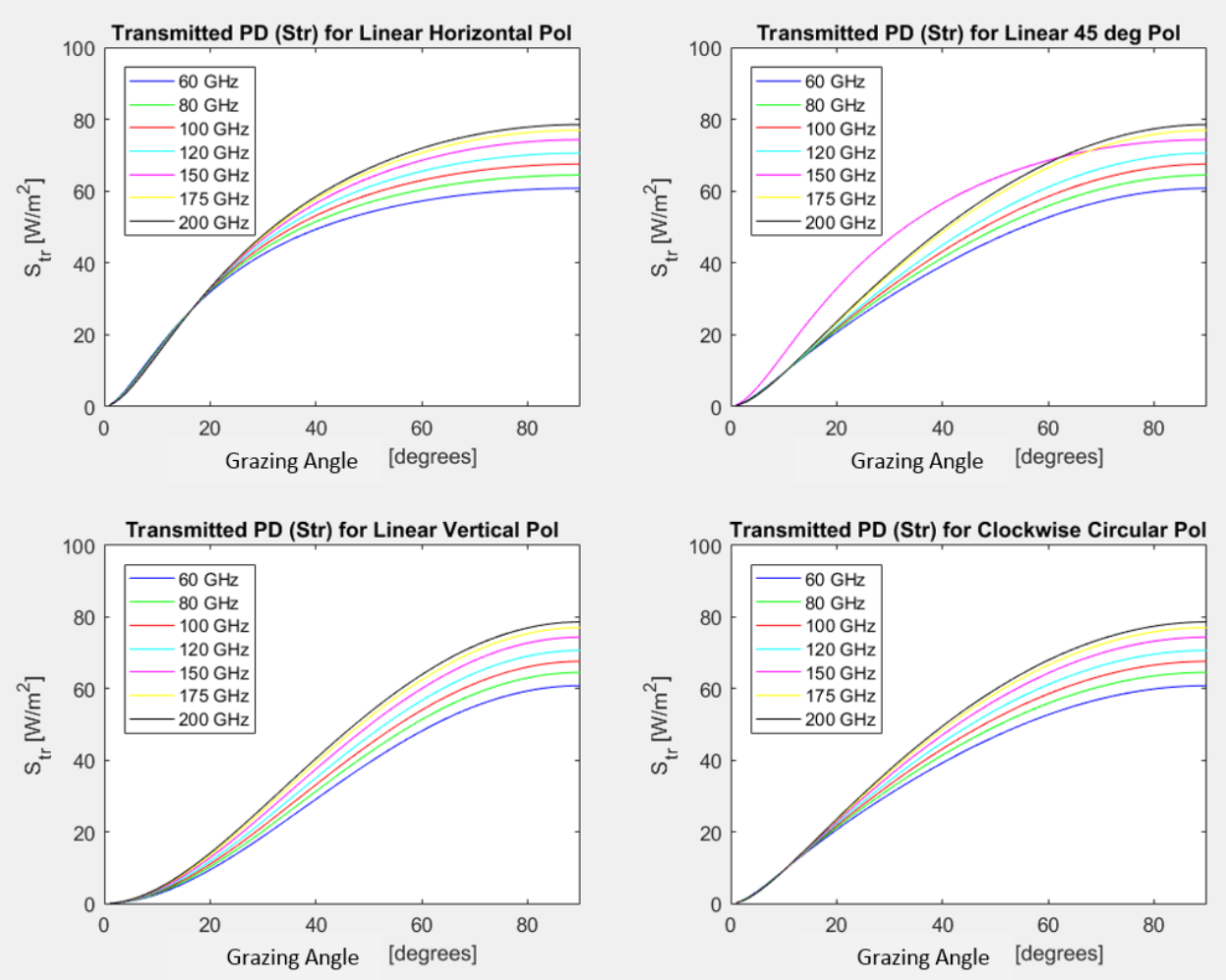

Figure B.5: Transmitted Power Density (S_{tr}) curves for layers of Air = ∞ / Epidermis = 80 µm / Dermis =1.25 mm / SAT= 14.3 mm / Muscle= ∞, S_{inc} = 100 W/m^2 (2D slices of frequency)

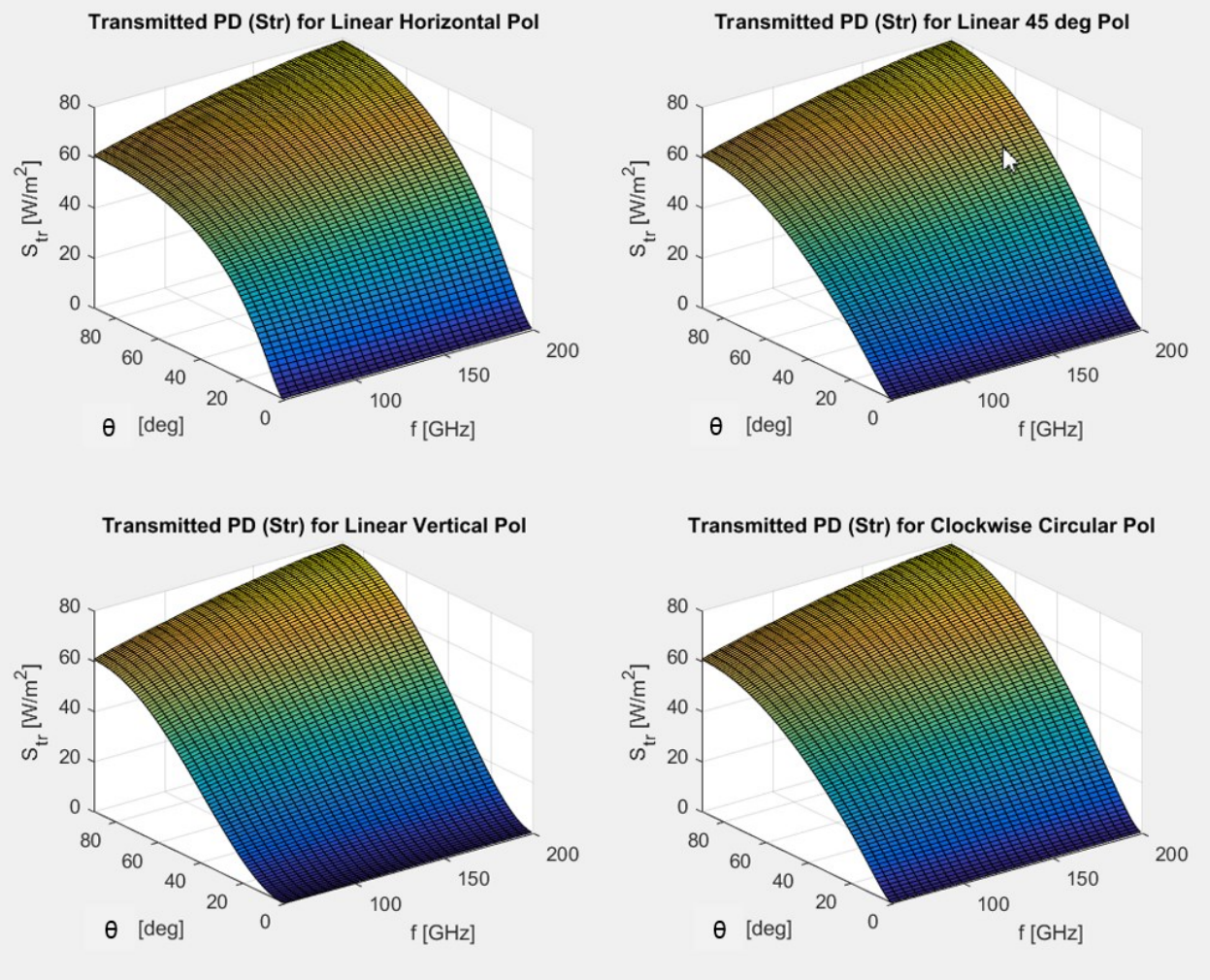

Figure B.6: Transmitted Power Density (S_{tr})curves for layers of Air = ∞ / Epidermis = 80 µm / Dermis =1.25 mm / SAT= 14.3 mm / Muscle= ∞, S_{inc} = 100 W/m^2 (3D surface plots)

As can be observed from the figures B.5 and B.6 above, the same conclusions stand for the 4-layer model in the frequency range of 60 GHz up to 200 GHz. Since the worst case exposure appear to be at normal incidence for any polarization state, the use of an approximate linearly polarized Gaussian beam at normal incidence model as a worst-case exposure model (i.e. maximum transmission in human tissues) for the evaluation of the ICNIRP guidelines appears to be justified.

B.2 Variation of transmitted power density coefficient in human skin

As mentioned above, since normal incidence is the worst case exposure scenario for a given frequency and the fact that polarization states do not affect transmitted power density (S_{TR}) at normal incidence, one can use this exposure condition to estimate the worst-case transmitted power density coefficient (ratio of transmitted power density / incident power density) as a function of frequency. In an effort to consider the variation of transmitted power density coefficient in human populations, the values of human tissue thicknesses were varied according to their distribution profiles (see figure B.7 and B.8)

where Monte Carlo simulations were performed as a function of frequency. Essentially for each frequency, 10,000 iterations were simulated where the value for skin and SAT thicknesses were generated randomly, for each iteration, within their respective distributions. The transmitted power density coefficients for the 95th percentile and 5th percentile were extracted as function of frequency to be compared against the ratio of ICNIRP's basic restrictions inside the body (i.e. absorbed power or energy density) to the reference levels outside the body (i.e. power or energy density). This ratio represents the absorption coefficient formula as a function of frequency considered by the (ICNIRP, 2020) Guidelines (same ratio found in IEEE, 2019). Using the new ICNIRP Guidelines Basic Restriction of S_{TR} (100 W/m^2) and the associated power density Reference Levels of (275 f_G $^{-0.177}$ W/m^2, f in GHz) the formula for the absorption coefficient can be calculated as being: 0.3636 f_G $^{0.177}$.

The statistical models of the skin and SAT thicknesses were derived from data contained in (Anderson *et al.*, 2010; Kakasheva *et al.*, 2011). The first reference gives average skin thicknesses for males and females in 3 age groups and for 8 different body sites resulting in a total of 48 thickness values. The second gives average thicknesses for 5 age groups and 15 body sites with no distinction between sexes. Some of the body sites in Kakasheva et al. were omitted from inclusion because of their location (e.g. soles, lower leg, etc.). There was a combined total of 93 data points used to estimate the distribution, which is shown in figure B.7(a) below. It was decided that a log-normal distribution would adequately model the distribution of skin thicknesses and it is shown in figure B.7(b) with its corresponding distribution parameters (geometric mean or GM and geometric standard deviation or GSD).

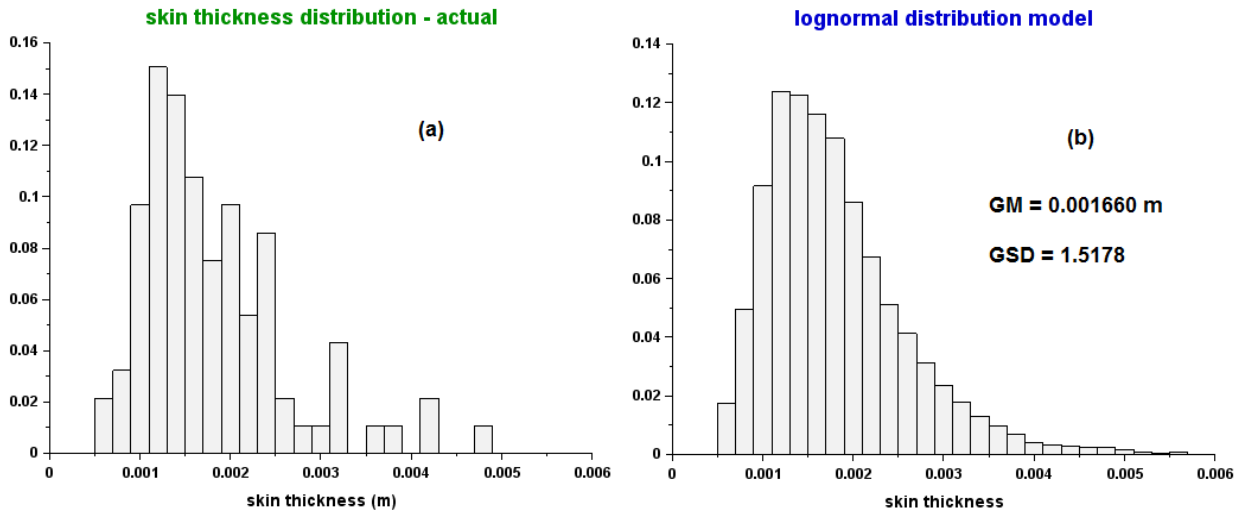

Figure B.7 (a) Distribution of average skin thicknesses for male and females in 3 age groups and 8 body sites (Anderson *et al.*, 2010; Kakasheva *et al.*, 2011), (b) Log-normal distribution used to model the distribution in (a).

The SAT data in (Anderson *et al.*, 2010;) was used for modelling the thickness of SAT. Average SAT thicknesses were tabulated for both sexes in 3 age groups and for 8 body sites. The distribution is shown in figure B.8(a) along with the log-normal distribution that closely approximates it in figure B.8(b).

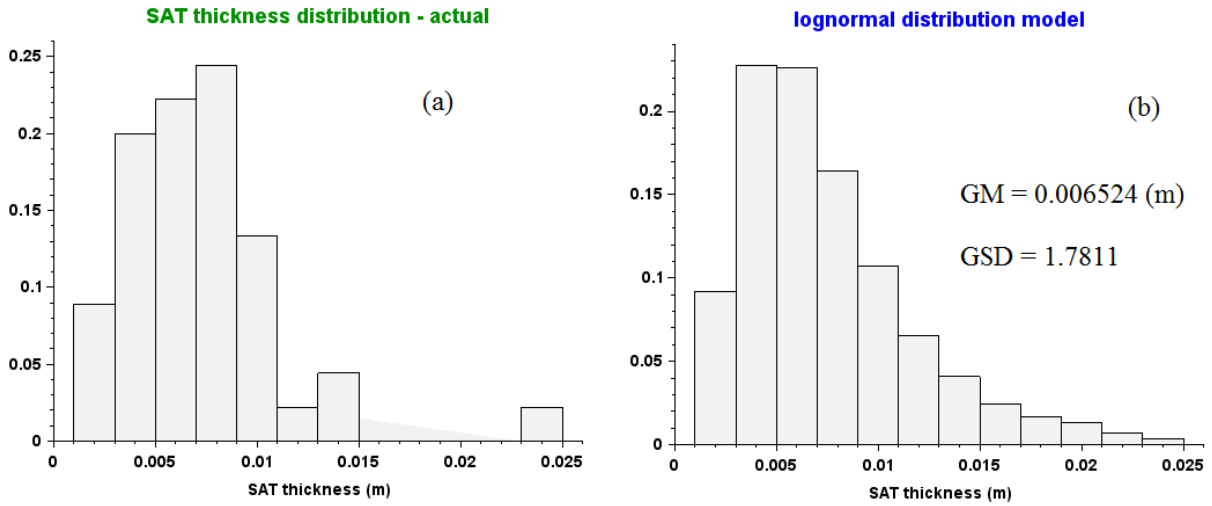

Figure B.8 (a) Distribution of average SAT thicknesses for male and females in 3 age groups and 8 body sites (Anderson *et al.* 2010), (b) Log-normal distribution used to model the distribution in (a).

For the 3-layer model, the skin and SAT tissue thicknesses were varied within the tissue thickness distributions (from Anderson *et al.*, 2010; Kakasheva *et al.*, 2011):

- Skin layer varied according to log-normal distribution of figure B.7(b).
- SAT layer varied according to log-normal distribution of figure B.8(b).
- Muscle – infinite thickness, no variation.

The blue curve represents the 95th percentile value of the transmitted power density coefficient of the Monte Carlo simulation while the magenta curve represents the 5th percentile value. The red curve represents the absorption coefficient (or alternatively the transmitted power density coefficient) formula considered by both ICNIRP and IEEE.

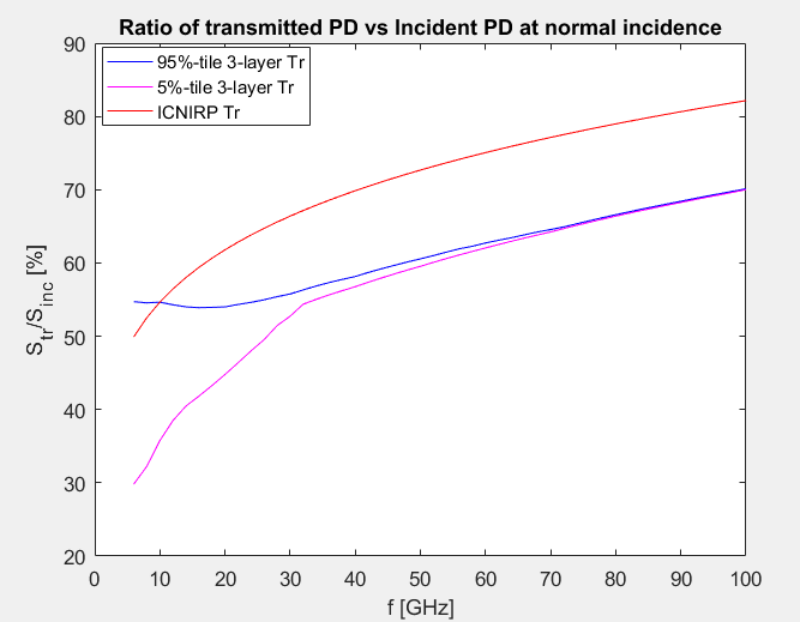

Figure B.9: Ratio of (S_{TR}/S_{inc}) calculated with the arbitrary plane wave algorithm for a 3-layer model based on IT'IS database (Hasgall PA *et al.*,2018), versus ICNIRP's absorption coefficient formula

For the 4-layer model, the skin and SAT tissue thicknesses were varied within the tissue thickness distributions (from Anderson *et al.*, 2010; Kakasheva *et al.*, 2011) with the exception that the skin thickness was subdivided into epidermis and dermis layers. In the absence of specific epidermis and dermis thickness distribution data, the sum of those two were taken to be equal to the skin thickness where the epidermis was assumed to represent 7% (~ 80 µm / 1.25 mm):

- Epidermis layer varied according to log-normal distribution of figure B.7(b) X 7%
- Dermis layer varied according to log-normal distribution of figure B.7(b) X 93%
- SAT layer varied according to log-normal distribution of figure B.8(b).
- Muscle – infinite thickness, no variation.

The curve colors have the same meaning as described for figure B.9.

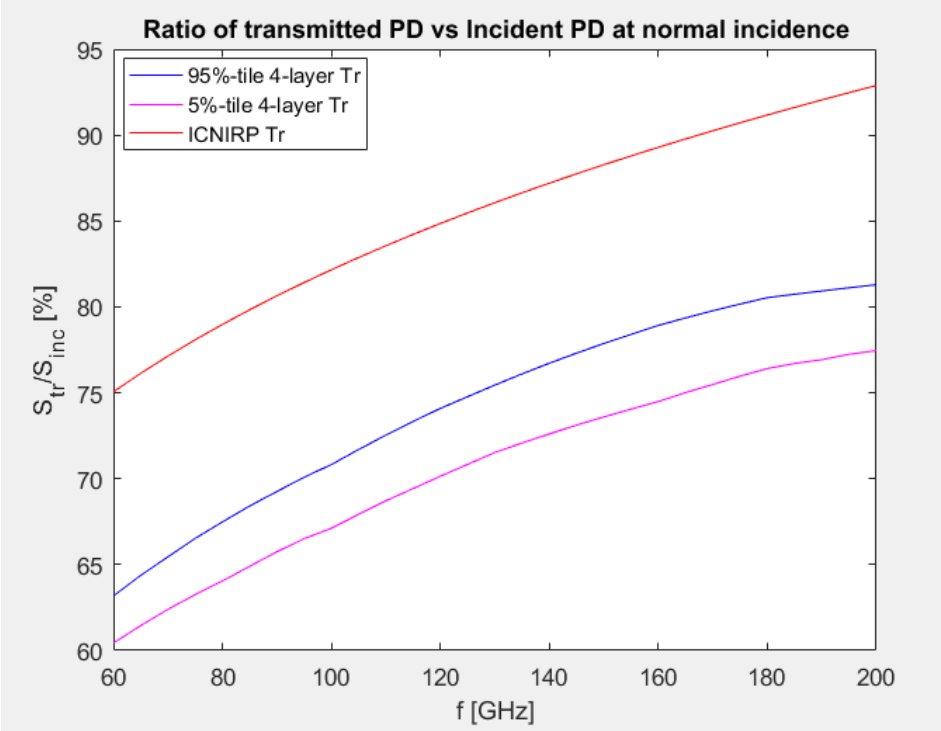

Figure B.10: Ratio of (S_{TR}/S_{inc}) calculated with the arbitrary plane wave algorithm for a 4-layer model based on Sasaki database (Sasaki K. *et al.*, 2014; Sasaki K. *et al.*, 2017) versus ICNIRP's absorption coefficient formula.

According to figure B.9 and B.10, ICNIRP's proposed absorption coefficient ratio appears to be more conservative than what was calculated using the 95th percentile estimate, in the frequency range from 30 GHz up to 200 GHz, by approximately 15%. Within that frequency range the estimated 5th percentile and 95th percentile power density transmission coefficients appear to be close together with more or less a small variation. This suggest that the absorption of the power density is mainly superficial and that potential "tuning effect" of multiple layers does not play a significant role. It should be mentioned that since ICNIRP's formula is proposing a power density absorption ratio between 93% up to 100 % for the frequency range of 200 GHz up to 300 GHz, there is no significant reason to model the absorption

coefficient in that frequency range. Those values are already very conservative because ICRNIP is assuming that almost all of the energy will be absorbed.

However, as can be seen in figure B.9, for lower frequencies there appears to be a significant impact on the transmission coefficient when varying the human tissue thicknesses. This can be readily observed by noticing the separation between the estimated 5th percentile power density transmission ratio versus the estimated 95th percentile value. This can likely be explained by the fact that the penetration depth in human tissues is greater at lower frequencies. In that situation, it appears that the multiple interfaces with different electromagnetic parameter values (e.g. permittivity, conductivity) can be adjusted (or tuned) in terms of thicknesses to either maximize or minimize the transmission coefficient.

Nevertheless, even when considering our worst-case 95th percentile estimate, ICNIRP's absorption coefficient formula as function of frequency appears to be sufficiently conservative down to approximately 10 GHz. At 6 GHz, our worst-case 95th percentile estimate for the transmitted power density coefficient is ~ 55% while ICNIRP proposes to use 50%. This difference is small enough considering the uncertainties that come with computational dosimetry estimates and is therefore not considered an issue. Based on the available data in the It'Is and Sasaki databases, it is reasonable to assume that validating the relationship between ICNIRP's basic restrictions and the related temperature increase should suffice for all frequencies above 6 GHz because the relationship considered between the incident power density and the absorbed power density of ICNIRP appear to be conservative at normal incidence. Therefore, the approximate unpolarised Gaussian beam at normal incidence model, which has the added feature of using Monte Carlo analysis to assess the effect of tissue variation across population, is appropriate for the evaluation of the ICNIRP guidelines basic restrictions.

B.3 References

Anderson V, Croft R and McIntosh RL, "SAR versus Sinc: What is the appropriate RF exposure metric in the range 1-10 GHz? Part1: Using planar body models," Bioelectromagnetics 31:454-466 (2010). DOI 10.1002/bem.20578

Hasgall PA, Di Gennaro F, Baumgartner C, Neufeld E, Gosselin MC, Payne D, Klingenböck A, Kuster N, "IT'IS Database for thermal and electromagnetic parameters of biological tissues," Version 3.0, September 01st, 2018, DOI: 10.13099/VIP21000-03-0.

Kakasheva-Mazenkovska L, Milenkova L, Gjokik G and Janevska V, "Variations of the histomorphological characteristics of human skin of different body regions in subjects of different age," Contributions, Sec. Biol. Med. Sci., MASA, XXXII/2:119-128 (2011).

Sasaki K, Wake K, Watanabe S, "Measurement of the dielectric properties of the epidermis and dermis at frequencies from 0.5 GHz to 110 GHz." Phys. Med. Biol. 59, 4739–4747, 2014

Sasaki K, Mizuno M, Wake K, Watanabe S, "Monte Carlo simulations of skin exposure to electromagnetic field from 10 GHz to 1 THz", Phys. Med. Biol. 62 6993-7010, 2017

Appendix C - Minimum beam diameter as function of frequency for typical telecommunication antennas

Appendix C - summary: An analysis of practical minimum beam diameters that can be emitted from existing radio communication devices. The minimum beam diameters for single element antennas and antenna arrays were theoretically investigated. It was found that, although array antennas have more directional radiation patterns (smaller angular beam width), the resulting beam diameter at the beginning of the far-field is not smaller than the beam diameter of a single element because the far-field is much further away for an antenna array. The minimum beam diameter that can be generated from a single element antenna (i.e. dipole antenna) in the practical far field is typically in the order of a wavelength. The results of this appendix was used to determined that the smallest beam diameter that should be considered for frequencies below and equal to 30 GHz is 10 mm while for frequencies above 30 GHz a beam diameter as low as 5 mm was considered.

Both the ICNIRP guidelines (ICNIRP, 2020) and IEEE standard (IEEE, 2019) use a fixed averaging area for evaluating either the basic restrictions (DRLs) or reference levels (ERLs). The fixed averaging area is 4 cm^2 for frequencies below 30 GHz and an additional averaging area of 1 cm^2 is recommended for evaluation of exposures above 30 GHz. The rationale behind this additional criterion is that the projected beam diameter can be smaller for higher frequencies and is typically thought to be in the order of a few wavelengths. (In the remaining discussion it should be emphasized that the “beam diameter” is a measure of the power or energy density projected on a planar tissue surface and should not be confused with the angular measure of beam width in classical antenna theory.) The localized exposure temperature increase is related to the actual beam diameter (i.e. not the averaging area). Therefore, if an averaging area much larger than the beam diameter is used, it could result in an under-estimatation of the thermally-significant power or energy density. Since our evaluation is based on temperature increase estimates for set beam diameters using an approximate Gaussian planar model, it is important to estimate the reasonable minimum beam diameter and related SAR spot size that can be achieved for communication antennas as a function of frequency. Analyzing a recommended limit using a beam diameter that is unachievable for a particular frequency could lead to a misleading conclusion, for instance that the limit is not conservative enough when in fact the exposure condition is impossible.

This appendix explores realistic minimal beam diameters that could be expected from telecommunication devices for applications above 6 GHz. First, the beam diameter obtained for simple, single radiating elements at the beginning of the far field is investigated. Secondly, because array antennas could be used for novel communication devices, the theoretical array form factor for a summation of single elements can be used to estimate the smallest beam spot size that can be achieved for high gain antennas in the far field. Finally, since the important factor to consider when estimating temperature increases is the actual SAR spot size, simulations have been conducted for both single radiating elements and small arrays of single elements to estimate the projected beam diameter on a tissue plane in the near-field and the related SAR spot size.

C.1 Estimated beam diameters of typical single elements

Beam diameters are estimated using the radiation properties of two radiators commonly used as elements of antenna arrays [Stutzman W. L., 2013 p. 329, Tab. 8-2]. In the pattern formulas for these elements, we have neglected the constant factors which arise from the amplitudes of the source distributions, as they are inessential for the analysis to follow. The concepts of the far zone and the radiation pattern which are employed below, are discussed in greater detail in Section C.2.2.

C.1.1 Half-wave dipole

Centre-fed half-wave dipoles have an omnidirectional pattern in the plane that includes the feed point (aka the H-plane) and a narrow pattern in the plane that includes the dipole axis (aka the E-plane). The estimate of beam diameter will be the average of the projected beam sizes in these two principle planes. For a center-fed linear wire antenna of total length d, the far-field radiation pattern in the E-plane under the thin wire approximation is given as [Balanis C, 2005 - Sec. 4.5.2, p. 173, Eq. (4-64)]

$$\mathrm{F_e} = \frac{\boldsymbol{\theta_0}}{\sin\theta}\left[\cos\left(\frac{\pi d}{\lambda}\cos\theta\right) - \cos\left(\frac{\pi d}{\lambda}\right)\right] \qquad \text{(Eq. C.1.1)}$$

Here $\boldsymbol{\theta_0}$ is the unit vector along θ of the spherical coordinate system L, θ, ϕ shown in Fig. C.1.1. To have one lobe, the length should satisfy $d < \lambda$. For a half-wavelength dipole ($d = \lambda/2$), the radiation maximum lies on the H-plane, i.e. is in the perpendicular direction ($\theta = \pm\pi/2$).

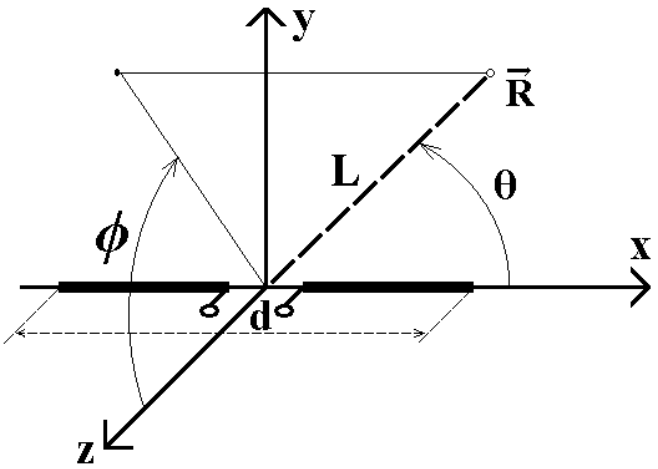

Fig. C.1.1: Spherical coordinate system L, θ, φ, and a center-fed dipole.

Since the projected beam diameter depends on the distance between the radiator and the projection plane, this will be taken as the smallest distance where far-field conditions can be established. Various definitions of the far-field distance exist, e.g. some are based on criteria for the establishment of the far-field pattern of arrays of single elements. At distances shorter than the minimal far-field distance, the

beam of an array of elements will not be properly formed (i.e. patterns of individual elements will be apparent).

In the case of single elements, the practical minimum far-field distance (not necessarily the exact far field distance but where a minimum spot size can be observed in human tissue) is:

$$L_{min} = \frac{2D^2}{\lambda} \qquad \text{(Eq. C.1.2)}$$

This equation (Eq. C.1.2) will be used to estimate the distance between the dipole and the projection plane and subsequently the half-power projected beam diameter (HPBD) from the formula (Eq. C.1.1). In the latter equation, the value of d/λ is replaced by ½. The angular beam width, $\Delta\theta_{3dB}$, for half-wave dipoles is known to be approximately 1.36 radians (or 78 degrees). The projected, E-plane beam diameter at the beginning of the far-field, $L_{min} = \frac{2D^2}{\lambda} = \frac{2}{\lambda}\left(\frac{\lambda}{2}\right)^2 = \frac{\lambda}{2}$ is therefore found to be:

$$HPBD_E \approx 2\left(\frac{\lambda}{2}\right)\tan\frac{\Delta\theta_{3dB}}{2} \qquad \text{(Eq. C.1.3)}$$

This estimate does not take into account path loss taper at the edges of the beam and is an approximation since, at such close distance between the dipole and projection plane, the pattern formula Eq. C.1.1 is less accurate. Using the angular beam width of 78 degrees, the $HPBD_E$ is approximately 0.8 λ.

For the H-plane, the antenna becomes a point source and the path loss taper is accounted for in the estimate of beam size. The path length to the projection plane is L_{min} while the length at the beam edge is $[L_{min}^2 + (HPBD_H/2)^2]^{1/2}$, where $HPBD_H$ is the half-power, projected beam diameter. Assuming square-law path loss and a 3 dB greater loss at the beam edge, the following relationship holds:

$$1/\left(L_{min}^{\ 2} + (HPBD_H/2)^2\right) = \frac{1}{2}\left(1/L_{min}^{\ 2}\right) \qquad \text{(Eq. C.1.4)}$$

Eq. C.1.4 gives $HPBD_H$ = λ when L_{min} = λ/2. Again, this is a gross estimate since square-law path attenuation was assumed at such close distance to the antenna.

The average of the E-plane and H-plane beam diameters gives $HPBD \approx 0.9$ λ. Given the large degree of approximation used in its derivation, it is reasonable to estimate the minimum beam diameter for a half-wave dipole in the practical far-field to be in the order of a wavelength.

C.1.2 Rectangular aperture antenna element

For the rectangular aperture of dimensions $a \times b$ ($a > b$; here the meaning of a, b differs from that of similar symbols used elsewhere in this Appendix) mounted on an infinite ground plane, assuming the TE_{10} mode distribution, the radiation pattern is given by [Balanis C, 2005 - pp. 672-673, Tab. 12.1]:

$$\mathrm{F_e} = (\boldsymbol{\theta_0}\ \sin\phi + \boldsymbol{\phi}_0 \cos\theta\ \cos\phi)\ \frac{\cos X}{X^2 - \left(\frac{\pi}{2}\right)^2}\ \frac{\sin Y}{Y} \qquad \text{(Eq. C.1.5)}$$

$$X = \frac{\pi a}{\lambda}\ \sin\theta\cos\phi \qquad \text{(Eq. C.1.6)}$$

$$Y = \frac{\pi b}{\lambda}\ \sin\theta\sin\phi \qquad \text{(Eq. C.1.7)}$$

Here $\boldsymbol{\theta_0}$ and $\boldsymbol{\phi}_0$ are the unit vectors along θ and ϕ, respectively, for the spherical coordinate system L, θ, ϕ shown in Fig. C.1.2. The practical minimum far zone distance for the aperture is defined by (Eq. C.1.2), where D should be replaced by $\sqrt{a^2 + b^2}$.

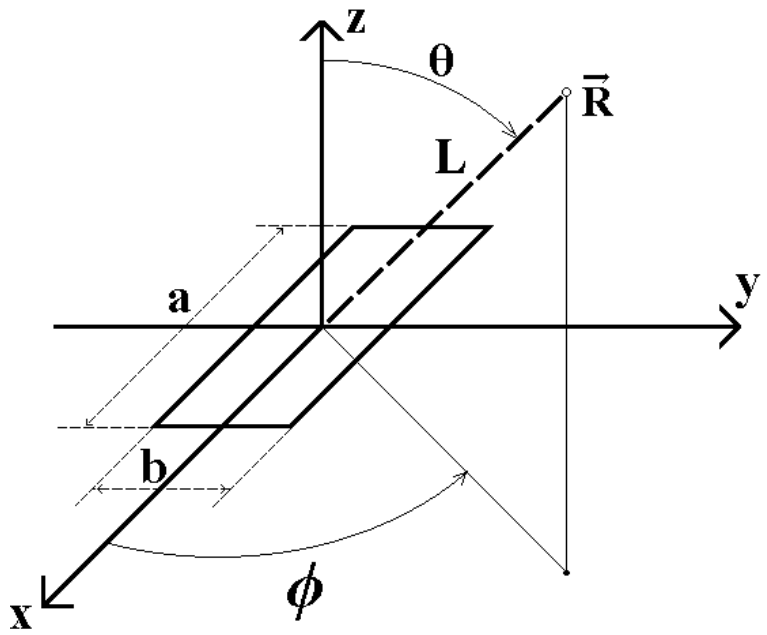

Fig. C.1.2: Spherical coordinate system L, θ, φ, and a rectangular aperture in a conducting plane.

To estimate the minimum beam diameter versus wavelength for the rectangular aperture antenna (assuming the TE_{10} mode), the far-field distance (Eq. C.1.2) is used along with the formula shown in (Eq. C.1.5). Since in the latter formula, the value of interest is the norm or modulus of the field vector, the equation can be simplified as:

$$|\boldsymbol{F_e}| = \sqrt{1\text{-}(\sin\theta\ \cos\phi)^2}\ \left|\frac{\cos X}{X^2 - \left(\frac{\pi}{2}\right)^2}\ \frac{\sin Y}{Y}\right| \qquad \text{(Eq. C.1.8)}$$

For the estimates of minimum beam diameters, multiple pairs of values have been used for a and b where the following condition has been respected $a > b$. For each pair, the angular beam width $\Delta\theta_{3dB}$ has been computed numerically for the two principle planes: $\varphi = 0$ and $\varphi = \pi/2$ upon which the average value is used to estimate the beam diameter in the far-field. The results obtained for the numerical computations are summarized in Table C.1.1.

Table C.1.1: Summary of the results obtained for the rectangular aperture antenna:

a	$\lambda/2$	0.3λ	λ	2λ	3λ	10λ	4λ	5λ
b	0.24λ	$\lambda/2$	$\lambda/2$	λ	2λ	5λ	2λ	2λ
D	0.693λ	0.781λ	1.118λ	2.236λ	3.606λ	11.18λ	4.472λ	5.385λ
L_{min}	.96 λ	1.22 λ	2.5 λ	10.0 λ	26 λ	250 λ	40 λ	58 λ
$\Delta\theta_{3dB}$, $\varphi = 0$	1.396	1.326	1.028	0.586	0.400	0.123	0.304	0.244
$\Delta\theta_{3dB}$, $\varphi = \frac{\pi}{2}$	2.513	2.304	2.304	0.950	0.460	0.183	0.460	0.460
$\Delta\theta_{3dB,ave}$	1.955	1.815	1.666	0.768	0.430	0.153	0.382	0.352
$\frac{HPBD}{\lambda}$	2.85	3.12	5.50	8.08	11.36	38.32	15.47	20.63

According to the few scenarios computed in Table C.1.1, the minimum beam diameter found for the rectangular aperture antenna (assuming TE_{10} mode distribution) is approximately 3 times the wavelength.

C.2 Theoretical beam diameters for antenna arrays

This section contains a brief analysis of the minimum attainable beam diameter created in the far zone by an antenna array.

C.2.1 Antenna arrays and super-directivity

Antenna arrays are typically composed of multiple identical antennas called elements (examples include waveguide horns, waveguide slots, micro-strip patch antennas, micro-strip patch slots, substrate integrated waveguides etc.) arranged in a regular manner on a plane or a straight line. The basic physics behind antenna arrays is the interference between the radiowaves radiated by each individual element.

These waves combine constructively in certain directions, and superpose destructively in other directions depending on their relative amplitude and phase. The interference phenomenon is controlled by properly choosing the excitations of the individual antennas. This principle permits effective beam shaping and steering, that is the array beam can be made much narrower than the radiation pattern of an individual element, and its direction can be altered electronically, without tilting the array, by changing the phase of the excitations. These and other performance characteristics [Balanis C, 2005 - Sec. 1.5.1], [Stutzman W. L., 2013- Ch. 8], together with a relatively low cost, have made phased antenna arrays a viable option in the 5G cellular networks especially for the implementation of the multiple-input multiple-output (MIMO) communication technology [Hussaini AS *et al.*, 2015 - Sec. 11.2.1], [Tölli A. *et al.*,2016], [Chien T. V. *et al.*, 2017].

Theoretically, it is possible to synthesize an antenna array that realizes *any given directivity* [Bouwkamp C. J. *et al.*, 1945], [Riblet H. J., 1948], [Yaru N., 1951]. A review of practical implementations of such super-directive, or super-gain, array antennas can be found in [Balanis C., 2005 - Sec. 6.9], [Hansen R. C., 2009 - Ch. 9] where it is noted that the super-directive arrays are quite difficult to build in view of the limitations imposed by Ohmic losses, high sensitivity to tolerances for design, construction and materials, and the exceedingly large currents required. An example of one of the latest developments in this area is provided in [Ziolkowski R. W., 2017] of a linear array which consists of the Huygens source multipoles and achieves *needle-like* radiation performance along the axis of the array (ie it beams to a point-like area). This paper demonstrates theoretically that a needle-like radiation can be realized by a single radiator driven by judiciously chosen electric and magnetic currents streaming over a spherical surface. However, the concept of needle-like radiation beam still lacks experimental verification. In view of all this, this analysis only focuses on the typical array designs that have found common applications in the practice of radio communications.

Note that in the derivations below the planar angles, arguments of trigonometric functions, and values of the inverse trigonometric functions are in *radians*, unless specified otherwise, and all the formulas are expressed in the SI units.

C.2.2 The far zone

The basic exposure scenario is for the radiated field of a communication antenna to be used in the far zone (sometimes called the far field or Fraunhofer zone). The EM field of any antenna in the far zone is a separable function of the angular variables and of distance $L = L(\mathbf{R})$ from the antenna to the observation point **R**, and the complex field amplitudes **E(R)**, **H(R)** each behave as an outgoing spherical wave with an angular dependent vector amplitude, viz [Kong J. A., 1986 - Sec. 4.4], [Balanis C., 2005 - Sec. 3.6], [Stutzman W. L., 2013 - Sec. 2.4.3]

$$\mathbf{E(R)} = \mathbf{F_e(I)}\frac{\exp(ikL)}{L} \qquad \text{(Eq. C.2.1)}$$

$$\mathbf{H(R)} = \mathbf{F_m(I)}\frac{\exp(ikL)}{L} \qquad \text{(Eq. C.2.2)}$$

Here $\mathbf{I} = \nabla L(\mathbf{R})$ is the unit vector along L, k is the free-space wavenumber, and the omitted time dependence is taken as $e^{-i\omega t}$ where ω is the circular frequency. (Note that in some texts [Balanis C., 2005], [Hansen R. C., 2009], [Stutzman W. L., 2013] a conjugate time dependence $e^{j\omega t}$ is assumed. The formulas cited in this note follow from the corresponding expressions in those texts after substituting j with $-i$.) Locally, the field amplitude vectors $\mathbf{F_e(I)}$, $\mathbf{F_m(I)}$ have the same structure as that of a plane wave propagating radially away from the antenna, ie

$$\eta\ \mathbf{F_m(I)} = \mathbf{I} \times \mathbf{F_e(I)}, \quad \mathbf{I}\cdot\mathbf{F_e(I)}=0 \qquad \text{(Eq. C.2.3)}$$

where

$$\eta = 376.730\ \ldots \Omega \qquad \text{(Eq. C.2.4)}$$

is the impedance of free space. We see that in the far zone the EM field of an antenna as a function of space coordinates is completely determined by either function $\mathbf{F_e(I)}$ or $\mathbf{F_m(I)}$. The time-average energy flux (Poynting vector) **S(R)** of the EM field (Eq. C.2.1), (Eq. C.2.2) can be expressed as follows:

$$\mathbf{S(R)} = \mathbf{I}\ \frac{|\mathbf{F_e(I)}|^2}{2\eta L^2} \qquad \text{(Eq. C.2.5)}$$

From this point onward, the performance of an antenna in the far zone is understood to be provided by the function $\mathbf{F_e(I)}$ which will be referred to as the electric field pattern, or simply (radiation) pattern. It is convenient to drop the subscript e in the notation for the pattern which henceforth is denoted as **F(I)**.

A typical radiation pattern associated with most antennas [Balanis C., 2005 - Sec. 2.2.1] (see also [Stutzman W. L., 2013 - Sec. 2.4.6]) consists of one or several major (main) lobes combined with a few minor lobes. A radiation lobe in any direction other than the intended direction is called a side lobe. Note that there may exist side lobes whose level is the same as that of the major lobe in the desired direction; such side lobes are called the *grating* lobes.

According to (Eq. C.2.5), the directions of half-power radiation are defined by an equation

$$|\mathbf{F(I)}| = \frac{F_{max}}{\sqrt{2}} \qquad \text{(Eq. C.2.6)}$$

where F_{max} is the value of $|\mathbf{F}|$ in the direction of pattern maximum. The directions where the radiation is absent,

$$|\mathbf{F(I)}| = 0 \qquad \text{(Eq. C.2.7)}$$

define the nulls of the radiation pattern. The beam width of an antenna is determined by the angular separation between the two characteristic points around the pattern maximum. There are two kinds of beam widths that are used in engineering practice, namely [Kong J. A., 1986 - Sec. 4.6, p. 269], [Balanis C., 2005 - Sec. 2.5, p. 43], the angular separation between the half-power (or -3 dB) points and the null points adjacent to the main lobe. These measures are called the half-power beam width (HPBW) and the first-null beam width (FNBW), respectively. We denote them by the symbols $\Delta\theta_{3dB}$ and $\Delta\theta_{FN}$. Here the notation $\Delta\theta$ means that the considered parameters are calculated as the difference of the values of a certain planar angle θ corresponding to the aforementioned characteristic points, the definition of θ usually being clear from the context. Commonly, the following approximate relationship between the two beam widths is assumed [Balanis C., 2005 - Sec. 2.5, p. 43]

$$\Delta\theta_{3dB} \approx \frac{\Delta\theta_{FN}}{2} \qquad \text{(Eq. C.2.8)}$$

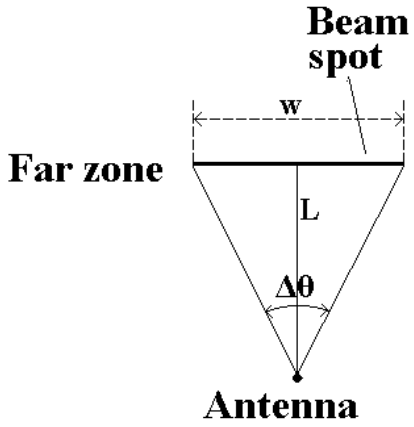

Fig. C.2.1: Evaluation of beam spot size *w* (not to scale).

From simple geometric considerations illustrated in Fig. C.2.1, the *linear* beam spot sizes w_{3dB}, w_{FN} corresponding to the beam widths $\Delta\theta_{3dB}$, $\Delta\theta_{FN}$ in the far zone can be calculated by

$$w_{3dB} = 2\,L\tan\frac{\Delta\theta_{3dB}}{2} \qquad \text{(Eq. C.2.9)}$$

$$w_{FN} = 2\,L\tan\frac{\Delta\theta_{FN}}{2} \qquad \text{(Eq. C.2.10)}$$

These expressions show that the functions w_{3dB}, w_{FN} increase linearly with L. Therefore, if we know the appropriate spot size $w = w_{3dB}, w_{FN}$ at some distance L_1 then the spot size at any distance L_2 can be calculated as

$$w(L_2) = \frac{L_2}{L_1} w(L_1) \qquad \text{(Eq. C.2.11)}$$

(naturally, L_1 and L_2 are implied to lie in the far zone of the antenna).

It is noted that the FNBW is, perhaps, more relevant to the issue of spatial resolution capabilities of field probes than the HPBW, because a probe that accurately measures the field values at the center of a spot where the field decays by factor $\sqrt{2}$ towards the boundary, may fail to do so if the field vanishes at the boundary of the spot. Therefore in the discussion of the arrays to follow, emphasis is placed on the beam spot size that corresponds to the first-null angular positions.

The mathematical analysis of derivations [Balanis C., 2005 - Sec. 3.6], [Kong J. A., 1986 - Sec. 4.4], [Stutzman W. L., 2013 - Sec. 2.4.3] of the far zone approximation for the radiation field reveals that they are valid under the following simultaneous conditions on the distance L:

$$L \gg \frac{\pi D^2}{4\lambda} \qquad \text{(Eq. C.2.12)}$$

$$L \gg \frac{D}{2} \qquad \text{(Eq. C.2.13)}$$

$$L \gg \frac{\lambda}{2\pi} \qquad \text{(Eq. C.2.14)}$$

where D is the maximum overall dimension of the antenna, and λ is the free-space wavelength,

$$\lambda = \frac{2\pi}{k} \qquad \text{(Eq. C.2.15)}$$

To be thorough, it must be pointed out that the above criteria (Eq. C.2.12)-(Eq. C.2.14) and subsequent requirements (Eq. C.2.16 - Eq. C.2.17) have been obtained under assumption that the reference point is taken at a geometric center of the antenna which is any point of space (not necessarily belonging in a physical sense to the antenna proper) such that the distance from it to any point of the antenna does not exceed $D/2$.

A set of *practical* far zone criteria formulated in [Stutzman W. L., 2013 - p. 43, Eqs. (2-100a)-(2.100c)] can be condensed as follows

$$L > L_{min} \qquad \text{(Eq. C.2.16)}$$

where L_{min} is the distance to the far zone defined by

$$L_{min} = \max\{\frac{2D^2}{\lambda}, 5D, \frac{8}{5}\lambda\} \quad \text{(Eq. C.2.17)}$$

This set of bounds is used for further analysis because it involves only the $>$ relations as compared to the criteria (Eq. C.2.12)-(Eq. C.2.14) which involve the imprecisely defined relation $\gg$.

Note that all the above criteria do not restrict the size D of antenna as compared to λ. It is remarked in [Stutzman W. L., 2013 - p. 44], that for large antennas whose size D satisfies the requirement

$$D > \frac{5}{2}\lambda \quad \text{(Eq. C.2.18)}$$

the practical minimum distance to the far zone is given by

$$L_{min} = \frac{2D^2}{\lambda} \quad \text{(Eq. C.2.19)}$$

because the remaining qualifications in Eq. (Eq. C.2.17) follow from (Eq. C.2.19). The latter is easily proven by the following chains of inequalities:

$$L > L_{min} = \frac{2D^2}{\lambda} = D \cdot \frac{2D}{\lambda} > \frac{5}{2}\lambda \cdot \frac{2D}{\lambda} = 5D \quad \text{(Eq. C.2.20)}$$

$$L > L_{min} = \frac{2D^2}{\lambda} > \frac{2}{\lambda} \cdot (\frac{5}{2}\lambda)^2 = \frac{25}{2}\lambda > \frac{8}{5}\lambda \quad \text{(Eq. C.2.21)}$$

C.2.3 Uniform linear array

According to the principle presented in [Balanis C., 2005 - p. 286, Eq. (6-5)], [Hansen R. C., 2009 - p. 7], the radiation pattern of an antenna array **F=F$_{array}$** is equal to the product of the radiation pattern **F$_{element}$** of a single array element (radiator), and a complex-valued dimensionless scalar quantity A which is called the array factor:

$$\mathbf{F}_{array}(\mathbf{l}) = \mathbf{F}_{element}(\mathbf{l})\ A(\mathbf{l}) \quad \text{(Eq. C.2.22)}$$

As examples of array elements, a wire antenna and a rectangular aperture in a conducting plane are briefly characterized in Appendix C.1. The array factor $A(\mathbf{l})$ is determined by the geometry of the array and the amplitudes and phases of the excitations, and does not depend on the radiation characteristics of the array elements. Since the beam width of very narrow array patterns is practically the same as that of the

array factor [Balanis C., 2005 - Sec. 7.1, p. 386], the parameters associated with the angular dependence of A can be examined.

Exactly as in the case of a radiation pattern, for the array factor $A(\mathbf{l})$, the directions where $|A(\mathbf{l})|$ attains the primary (ie global) maximum value A_{max} and the -3dB directions shall be introduced where

$$|A(\mathbf{l})| = \frac{A_{max}}{\sqrt{2}} \qquad \text{(Eq. C.2.23)}$$

the null directions where

$$|A(\mathbf{l})| = 0 \qquad \text{(Eq. C.2.24)}$$

the corresponding angular distances $\Delta\theta_{3dB}^{AF}$, $\Delta\theta_{FN}^{AF}$ between the nearest -3dB or null points on both sides of the desired principal maximum of $|A(\mathbf{l})|$, and the appertaining spot sizes at a distance L from the (center of the) array. It can be deduced from Fig. C.2.1 that :

$$w_{3dB}^{AF} = 2L\tan\frac{\Delta\theta_{3dB}^{AF}}{2} \qquad \text{(Eq. C.2.25)}$$

$$w_{FN}^{AF} = 2L\tan\frac{\Delta\theta_{FN}^{AF}}{2} \qquad \text{(Eq. C.2.26)}$$

Note that the superscript AF has been added to the above quantities to clearly distinguish them from the parameters $\Delta\theta_{3dB}$, $\Delta\theta_{FN}$, w_{3dB},w_{FN} which henceforth are understood to refer to the radiation pattern of the array.

From (Eq. C.2.22) it can be seen that the null directions of the array factor are the same as the null directions of the array pattern. Since for practical arrays

$$\Delta\theta_{FN} = \Delta\theta_{FN}^{AF} \qquad \text{(Eq. C.2.27)}$$

and consequently

$$w_{FN} = w_{FN}^{AF} \qquad \text{(Eq. C.2.28)}$$

the parameters $\Delta\theta_{FN}^{AF}$ and w_{FN}^{AF} are replaced by $\Delta\theta_{FN}$ and w_{FN}, respectively.

Consideration is given to a special case of *separable* array factors which take the form of a product of the array factors in the two mutually orthogonal principal directions [Balanis C., 2005 - Sec. 6.10.1, p. 351]. In such a case the beam widths in each of those directions are determined by a linear array along the corresponding direction. This model significantly simplifies the problem, and at the same time reveals the basic features of beamforming.

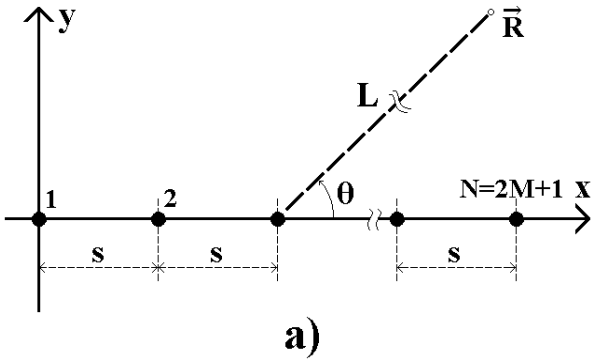

a)

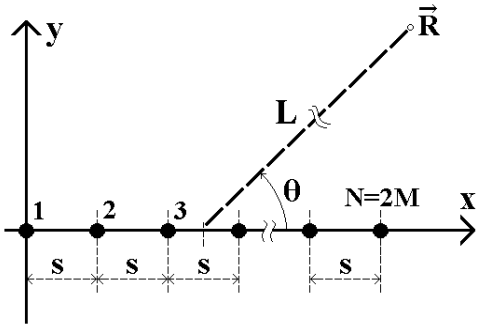

b)

Fig. C.2.2: Coordinate system, with the z-axis (not shown) pointing towards the observer, and linear array geometry with odd (a) and even (b) number of elements.

In conformance with the preceding, consideration is given to a linear array of N elements positioned along the x axis with the spacing s, as shown in Fig. C.2.2. The array elements are numbered by the index n, and the *complex* excitation amplitude of each element is I_n (a dimensionless quantity). Then the appertaining array factor $A = A(\theta)$ assumes the following form:

$$A(\theta) = e^{\frac{i}{2}(N-1)ks\cos\theta} \sum_{n=1}^{N} I_n e^{-i(n-1)ks\cos\theta} \qquad \text{(Eq. C.2.29)}$$

where θ is the observation angle. By considering the maximum overall dimension of this array the quantity

$$D = (N-1)\,s + d \qquad \text{(Eq. C.2.30)}$$

where d ($0<d<s$) is the linear size of one array element along x. From (Eq. C.2.30) it is given that

$$D < Ns < D + s \qquad \text{(Eq. C.2.31)}$$

Based on the *mechanical* structure of the linear array, we will refer to the directions that are perpendicular (θ = ± π/2) or parallel (θ = 0, π) to the line containing the array elements as the boresight [Leonov S. A., 1998a] and endfire [Leonov S. A., 1998b] directions, respectively. (The term 'boresight' is sometime used to refer to an electrical reference axis coinciding with the direction of maximum radiation; this is not the intended interpretation in this document).

The *uniform* linear array shall be the focus of this analysis because, as summarized in [Balanis C., 2005 - Sec.6.8, pp. 325-326], of the three distributions with most practical applications (uniform, binomial [Stone J. R., 1927], [Stone J. R., 1929], and Dolph-Chebyshev [Dolph C. L., 1946]), a uniform array produces the smallest half-power beam width. The analysis below is based on the content in [Balanis C., 2005 - Sec. 6.3, and Sec. 4.6, pp. 264-272], [Hansen R. C., 2009 - Sec. 2.1].

The uniform linear array is characterized by the following excitation coefficients and the array factor [Kong J. A., 1986 - p. 266, Eqs. (5)-(7)], [Balanis C., 2005 - p. 297, Eqs. (6-7), (6-7a)], [Hansen R. C., 2009 - p. 9, Eq. (2-2)]:

$$I_n = e^{i(n-1)ks\cos\theta_0} \qquad \text{(Eq. C.2.32)}$$

$$A(\theta) = \frac{\sin\frac{\pi\psi}{a}}{\sin\frac{\pi\psi}{b}} \cdot e^{\frac{i}{2}(N-1)ks\cos\theta_0} \qquad \text{(Eq. C.2.33)}$$

where

$$a = \frac{\lambda}{Ns} \qquad \text{(Eq. C.2.34)}$$

$$b = \frac{\lambda}{s} \qquad \text{(Eq. C.2.35)}$$

$$\psi = \cos\theta - \cos\theta_0 \qquad \text{(Eq. C.2.36)}$$

and θ_0 is the scan angle. The maximum values of $|A(\theta)|$ are realized along those directions θ where $s\psi$ is an integer multiple of λ, with $A_{max} = N$ [Balanis C., 2005 - p. 294].

To simplify the exposition, consideration is given to the two characteristic cases where the maximum of the array factor is directed along the boresight (θ = ± π/2) or the end-fire directions (θ = 0, π). These cases are termed the broadside and end-fire arrays, respectively.

All further analysis will be conducted assuming that

$$a < 1 \qquad \text{(Eq. C.2.37)}$$

because otherwise, as is apparent from subsequent (Eq. C.2.42), (Eq. C.2.59), no null direction of the array factor exists ($a > 1$) or, for $a = 1$, the angular distance $\Delta\theta_{FN}^{AF}$ assumes the maximum admissible value of π. By the left inequality in (Eq. C.2.31), one can easily prove that

$$a < \overline{a} \qquad \text{(Eq. C.2.38)}$$

where

$$\overline{a} = \frac{\lambda}{D} \qquad \text{(Eq. C.2.39)}$$

Therefore, the inequality (Eq. C.2.37) holds true when

$$D > \lambda \qquad \text{(Eq. C.2.40)}$$

- eg for the large arrays defined by (Eq. C.2.18)

C.2.4 The broadside array

The broadside array [Balanis C., 2005 - Sec. 6.3.1] is produced by setting the scan angle θ_0 to $\pi/2$; in order to avoid the grating lobes, it is further assumed that the separation between the elements is smaller than the wavelength,

$$s < \lambda \qquad \text{(Eq. C.2.41)}$$

The first-null beam width $\Delta\theta_{FN}$ is given by an exact formula

$$\Delta\theta_{FN} = 2 \arcsin a \qquad \text{(Eq. C.2.42)}$$

This result can be obtained either by a direct inspection of the numerator in (Eq. C.2.33), or by simplifying the corresponding expression in [Balanis C., 2005 - p. 300, Tab. 6.2] with the help of an identity $\pi/2 - \arccos a = \arcsin a$). After simple manipulations, the first-null spot size w_{FN} from (Eq. C.2.26) can be expressed in the explicit form as

$$w_{FN}(L) = \frac{2La}{\sqrt{1 - a^2}} \qquad \text{(Eq. C.2.43)}$$

It is emphasized that the concept of the spot size, as defined in this Appendix, is only applicable in the array's far field – cf Eqs. (Eq. C.2.16), (Eq. C.2.17).

In the following equations, the quantity $w_{FN}(L)$ shall be estimated. The lower bound for a, with the help of the right inequality in (Eq. C.2.31) and (Eq. C.2.34), (Eq. C.2.41), can be written as

$$a > \underline{a} \qquad \text{(Eq. C.2.44)}$$

where

$$\underline{a} = \frac{\lambda}{D + \lambda} \qquad \text{(Eq. C.2.45)}$$

Then (Eq. C.2.43), (Eq. C.2.44) provide for the following simple estimate $\underline{w}_{FN}(L)$ from below for the parameter $w_{FN}(L)$:

$$w_{FN}(L) > \underline{w}_{FN}(L) \qquad \text{(Eq. C.2.46)}$$

where

$$\underline{w}_{FN}(L) = \frac{2L\underline{a}}{\sqrt{1 - \underline{a}^2}} \qquad \text{(Eq. C.2.47)}$$

$$= \frac{\lambda}{D} \frac{2L}{\sqrt{1 + \frac{2\lambda}{D}}} \qquad \text{(Eq. C.2.48)}$$

Henceforth this analysis of the broadside array will be restricted to the *large* arrays in the sense of (Eq. C.2.18). As mentioned in the preceding, the practical far zone for such an array lies at $L > L_{min}$, where L_{min} is defined by (Eq. C.2.19). Next, an estimate for $w_{FN}(L)$ at the boundary $L = L_{min}$ of the far zone shall be derived. Using (Eq. C.2.19), (Eq. C.2.48), gives

$$\underline{w}_{FN}(L_{min}) = \frac{4D}{\sqrt{1 + \frac{2\lambda}{D}}} \qquad \text{(Eq. C.2.49)}$$

To get an idea of the numerical value of $\underline{w}_{FN}(L_{min})$, it can be shown from (Eq. C.2.18)

$$1 + \frac{2\lambda}{D} < 1 + 2\lambda \frac{2}{5\lambda} = \frac{9}{5} \qquad \text{(Eq. C.2.50)}$$

so that by (Eq. C.2.18), (Eq. C.2.49)

$$\underline{w}_{FN}(L_{min}) > \frac{4 \cdot \frac{5\lambda}{2}}{\sqrt{\frac{9}{5}}} = \frac{10\sqrt{5}}{3} \lambda > 7.45\, \lambda \qquad \text{(Eq. C.2.51)}$$

This, in conjunction with (Eq. C.2.46), leads to the following (conservative) estimate below:

$$w_{FN}(L_{min}) > 7.45\, \lambda \qquad \text{(Eq. C.2.52)}$$

provided $D > 2.5\, \lambda$ – cf (Eq. C.2.18).

To conclude the analysis of the broadside array, an estimate of $\overline{w}_{FN}(L)$ is given for the parameter $w_{FN}(L)$ for later use. Namely, (Eq. C.2.38), (Eq. C.2.39) and (Eq. C.2.43) yield

$$w_{FN}(L) < \overline{w}_{FN}(L) \qquad \text{(Eq. C.2.53)}$$

with

$$\overline{w}_{FN}(L) = \frac{2L\bar{a}}{\sqrt{1 - \bar{a}^2}} \qquad \text{(Eq. C.2.54)}$$

$$= \frac{\lambda}{D} \frac{2L}{\sqrt{1 - \left(\frac{\lambda}{D}\right)^2}} \qquad \text{(Eq. C.2.55)}$$

provided that $\overline{a} < 1$. The latter requirement is equivalent to (Eq. C.2.40) which obviously holds for the large arrays (Eq. C.2.18).

C.2.5 The end-fire array

In the end-fire array the scan angle θ_0 is set to either to 0 or π, and the separation s between the elements is limited by

$$s < \frac{\lambda}{2} \qquad \text{(Eq. C.2.56)}$$

These conditions produce the array factor with only one end-fire maximum (directed toward θ = 0 or θ = π, respectively) without any grating lobes [Balanis C., 2015 - Sec. 6.3.2, p. 299]. Note that at this stage no restrictions are imposed on the size D of the array or the number of elements N other than those arising from the assumptions (Eq. C.2.37), (Eq. C.2.56). By Eq. (Eq. C.2.30), the inequality (Eq. C.2.37) is equivalent to

$$D > \lambda - s + d \qquad \text{(Eq. C.2.57)}$$

Taking into further consideration of (Eq. C.2.56), which can be written as $-s > -\lambda/2$, results in the following consequence of (Eq. C.2.37):

$$D > \frac{\lambda}{2} + d \qquad \text{(Eq. C.2.58)}$$

where d>0.

The first-null beam width $\Delta\theta_{FN}$ is given by an exact formula [Balanis C., 2005 - p. 303, Tab. 6.4]

$$\Delta\theta_{FN} = 2 \arccos(1 - a) \qquad \text{(Eq. C.2.59)}$$

where the parameter a is defined by (Eq. C.2.34). Inserting the above formula into (Eq. C.2.26), an explicit expression for the first-null spot size is obtained:

$$w_{FN}(L) = \frac{2L\sqrt{a\,(2-a)}}{1-a} \qquad \text{(Eq. C.2.60)}$$

Much as in the analysis of the broadside array, an estimate of $\underline{w}_{FN}(L)$ is derived from Eq. C.2.61 for the parameter $w_{FN}(L)$ by taking note of the fact that

$$\underline{a} < a < \overline{a} \qquad \text{(Eq. C.2.61)}$$

where $\overline{a}$ is given by (Eq. C.2.39), and $\underline{a}$, not to be confused with a similar quantity from Eq. (Eq. C.2.45), is defined now by

$$\underline{a} = \frac{\lambda}{D + \frac{\lambda}{2}} \qquad \text{(Eq. C.2.62)}$$

The above expression for $\underline{a}$ has been derived by taking together the left inequality in (Eq. C.2.31) and (Eq. C.2.34), (Eq. C.2.56). Then it can be easily seen from (Eq. C.2.60), (Eq. C.2.61) that $w_{FN}(L)$ satisfies the inequality (Eq. C.2.46) with

$$\underline{w}_{FN}(L) = \frac{2L\sqrt{\underline{a}\,(2-\overline{a})}}{1-\underline{a}} \qquad \text{(Eq. C.2.63)}$$

$$= 2L\left(\frac{\lambda}{D}\cdot\frac{1+\frac{\lambda}{2D}}{1-\frac{\lambda}{2D}}\right)^{1/2} \qquad \text{(Eq. C.2.64)}$$

provided that $\underline{a}$ <1 and $\overline{a}$<2. The latter two constraints are equivalent to

$$D > \frac{\lambda}{2} \qquad \text{(Eq. C.2.65)}$$

which is satisfied automatically in view of (Eq. C.2.58). Further, for such D we have

$$\frac{1+\frac{\lambda}{2D}}{1-\frac{\lambda}{2D}} > 1 \qquad \text{(Eq. C.2.66)}$$

so that

$$\underline{w}_{FN}(L) > 2L\sqrt{\frac{2\lambda}{D}} \qquad \text{(Eq. C.2.67)}$$

Focussing on the *large* end-fire arrays described by (Eq. C.2.18), it is possible to estimate the first-null beam spot size $w_{FN}(L)$ at the boundary $L = L_{min}$ of the array's far zone. If the value of L is substituted in the inequality (Eq. C.2.67) to $L = L_{min}$ as given by (Eq. C.2.19), the result is

$$\underline{w}_{FN}(L_{min}) > 4D\sqrt{\frac{2D}{\lambda}} \qquad \text{(Eq. C.2.68)}$$

Since in view of (Eq. C.2.18)

$$4D\sqrt{\frac{2D}{\lambda}} > 4 \cdot \frac{5\lambda}{2} \cdot \sqrt{\frac{2}{\lambda} \cdot \frac{5\lambda}{2}} = 10\sqrt{5}\,\lambda \qquad \text{(Eq. C.2.69)}$$

it follows that

$$\underline{w}_{FN}(L_{min}) > 10\sqrt{5}\,\lambda > 22.3\,\lambda \qquad \text{(Eq. C.2.70)}$$

This, in conjunction with (Eq. C.2.46), leads to the following (conservative) estimate from Eq. C.2.71:

$$w_{FN}(L_{min}) > 22.3\,\lambda \qquad \text{(Eq. C.2.71)}$$

provided $D > 2.5\,\lambda$ – cf. (Eq. C.2.18).

C.2.6 Comparison between broadside and end-fire configuration

This section compares the linear sizes of the first-null beam spots for the broadside and end-fire arrays of the same overall length D. In this consideration, the subscripts B or E will be added where necessary to clearly distinguish between the quantities referring to the broadside or end-fire array, respectively. All discussions are restricted to the case where the appertaining bounds (Eq. C.2.41), (Eq. C.2.56) on s have been met for each array. So we are going to evaluate the ratio

$$r = \frac{w_{FN,E}(L)}{w_{FN,B}(L)} \qquad \text{(Eq. C.2.72)}$$

This ratio can be estimated with the help of the quantities $\overline{w}_{FN,B}(L)$ and $\underline{w}_{FN,E}(L)$, viz

$$r > \frac{\underline{w}_{FN,E}(L)}{\overline{w}_{FN,B}(L)} \qquad \text{(Eq. C.2.73)}$$

First it is assumed that the array size D satisfies the requirement (Eq. C.2.40). This allows the use, in the above inequality, of the expression (Eq. C.2.55) for $\overline{w}_{FN,B}(L)$ and an estimate (Eq. C.2.67) for $\underline{w}_{FN,E}(L)$ to further obtain

$$r > \sqrt{\frac{2D}{\lambda}} \cdot \sqrt{1 - \left(\frac{\lambda}{D}\right)^2} \qquad \text{(Eq. C.2.74)}$$

Next, consideration is given to the case where the array is *large* in the sense of (Eq. C.2.18). Then taking the estimates

$$\frac{2D}{\lambda} > \frac{2}{\lambda} \cdot \frac{5\lambda}{2} = 5 \qquad \text{(Eq. C.2.75)}$$

$$1 - \left(\frac{\lambda}{D}\right)^2 > 1 - \left(\lambda \cdot \frac{2}{5\lambda}\right)^2 = 1 - \frac{4}{25} = \frac{21}{25} \qquad \text{(Eq. C.2.76)}$$

into account, the resulting bound is:

$$r > \sqrt{5} \cdot \sqrt{\frac{21}{25}} > 2.04 \qquad \text{(Eq. C.2.77)}$$

It is shown that for large arrays of the same total length D, the linear size of the end-fire first-null beam diameter is at least *twice as large* as that of the broadside beam diameter - cf [Kong J. A., 1986 - p. 270]. Therefore, the end-fire arrays do not need to be considered in establishing the smallest beam diameter dimensions.

For comparison purposes, Table C.2.1 gives the calculated parameters of the radiation pattern and array factor for a linear array of N half-wavelength ($d = \lambda$) center-fed dipoles. (It is worth noting that in order to calculate the data presented below, the wavelength λ need not be specified.) The dipoles are oriented along the axis of the array (which is the x axis in Fig. C.2.2). The absolute value of the radiation pattern of a single element has the form

$$|\mathbf{F}_{\mathbf{element}}| = \left| \frac{\cos\left(\frac{\pi}{2}\cos\theta\right)}{\sin\theta} \right| \qquad \text{(Eq. C.2.78)}$$

where θ is shown in Fig. C.1.1. The maximum of the function (Eq. C.2.78) is achieved in the directions θ = ± π/2 perpendicular to the dipole axis; the nulls are at θ = 0, π; the -3dB and first-null beam widths are,

respectively, $1.363\ldots$ ($\approx 78^{\mathrm{o}}$) and π (180^{o}). All of this is discussed in [Balanis C., 2005 - Sec. 4.6], and can be easily deduced from a summary for the linear wire antenna given in Section C.1.1 of this Appendix.

The dipoles are excited in phase, and are spaced at a distance $s = \frac{2}{3}\lambda$. According to the preceding, this yields a broadside array (maximum radiation at $\theta = \pm\pi/2$) with no grating lobes. With regards to the array pattern, the -3dB angular points were determined numerically by solving an equation equivalent to (Eq. C.2.6); the first-null beam width was calculated analytically with the help of formula (Eq. C.2.42) It can be seen from the table below that, for any $N \geqslant 2$, the 3-dB and first-null spot sizes at the boundary $L = L_{min}$ of the far zone exceed the wavelength λ by a factor of at least 4 and 10, respectively. As expected, both spot sizes increase with the number of elements N.

Table C.2.1: Beam and spot size characteristics for a broadside array of half-wavelength dipoles.

N	2	3	4	5	6	7	8	9	10
D/λ	1.2	1.8	2.5	3.2	3.8	4.5	5.2	5.8	6.5
L_{min}/λ	5.8	9.2	12.5	20.1	29.4	40.5	53.4	68.1	84.5
a	0.75	0.5	0.375	0.3	0.25	0.21	0.19	0.17	0.15
$\Delta\theta_{3dB}$, o	38.7	25.6	19.1	15.3	12.7	10.9	9.5	8.5	7.6
$\Delta\theta_{3FN}$, o	97.2	60.0	44.0	34.9	29.0	24.7	21.6	19.2	17.3
w_{3dB}/λ	4.1	4.2	4.2	5.4	6.5	7.7	8.9	10.1	11.3
w_{FN}/λ	20.0	12.2	10.9	13.2	15.7	18.2	20.8	23.3	25.9

Table C.2.2: Summary of basic expressions

<table>
<tr><td colspan="3">Definition of the far zone: $L > L_{min}$</td></tr>
<tr><td colspan="2">Antenna of arbitrary size D:
$L_{min} = \max\{\frac{2D^2}{\lambda}, 5D, 1.6\lambda\}$</td><td>Large antenna ($D$ >2.5 λ):
$L_{min} = \frac{2D^2}{\lambda}$</td></tr>
<tr><td colspan="3">Uniform linear array (D – array length, s – spacing)</td></tr>
<tr><td></td><td>Large Broadside array</td><td>Large End-fire array</td></tr>
<tr><td>Condition on s to have the maximum in the desired direction and to avoid the grating lobes</td><td>$s<\lambda$</td><td>$s < 0.5\ \lambda$</td></tr>
<tr><td>First-null spot size $w_{FN}(L)$ under the above condition at the boundary $L = L_{min}$ of the far zone</td><td>$w_{FN}(L_{min}) > 7.45\ \lambda$</td><td>$w_{FN}(L_{min}) > 22.3\ \lambda$</td></tr>
<tr><td>Ratio r of the first-null spot size of the end-firre array to that of the broadside array of the same length D</td><td colspan="2">$r > 2.04$</td></tr>
</table>

C.3 Simulated power density beam diameters and associated SAR spot sizes in near-field

Estimates of temperature rise require knowledge of the transverse distribution of SAR in tissue (termed the “spot size” in this work). The distribution width at its half -power intensity is defined as the Full Width at Half Maximum or FWHM. However, the external field metric used in most standards above 6 GHz is the spatially averaged, unperturbed power density projected on a planar surface. The diameter of the projected beam at its half-power intensity is defined as the Half-Power Projected Beam Diameter (HPBD). Thus, for a given radiator and exposure range, it is necessary to estimate a realistic minimum SAR spot size for estimating temperature rise and the associated HPBD for comparison against the exposure limits.

This section investigates SAR spot sizes (FWHM) and power density beam diameters (HPBD) that can typically be expected on a planar tissue model in the frequency range of 10 - 30 GHz. In particular, it attempts to determine the lower frequency bound at which the SAR spot size of FWHM = 0.005 m is practically realizable considering potential near-field exposures. In addition, the relationship between SAR spot sizes and related beam diameters is examined in order to allow estimates of temperature rise based on measures of HPBD rather than FWHM. This information is vital for assessing the validity of exposure standards above 6 GHz.

Half-wave resonant elements such as dipoles, slots and patches are typically the smallest radiating structure used in single-element and array antennas. In the mm-wave range, they become very small and are therefore spatially efficient. While sub-resonant-length elements can be designed and are typically used at low frequencies where the antenna device size is constrained and space is important, at mm-wave frequencies, such requirements are unnecessary.

This study examines half-wave dipoles both as single elements and as part of arrays. The EM simulation package WIPL-D Pro (WIPL-D d.o.o., Gandijeva 7 apt 32, 11073 Belgrade, Serbia) is utilized to calculate spot-sizes (FWHM) of dipoles illuminating a tissue block (representing skin) at various distances (offsets) from the radiator. It is also used to determine projected power density beam diameters (HPBDs) that would occur on the surface of the tissue block without the presence of the block itself. The relationship between these two parameters (i.e. the ratio FWHM/HPBD) is estimated for use in assessing the OBRs for spatially averaged power densities throughout Chapter 5.

C.3.1 Vertical broadside array of 3 dipoles

The purpose of this part of the investigation is to compare the spot size produced by a small array with that of a single element as the distance between array/element and the target tissue is varied. The array consists of 3 half-wavelength dipoles arranged vertically as in Fig. C.3.1. All dipoles are fed uniformly and in-phase which produces maximum radiation in a direction perpendicular to the axis of the array (i.e. the broadside direction). Calculations are carried out only at 10 GHz, however, the results scale with the wavelength and conclusions can be generalized to any frequency.

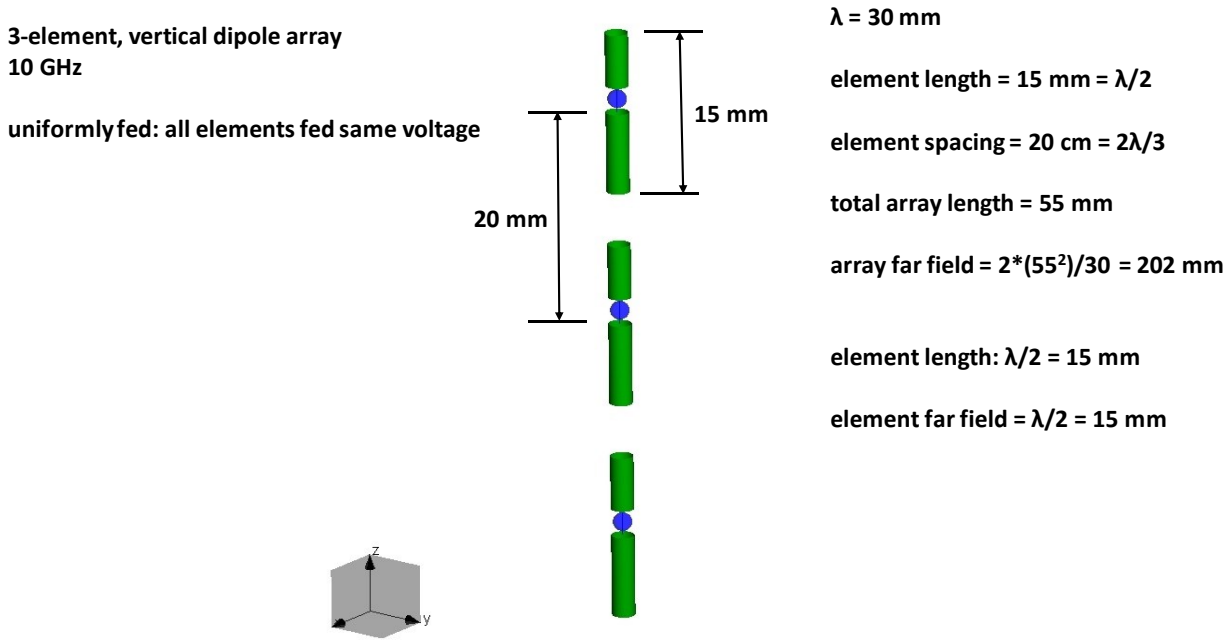

Fig. C.3.1: Vertical array of λ/2 dipoles spaced 2λ/3 apart and uniformly fed in broadside configuration.

The far-field, free-space, E-plane radiation patterns of the single dipole and the array (i.e. in the absence of the human tissue block) obtained with WIPL-D are plotted in linear-polar form in Fig. C.3.2. The same plots using a logarithmic scale are shown in Fig. C.3.3 where the angular beam width has been identified at the – 3dB point (or half power value). The polar graphs clearly demonstrate that the array has better directivity or alternatively, smaller angular beam width than the single dipole.

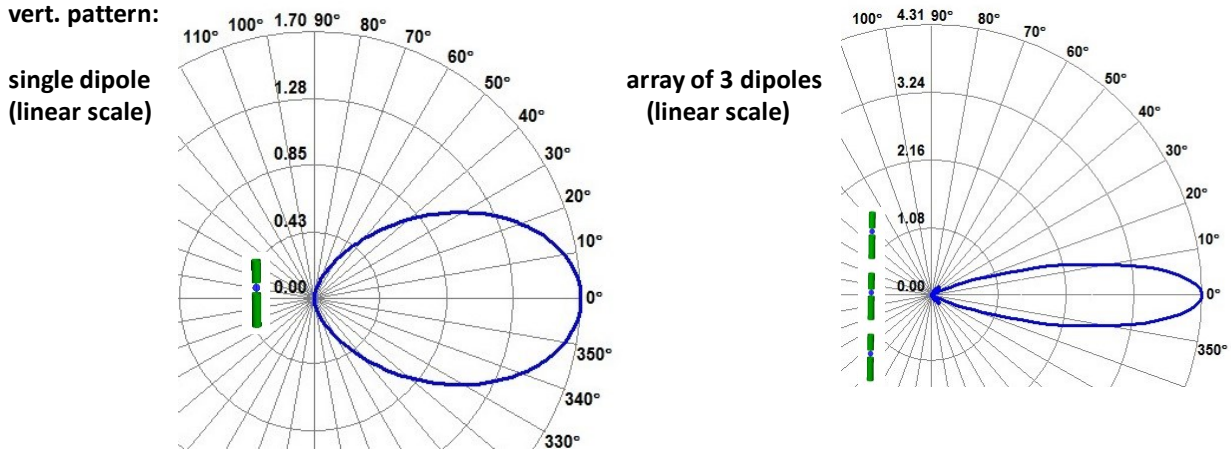

Fig. C.3.2: Polar, E-plane radiation patterns of single element (left) and 3-dipole array (right). Scale is linear (power) and represents directivity. Theoretical maximum directivity of a λ/2 dipole is 1.64.

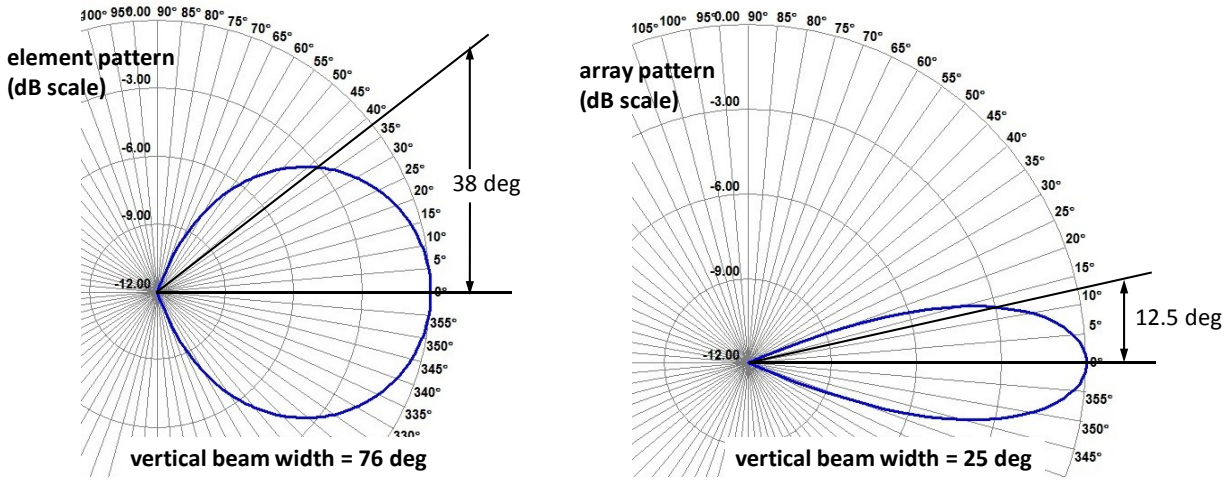

Fig. C.3.3: Polar, E-plane radiation patterns of single element (left) and 3-dipole array (right). Scale is in decibels (normalized power). Theoretical maximum directivity of a λ/2 dipole is 2.15 dB.

SAR spot size vs offset of the array

A tissue block with dielectric properties of human skin (Hasgall PA. *et al.*, 2018) is introduced in front of the array to compute SAR spot sizes inside the tissue block. A symmetry plane is placed on the YZ plane in the WIPL-D computations to conserve the "unknown" budget (max allowable unknowns = 5000). The SAR inside the tissue is scanned along a line parallel to the array axis (i.e. y-axis) at a depth of 0.1 mm in the tissue (see Fig. C.3.4). The distance between the array and the tissue block (i.e. the offset– see figure C.3.5) is varied in a series of simulations to determine the SAR spot size versus offset. A similar set of calculations were performed with a single element for comparison.

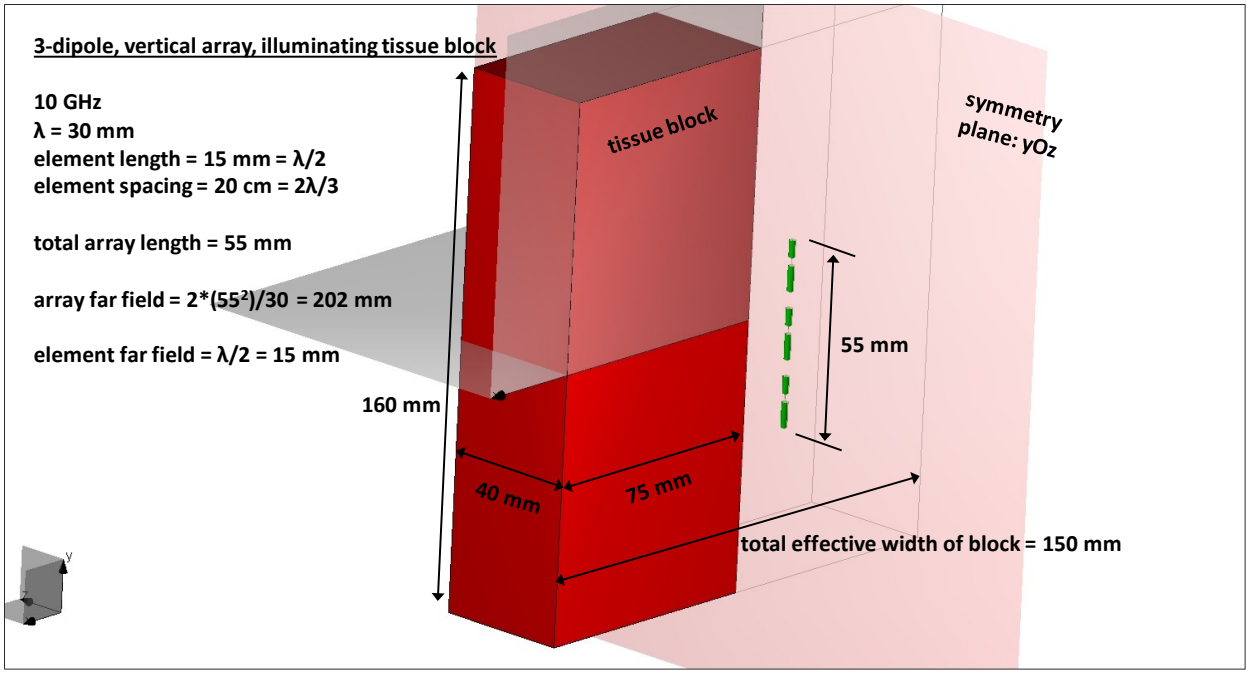

Fig. C.3.4: 3-dipole array illuminating a tissue block with dielectric parameters of skin @ 10 GHz.

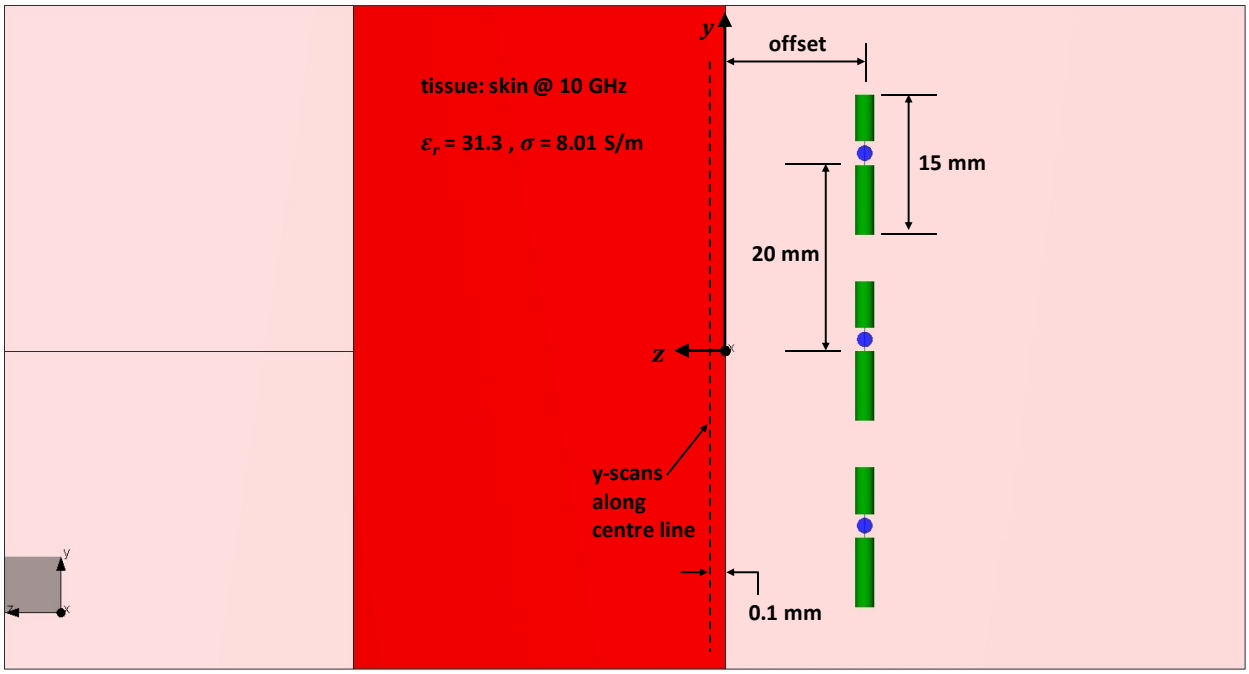

Fig. C.3.5: 3-dipole array illuminating a tissue block with dielectric parameters of skin @ 10 GHz.

It should be noted that the dipole wire diameter is 2 mm so that the actual gap between the wire edge and the tissue block surface is equal to the offset value minus the radius of the wire (i.e. 1 mm). The normalized SAR distributions of the single dipole and array are shown in Fig. C.3.6 for offset = 2 mm. In such close proximity to the tissue block, it can be seen that the main beam of the array is not formed (obviously the far-field condition is not met). Instead, all 3 elements composing the array can be identified on the SAR distribution and the spot size from a single element of the array is equivalent to the SAR spot size of a single dipole (see Fig. C.3.6).

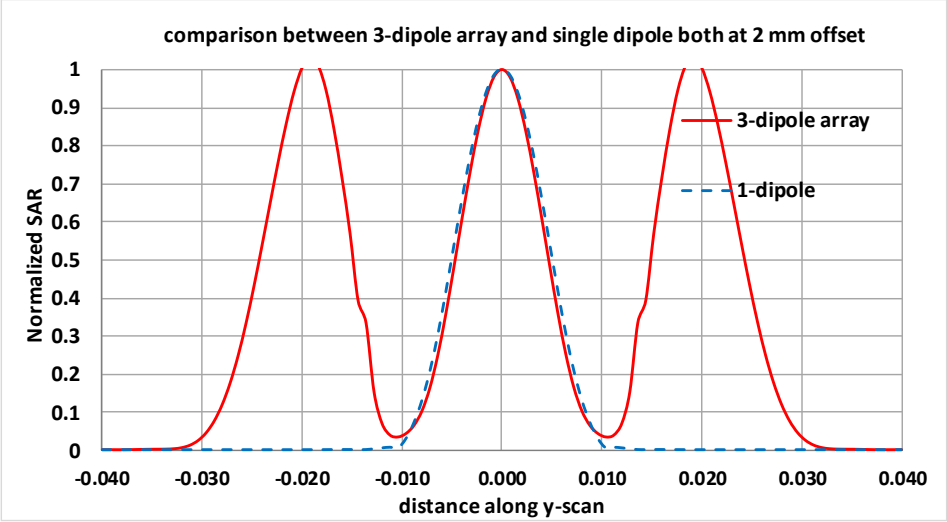

Fig. C.3.6: Normalized SAR distributions of 3-dipole array and single dipole, both at an offset of 2 mm.

The next three figures (Figs. C.3.7, C.3.8 and C.3.9) show the SAR scans for a range of offsets. As the offset is increased, the SAR distribution gradually takes on the appearance of a single lobe. For the present example, this occurs around an offset of 20 mm. The lobe is initially quite broad but narrows as the offset is increased to reach a minimum SAR spot size at approximately 45 mm offset distance.

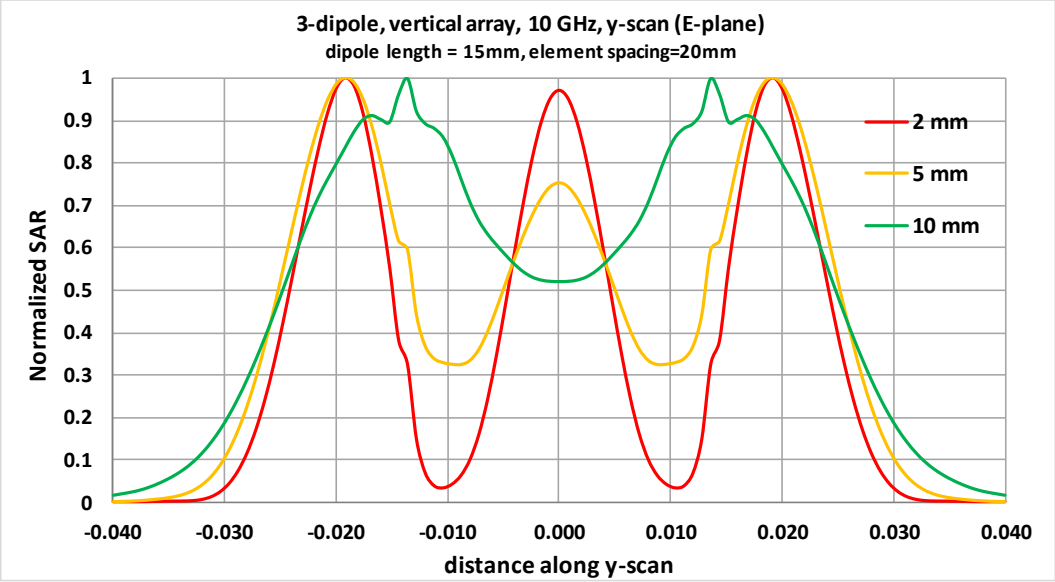

Fig. C.3.7: Normalized SAR distribution (i.e. *SAR*(*y*)*/peak SAR*) for 2, 5 and 10 mm offset.

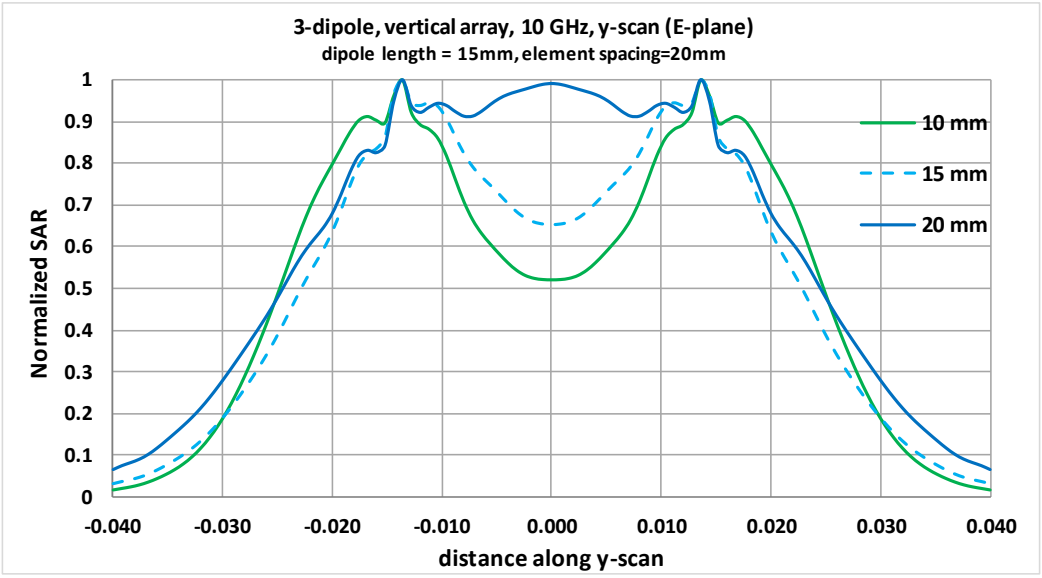

Fig. C.3.8: Normalized SAR distribution (i.e. *SAR*(*y*)*/peak SAR*) for 10, 15 and 20 mm offset.

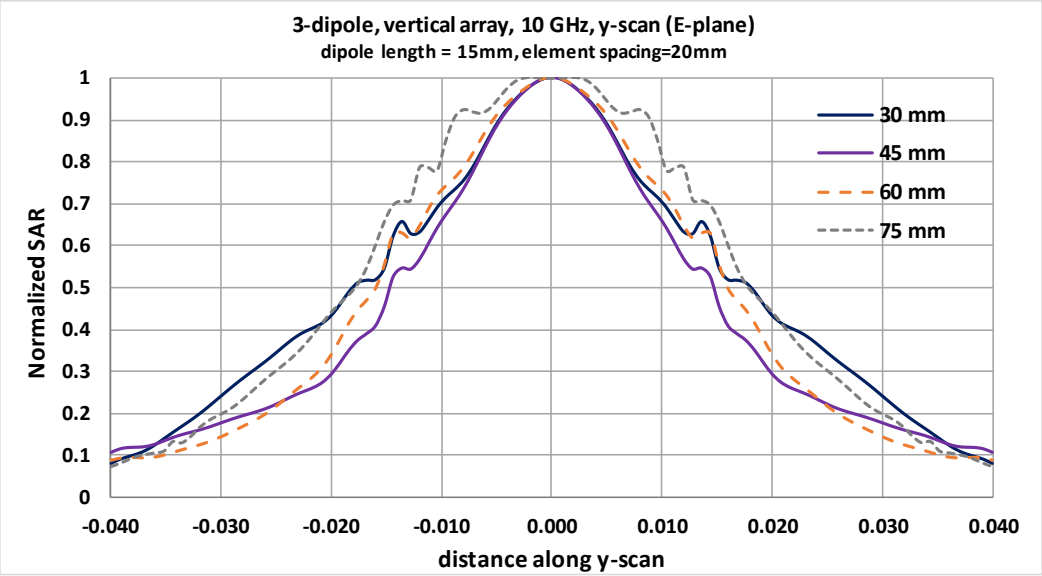

Fig. C.3.9: Normalized SAR distribution (i.e. *SAR*(*y*)*/peak SAR*) for 30, 45, 60 and 75 mm offset.

Note: It is believed that the "bumps" in the SAR distributions are computational artefacts caused by insufficient subdivision of the dielectric domains in WIPL-D. The software has tools for smoothing or eliminating these artefacts but, this feature was not available during this analysis.

In conclusion, even though the overall directivity of the array is greater than a single element, the smallest SAR spot size simulated for the array (offset ≈ 45 mm) is still larger than the SAR spot size of a single element in the near-field (offset = 2 mm) as shown in Fig. C.3.10. An exposure to the array very close to the tissue surface would produce the same spot size as a single element at the same offset.

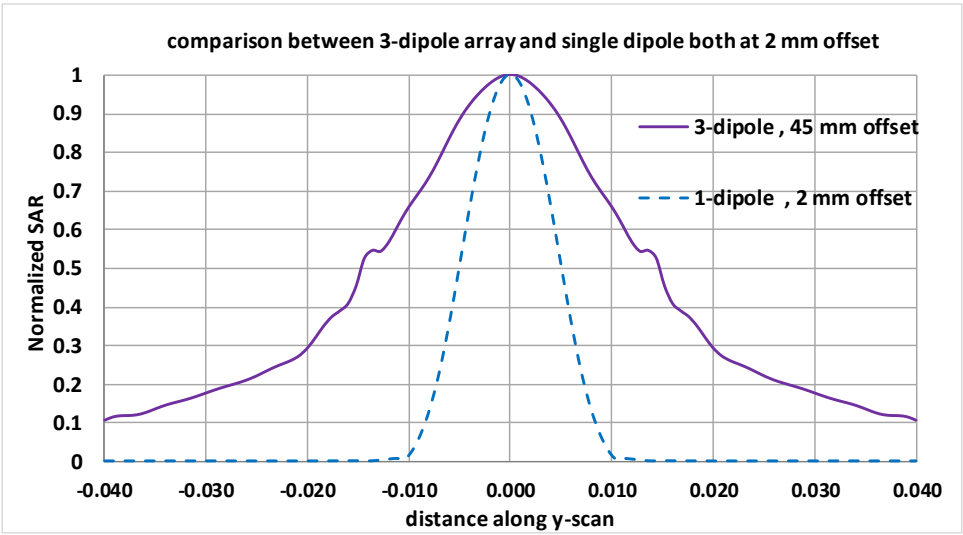

Fig. C.3.10: Normalized SAR distributions of 3-dipole array at 45 mm offset (narrowest distribution of the array) and single dipole at 2mm offset (producing the narrowest distribution of the single element).

C.3.2 Single dipole versus small array of 3 dipoles (end-fire configuration)

Like the previous section, the purpose of this section is to compare the spot size produced by a small end-fire array with that of a single element as the distance between array/element and the target tissue is varied. The end-fire configuration consists of dipoles arranged side-by-side (on a plane) as in Fig. C.3.11. Maximal radiation in the end-fire direction is achieved by feeding the dipoles with alternating phase voltages (i.e. +1 V, -1 V, +1 V as in the figure). Since the purpose is only to observe the relationships between SAR distributions, calculations are carried out at 10 GHz, however, the results scale with the wavelength and conclusions can be generalized to any frequency.

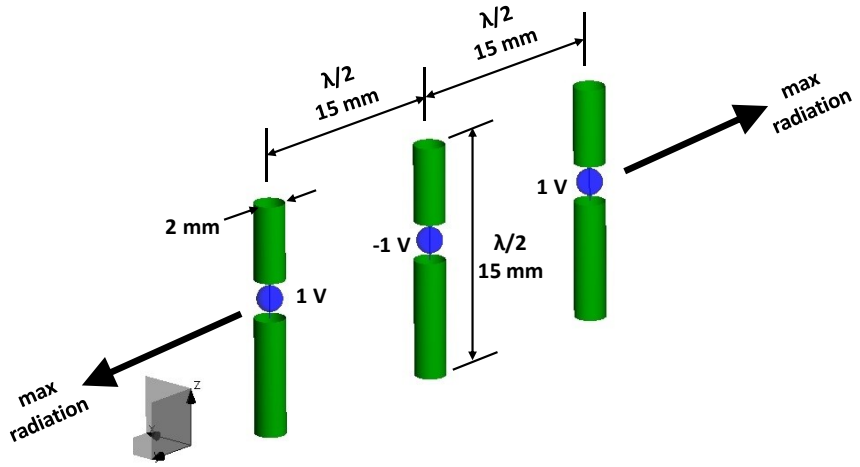

Fig. C.3.11: Array composed of 3 dipoles in the end-fire configuration at 10 GHz.

The far-field, free-space radiation patterns (i.e. in the absence of the human tissue block) obtained with WIPL-D are plotted in linear-polar form in Fig. C.3.11. As seen on the polar graphs, this array configuration produces a narrow beam in a direction formed by a line drawn through its feed points.

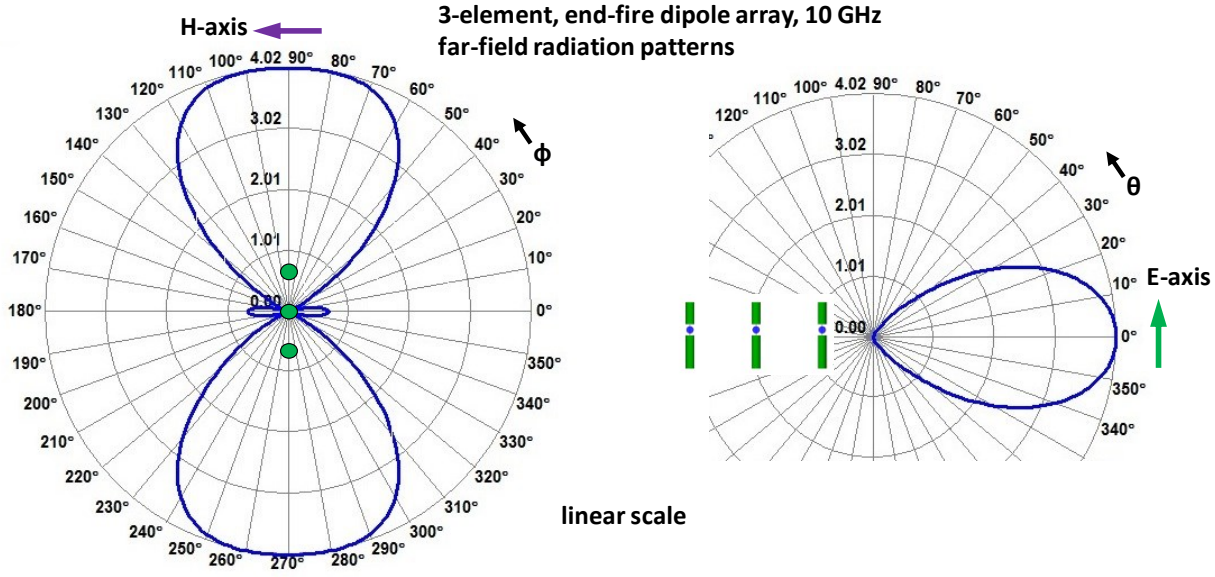

Fig. C.3.12: Polar radiation patterns in free space of the 3-dipole end-fire array. The scale is linear (power) and represents directivity.

SAR spot size vs offset of the array

A tissue block with dielectric properties of human skin (Hasgall PA. *et al.*, 2018) is introduced in front of the array (see figure C.3.13) to compute SAR spot sizes inside the body. The SAR is scanned along both the E-axis (parallel to the element or y-axis) and the H-axis at a depth of 0.1 mm inside the tissue. The distance (i.e. offset) between the array and the tissue block is varied in the series of simulations with the offset defined as the distance between the most proximal element and the tissue surface. A similar set of calculations were performed with a single element for comparison.

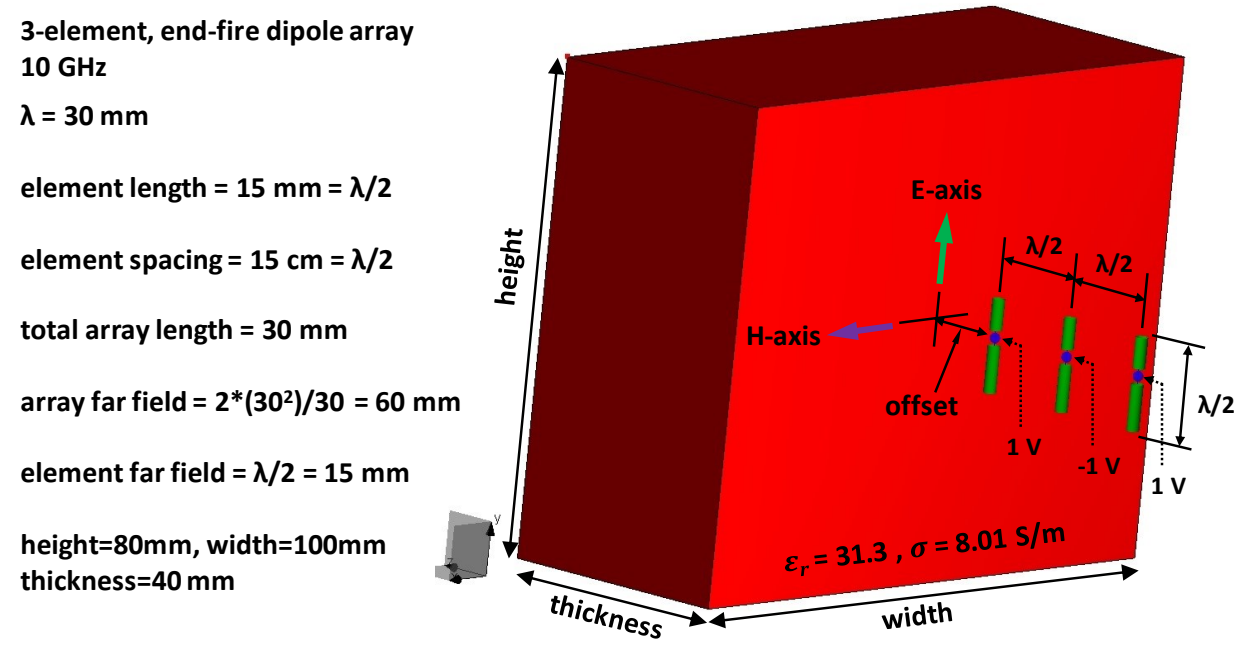

Fig. C.3.13: End-fire array illuminating the tissue block with dielectric parameters of skin @ 10 GHz.

The shape of the SAR distributions along both the E and H-axes resemble the ones for a single element illuminating the block at the same offset (not shown). In terms of spot size, a single element produces a narrower distribution width along both principal axes, which is shown in Fig. C.3.14.

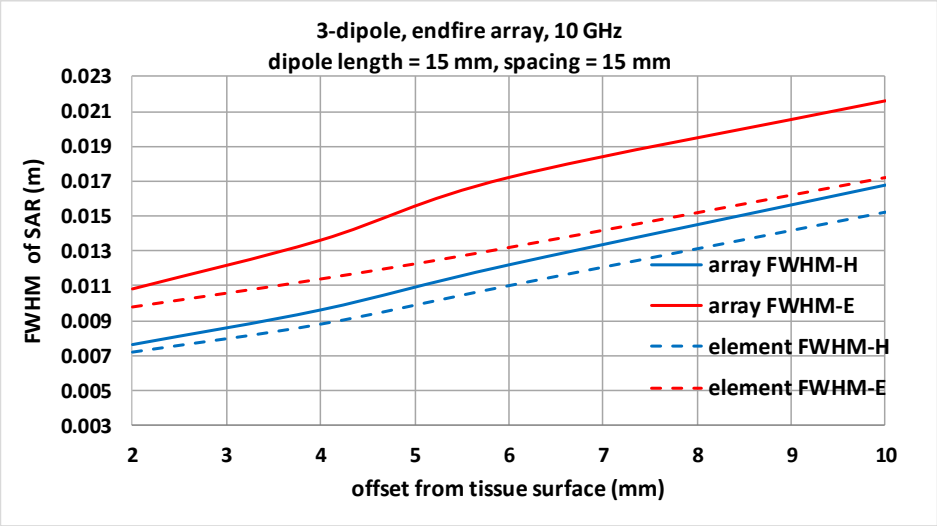

Fig. C.3.14: SAR spot size along both principal axes at a depth of 0.1 mm in the tissue block (skin) as a function of offset for the 3-dipole end-fire array and for a single element.

C.3.3 SAR spot sizes versus power density beam widths for a single dipole

From the previous two sections it is seen that arrays composed of half-wave resonant elements do not produce narrower SAR spot sizes than the ones produced by a single element of the array in close proximity to the skin. This section looks at the smallest SAR spot sizes that can be achieved in the near-field of single elements and their relationship to the power density beam diameters (HPBD).

Computations of SAR spot sizes (FWHM) were performed with WIPL-D for a dipole illuminating a homogeneous tissue block with dielectric parameters of skin (Hasgall PA. *et al.*, 2018) at 10, 15, 20 and 30 GHz. The SAR distribution is computed along two principal axes (defined here as the E- and H-axes – see Fig. C.3.15) at a depth of 0.1 mm inside the tissue for all frequencies.

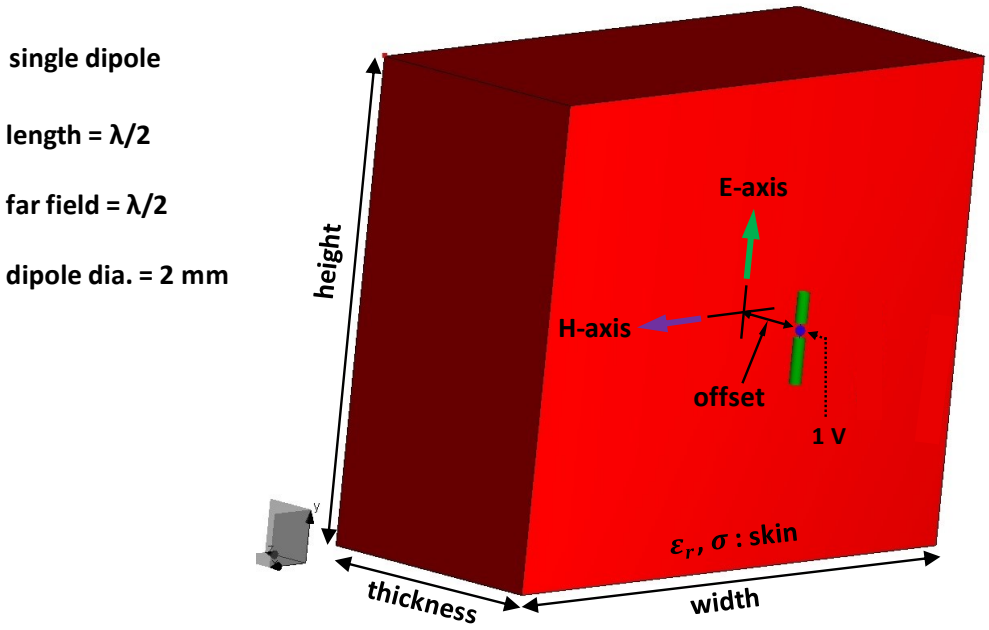

Fig. C.3.15: Single dipole illuminating a tissue block with dielectric parameters of skin.

The front surface of the tissue block is fixed at z = 0 mm and the dipole is moved in the negative *z* direction to achieve different offset distances between the antenna and the surface. The SAR inside the tissue is scanned along both the E-axis (parallel to the element or y-axis) and the H-axis at a depth of 0.1 mm inside the tissue. Table C.3.1 shows the simulation parameters that were used in the WIPL-D calculations.

frequency GHz	wavelength mm	ε_r	σ S/m	thickness mm	width mm	height mm
10	30	31.3	8.01	40	100	80
15	20	26.4	13.8	20	60	60
20	15	22.0	19.2	15	44	44
30	10	15.5	27.1	7	40	38

Table C.3.1: Physical/electrical parameters used in the WIPL-D calculations depicted in Fig. C.3.15.

All computed SAR distributions were bell-shaped and FWHMs were measured using the cursor on the screen in the WIPL-D software post processor display. The FWHM versus offset is plotted in the following two figures (Figs. C.3.16 and C.3.17).

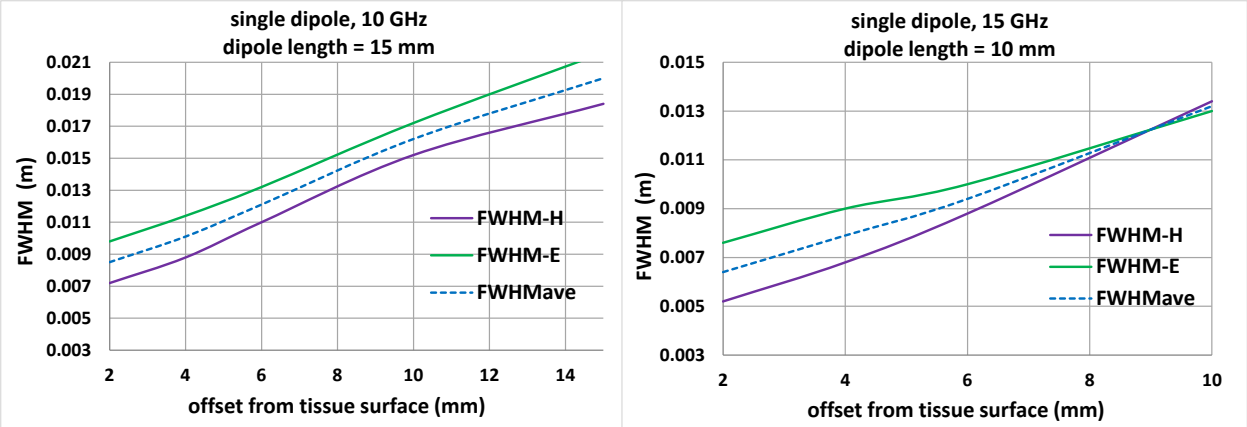

Fig. C.3.16: FWHM of SAR distributions along H and E axes and average FWHM versus offset for 10 and 15 GHz.

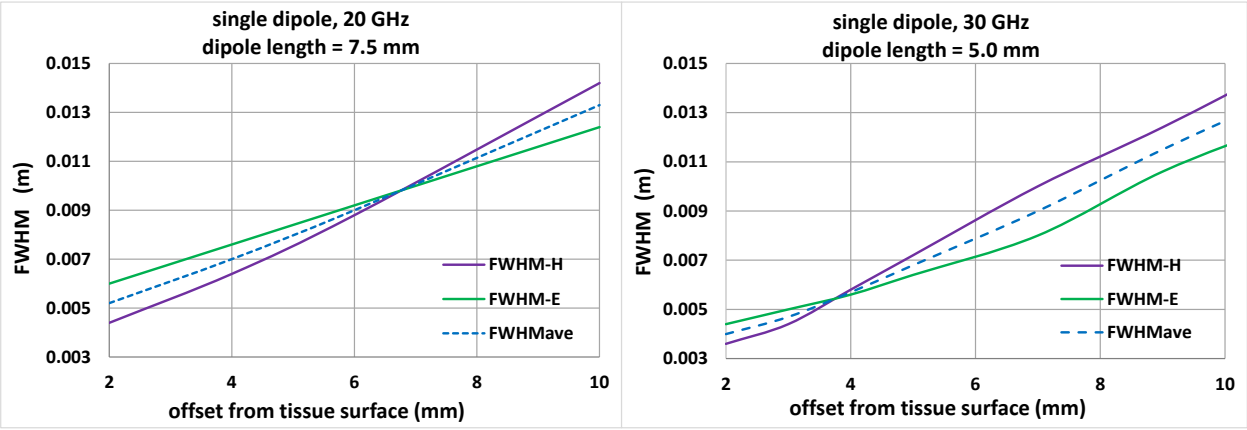

Fig. C.3.17: FWHM of SAR distributions along H and E axes and average FWHM versus offset for 20 and 30 GHz.

To quantify the corresponding diameter of the projected power density beam (HPBD), the same configuration as indicated in Fig. C.3.15 was used except with the tissue block removed. This creates an "unperturbed power density" beam whose dimensions can be measured on the surface where the tissue was once located (the plane defined by z = 0 mm).

The computed power density distributions were bell-shaped and the HPBDs were measured using the cursor in the WIPL-D post processor display. Rather than plotting the resulting HPBDs directly, the ratio FWHM/HPBD for the same offset and axis (E or H) is plotted in Figs. C.3.19 & C.3.20. This ratio is meaningful since its assumed value (i.e. FWHM/HPBD = 0.8) is the basis for the evaluation of the spatially-averaged ICNIRP operational basic restrictions in Chapter 5.

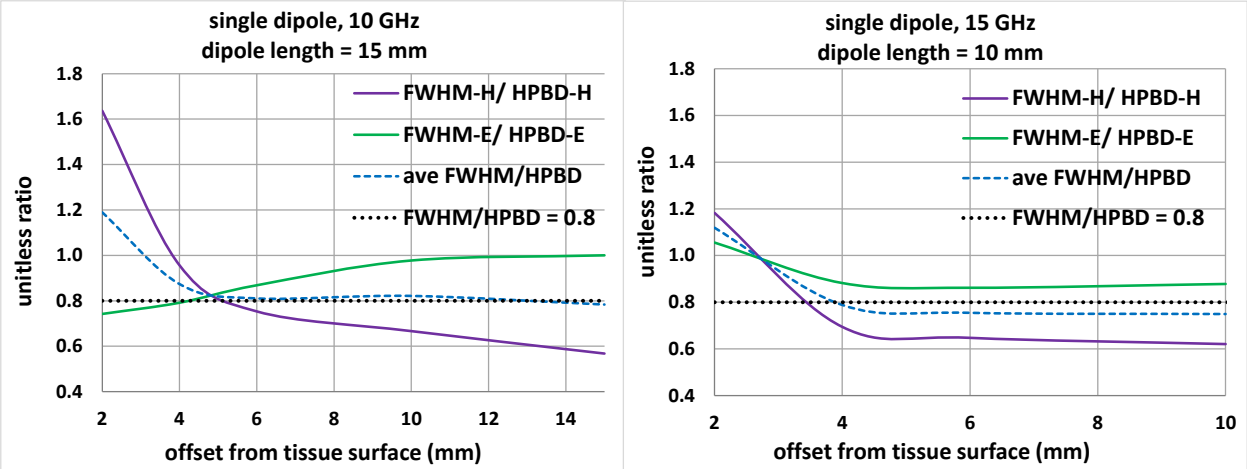

Fig. C.3.19: FWHM/HPBD ratio for the E and H axes, and averaged value versus offset for 10 and 15 GHz.

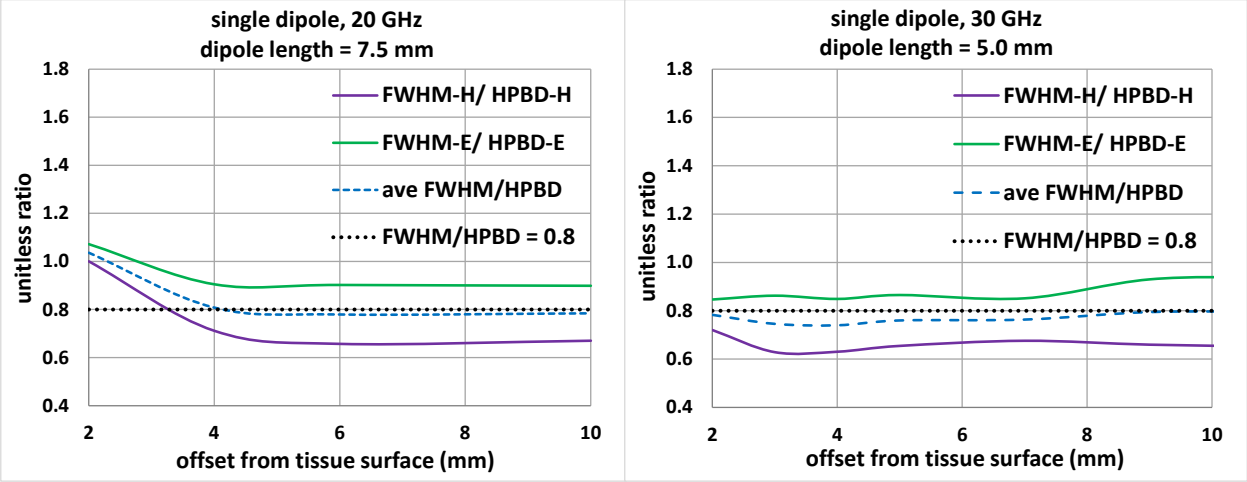

Fig. C.3.20: FWHM/HPBD ratio for the E and H axes, and averaged value versus offset for 20 and 30 GHz.

Discussion

For temperature rise estimates, unequal spot sizes would be averaged since the temperature-rise solver used in chapter 5 (Gajda et al., 2019) only accepts equal spot size dimensions in the two principal axes. The principal axes spot sizes from this study are in general unequal but have ratios typically within 20% at short ranges and closer in value at longer ranges. An average spot size of FWHM = 0.005 m is realizable at 20 GHz only for extremely close range (offset = 2 mm or for a gap between tissue and dipole of 1 mm) which are not likely to occur because the antenna for radio communication purposes are embedded in a product. For frequencies equal to or above 30 GHz, a minimum SAR spot size of FWHM = 0.005 m can be considered to account for the fact that smaller SAR spot sizes are realizable at higher frequencies. From the graphs above, a fixed FWHM/HPBD ratio of 0.8 appears to be an reasonable average ratio for a wide range of offsets.

C.4 Conclusion

In this Appendix, multiple avenues have been explored to assess the minimum beam diameter that can be emitted by antennas that can be found in telecommunication devices and their related SAR spot size in human tissues. A theoretical investigation of the minimum beam diameter of single element antenna and array antenna at the beginning of the far-fieldwas presented in Appendix C.1 and C.2. It was found that a simple half-wave dipole could generate a beam diameter that is approximately the size of the wavelength (λ), essentially one of the smallest relative beam diameters. The array factor was found to increase directivity (or gain) of the antenna but was not necessarily lowering the beam diameter, at the beginning of the far-field, because the distance to the far-field also increased with the number of elements composing the array. For instance, an array antenna composed of 10 half-wave dipoles would theoretically generate a beam diameter that is approaching 11.3λ which is more than if the array had only one element (i.e. a single half-wave dipole).

Simulation results were discussed in Appendix C.3, to verify the half-power projected beam width (HPBD) in free-space as compared to the SAR pattern full width half-maximum (FWHM) for a variety of spacings between the tissue block and the radiator. In this case, the radiator was either a single dipole or an array composed of three dipoles. The same conclusion has been drawn with respect to array antennas, which is that the directionality is increased but does not necessarily create a smaller spot size. When the separation distance is small (in the near field), the benefit of increased directionality of array antennas cannot be observed because each single element composing the array can still be resolved. In other words, the summation of each individual element patterns does not yet resemble one single pattern, rather it looks like separate individual patterns stitched together side by side. This means that there is no need to assess minimum beam spot sizes in the near-field from an array antenna. However, it was demonstrated that in the near-field when a tissue block is inserted in front of a single element antenna (i.e. half-wave dipole), a beam spot size smaller than the wavelength can be observed. Therefore, based on the discussion of this part of Appendix C.3, the following conclusions should be considered for assessing the impact of averaging areas proposed by the ICNIRP Guidelines (ICNIRP, 2020):

- A minimum SAR spot size of FWHM = 0.010 m should be considered for frequencies below 30 GHz when assessing exposure guidelines limits in section 5, otherwise this could lead to a misleading conclusions about the conservativeness (i.e. that the limit is not conservative enough when in fact the exposure condition is impossible).
- A minimum SAR spot size of FWHM = 0.005 m should be considered for frequencies equal to or above 30 GHz when assessing exposure guidelines limits in Section 5, to account for the fact that smaller SAR spot sizes are theoretically possible at higher frequencies.
- A fixed FWHM/HPBD ratio of 0.8 can reasonably be used for assessing the effect of proposed averaging areas (i.e. 1 cm^2 and 4 cm^2) on the unperturbed incident power density.

C.5 References

Balanis C. A. *Antenna Theory. Analysis and Design*. 3rd ed. Hoboken, NJ: Wiley, 2005.

Bouwkamp C. J., de Bruijn N. G. “The problem of optimum antenna current distribution.” *Philips Res. Rep*., vol. 1, pp. 135-158, Oct. 1945.

Chien T. V., Björnson E. “Massive MIMO communications.” In: *5G Mobile Communications*. Weng X., Zheng K., Shen X., Eds. S. L.: Springer, 2017, pp. 77-116. [Electronic resource].

Dolph C. L. “A current distribution for broadside arrays which optimizes the relationship between beam width and side-lobe level.” *Proc. IRE,* vol. 34, no. 6, pp. 335-348, Jun. 1946. DOI:10.1109/JRPROC.1946.225956

Hansen R. C. *Phased Array Antennas*. 2nd ed. Hoboken, NJ: Wiley, 2009.

Hussaini A. S., Abdulraheem Y. I., Voudouris K. N., Mohammed B. A., Abd-Alhameed R.A., Mohammed H. J., Elfergani I., Abdullah A. S., Makris D., Rodriguez J., Noras JM., Nche C., Fonkam M. “Green Flexible RF for 5G.” In: *Fundamentals of 5G Mobile Networks.* Rodriguez J., Ed. Chichester, West Sussex, UK: Wiley, 2015, pp. 241-272.

Kong J. A. *The Electromagnetic Wave Theory.* New York, NY: Wiley, 1986.

Leonov S. A. “Axis.” In: *Radar Technology Encyclopedia. Electronic edition.* Barton D. K., Leonov S. A., Eds. Boston, MA: Artech House, 1998, p. 60, left col.

Leonov S. A. “End-fire array.” In: *Radar Technology Encyclopedia. Electronic edition.* Barton D. K., Leonov S. A., Eds. Boston, MA: Artech House, 1998, p. 44, right col.

Riblet H. J. “Note on the maximum directivity of an antenna.” *Proc. IRE,* vol. 36, no. 5, pp. 620-623, May 1948. DOI:10.1109/JRPROC.1948.229955

Stone J. R. “Directive antenna array,” US patent 1,643,323, United States Patent Office, 27 Sep. 1927.

Stone J. R. “Antenna array,” US patent 1,715,433, United States Patent Office, 04 Jun. 1929.

Stutzman W. L., Thiele G. A. *Antenna Theory and Design,* 3rd ed. New York, NY: Wiley, 2013.

Tölli A., Thiele L., Suyama S., Fodor G., Rajatheva N., De Carvalho E., Zirwas W., Sorensen J. H. “Massive multiple-input multiple-output (MIMO) systems.” In: Osseiran A., Monserrat J. F., Marsch P., Eds. *5G Mobile and Wireless Communications Technology.* New York, NY: Cambridge University Press, 2016, pp. 208-247.

Yaru N. “A note on super-gain antenna arrays.” *Proc. IRE,* vol. 39, no. 9, pp. 1081-1085, Sep. 1951. DOI:10.1109/JRPROC.1951.273753

Ziolkowski R. W. “Using Huygens multipole arrays to realize unidirectional needle-like radiation.” *Phys. Rev. X,* vol. 7, no. 3, pp. 031017-1 - 031017-13, Jul. 2017. DOI:10.1103/PhysRevX.7.031017

Appendix D

Appendix D.1 - Finite difference solution of the dynamic BHTE

D.1.1 Coordinate system & assumptions:

The origin of the coordinate system lies at the air-tissue interface. The TEM wave is assumed to travel in the positive *z* (axial) direction. The term "transverse" refers to any direction orthogonal to the propagation axis, *z* (i.e. *x* and *y* in Cartesian and *r* in polar coordinates). The tissues theoretically extend to $z = \infty$, but, for the purposes of finite difference (FD) solution, are truncated to a depth of 0.050 m (which represents approximately 5 $R_{1\text{-}eff}$, at which point the steady-state TR will have decayed to approximately e^{-5}).

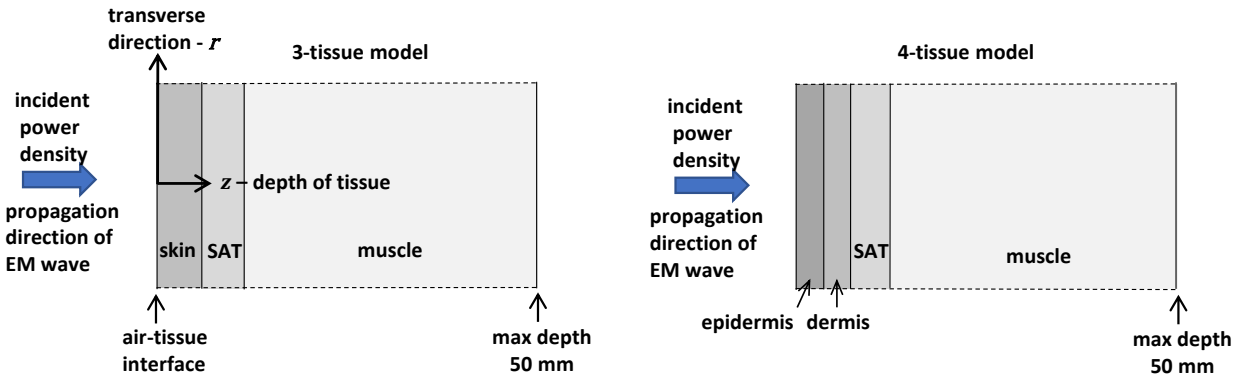

Fig D.1.1 Electromagnetic/thermal models composed of EM waves incident on tissue half-spaces.

D.1.2 1D BHTE

Although the 1D BHTE applies to plane waves, the TR for wide beams for which $FWHM \geq 10\ R_{1\text{-}eff}$ can be reasonably approximated by solution of the 1D formulation. The incident plane wave power density of intensity S_{inc} produces an axial SAR distribution, $SAR(t, z)$, which is the input energy term in the 1D dynamic BHTE given by:

$$\rho C \frac{\partial U(t,z)}{\partial t} = \frac{\partial k}{\partial z}\frac{\partial U(t,z)}{\partial z} + k\frac{\partial^2 U(t,z)}{\partial z^2} - \rho m_b\, \rho_b C_b\, U(t,z) + \rho\, SAR(t,z) \qquad (D.1.1)$$

where $U(t, z) = T(t, z) - T_{blood}$, $T(t, z)$ is the temperature in the tissues (measured in °C) and T_{blood} is the blood temperature taken to be 37 °C.

For layered tissues, the *z*-dependent thermal/physical parameters are: m_b, the blood perfusion (volumetric) rate in units $m^3kg^{-1}s^{-1}$, ρ, the mass density of the tissue layer in units of kg m^{-3}, *C*, the specific heat capacity of the tissue in units of J $kg^{-1}{}^{o}C^{-1}$ and *k*, the tissue heat conductivity in units of $Wm^{-1}{}^{o}C^{-1}$.

Parameters that are uniform throughout all layers are: C_b, the specific heat capacity of blood in units of J $kg^{-1}{}^{o}C^{-1}$ and ρ_b, the mass density of blood in units of kg m^{-3}.

The TR solver provides Finite Difference solutions to the dynamic BHTE (subject to convective surface boundary conditions) by discretizing the space z = 0 to z = 50 mm and converting the differential equation into a set of coupled difference equations. The time derivative is also represented as a finite difference and the time course of the solution is computed in a series of steps, referred to as a "time-stepping" process. This means that the solution at a given time depends on the one calculated at the previous time step. The "implicit" time-stepping scheme used by the solver provides stable solutions at any length of time step (although shorter steps provide greater accuracy).

Boundary conditions

The convective boundary condition on the surface of the skin states that the rate of heat flow away from the surface is proportional to the temperature difference between the surrounding air and the outermost tissue temperature. It can be expressed as:

$$-k\left.\frac{\partial T(t,z)}{\partial z}\right|_{z=0} = h\big(T_{air} - T(t,0)\big) \quad \text{or} \quad k\left.\frac{\partial U(t,z)}{\partial z}\right|_{z=0} = h(U(t,0) + T_{blood} - T_{air}) \quad (D.1.2)$$

where h is the convective heat loss coefficient in W $m^{-2}\,{}^{o}C^{-1}$, T_{air} is the ambient temperature of the air surrounding the skin and $T(t,0)$ is the surface temperature of the skin. All solutions were carried out with h = 10 W $m^{-2}\,{}^{o}C^{-1}$, which provides a nominal 31-33 ^{o}C skin surface temperature (depending on the tissue model) at room temperature (assumed to be 22 ^{o}C) in the absence of exposure. An additional boundary condition is used to solve eqn (D.1.1) consisting of $U(t,z_{max}) = 0$, where z_{max} is the truncation depth in the muscle layer. This ensures that temperatures in deeper tissues approach T_{blood}.

Solver description

The solver first computes the SAR distribution, power transmission coefficient, T_R, and the APD, S_{ab}, and AED, U_{ab}. Before time stepping, the initial (temperature) conditions in the tissues are computed by setting $\partial U/\partial t = 0$ in eqn (D.1.1) and solving it for $SAR(z) = 0$. This results in the steady-state distribution of temperature in the tissues in the absence of exposure, $U_{null}(z)$, and is the normal equilibrium temperature profile due to surface convection (temperatures at the surface will be significantly lower than 37 ^{o}C and rise with increasing depth to eventually equal 37 ^{o}C).

Starting with the equilibrium temperature distribution at t = 0, the program sets the SAR to the appropriate value and then solves for the temperature over the desired time course using the time-stepping scheme. This scheme provides temperatures in the whole FD spatial grid at each time-step, however, usually only the surface temperature is sought and stored at each time step. For a single isolated (non-recurring) pulse, the solver time-steps to the desired exposure duration then sets the SAR equal to zero and time-steps for an additional duration (chosen by the user, if desired). This is to observe the decay of temperature once the exposure has ceased. For groups of isolated pulses or continuous pulse trains,

the solver turns the SAR "ON" or "OFF" at the appropriate times while it time-steps over the desired total duration.

D.1.3 3D BHTE

Narrow beams are assumed to have rotational symmetry and thus, the 3D BHTE is formulated in cylindrical coordinates in terms of the radial coordinate, *r*, and the axial coordinate, *z*. The 3D SAR distribution (i.e. *SAR*(*t,r,z*)) is obtained from the axial 1D SAR distribution by multiplying the latter by a Gaussian term in *r* given by:

$$SAR(t,r,z) = SAR(t,z)\, exp\left\{-r^2/g^2\right\} \qquad (D.1.3)$$

where *g* is the Gaussian distribution parameter equal to *g* = 0.601 *FWHM.*

The axial SAR distribution in eqn (D.1.3), i.e. *SAR*(*t,z*), is the same as the one computed for the 1D case. For this purpose, it is assumed that the maximum intensity in the centre of the narrow beam is equal to the plane wave incident power density, S_{inc}, used to compute *SAR*(*t,z*).

The 3D dynamic BHTE is given by:

$$\rho C \frac{\partial U(t,r,z)}{\partial t} = \nabla \cdot \left(k\, \nabla U(t,r,z)\right) - \rho_b C_b\, \rho\, m_b\, U(t,r,z) + \rho\, SAR(t,r,z)$$
$$\text{where:} \quad \nabla \cdot (k\, \nabla U) = k\left\{\frac{1}{r}\frac{\partial U}{\partial r} + \frac{\partial^2 U}{\partial r^2}\right\} + \left(\frac{\partial U}{\partial z}\right)\left(\frac{\partial k}{\partial z}\right) + k\frac{\partial^2 U}{\partial z^2} \qquad (D.1.4)$$

where $U(t,r,z) = T(t,r,z) - T_{blood}$ represents the difference between the local tissue temperature, *T*(*t,r,z*), and the blood temperature. Also, like the 1D case, *k*, *ρ*, m_b and *C* are functions of *z*. Theoretically, the axial (*z*) and radial (*r*) dimensions extend to infinity, however, for FD solution, they are truncated to z_{max} = 0.05m and r_{max} (value dependent on *FWHM*) and appropriate boundary conditions are assigned to ensure proper behaviour of the solution.

Boundary conditions

Eqn (D.1.4) is solved subject to the convective boundary condition on the surface:

$$k\frac{dU(t,r,z)}{dz}\bigg|_{z=0} = h(U(t,r,0) + T_{blood} - T_{air}) \qquad (D.1.5)$$

Two additional boundary conditions and an initial condition are used to solve eqn (D.1.4). As with the 1D case, the condition *U* = 0 as z reaches z_{max}, ensures that deeper tissues approach T_{blood}. The boundary condition at the radial truncation length, r_{max}, is $U(t, r_{max}, z) = U_{null}(z)$ where U_{null} is the SS 1D solution with SAR = 0. This ensures that the temperature profile with respect to *z* at the radial distance r_{max} is equal to the equilibrium distribution of temperature in the tissues in the absence of exposure. The initial condition

consists of $U(0, r, z) = U_{null}(z)$. This condition ensures that all starting temperatures within the computation domain are again equal to the equilibrium distribution of temperature in the tissues in the absence of exposure. Thus, the net temperature-rise at any point in time in the computation domain is given by $\Delta T(t,r,z) = U(t, r, z) - U_{null}(z)$ where $U(t, r, z)$ is the time-stepped solution of eqn (D.1.4) subject to all initial and boundary conditions.

Appendix D.2 - Solutions of the BHTE for very short exposure durations

As mentioned in Section 5.4.1, heat transfer mechanisms in the BHTE have characteristic times of the order 1-2 s for diffusion and hundreds of seconds for perfusion (heat removal by blood flow). When the exposure duration is so short that there is insufficient time for diffusion, the BHTE can be greatly simplified by ignoring the diffusion and perfusion terms. This yields a first-order differential equation for both the 1D and 3D cases with a solution for the skin surface TR given by:

$$\Delta T|_{t_d \to 0} = \frac{SAR(0)}{C_{skin}} t_d \qquad (D.2.1)$$

where $SAR(0)$ is the SAR on the surface of the skin, C_{skin} is the specific heat capacity of skin in J kg^{-1} ^{o}C^{-1} and t_d is the pulse width or exposure duration. For the 1D case, this solution applies over the whole surface while for the 3D case, it applies at the centre of the projected beam.

The TR, normalized to the AED, is therefore given by:

$$\Delta T/U_{ab}\Big|_{t_d \to 0} = \frac{SAR(0)}{C_{skin} S_{inc} T_R} = \frac{1}{C_{skin}} \frac{SAR(0)/S_{inc}}{T_R} \qquad (D.2.2)$$

Eqn (D.2.2) states that in the limit as $t_d \to 0$, the ratio $\Delta T/U_{ab}$ approaches a fixed value that is largely dependent on the ratio of two factors: $SAR(0)/S_{inc}$ and T_R. Both these factors are functions of frequency and the distribution of permittivity and conductivity in the tissue layers. Because of this, Monte Carlo simulation by variation of tissue thicknesses is appropriately suited to derive statistics of $\Delta T/U_{ab}$ using (Eq. D.2.2).

In order to test the threshold exposure duration at which the short-pulse approximation of (Eq. D.2.2) is no longer valid, 1D FD MC simulations (i.e. solutions of the full 1D BHTE) were carried out for a 3-tissue configuration with increasingly smaller values of t_d. For these simulations, the grid sizes in the skin and shallower regions of SAT were reduced to 0.05 mm at 30 GHz and 0.025 mm at 80 GHz. This was done to allow for the extremely small amount of diffusion that would occur in such short time spans. In the same simulations, MC distributions of the results of eqn (D.2.2) were generated. These do not require solution of the BHTE, however they make use of the variation in $SAR(0)/S_{inc}$ and T_R with tissue thickness. The results for the 95th percentile $U_{ab\text{-}5}$ at 30 and 80 GHz are given in Fig. D.2.1 along with the results of the full 1D BHTE MC simulations. The graph confirms that (Eq. D.2.2) can be used to compute the asymptotic value of $U_{ab\text{-}5}$ as $t_d \to 0$ without the need for a full BHTE solution .

The graph of Fig. D.2.1 indicates that the approximation of (Eq. D.2.2) is within 2% of the full 1D BHTE MC result for t_d = 0.005 s (30 GHz) and t_d = 0.001 s (80 GHz). As a result, (Eq. D.2.2) was used for deriving U_{ab5} data for the shortest exposure durations (t_d = 0.001 s) in section 5.4.1 rather than a solution of the BHTE.

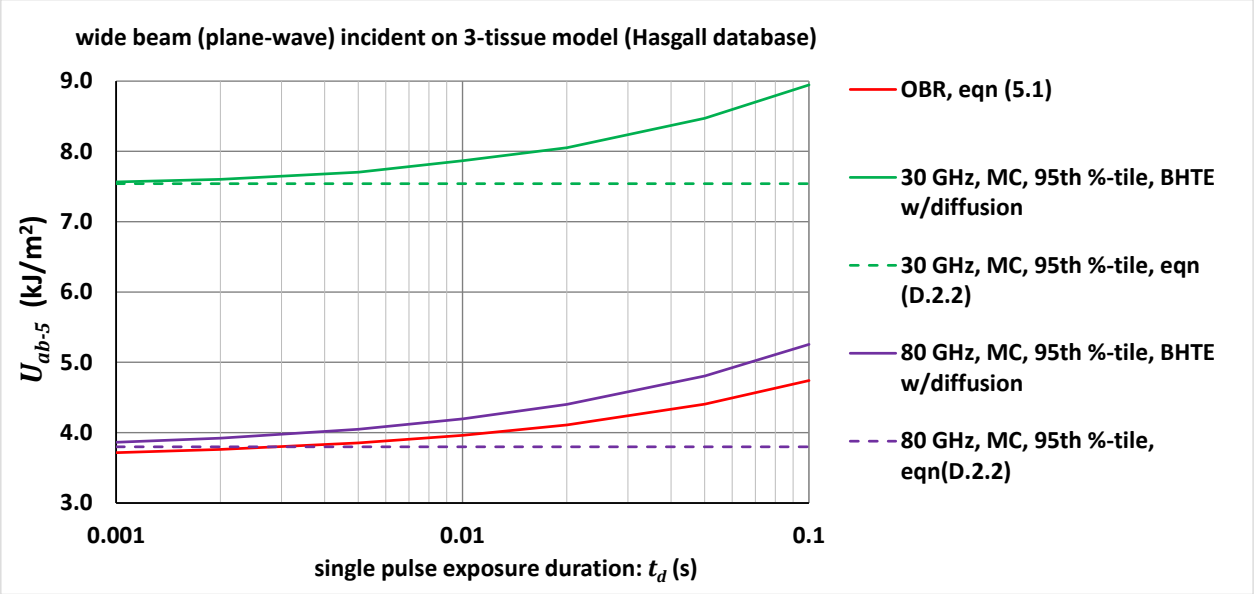

Fig. D.2.1, Comparison of full 1D MC FD solver results of U_{ab-5} (i.e. with diffusion) against MC determinations of (Eq. D.2.2) for a 3-tissue configuration (Hasgall database). Also shown is the ICNIRP OBR versus exposure duration, t_d.

It should also be noted that the resulting distributions of $\Delta T/U_{ab}$ from either the full 1D MC FD solver or the MC simulations of (Eq. D.2.2) were extremely narrow. This is likely due to both the shallow penetration of electromagnetic energy and the negligible amount of diffusion. In both cases, the resulting surface TR is nearly unaffected by the variation in the thickness of skin (and even less so by the variation of SAT thickness). Additionally, the ratio of $SAR(0)/S_{inc}$ to T_R is relatively constant as a function of skin and SAT thickness since they are closely correlated. This would account for the narrow distributions in the MC results of (Eq. D.2.2).

Appendix D.3 – Continuous pulse trains in the steady state

D.3.1 Conditions for maximum peak TR in the steady state

As described in Section 5.5.1, pulsed exposures produce TR oscillations that are superimposed on a constant TR, the latter of which corresponds to the time-averaged exposure intensity. Fig. 5.23 shows that the rise-time dynamics of pulsed responses are the same as for a CW step of the same time-average intensity. So long as the oscillation amplitudes are small, the pulsed TR response can be treated as if it were from a CW of the same average exposure intensity. However, some pulse conditions produce relatively large TR oscillations and, in these cases, the temporal peak TR becomes a limiting factor. Thus, it is important to determine the temporal conditions of the pulse train that produce the highest temporal peak TR for testing the OBRs.

A set of examples of pulsed responses is shown in Figs. D.3.1 and D.3.2 that help to visualize the optimal conditions for high peak TR. In Fig. D.3.1, two 50% DF pulse trains are compared; one with a pulse width of 50 s and the other with a pulse width of 5 s.

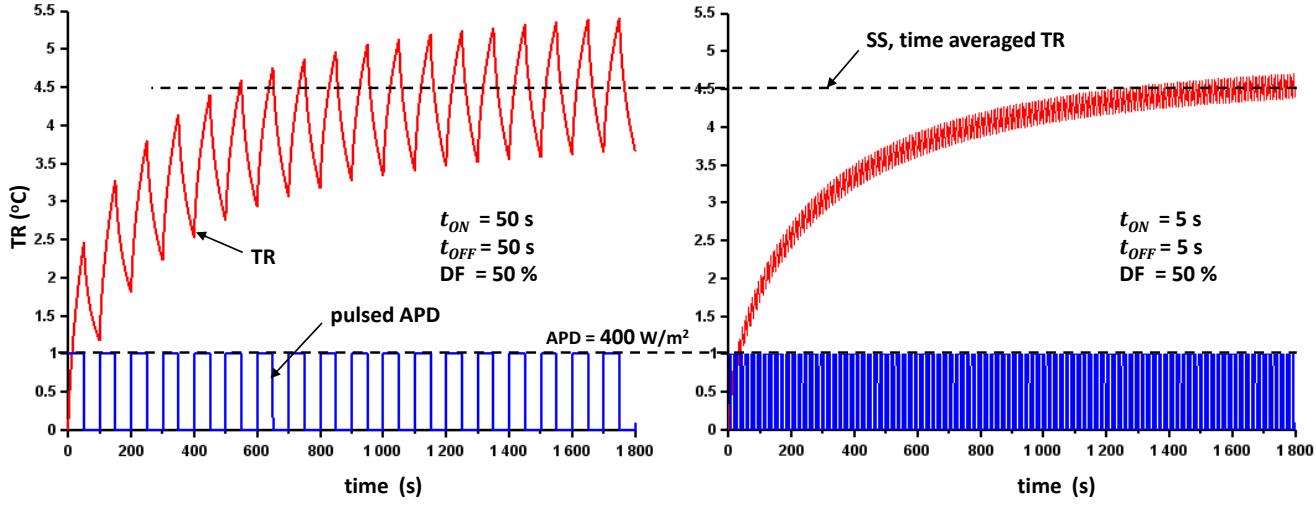

Fig. D.3.1, TR responses of 50% duty factor exposures having 50 s and 5 s pulse widths on the 3-tissue model (wide beam) at 30 GHz. Both exposures have time averaged APDs of 200 W/m^2.

Both responses are from exposures with the same average intensity and have the same average TR in the SS. However, the wider pulse width results in greater TR oscillation amplitude and peak TR. For a set duty factor, it is concluded that wider pulse widths produce greater peak TR for the same average exposure intensity. For some combinations of pulse width and duty factor, the oscillation amplitudes are insignificant and the exposure can be considered like a CW one.

In a second set of examples (Fig. D.3.2), the pulse width is fixed at 20 s and the inter-pulse period (or duty factor) is varied. For these calculations, the same time averaged APD is maintained.

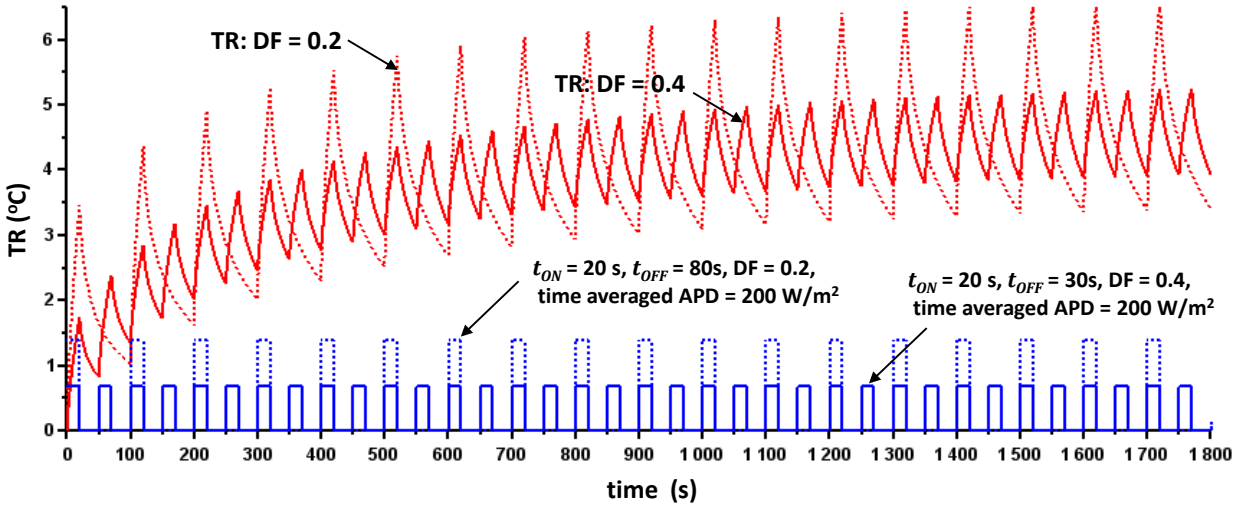

Fig. D.3.2, TR responses of exposures having the same pulse width but different duty factors on the same tissue and at the same spot-size and frequency.

Both responses have the same time averaged TR as the steady state is approached. However, the pulse train with the longer inter-pulse period produces a larger TR oscillation amplitude and peak TR. Both responses have the same heating durations (pulse width), however, the lower DF example has higher energy per pulse and consequently higher TR per pulse. This example also has a longer cooling time, allowing the TR to drop further before the onset of the next pulse.

From these examples, it is seen that for the same pulse width and average exposure intensity, wider inter-pulse periods (or lower duty factors) produce greater TR oscillation. If the pulses were spaced wide enough to allow complete cooling, the TR would return to zero before the next pulse arrives, resulting in the largest possible oscillation amplitude.

To summarize, pulse trains with low duty factors and high peak-to-average intensity, along with relatively wide pulse widths, produce significant peak TR that should be addressed in an examination of AED limits.

D.3.2 Maximum peak TR in the context of the 360 s reference period

The 360 s reference period (averaging window) imposes an additional constraint on continuous pulse trains with low duty factor and high peak-to-average intensity. This is because the reference period is applied as a “rolling window” meaning that it is intended to be scanned over a waveform looking for the maximal cumulative exposure. For testing the conservatism of the OBRs, the pulse pattern should therefore be repeated every 360 s in order to produce consistent average exposure intensity independent of window location.

In terms of the number of pulses to use in each 360 s reference period, it was shown in Section 5.4.4.2 that for an exposure duration defined as the TOT, the highest TR is produced when all of the AED is concentrated in a single pulse. This suggests that a single pulse per reference period constitutes the worst-case pulse pattern for a continuous pulse train (in the context of a rolling averaging window). This was

investigated in a series of calculations utilizing a constant pulse width of 1 s and different number of periods in a 360s window. (Examples of some of the pulse patterns in the first reference period are shown in Fig. D.3.3).

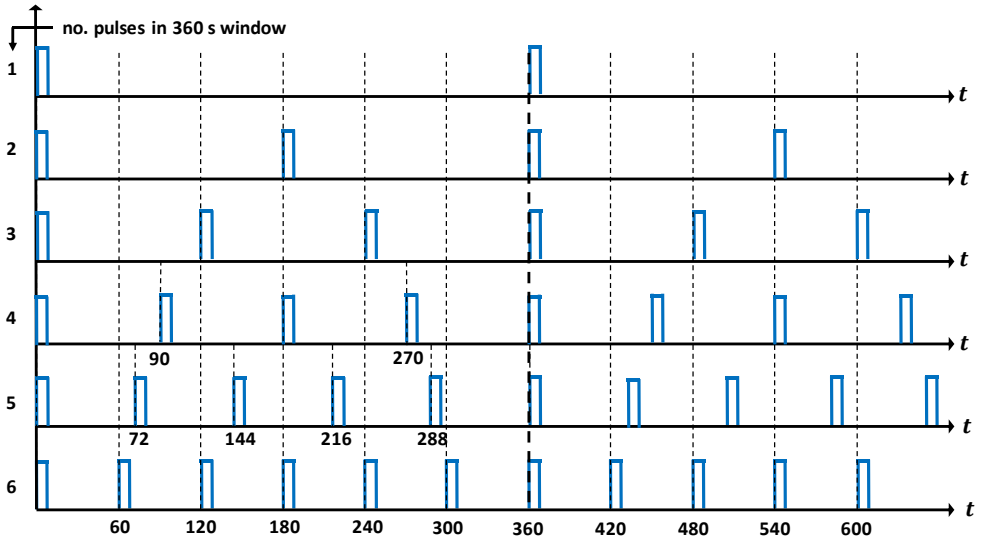

Fig. D.3.3, Examples of continuous pulse trains with different groups of 1 s pulses occurring in a reference period. These are used to determine the worst-case TR per AED in the context of a 360 s rolling window.

The TR calculations were carried out for various beam diameters at 30 GHz, incident on the 3-tissue model (skin: 0.6 mm, SAT: 6.0 mm and muscle: 43 mm). The number of whole periods in a 360 s window ranged from 1 to a maximum of 24. Time stepping calculations were carried out to a total time duration of 1440 s (4 reference periods) with an additional 1 s pulse appended at the end for a total time of 1441s. This total time duration was determined to be sufficient to reach 95 % of the SS TR for wide beams and 99.96 % of the SS TR for the narrowest beam tested (*FWHM* = 0.005 m).

The results are given in Figs. D.3.4 – D.3.8, which show the total AED in a 360 s reference period (spatially averaged and non-spatially averaged) that produces 5 ^{o}C SS peak temporal TR and the time-averaged APD (spatially averaged and non-spatially averaged) that produces 5 ^{o}C SS peak temporal TR. (Note that continuous pulse trains possess both an AED and a time-averaged APD, both of which can be compared to their respective OBRs.) All quantities are plotted versus the number of whole periods in a 360 s reference period. The graphs also depict the AED and APD OBRS that correspond to the various pulse patterns versus the number of whole periods in a 360 s reference period.

For the calculations, the total AED is the TOT in the 360 s reference period multiplied by the pulse heights: $U_{ab} = \sum S_{ab,pk}$ *(1 s). The time averaged APD is the sum of the 1 s pulses in the 360 s period, multiplied by the pulse heights and divided by 360s i.e. $S_{ab,ave} = (\sum S_{ab,pk}$ *(1 s))/360 s. Thus, the AED and APD are related by the factor 360 s. The quantities in the legends in Figs. D.3.4 – D.3.8 have the following meaning:

AED-*X*cm-5: total AED in a reference period, averaged over ***X*** cm^2, that produces 5 ^{o}C maximum TR in the SS where ***X*** has values 1, 4 and 0 (i.e spatial peak).

AED OBR-*X*cm: the OBR applicable to ***X*** cm^2 spatial average, where ***X*** has values 1 (eqn 5.2) and 4 (eqn 5.1) and exposure duration is taken to be the TOT in a reference period.

time ave APD-*X*cm-5: the time averaged APD (averaged over a reference period), spatially averaged over ***X*** cm^2, that produces 5 ^oC maximum TR in the SS where ***X*** has values 1, 4 and 0 (i.e spatial peak).

APD OBR-*X*cm: the OBR applicable to ***X*** cm^2 spatial average, where ***X*** has values 1 (equal to 400 W/m^2) and 4 (equal to 200 W/m^2) and exposure duration is taken to be the TOT in a reference period.

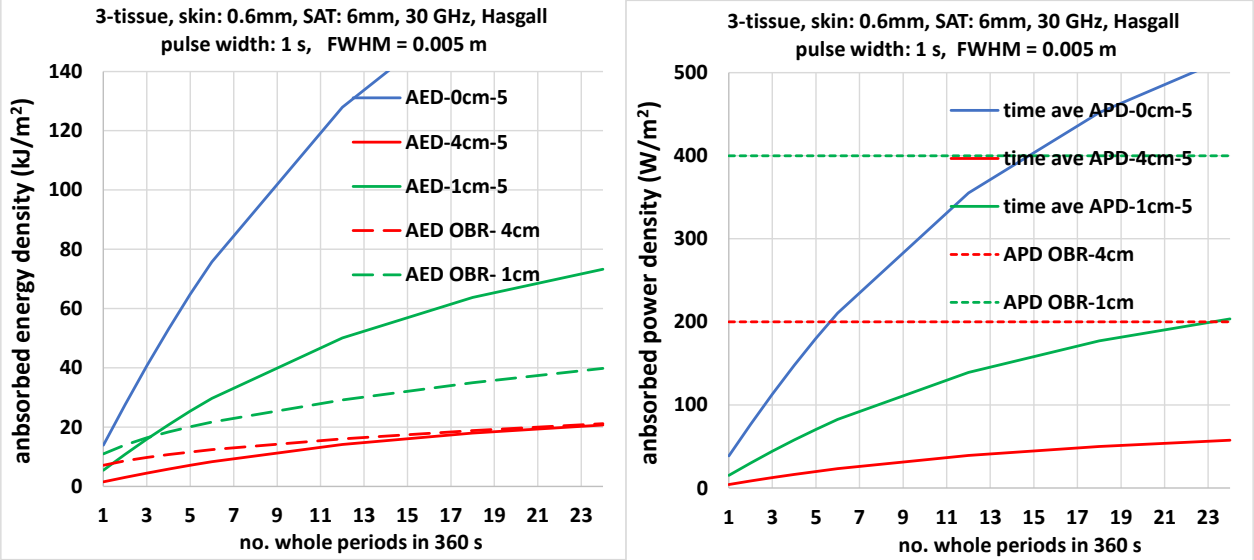

Fig. D.3.4, Comparison metrics and AED OBRs vs no. of periods in 360s window (left graph) and comparison metrics and APD OBRs vs no. of periods in 360s window (right graph) for a spot size *FWHM* = 0.005 m.

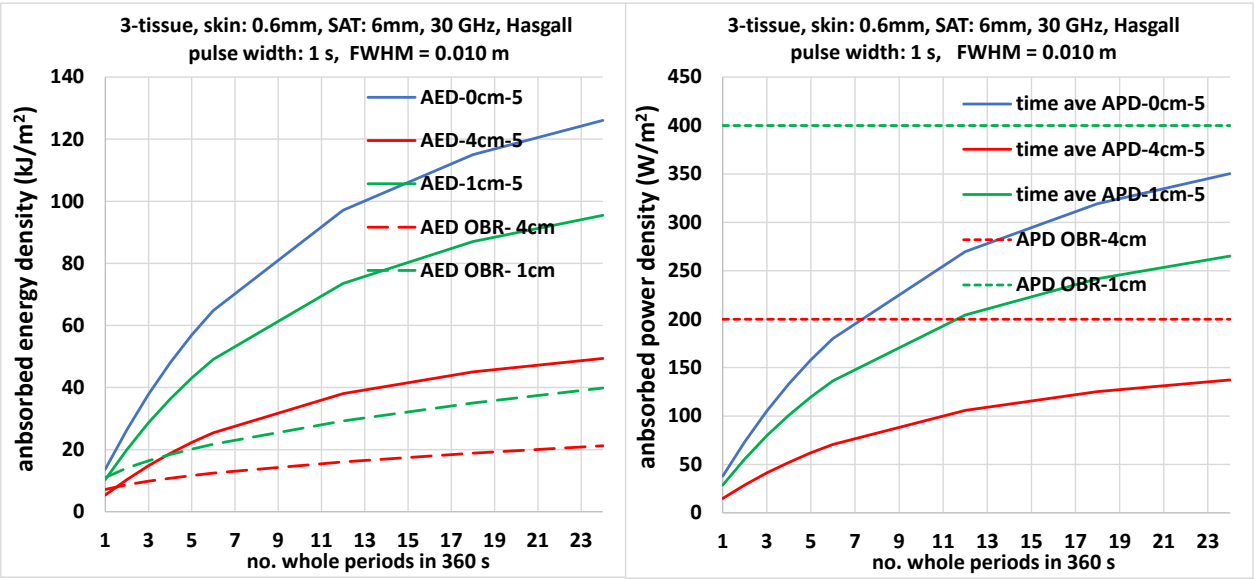

Fig. D.3.5, Comparison metrics and AED OBRs vs no. of periods in 360s window (left graph) and comparison metrics and APD OBRs vs no. of periods in 360s window (right graph) for a spot size *FWHM* = 0.010 m.

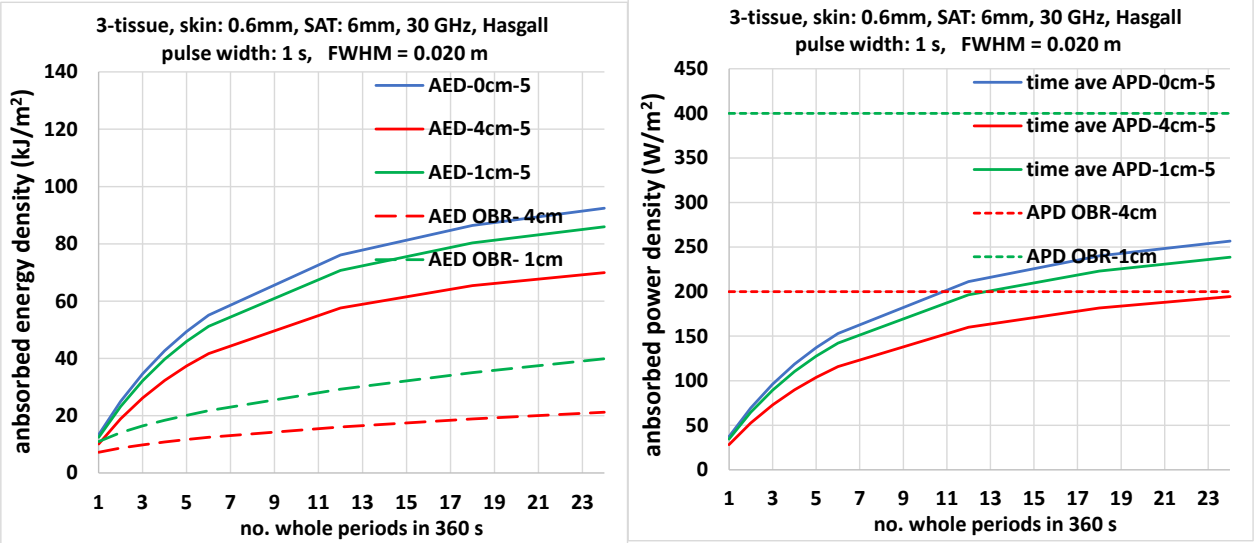

Fig. D.3.6, Comparison metrics and AED OBRs vs no. of periods in 360s window (left graph) and comparison metrics and APD OBRs vs no. of periods in 360s window (right graph) for a spot size *FWHM* = 0.020 m.

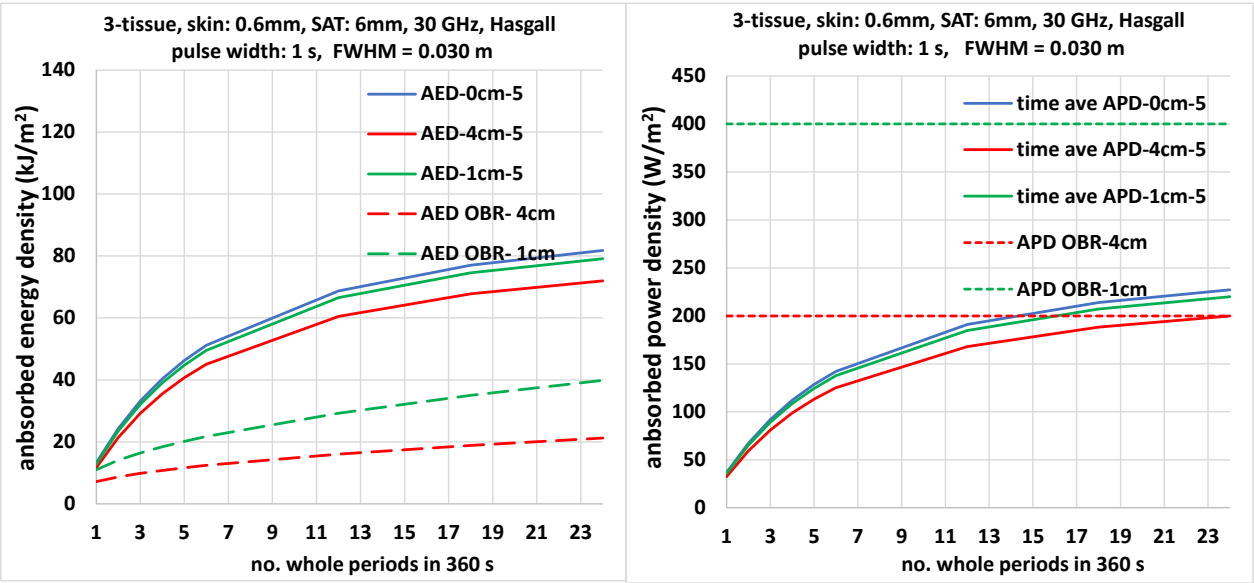

Fig. D.3.7, Comparison metrics and AED OBRs vs no. of periods in 360s window (left graph) and comparison metrics and APD OBRs vs no. of periods in 360s window (right graph) for a spot size *FWHM* = 0.030 m.

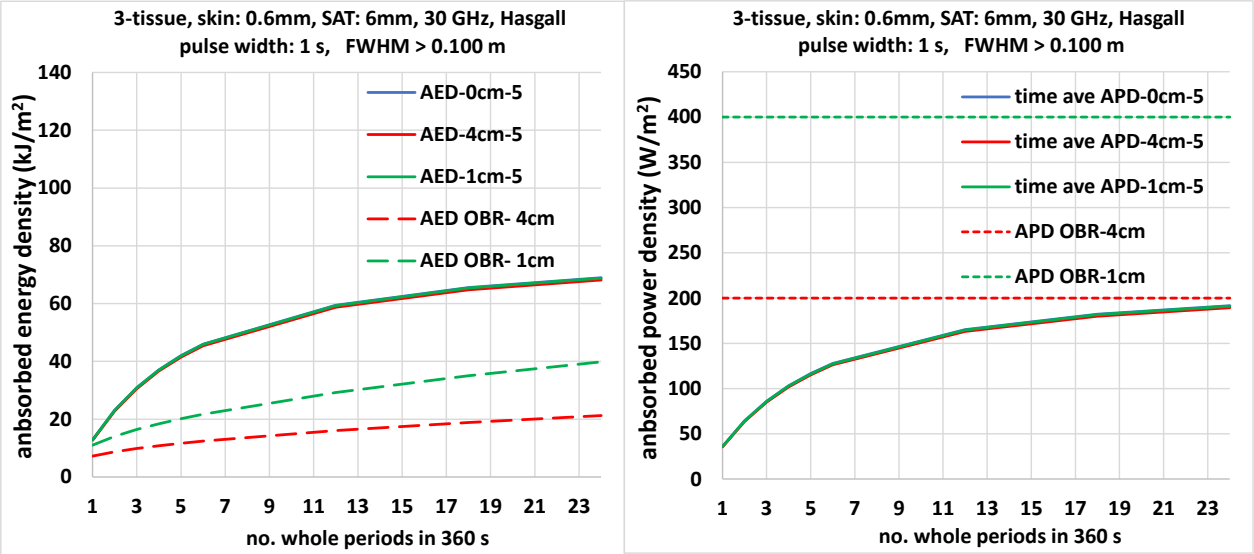

Fig. D.3.8, Comparison metrics and AED OBRs vs no. of periods in 360s window (left graph) and comparison metrics and PD OBRs vs no. of periods in 360s window (right graph) for a spot size *FWHM* > 0.100 m (wide-beam approximation).

The results in Figs. D.3.4 – D.3.8 confirm that the lowest AED that produces 5 °C SS peak TR occurs for 1 pulse per reference period. This is true whether the AED is spatially averaged or not. Thus, in the context of a 360s averaging window, a single pulse per 360 s window constitutes the worst-case pulse repetition rate for testing the ICNIRP OBRs. This pulse repetition rate is used in the evaluation trials for continuous pulse trains with a range of pulse widths utilized.

The information in Figs. D.3.4 – D.3.8 also show the degree of conservatism of the OBRs for the pulse trains used in the trials (with 1 s pulse widths). For spot sizes greater than FWHM = 0.020 m, all AED curves lay above their respective OBRs, indicating that the OBR is conservative for these example pulse trains, tissue model and frequency. Instances where the AED curve lies below the OBR indicates non-conservatism and is found for small spot sizes and low numbers of pulses per reference period.

With respect to the time averaged APD that produces 5 °C SS peak temporal TR, it is noted that in all graphs, all curves lie below their respective OBRs. However, for spot sizes of FWHM = 0.020 m and greater, the 4cm^2-averaged curve asymptotically approaches the OBR (200 W/m^2) as the number of periods increases beyond 24. This suggests that as the duty factor further increases, a time averaged APD that produces 5 °C TR would eventually approach 200 W/m^2, the 4 cm^2-averaged APD OBR. Compliance to both the AED and APD limits would be satisfied.

The results in Figs. D.3.4 – D.3.8 reveal that continuous pulse trains must meet the AED BRs since they form the more stringent requirements of the two. For example, a pulse train with 2 s pulse width and 360 s period has a 4 cm^2-averaged AED limit of 3.6+ 3.6*2^.5 = 8.7 kJ/m^2 (from eqn 5.1) and an APD limit of 200 W/m^2. For this AED limit, the maximum allowable pulse height or peak APD is 8700/2 = 4350 W/m^2. For the APD allowed by the limit, this results in a peak-to-average ratio equal to 4350/200 = 21.7. For this particular pulse train, however, the peak-to-average ratio is the reciprocal of its duty factor: 360/2 = 180.

Thus, as the peak power is increased, the AED limit will be reached before the APD limit and will serve to restrict any further increases in peak power.

Appendix D.4 - Spatial distribution of temperature-rise for extremely narrow beams

It was noted in the OBR evaluation results in Chapter 5 that the smallest spot size in the tests (*FWHM* = 0.005 m) consistently produces non-conservative results. To investigate the area and depth of the resulting hot spot for this beam diameter, distributions of TR with respect to the axial (along the z-axis) and radial (on the surface) distances were computed and are shown in Fig. D.4.1 for exposure durations of 1s, 10 s, 100s and 1000 s. They correspond to the 4-tissue, fixed-thickness configuration (Sasaki database) at 80 GHz. In each calculation, the incident (unperturbed) power density was adjusted to produce a 5 °C maximum TR at the end of the exposure.

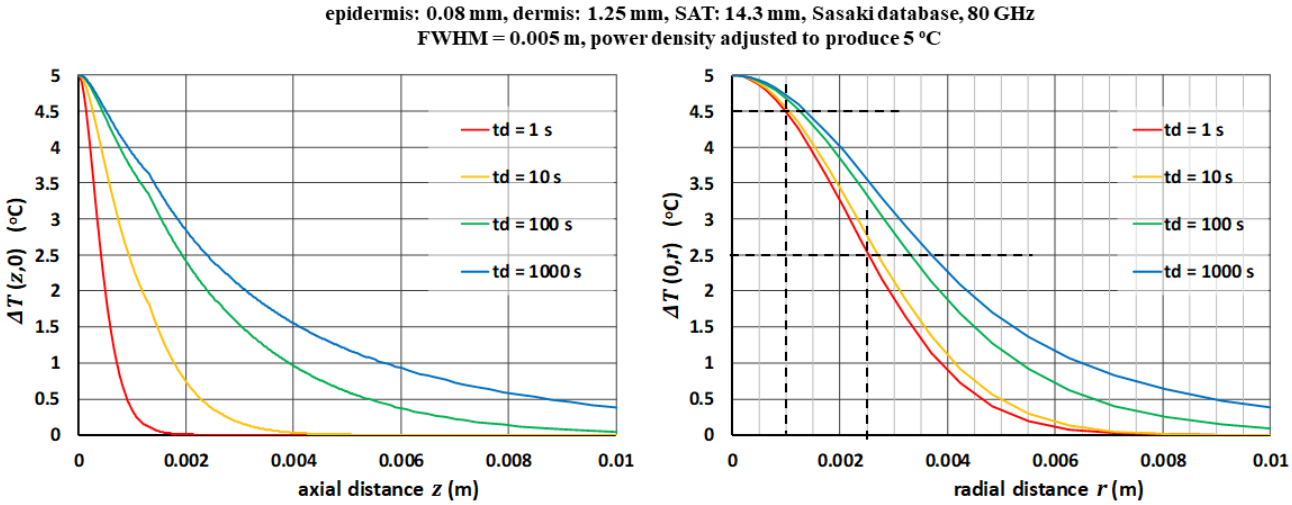

Fig. D.4.1, TR distributions in a fixed-thickness, 4-tissue configuration at 80 GHz for exposure durations of 1 s to 1000 s.

The axial distributions demonstrate the effect of diffusion and perfusion on the "penetration" of TR over time. For t_d = 1000 s, the maximum surface temperature reaches 99.8 % of the steady-state value. For this exposure duration, the tissues within only the first 1 cm experience any significant temperature-rise. This is reduced to approximately the first 1 mm for t_d = 1 s.

The radial distributions show that there is negligible spreading of the ΔT distribution beyond the SAR distribution (i.e. the 50% ΔT isotherm diameter ≈ *FWHM*) for short exposure durations (i.e. t_d < 10 s). Above t_d = 10 s, there is some additional spreading but it is not large (e.g. the 50% ΔT isotherm diameter = 0.0072 m at steady state or infinite exposure duration). This is consistent with the SS, 50 % isotherm diameter estimation formula in (Gajda et al. 2019) that predicts a value of 0.0076 m for this frequency and *FWHM*.

In terms of the diameter of the "hot-spot" on the surface (e.g. where the ΔT is within 90% of the maximum), the radial distributions show that it ranges from a value of 2 mm at short durations (t_d < 10 s) to approximately 2.6 mm in the steady state. The depth of the hot-spot is highly dependent on the exposure duration but even at the shortest duration (t_d = 1 s) is 0.15 mm.

Appendix D.5 - Spatial averaging power and energy densities:

The absorbed power density (APD), S_{ab}, and absorbed energy density (AED), U_{ab}, are assumed to be rotationally symmetric and have a Gaussian intensity distribution with respect to the radial distance, r. In the case of the APD, it can be written as:

$$S_{ab}(r) = S_{ab,o}\, exp\left\{-r^2/g_s{}^2\right\} = S_{ab,o}\, exp\left\{-(x^2+y^2)/g_s{}^2\right\}, \quad g_s = 0.601\, HPBD \qquad (D.5.1)$$

Over a square area with dimensions $2x_o$ x $2y_o$, the spatially averaged, APD is:

$$S_{ab,Xcm} = \frac{4}{(2x_o)(2y_o)} \int_0^{y_o} \int_0^{x_o} S_{ab,o}\, exp\left\{-(x^2+y^2)/g_s{}^2\right\} dx\, dy$$

$$= \frac{S_{ab,o}}{x_o y_o} \left[\int_0^{y_o} exp\left\{-y^2/g_s{}^2\right\} dy\right]\left[\int_0^{y_o} exp\left\{-x^2/g_s{}^2\right\} dx\right]$$

$$= \frac{\pi\, g_s{}^2 S_{ab,o}}{4\, x_o y_o} \quad erf\left(\frac{x_o}{g_s}\right) erf\left(\frac{y_o}{g_s}\right) \qquad (D.5.2)$$

where the subscript "X" has the symbol "4" when $2x_o = 2y_o$ = 2 cm and the symbol "1" when $2x_o = 2y_o$ = 1 cm, corresponding to 4 cm^2 and 1 cm^2 spatial averages, respectively.

This can be compared to the circular spatial average over the radius R_a given by:

$$S_{ab,Xcm} = \frac{1}{\pi R_a{}^2} \int_0^{R_a} S_{ab,o}\, exp\left\{-r^2/g_s{}^2\right\} 2\pi r\, dr \quad , \quad g_S = 0.601\, HPBD$$

$$= S_{ab,o} \frac{g_S{}^2}{R_a{}^2}\left[1 - exp\left\{-R_a{}^2/g_S{}^2\right\}\right] \qquad (D.5.3)$$

For a 4 cm^2 square area, $x_o = y_o$ = 1.00 cm while for the same circular area, R_a = 1.128 cm. For a 1 cm^2 square area, $x_o = y_o$ = 0.50 cm while for the same circular area, R_a = 0.564 cm. The two averaging formulae, eqns (D.5.2) and (D.5.3) produce results within 1.5 % of each other for the same $S_{ab,o}$ and over all values of HPBD.

Appendix D.6 - Sasaki tissue parameter data base

D.6.1 Dielectric properties

- The dielectric properties were measured *in vitro* using porcine tissues at body temp (approx. 35 ^{o}C).
- Dermis (to 1000 GHz), SAT (to 1000 GHz), and muscle (to 100 GHz) were measured and reported in Sasaki et al. 2017.
- Epidermis and dermis (both to 110 GHz) were measured and reported in Sasaki et al. 2014.
- Data for epidermis (100 to 300 GHz) from Pickwell et al 2004 was reported in Sasaki et al. 2014. This data facilitated extrapolation of the Sasaki epidermis data to 200 GHz.
- Graphs in the publications were enlarged and overlaid with a precision grid to allow reading of the values. This method results in values of the real and imaginary parts of ε_r having an estimated 2 ½ significant digits of precision. The values are given in the table below with the imaginary part of ε_r converted to the equivalent conductivity (showing 3 significant digits).

Table D.6.1 Dielectric values for the Sasaki database

freq	Epidermis			Dermis			SAT			Muscle		
GHz	$re\{\varepsilon_r\}$	$-im\{\varepsilon_r\}$	σ (S/m)	$re\{\varepsilon_r\}$	$-im\{\varepsilon_r\}$	σ (S/m)	$re\{\varepsilon_r\}$	$-im\{\varepsilon_r\}$	σ (S/m)	$re\{\varepsilon_r\}$	$-im\{\varepsilon_r\}$	σ (S/m)
10	26.0	9.6	5.3	32.8	14.1	7.8	14.6	5.6	3.1	38.0	18.0	10.0
20	20.3	12.4	13.8	24.3	16.6	18.4	11.0	6.8	7.6	27.0	20.6	22.9
30	15.5	12.8	21.3	18.4	16.0	26.7	8.5	6.5	10.8	19.7	19.5	32.5
60	8.5	10.0	33.3	10.3	11.9	39.7	5.6	4.6	15.3	10.6	13.6	45.3
70	7.5	9.0	35.0	9.2	10.7	41.6	5.3	4.3	16.5	9.7	12.5	48.6
80	6.8	8.2	36.4	8.4	9.9	43.8	5.1	4.0	17.8	8.9	11.4	50.5
90	6.2	7.5	37.5	7.7	9.0	45.0	5.0	3.8	18.8	8.0	10.5	52.5
94	6.0	7.3	37.9	7.5	8.7	45.2	4.9	3.7	19.3	7.7	10.2	53.3
100	5.7	6.9	38.5	7.3	8.3	46.0	4.8	3.6	20.0	7.3	9.9	54.9
120	5.1	5.8	38.9	6.6	7.0	46.7	4.7	3.3	22.0	6.1	8.6	57.5
130	4.9	5.4	39.0	6.3	6.5	46.9	4.6	3.2	23.1	5.6	8.1	58.5
140	4.7	5.0	39.1	6.1	6.1	47.5	4.5	3.1	23.9	5.2	7.6	58.7
160	4.5	4.4	39.1	5.9	5.4	48.3	4.4	2.9	25.8	4.7	6.8	60.5
180	4.5	3.9	39.2	5.7	5.0	50.0	4.3	2.8	28.0	4.4	6.3	63.0
200	4.4	3.7	41.1	5.6	4.6	51.1	4.3	2.7	30.0	4.2	6.1	67.8

D.6.2 Thermal/physical properties:

Table D.6.2 Thermal / physical constants for the Sasaki database

	epidermis	dermis	SAT	muscle	blood
thermal conductivity: *k*	0.42	0.42	0.25	0.50	-

mass density: ρ	1109	1109	911	1090	1050
blood perfusion rate: m_b	0	1.99×10^{-6}	0.452×10^{-6}	0.452×10^{-6}	-
specific heat capacity: C	3391	3391	2348	3421	3930

Appendix D.7 - Test of ICNIRP (2020) Table3 - Note 5 interpretation

Testing of the ICNIRP 2020, Table3 - Note 5 interpretation of eqn (5.4) is carried out for equally spaced, 1 s width pulses in groups of 2, 3 and an arbitrary number, *N*, pulses. The exposure conditions used in the tests will be a 30 GHz wide-beam (FWHM > 0.1 m) as well as 30 and 60 GHz narrow beams (both *FWHM* = 0.010 m) incident on a 3-tissue model (skin: 0.6 mm & SAT: 6.0 mm). The AED OBR that will be used in the tests is eqn (5.1), normally corresponding to a 4 cm^2 spatial average, however, the spatial average used in the tests will be 1 cm^2. While this is not the OBR/averaging combination specified in the ICNIRP 2020 guideline, it is one that results in lower overall temperature-rises and thus is able to highlight any exceedances of the target OAHE temperature rises.

D.7.1 2-pulse group

Define the 2-pulse group parameters according to the figure below:

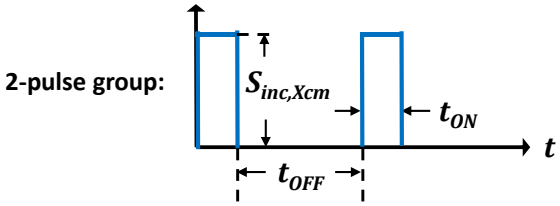

Fig. D.7.1

where $S_{inc,Xcm}$ is the temporal peak, incident power density that is spatially averaged over X cm^2. As noted above, the averaging area will be taken to be 1 cm^2 (i.e. X = 1) for testing of spot sizes with FWHM = 0.010 m and X = 0 (i.e. spatial peak) for wide beams (FWHM > 0. 10 m) in order to produce generally more conservative results than the ICNIRP 2020 recommended combination.

According to the Table 3- Note 5 interpretation, eqn (5.4) should hold for any time duration, Δt. For this simple example, Δt has two pivotal values. The first is $\Delta t = t_{ON}$ (i.e. integration over the first pulse) and the second is $\Delta t = t_{ON} + t_{OFF} + t_{ON}$ (i.e. integration over both pulses and the inter-pulse period). Integrating over the first pulse results in eqn (5.4) being written as (for localized exposure general public basic restriction):

$$\int_0^{t_{on}} S_{ab,1cm}(t)dt \leq 7200\left[0.05 + 0.95\sqrt{t_{on}/360}\right] \qquad (D.7.1)$$

or

$$S_{inc,1cm} T_R t_{ON} \leq 360 + 360\sqrt{t_{on}} \qquad (D.7.2)$$

where $S_{inc,1cm}\, T_R = S_{ab,1cm}$ during the pulse ON time and T_R is the transmission coefficient of power across the air-tissue interface. The inequality above is written in terms of the incident power density, S_{inc}, because

this is the input quantity utilized by the finite difference (FD) solver. The transmission coefficient is accounted for in the solution of the SAR distribution and the spatially averaged power density, $S_{inc,1cm}$, is found from the spatial peak value using a coefficient (factor) based on the formulae in Appendix D.5. Also, in eqn (D.7.2), the multiplication of constant terms in the OBR has been carried through and rounded off to make it easier for the reader to follow.

Solving for the temporal peak APD (or pulse height) gives:

$$S_{inc,1cm}T_R \leq \frac{360 + 360\sqrt{t_{on}}}{t_{ON}} \qquad (D.7.3)$$

where t_{ON} is in units of s giving a $S_{inc,1cm}$ in units of W/m^2.

Integrating to the end of the second pulse results in eqn (5.4) being written as:

$$\int_0^{t_{on}+t_{OFF}+t_{on}} S_{ab,1cm}(t)dt \leq 360 + 360\sqrt{2t_{on} + t_{OFF}} \qquad (D.7.4)$$

or

$$S_{inc,1cm}T_R(2t_{on}) \leq 360 + 360\sqrt{2t_{on} + t_{OFF}} \qquad (D.7.5)$$

Solving for the APD pulse height gives:

$$S_{inc,1cm}T_R \leq \frac{360 + 360\sqrt{2t_{on} + t_{OFF}}}{2\ t_{ON}} \qquad (D.7.6)$$

The Note 5 interpretation requires that both conditions (eqns D.7.3 and D.7.6) must be satisfied, implying that the lesser value of $S_{inc,1cm}\ T_R$ evaluated is the maximum APD pulse height allowed by the OBR for the 2-pulse group.

Table D.7.1 gives the maximum allowable $S_{inc,1cm}\ T_R$ values for a fixed pulse width of 1 s (i.e. t_{ON} = 1) for different durations of t_{OFF}. It also gives the peak TRs on the 3-tissue model (skin: 0.6 mm & SAT: 6.0 mm) at 30 GHz (wide-beam), 30 GHz (*FWHM* = 0.010 m) and 60 GHz (*FWHM* = 0.010 m) for the lesser of the two values of $S_{inc,1cm}\ T_R$ from either eqns (D.7.3) or (D.7.6).

For the last two columns in the table, the ratio *FWHM/HPBD* was assumed to have a value of 0.8 so that a spot size of *FWHM* = 0.010 m is equivalent to *HPBD* = 0.01/.8 = 0.0125 m. This yields a 1cm^2 spatial averaging factor of 0.757 (meaning $S_{inc,1cm}$ = 0.757 S_{inc}) from which S_{inc} is solved and input into the FD solver. Transmission coefficients for this tissue model at 30 GHz and 60 GHz are T_R = 0.484 and 0.623, respectively.

Table D.7.1, Pulse parameters used in the test of the Note 5 interpretation for a 2-pulse group and the corresponding maximal TR in the 3-tissue model. All calculations use t_{ON} = 1s.

1 t_{OFF} s	2 $S_{inc,1cm}\ T_R$ eqn (D.7.3) W/m²	3 $S_{inc,1cm}\ T_R$ eqn (D.7.6) W/m²	TR for lesser $S_{inc,1cm}\ T_R$ of cols. 2 & 3		
			30 GHz wide-beam °C	30 GHz *FWHM* = 0.010 m °C	60 GHz *FWHM* = 0.010 m °C
0	720	435	0.28	0.37	0.52
0.5	720	465	0.29	0.39	0.53
1	720	492	0.30	0.40	0.55
2	720	540	0.31	0.42	0.58
3	720	583	0.33	0.44	0.61
4	720	621	0.34	0.46	0.64
5	720	656	0.35	0.48	0.66
7	720	720	0.38	0.50	0.70
8	720	749	0.37	0.50	0.69
10	720	804	0.36	0.48	0.68
15	720	922	0.35	0.46	0.65

The optimum TR (in the sense that TR is maximized) is reached when the right-hand sides of conditions (D.7.3) and (D.7.6) are equal. This is solved for the optimum t_{OFF} as:

$$t_{OFF} = 1 + 4\sqrt{t_{on}} + 2t_{on}$$

which results in a value of t_{OFF} = 7 s when t_{ON} = 1 s.

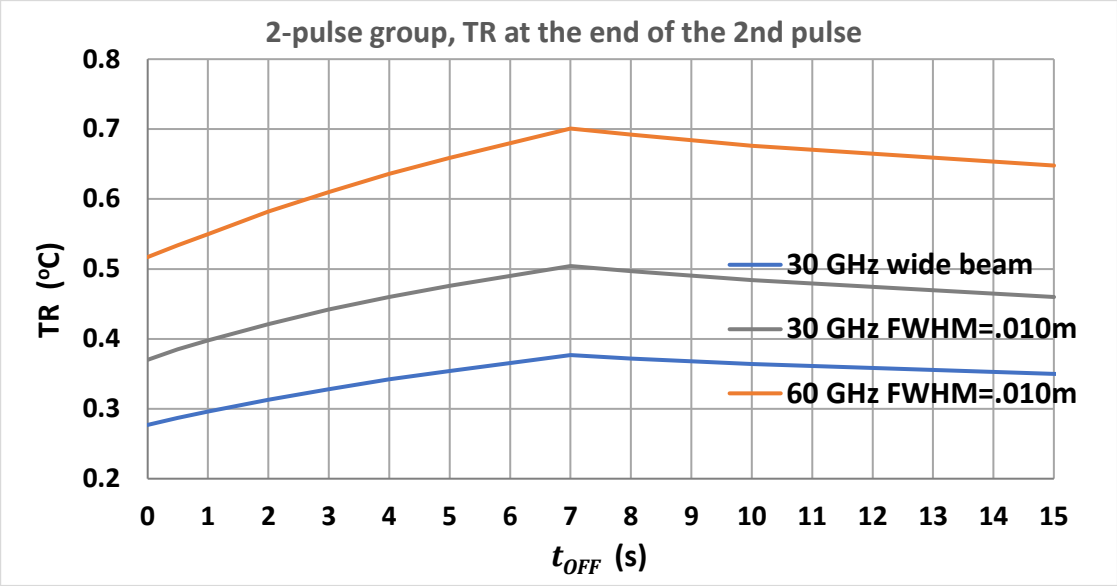

Fig. D.7.2, TR due to a 2-pulse group satisfying the ICNIRP Note 5 interpretation vs t_{OFF}. Results are for the 3-tissue model (skin: 0.6 mm & SAT: 6.0 mm).

D.7.2 3-pulse group

Define the 3-pulse group parameters according to the figure below:

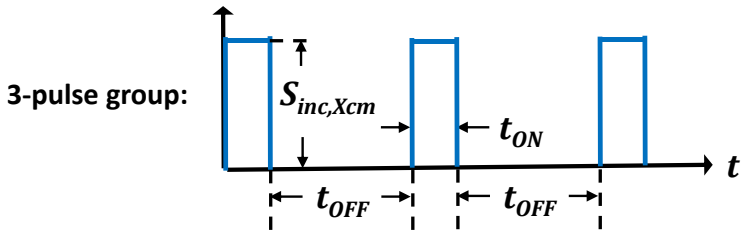

Fig. D.7.3

The same two conditions as eqns (D.7.3) and (D.7.6) apply to this group as well as a third:

$$S_{inc,1cm}T_R \leq \frac{360 + 360\sqrt{3t_{on} + 2t_{OFF}}}{3\ t_{ON}} \qquad (D.7.7)$$

Table D.7.2 gives the maximum allowable $S_{inc,1cm}\ T_R$ for a fixed pulse width t_{ON} = 1s for different durations of t_{OFF} for the 3-pulse group. It also gives the final TRs of the 3-tissue model (skin: 0.6 mm & SAT: 6.0 mm) at 30 GHz (wide-beam), 30 GHz (*FWHM* = 0.010 m) and 60 GHz (*FWHM* = 0.010 m) for the lesser of the values of $S_{inc,1cm}\ T_R$ from conditions (D.7.3), (D.7.6) and (D.7.7).

For the last two columns in the table, the ratio *FWHM/HPBD* was assumed to have a value of 0.8, yielding a 1cm^2 spatial averaging factor of 0.757. Transmission coefficients for this tissue model at 30 GHz and 60 GHz are T_R = 0.484 and 0.623, respectively.

Table D.7.2, Pulse parameters used in the test of the Note 5 interpretation for a 3-pulse group and the corresponding maximal TR in the 3-tissue model. All calculations use t_{ON} = 1s.

1	2	3	4	TR for lesser $S_{inc,1cm}\ T_R$ of cols. 2, 3 & 4		
t_{OFF} s	$S_{inc,1cm}\ T_R$ eqn (D.7.3) W/m^2	$S_{inc,1cm}\ T_R$ eqn (D.7.6) W/m^2	$S_{inc,1cm}\ T_R$ eqn (D.7.7) W/m^2	30 GHz wide beam °C	30 GHz *FWHM* = 0.010 m °C	60 GHz *FWHM* = 0.010 m °C
0	720	435	328	0.29	0.39	0.52
0.5	720	465	360	0.30	0.41	0.54
1	720	492	388	0.31	0.42	0.56
2	720	540	438	0.33	0.45	0.60
3	720	583	480	0.35	0.47	0.62
5	720	656	553	0.38	0.50	0.67
7	720	720	615	0.40	0.53	0.71
8	720	749	643	0.41	0.54	0.73
10	720	804	696	0.43	0.56	0.76
11	720	829	720	0.44	0.57	0.77
12	720	854	744	0.43	0.56	0.76

13	720	877	766	0.43	0.55	0.75
20	720	1024	907	0.40	0.50	0.69

The optimum TR is reached when the right-hand sides of conditions (D.7.3) and (D.7.7) are equal. This is solved for the optimum t_{OFF} as:

$$t_{OFF} = 2 + 6\sqrt{t_{ON}} + 3t_{ON}$$

which results in a value of t_{OFF} = 11 s when t_{ON} = 1 s.

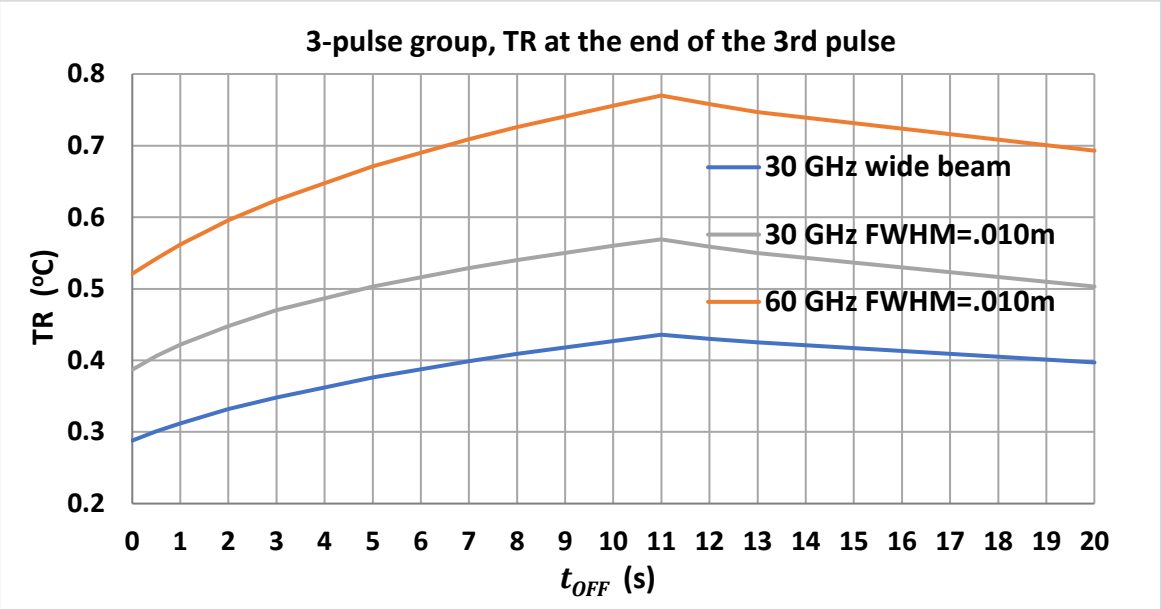

Fig. D.7.4, TR due to a 3-pulse group satisfying the ICNIRP Note 5 interpretation vs t_{OFF}. Results are for the 3-tissue model (skin: 0.6 mm & SAT: 6.0 mm).

D.7.3 N-pulse group

From the previous two examples it was observed that the lowest allowable pulse heights occur for the case when the integration is over all *N* pulses (up to the optimum t_{OFF}). Beyond the optimum t_{OFF}, the lowest allowable pulse height corresponds to integration over a single pulse. Thus, only these two criteria are needed to characterize the lowest allowable pulse heights. The *N*-th condition resulting from the integration over all *N* pulses is given by:

$$S_{inc,1cm}T_R \leq \frac{360 + 360\sqrt{N\,t_{ON} + (N-1)t_{OFF}}}{N\,t_{ON}} \qquad (D.7.8)$$

Following the same procedure as the previous two examples, the optimum TR is reached when the right-hand sides of conditions (D.7.3) and (D.7.8) are equal. This is solved for the optimum t_{OFF} as:

$$t_{OFF} = N\left(1 + \sqrt{t_{ON}}\right)^2 - 1 \qquad (D.7.9)$$

For reference, the exact version of eqn (D.7.9) is given by:

$$\frac{t_{OFF}}{360} = \frac{N}{(.95)^2}\left(.05 + .95\sqrt{t_{ON}/360}\right)^2 - \frac{(.05)^2}{(.95)^2} \qquad (D.7.10)$$

Since the equality of the conditions (D.7.3) and (D.7.8) are used to find the optimum t_{OFF}, then at this value of t_{OFF}, the maximum allowable $S_{inc,1cm}T_R$ is simply given by eqn (D.7.3) (i.e. it is defined by the integration over a single pulse). Thus, all values of maximum allowable $S_{inc,1cm}T_R$ associated with the optimum value of t_{OFF} in eqn (D.7.9) are identical and are equal to the single pulse value of 720 W/m^2 (for t_{ON} = 1 s).

Table D.7.3 gives values of optimum t_{OFF} found using eqn (D.7.9) for a range of *N* (all for t_{ON} = 1s). It also gives the peak TR on the 3-tissue model at 30 GHz (wide-beam), 30 GHz (*FWHM* = 0.010 m) and 60 GHz (*FWHM* = 0.010 m) for $S_{inc,1cm}T_R$ = 720 W/m^2.

Table D.7.3, Pulse parameters used in the test of the Note 5 interpretation for a *N*-pulse group and the corresponding optimal peak TR on the 3-tissue model. All calculations use t_{ON} = 1s and $S_{inc,1cm}T_R$ = 720 W/m^2.

number of pulses in the group *N*	optimum t_{OFF} (i.e. optimizes the peakTR) s	TR		
		30 GHz wide-beam °C	30 GHz *FWHM* = 0.010 m °C	60 GHz *FWHM* = 0.010 m °C
2	7	0.38	0.50	0.70
3	11	0.44	0.57	0.77
4	15	0.47	0.59	0.79
5	19	0.49	0.58	0.78
6	23	0.50	0.57	0.76
7	27	0.50	0.55	0.74

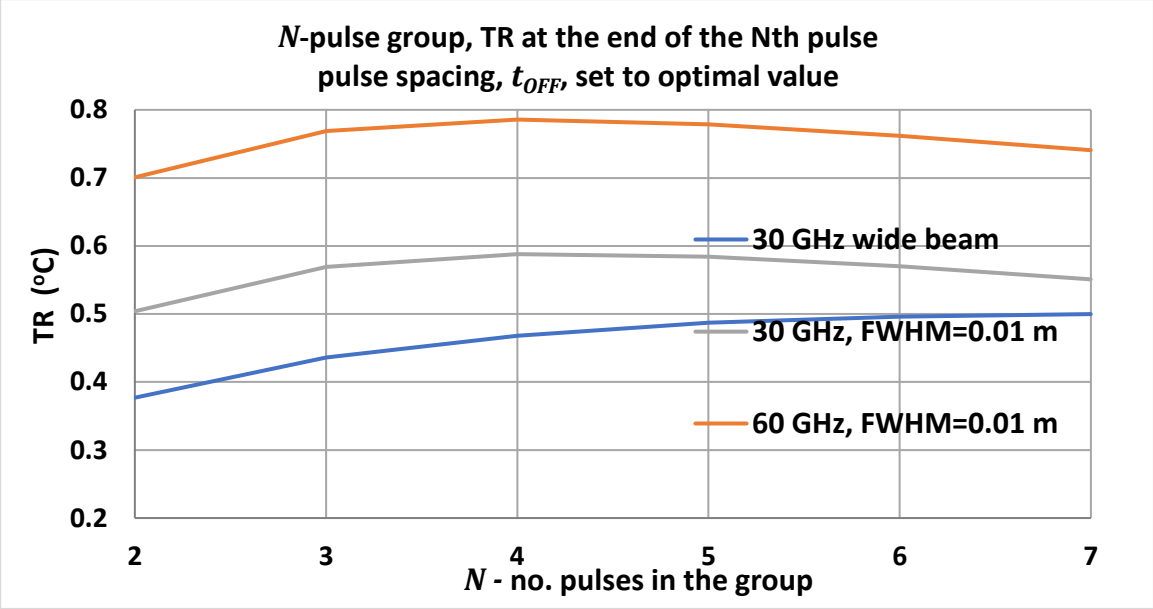

Fig. D.7.5, Optimal TR (in the sense that it maximizes TR) of a *N*-pulse group for the 3-tissue model vs number of pulses. Pulse spacing is set to the optimum value given by eqn (D.7.9).

D.7.4 Discussion: Test of ICNIRP (2020) Table 3 - Note 5

60 GHz / FWHM=0.01m / 1 cm² spatial average / t_{ON} = 1 s:

The worst-case (optimal) TR for this example occurs for a 4-pulse group with a t_{OFF} = 15 s, which yields an optimal TR of 0.79 °C. If the total energy in the 4 pulses were confined to a single pulse, the maximum allowable APD would be:

$$S_{inc,1cm}T_R \leq \frac{360 + 360\sqrt{4}}{4} = 270\ \mathrm{W/m^2}$$

For a transmission coefficient of 0.623 and a 1cm² averaging factor of 0.757, the spatial-peak, input power density allowed by the OBR is 270/(0.623*0.757) = 573 W/m². This exposure produces a peak TR of 0.53 °C, which is close to the OAHET goal of 0.5 °C. Thus, the net increase in peak TR of the optimally spaced, 4-pulse group is 0.79/0.53 = 1.50 or 50 %.

30 GHz / FWHM=0.01m / 1 cm² spatial average / t_{ON} = 1 s:

The worst case (optimal) TR is also for a 4-pulse group with a t_{OFF} = 15 s, which yields an optimal TR of 0.59 °C. The spatial-peak, incident power density allowed by the OBR for a single 4 s pulse is 270/(0.484*0.757) = 737 W/m². This exposure produces a peak TR of 0.40 °C, therefore resulting in a net increase in peak TR of 0.59/0.40 = 1.48 or 48 % for the optimally spaced, 4-pulse group.

D.7.5 Conclusion

For isolated, multiple-pulse exposures at the limit determined by the ICNIRP (2020) “Note 5” (embodied in Eq. 5.4), can lead to peak TR that are higher than the TR occurring from an isolated single pulse having an energy density allowed by (Eq. 5.1) or (Eq. 5.2). For the two narrow beam examples, increases in peak TR of up to 50 % are obtained if their energy is divided into multiple pulses and spaced in an optimal fashion. For frequencies and exposure durations that are already at the threshold of conservatism for an isolated single pulse, implementation of the Note 5 procedure could result in significant non-conservatism if the energy is split into multiple pulses.

Appendix E – List of excluded papers from scientific literature analysis in section 4.0

The following papers were excluded from analysis as they were either review papers, editorial or commentary articles or were conducted on cells *in vitro*:

Alekseev SI, Radzievsky AA, Logani MK, Ziskin MC. Millimeter wave dosimetry of human skin. Bioelectromagnetics. 2008 Jan;29(1):65-70.

Alekseev SI, Ziskin MC. Effects of millimeter waves on ionic currents of Lymnaea neurons. Bioelectromagnetics. 1999;20(1):24-33.

Alekseev SI, Ziskin MC, Kochetkova NV, Bolshakov MA. Millimeter waves thermally alter the firing rate of the Lymnaea pacemaker neuron. Bioelectromagnetics. 1997;18(2):89-98.

Alekseev SI, Ziskin MS, Kochetkova NV. Effects of millimeter wavelength electromagnetic radiation on neurons: electrophysiological study. Crit Rev Biomed Eng. 2000;28(5-6):52-9.

Badzhinyan SA, Sayadyan AB, Sarkisyan NK, Grigoryan RM, Gasparyan GG. Lethal effect of electromagnetic radiation of the millimeter wavelength range on cell cultures of chicken embryo. Dokl Biochem Biophys. 2001 Mar-Apr;377:94-5.

Belyaev IY, Kravchenko VG. Resonance effect of low-intensity millimeter waves on the chromatin conformational state of rat thymocytes. Z Naturforsch C J Biosci. 1994 May-Jun;49(5-6):352-8.

Beneduci A. Evaluation of the potential in vitro antiproliferative effects of millimeter waves at some therapeutic frequencies on RPMI 7932 human skin malignant melanoma cells. Cell Biochem Biophys. 2009;55(1):25-32. doi: 10.1007/s12013-009-9053-8.

Beneduci A, Chidichimo G, Tripepi S, Perrotta E, Cufone F. Antiproliferative effect of millimeter radiation on human erythromyeloid leukemia cell line K562 in culture: ultrastructural- and metabolic-induced changes. Bioelectrochemistry. 2007 May;70(2):214-20.

Beneduci A, Chidichimo G, De Rose R, Filippelli L, Straface SV, Venuta S. Frequency and irradiation time-dependant antiproliferative effect of low-power millimeter waves on RPMI 7932 human melanoma cell line. Anticancer Res. 2005 Mar-Apr;25(2A):1023-8.

Beneduci A, Chidichimo G, Tripepi S, Perrotta E. Transmission electron microscopy study of the effects produced by wide-band low-power millimeter waves on MCF-7 human breast cancer cells in culture. Anticancer Res. 2005 Mar-Apr;25(2A):1009-13.

Berteaud AJ, Dardalhon M, Rebeyrotte N, Averbeck D. [The effect of electromagnetic radiation of wavelength in the millimeter range on bacterial growth]. C R Acad Hebd Seances Acad Sci D. 1975 Sep 22;281(12):843-6.

Betzalel N, Feldman Y, Ishai PB. 2017. The Modeling of the Absorbance of Sub-THz Radiation by Human Skin. IEEE Transactions on Terahertz Science and Technology, 7, 521-528.

Betzalel N; Ben Ishai P; Feldman Y; The human skin as a sub-THz receiver - Does 5G pose a danger to it or not?.Environmental Research. 2018 163:208-216.

Bush LG, Hill DW, Riazi A, Stensaas LJ, Partlow LM, Gandhi OP. Effects of millimeter-wave radiation on monolayer cell cultures. III. A search for frequency-specific athermal biological effects on protein synthesis. Bioelectromagnetics. 1981;2(2):151-9.

Bushberg JT, Chou CK, Foster KR, Kavet R, Maxson DP, Tell RA, Ziskin MC. IEEE Committee on Man and Radiation-COMAR Technical Information Statement: Health and Safety Issues Concerning Exposure of the General Public to Electromagnetic Energy from 5G Wireless Communications Networks. Health Phys. 2020 Jun 22. doi: 10.1097/HP.0000000000001301.

Carrasco E, Colombi D, Foster KR, Ziskin M, Balzano Q. Exposure Assessment of Portable Wireless Devices Above 6 GHz. Radiat Prot Dosimetry. 2019 Jun 1;183(4):488-495. doi: 10.1093/rpd/ncy177.

Chemeris NK, Gapeyev AB, Sirota NP, Gudkova OY, Tankanag AV, Konovalov IV, Buzoverya ME, Suvorov VG, Logunov VA. Lack of direct DNA damage in human blood leukocytes and lymphocytes after in vitro exposure to high power microwave pulses. Bioelectromagnetics. 2006 Apr;27(3):197-203.

Chemeris NK, Gapeyev AB, Sirota NP, Gudkova OY, Kornienko NV, Tankanag AV, Konovalov IV, Buzoverya ME, Suvorov VG, Logunov VA. DNA damage in frog erythrocytes after in vitro exposure to a high peak-power pulsed electromagnetic field. Mutat Res. 2004 Mar 14;558(1-2):27-34.

Chen Q, Zeng QL, Lu DQ, Chiang H. Millimeter wave exposure reverses TPA suppression of gap junction intercellular communication in HaCaT human keratinocytes. Bioelectromagnetics. 2004 Jan;25(1):1-4.

Chidichimo G, Beneduci A, Nicoletta M, Critelli M, De Rose R, Tkatchenko Y, Abonante S, Tripepi S, Perrotta E. Selective inhibition of tumoral cells growth by low power millimeter waves. Anticancer Res. 2002 May-Jun;22(3):1681-8.

Christ A, Samaras T, Neufeld E, Kuster N. RF-induced temperature increase in a stratified model of the skin for plane-wave exposure at 6-100 GHz. Radiat Prot Dosimetry. 2020 Jan 16. pii: ncz293. doi: 10.1093/rpd/ncz293.

Chukova YuP. Reasons of poor replicability of nonthermal bioeffects by millimeter waves. Bioelectrochem Bioenerg. 1999 May;48(2):349-53.

Cohen I, Cahan R, Shani G, Cohen E, Abramovich A. Effect of 99 GHz continuous millimeter wave electro-magnetic radiation on E. coli viability and metabolic activity. Int J Radiat Biol. 2010 May;86(5):390-9.

Colombi D, Thors B, Törnevik C, Balzano Q. RF Energy Absorption by Biological Tissues in Close Proximity to mmW 5G Wireless Equipment. IEEE Access 6: 4974 - 4981.

Colombi D, Thors B, Törnevik C. Implications of EMF Exposure Limits on Output Power Levels for 5G Devices Above 6 GHz. 2015. Implications of EMF Exposure Limits on Output Power Levels for 5G Devices Above 6 GHz 14:1247 – 1249.

Crouzier D, Perrin A, Torres G, Dabouis V, Debouzy JC. Pulsed electromagnetic field at 9.71 GHz increase free radical production in yeast (Saccharomyces cerevisiae). Pathol Biol (Paris). 2009 May;57(3):245-51.

De Amicis A, Sanctis SD, Cristofaro SD, Franchini V, Lista F, Regalbuto E, Giovenale E, Gallerano GP, Nenzi P, Bei R, Fantini M, Benvenuto M, Masuelli L, Coluzzi E, Cicia C, Sgura A. Biological effects of in vitro THz radiation exposure in human foetal fibroblasts. Mutat Res Genet Toxicol Environ Mutagen. 2015 Nov;793:150-60.

Debouzy JC, Crouzier D, Dabouis V, Malabiau R, Bachelet C, Perrin A. [Biologic effects of millimeteric waves (94 GHz). Are there long term consequences?]. Pathol Biol (Paris). 2007 Jun;55(5):246-55.
.
Di Ciaula A. Towards 5G communication systems: Are there health implications? Int J Hyg Environ Health. 2018 Apr;221(3):367-375. doi: 10.1016/j.ijheh.2018.01.011.

Donato A, Ceci P, Cannavo A, Tomei F, Naro F. Low power microwave interaction with phospholipase C and D signal transduction pathways in myogenic cells. Cell Biol Int. 2004;28(10):683-8.

Foster KR, Ziskin MC, Balzano Q, Hirata A. Thermal Analysis of Averaging Times in Radiofrequency Exposure Limits Above 1 GHz. 2018. IEEE Access PP(99):1-1 , DOI: 10.1109/ACCESS.2018.2883175

Foster KR, Ziskin MC, Balzano Q. Comments on Betzalel et al. "The human skin as a sub-THz receiver-Does 5G pose a danger to it or not?" Environ Res. 2020 Apr;183:109008. doi: 10.1016/j.envres.2019.109008.

Foster KR. Comments on Neufeld and Kuster, "Systematic Derivation of Safety Limits for Time-varying 5G Radiofrequency Exposure Based on Analytical Models and Thermal Dose". Health Phys. 2019 Jul;117(1):67-69.

Foster KR, Ziskin MC, Balzano Q. Thermal Modeling for the Next Generation of Radiofrequency Exposure Limits: Commentary. Health Phys. 2017 Jul;113(1):41-53.

Foster KR, Ziskin MC, Balzano Q. Thermal Response of Human Skin to Microwave Energy: A Critical Review. Health Phys. 2016 Dec;111(6):528-541.

Franchini V, Regalbuto E, De Amicis A, De Sanctis S, Di Cristofaro S, Coluzzi E, Marinaccio J, Sgura A, Ceccuzzi S, Doria A, Gallerano GP, Giovenale E, Ravera GL, Bei R, Benvenuto M, Modesti A, Masuelli L, Lista F. Genotoxic Effects in Human Fibroblasts Exposed to Microwave Radiation. Health Phys. 2018 Jul;115(1):126-139.

Franchini V, De Sanctis S, Marinaccio J, De Amicis A, Coluzzi E, Di Cristofaro S, Lista F, Regalbuto E, Doria A, Giovenale E, Gallerano GP, Bei R, Benvenuto M, Masuelli L, Udroiu I, Sgura A. Study of the effects of 0.15 terahertz radiation on genome integrity of adult fibroblasts. Environ Mol Mutagen. 2018 Jul;59(6):476-487.

Funahashi D, Hirata A, Kodera S, Foster K. Area-averaged transmitted power density at skin surface as metric to estimate surface temperature elevation. IEEE Access, 2018, Volume 6: 77665-77674.

Gajda GB, Lemay E, Paradis J. Model of Steady-state Temperature Rise in Multilayer Tissues Due to Narrow-beam Millimeter-wave Radiofrequency Field Exposure. Health Phys. 2019 Sep;117(3):254-266.

Gapeyev AB, Lukyanova NA. Pulse-modulated extremely high-frequency electromagnetic radiation protects cellular DNA from the damaging effects of physical and chemical factors in vitro. Biophysics 2015; 60 (5): 732-738.

Gapeyev AB, Lukyanova NA, Gudkov SV. Hydrogen peroxide induced by modulated electromagnetic radiation protects the cells from DNA damage. Central European Journal of Biology. (2014) 9(10): 915-921.

Gapeyev AB, Safronova VG, Chemeris NK, Fesenko EE. Inhibition of the production of reactive oxygen species in mouse peritoneal neutrophils by millimeter wave radiation in the near and far field zones of the radiator. Bioelectrochemistry and Bioenergetics. 1997; 43(2): 217-220.

Gapeyev AB, Chemeris NK. Model analysis of nonlinear modification of neutrophil calcium homeostasis under the influence of modulated electromagnetic radiation of extremely high frequencies. J Biol Phys. 1999 Jun;25(2-3):193-209.

Geletyuk VI, Kazachenko VN, Chemeris NK, Fesenko EE. Dual effects of microwaves on single Ca(2+)-activated K+ channels in cultured kidney cells Vero. FEBS Lett. 1995 Feb 6;359(1):85-8.

Glushkova OV, Khrenov MO, Novoselova TV, Lunin SM, Parfenyuk SB, Alekseev SI, Fesenko EE, Novoselova EG. The role of the NF-κB, SAPK/JNK, and TLR4 signalling pathways in the responses of RAW 264.7 cells to extremely low-intensity microwaves. Int J Radiat Biol. 2015 Apr;91(4):321-8.

Grundler W, Keilmann F. Nonthermal effects of millimeter microwaves on yeast growth. Z Naturforsch C. 1978 Jan-Feb;33(1-2):15-22.

Guraliuc AR, Zhadobov M, Sauleau R, Marnat L, Dussopt L. Near-Field User Exposure in Forthcoming 5G Scenarios in the 60-GHz Band. IEEE Trans Antennas Propag 2017. doi:10.1109/TAP.2017.2754473

Haas AJ, Le Page Y, Zhadobov M, Boriskin A, Sauleau R, Le Dréan Y. Impact of 60-GHz millimeter waves on stress and pain-related protein expression in differentiating neuron-like cells. Bioelectromagnetics. 2016 Oct;37(7):444-54.

Haas AJ, Le Page Y, Zhadobov M, Sauleau R, Dréan YL, Saligaut C. Effect of acute millimeter wave exposure on dopamine metabolism of NGF-treated PC12 cells.J Radiat Res. 2017 Jul 1;58(4):439-445.

Haas AJ, Le Page Y, Zhadobov M, Sauleau R, Le Dréan Y. Effects of 60-GHz millimeter waves on neurite outgrowth in PC12 cells using high-content screening. Neurosci Lett. 2016 Apr 8;618:58-65.

Habauzit D, Le Quément C, Zhadobov M, Martin C, Aubry M, Sauleau R, Le Dréan Y. Transcriptome analysis reveals the contribution of thermal and the specific effects in cellular response to millimeter wave exposure. PLoS One. 2014 Oct 10;9(10):e109435.

Hadjiloucas S, Chahal MS, Bowen JW. Preliminary results on the non-thermal effects of 200-350 GHz radiation on the growth rate of S. cerevisiae cells in microcolonies. Phys Med Biol. 2002 Nov 7;47(21):3831-9.

Hansteen IL, Lageide L, Clausen KO, Haugan V, Svendsen M, Eriksen JG, Skiaker R, Hauger E, Vistnes AI, Kure EH. Cytogenetic effects of 18.0 and 16.5 GHz microwave radiation on human lymphocytes in vitro. Anticancer Res. 2009 Aug;29(8):2885-92.

Hardell L, Nyberg R. Appeals that matter or not on a moratorium on the deployment of the fifth generation, 5G, for microwave radiation. Mol Clin Oncol. 2020 Mar;12(3):247-257.

Hashimoto Y, Hirata A, Morimoto R, Aonuma S, Laakso I, Jokela K, Foster KR. On the averaging area for incident power density for human exposure limits at frequencies over 6 GHz. Phys Med Biol. 2017 Apr 21;62(8):3124-3138.

He W, Xu B, Gustafsson M, Ying Z, He S. RF Compliance Study of Temperature Elevation in Human Head Model Around 28 GHz for 5G User Equipment Application: Simulation Analysis. IEEE Access. 2017 DOI: 10.1109/ACCESS.2017.2776145

Hintzsche H, Jastrow C, Kleine-Ostmann T, KÃ¤rst U, Schrader T, Stopper H. Terahertz electromagnetic fields (0.106 THz) do not induce manifest genomic damage in vitro. PLoS One. 2012;7(9):e46397. doi: 10.1371/journal.pone.0046397.

Hintzsche H, Jastrow C, Kleine-Ostmann T, Stopper H, Schmid E, Schrader T. Terahertz radiation induces spindle disturbances in human-hamster hybrid cells. Radiat Res. 2011 May;175(5):569-74.

Hirata A, Funahashi D, Kodera S. Setting exposure guidelines and product safety standards for radio-frequency exposure at frequencies above 6 GHz: brief review. Annals of Telecommunications (2019) 74:17–24.

Hovnanyan K, Kalantaryan V, Trchounian A. The distinguishing effects of low intensity electromagnetic radiation of different extremely high frequences on Enterococcus hirae: growth rate inhibition and scanning electron microscopy analysis. Lett Appl Microbiol. 2017 Sep;65(3):220-225.

Kanezaki A, Hirata A, Watanabe S, Shirai H. Effects of dielectric permittivities on skin heating due to millimeter wave exposure. Biomed Eng Online. 2009 Sep 23;8:20. doi: 10.1186/1475-925X-8-20.

Karaca E, Durmaz B, Aktug H, Yildiz T, Guducu C, Irgi M, Koksal MG, Ozkinay F, Gunduz C, Cogulu O. The genotoxic effect of radiofrequency waves on mouse brain. J Neurooncol. 2012 Jan;106(1):53-8.

Karampatzakis A, Samaras T. Numerical modeling of heat and mass transfer in the human eye under millimeter wave exposure. Bioelectromagnetics. 2013 May;34(4):291-9.

Keller H. On the Assessment of Human Exposure to Electromagnetic Fields Transmitted by 5G NR Base Stations. Health Phys. 2019 Nov;117(5):541-545.

Khadir Fall A, Lemoine C, Besnier P, Sauleau R, Le Dréan Y, Zhadobov M. Exposure Assessment in Millimeter-Wave Reverberation Chamber Using Murine Phantoms. Bioelectromagnetics. 2020 Feb;41(2):121-135.

Kodera S, Hirata A, Funahashi D, Watanabe S, Jokela K, Croft RJ. Temperature Rise for Brief Radio-Frequency Exposure Below 6 GHz. IEEE Access 2018 6:65737 - 65746.

Kodera S, Hirata A. Comparison of Thermal Response for RF Exposure in Human and Rat Models. Int J Environ Res Public Health. 2018 Oct 22;15(10). pii: E2320. doi: 10.3390/ijerph15102320.

Kodera S, Gomez-Tames J, Hirata A. Temperature elevation in the human brain and skin with thermoregulation during exposure to RF energy. Biomed Eng Online 17 (1): 1

Kodera S, Gomez-Tames J, Hirata A, Masuda H, Arima T, Watanabe S. Multiphysics and Thermal Response Models to Improve Accuracy of Local Temperature Estimation in Rat Cortex under Microwave Exposure. Int J Environ Res Public Health. 2017 Mar 30;14(4).

Korenstein-Ilan A, Barbul A, Hasin P, Eliran A, Gover A, Korenstein R. Terahertz radiation increases genomic instability in human lymphocytes. Radiat Res. 2008 Aug;170(2):224-34.

Kostoff RN, Heroux P, Aschner M, Tsatsakis A. Adverse Health Effects of 5G Mobile Networking Technology Under Real-Life Conditions. Toxicol Lett. 2020 Jan 25. pii: S0378-4274(20)30028-X. doi: 10.1016/j.toxlet.2020.01.020.

Koyama S, Narita E, Suzuki Y, Shiina T, Taki M, Shinohara N, Miyakoshi J. Long-term exposure to a 40-GHz electromagnetic field does not affect genotoxicity or heat shock protein expression in HCE-T or SRA01/04 cells. J Radiat Res. 2019 Jul 1;60(4):417-423.

Koyama S, Narita E, Shimizu Y, Suzuki Y, Shiina T, Taki M, Shinohara N, Miyakoshi J. Effects of Long-Term Exposure to 60 GHz Millimeter-Wavelength Radiation on the Genotoxicity and Heat Shock Protein (Hsp) Expression of Cells Derived from Human Eye. Int J Environ Res Public Health. 2016 Aug 8;13(8). pii: E802. doi: 10.3390/ijerph13080802.

Laakso I, Morimoto R, Heinonen J, Jokela K, Hirata A. Human exposure to pulsed fields in the frequency range from 6 to 100 GHz. Phys Med Biol. 2017 Aug 9;62(17):6980-6992.

Le Quément C, Nicolaz CN, Habauzit D, Zhadobov M, Sauleau R, Le Dréan Y. Impact of 60-GHz millimeter waves and corresponding heat effect on endoplasmic reticulum stress sensor gene expression. Bioelectromagnetics. 2014 Sep;35(6):444-51.

Le Quément C, Nicolas Nicolaz C, Zhadobov M, Desmots F, Sauleau R, Aubry M, Michel D, Le Dréan Y. Whole-genome expression analysis in primary human keratinocyte cell cultures exposed to 60 GHz radiation. Bioelectromagnetics. 2012 Feb;33(2):147-58.

Leduc C, Zhadobov M. Thermal Model of Electromagnetic Skin-Equivalent Phantom at Millimeter Waves. IEEE Trans Microw Theory Tech 2017. doi:10.1109/TMTT.2016.2638816.

Li K, Sasaki K, Watanabe S, Shirai H. Relationship between power density and surface temperature elevation for human skin exposure to electromagnetic waves with oblique incidence angle from 6 GHz to 1 THz. Phys Med Biol. 2019 Mar 14;64(6):065016.

Li X, Liu C, Liang W, Ye H, Chen W, Lin R, Li Z, Liu X, Wu M. Millimeter wave promotes the synthesis of extracellular matrix and the proliferation of chondrocyte by regulating the voltage-gated K+ channel. J Bone Miner Metab. 2014 Jul;32(4):367-77.

Li X, Ye H, Yu F, Cai L, Li H, Chen J, Wu M, Chen W, Lin R, Li Z, Zheng C, Xu H, Wu G, Liu X. Millimeter wave treatment promotes chondrocyte proliferation via G1/S cell cycle transition. Int J Mol Med. 2012 May;29(5):823-31.

Li X, Ye H, Cai L, Yu F, Chen W, Lin R, Zheng C, Xu H, Ye J, Wu G, Liu X. Millimeter wave radiation induces apoptosis via affecting the ratio of Bax/Bcl-2 in SW1353 human chondrosarcoma cells. Oncol Rep. 2012 Mar;27(3):664-72.

Li X, Wu G, Wu M, Chen W, Liu X. In vitro study of inhibitory millimeter wave treatment effects on the TNF-α-induced NF-κB signal transduction pathway. Int J Mol Med. 2011 Jan;27(1):71-8.

Li X, Du M, Liu X, Chen W, Wu M, Lin J, Wu G. Millimeter wave treatment promotes chondrocyte proliferation by upregulating the expression of cyclin-dependent kinase 2 and cyclin A. Int J Mol Med 26: 77-84, 2010.

Li X, Du M, Liu X, Wu M, Ye H, Lin J, Chen W, Wu G. Millimeter wave treatment inhibits NO-induced apoptosis of chondrocytes through the p38MAPK pathway. Int J Mol Med. 2010 Mar;25(3):393-9.

McClelland S 3rd, Jaboin JJ. The Radiation Safety of 5G Wi-Fi: Reassuring or Russian Roulette? Int J Radiat Oncol Biol Phys. 2018 Aug 1;101(5):1274-1275. doi: 10.1016/j.ijrobp.2018.04.051.

Morimoto R, Hirata A, Laakso I, Ziskin MC, Foster KR. Time constants for temperature elevation in human models exposed to dipole antennas and beams in the frequency range from 1 to 30 GHz. Phys Med Biol. 2017 Mar 7;62(5):1676-1699.

Nakae T, Funahashi D, Higashiyama J, Onishi T, Hirata A. Skin Temperature Elevation for Incident Power Densities from Dipole Arrays at 28 GHz. IEEE Access. 2020. (IN PRESS)

Narinyan L, Ayrapetyan S. Cyclic AMP-dependent signaling system is a primary metabolic target for non-thermal effect of microwaves on heart muscle hydration. Electromagn Biol Med. 2017;36(2):182-191.

Nasim I, Kim S. Mitigation of human EMF exposure in downlink of 5G. Ann Telecommun 2019; 74 (1-2): 45–52.

Natarajan M, Vijayalaxmi, Szilagyi M, Roldan FN, Meltz ML. NF-kappaB DNA-binding activity after high peak power pulsed microwave (8.2 GHz) exposure of normal human monocytes. Bioelectromagnetics. 2002 May;23(4):271-7.

National Research Council (US) Committee to Assess Potential Health Effects from Exposures to PAVE PAWS Low-Level Phased Array Radiofrequency Energy. Assessment of Potential Health Effects from

Exposure to PAVE PAWS Low-Level Phased Array Radiofrequency Energy: Letter Report. Washington (DC): National Academies Press (US); 2002.

Neufeld E, Samaras T, Kuster N. Discussion on Spatial and Time Averaging Restrictions Within the Electromagnetic Exposure Safety Framework in the Frequency Range Above 6 GHz for Pulsed and Localized Exposures. Bioelectromagnetics. 2019 Dec 30. doi: 10.1002/bem.22244.

Neufeld E, Kuster N. Response to Professor Foster's Comments. Health Phys. 2019 Jul;117(1):70-71. doi: 10.1097/HP.0000000000001091.

Neufeld E, Carrasco E, Murbach M, Balzano Q, Christ A, Kuster N. Theoretical and numerical assessment of maximally allowable power-density averaging area for conservative electromagnetic exposure assessment above 6 GHz. Bioelectromagnetics. 2018 Dec;39(8):617-630.

Neufeld E, Kuster N. Systematic Derivation of Safety Limits for Time-Varying 5G Radiofrequency Exposure Based on Analytical Models and Thermal Dose. Health Phys. 2018 Sep 21. doi: 10.1097/HP.0000000000000930

Neufeld E, Samaras T, Kuster N. Response to Enders' Comment on "Discussion on Spatial and Time Averaging Restrictions Within the Electromagnetic Exposure Safety Framework in the Frequency Range Above 6 GHz for Pulsed and Localized Exposures". Bioelectromagnetics. 2020 Jun 26. doi: 10.1002/bem.22279.

Nguyen TH, Shamis Y, Croft RJ, Wood A, McIntosh RL, Crawford RJ, Ivanova EP. 18 GHz electromagnetic field induces permeability of Gram-positive cocci. Sci Rep. 2015 Jun 16;5:10980. doi: 10.1038/srep10980. Erratum in: Sci Rep. 2015;5:13507.

Nguyen THP, Pham VTH, Baulin V, Croft RJ, Crawford RJ, Ivanova EP. The effect of a high frequency electromagnetic field in the microwave range on red blood cells. Sci Rep. 2017 Sep 7;7(1):10798.

Nicolaz CN, Zhadobov M, Desmots F, Ansart A, Sauleau R, Thouroude D, Michel D, Le Drean Y. Study of narrow band millimeter-wave potential interactions with endoplasmic reticulum stress sensor genes. Bioelectromagnetics. 2009 Jul;30(5):365-73.

Nicolas Nicolaz C, Zhadobov M, Desmots F, Sauleau R, Thouroude D, Michel D, Le Drean Y. Absence of direct effect of low-power millimeter-wave radiation at 60.4 GHz on endoplasmic reticulum stress. Cell Biol Toxicol. 2009 Oct;25(5):471-8.

Orlacchio R, Le Page Y, Le Dréan Y, Le Guével R, Sauleau R, Alekseev S, Zhadobov M. Millimeter-wave pulsed heating in vitro: cell mortality and heat shock response. Sci Rep. 2019 Oct 24;9(1):15249.

Owda AY, Salmon N, Casson AJ, Owda M. The Reflectance of Human Skin in the Millimeter-Wave Band. Sensors (Basel). 2020 Mar 8;20(5). pii: E1480. doi: 10.3390/s20051480.

Pakhomov AG, Prol HK, Mathur SP, Akyel Y, Campbell CBGBG. Role of field intensity in the biological effectiveness of millimeter waves at a resonance frequency. Bioelectrochem. Bioenerg. 1997, 43, 27–33.

Pakhomov AG, Doyle J, Stuck BE, Murphy MR. Effects of high power microwave pulses on synaptic transmission and long term potentiation in hippocampus. Bioelectromagnetics. 2003 Apr;24(3):174-81.

Pakhomov AG, Gajsek P, Allen L, Stuck BE, Murphy MR. Comparison of dose dependences for bioeffects of continuous-wave and high-peak power microwave emissions using gel-suspended cell cultures. Bioelectromagnetics. 2002 Feb;23(2):158-67.

Pakhomov AG, Prol HK, Mathur SP, Akyel Y, Campbell CB. Search for frequency-specific effects of millimeter-wave radiation on isolated nerve function. Bioelectromagnetics. 1997;18(4):324-34.

Pakhomov AG, Mathur SP, Doyle J, Stuck BE, Kiel JL, Murphy MR. Comparative effects of extremely high power microwave pulses and a brief CW irradiation on pacemaker function in isolated frog heart slices. Bioelectromagnetics. 2000 May;21(4):245-54.

Partlow LM, Bush LG, Stensaas LJ, Hill DW, Riazi A, Gandhi OP. Effects of millimeter-wave radiation on monolayer cell cultures. I. Design and validation of a novel exposure system. Bioelectromagnetics. 1981;2(2):123-40.

Pawlak R, Krawiec P, Żurek J. (2019). On Measuring Electromagnetic Fields in 5G Technology. IEEE Access, 7, 29826-29835.

Perera PGT; Nguyen THP; Dekiwadia C; Wandiyanto JV; Sbarski I; Bazaka O; Bazaka K; Crawford RJ; Croft RJ; Ivanova EP. Exposure to high-frequency electromagnetic field triggers rapid uptake of large nanosphere clusters by pheochromocytoma cells. International Journal of Nanomedicine. 13:8429-8442, 2018.

Pfeifer S, Carrusco E, Crespo-Valero P, Neufeld E, Kuhn S, Samaras T, Capstick M, Christ A, Kuster N. Total field reconstruction in the near-field using pseudo-vector e-field measurements. IEEE Trans. Electromag. Compat. 2018, DOI: 10.1109/TEMC.2018.2837897

Pikov V, Arakaki X, Harrington M, Fraser SE, Siegel PH. Modulation of neuronal activity and plasma membrane properties with low-power millimeter waves in organotypic cortical slices. J Neural Eng. 2010 Aug;7(4):045003.

Ramundo-Orlando A. Effects of Millimeter Waves Radiation on Cell Membrane - A Brief Review. 2010. J Infrared Milli Terahz Waves 31:1400–1411.

Romanenko S, Siegel PH, Wagenaar DA, Pikov V. Effects of millimeter wave irradiation and equivalent thermal heating on the activity of individual neurons in the leech ganglion. J Neurophysiol. 2014 Nov 15;112(10):2423-31.

Russell CL. 5 G wireless telecommunications expansion: Public health and environmental implications. Environ Res. 2018 Apr 11. pii: S0013-9351(18)30016-1. doi: 10.1016/j.envres.2018.01.016.

Ryan KL, D'Andrea JA, Jauchem JR, Mason PA. Radio frequency radiation of millimeter wave length: potential occupational safety issues relating to surface heating. Health Phys. 2000 Feb;78(2):170-81.

Safronova VG, Gabdoulkhakova AG, Santalov BF. Immunomodulating action of low intensity millimeter waves on primed neutrophils. Bioelectromagnetics. 2002 Dec;23(8):599-606.

Samsonov A, Popov SV. The effect of a 94 GHz electromagnetic field on neuronal microtubules. Bioelectromagnetics. 2013 Feb;34(2):133-44.

Sarapultseva EI, Igolkina JV, Tikhonov VN, Dubrova YE. The in vivo effects of low-intensity radiofrequency fields on the motor activity of protozoa. Int J Radiat Biol. 2014 Mar;90(3):262-7.

Sasaki K, Mizuno M, Wake K, Watanabe S. Monte Carlo simulations of skin exposure to electromagnetic field from 10 GHz to 1 THz. Phys Med Biol. 2017 Aug 9;62(17):6993-7010.

Sasaki K, Wake K, Watanabe S. Measurement of the dielectric properties of the epidermis and dermis at frequencies from 0.5 GHz to 110 GHz. Phys Med Biol. 2014 Aug 21;59(16):4739-47.

Sasaki K, Isimura Y, Fujii K, Wake K, Watanabe S, Kojima M, Suga R, Hashimoto O. Dielectric property measurement of ocular tissues up to 110 GHz using 1 mm coaxial sensor. Phys Med Biol. 2015 60(16):6273-88.

Scarfi MR, Lioi MB, D'Ambrosio G, Massa R, Zeni O, Di Pietro R, Di Berardino D. Genotoxic effects of mitomycin-C and microwave radiation on bovine lymphocytes. Electromagnetic Biology and Medicine 15(2): 99-107.

Seaman RL. Effects of exposure of animals to ultra-wideband pulses. Health Phys. 2007 Jun;92(6):629-34.

Shafirstein G, Moros EG. Modelling millimetre wave propagation and absorption in a high resolution skin model: the effect of sweat glands. Phys Med Biol. 2011 Mar 7;56(5):1329-39.

Shamis Y, Taube A, Mitik-Dineva N, Croft R, Crawford RJ, Ivanova EP. Specific electromagnetic effects of microwave radiation on Escherichia coli. Appl Environ Microbiol. 2011 May;77(9):3017-22.

Shapiro MG, Priest MF, Siegel PH, Bezanilla F. Thermal mechanisms of millimeter wave stimulation of excitable cells. Biophys J. 2013 Jun 18;104(12):2622-8.

Sharaf MH, Zaki AI, Hamad RK, Omar MMM. A Novel Dual-Band (38/60 GHz) Patch Antenna for 5G Mobile Handsets. Sensors (Basel). 2020 Apr 29;20(9). pii: E2541. doi: 10.3390/s20092541.

Shcheglov VS, Alipov ED, Belyaev IY. Cell-to-cell communication in response of E. coli cells at different phases of growth to low-intensity microwaves. Biochim Biophys Acta. 2002 Aug 15;1572(1):101-6.

Shckorbatov YG, Pasiuga VN, Goncharuk EI, Petrenko TP, Grabina VA, Kolchigin NN, Ivanchenko DD, Bykov VN, Dumin OM. Effects of differently polarized microwave radiation on the microscopic structure of the nuclei in human fibroblasts. J Zhejiang Univ Sci B. 2010 Oct;11(10):801-5.

Shckorbatov YG, Pasiuga VN, Kolchigin NN, Grabina VA, Batrakov DO, Kalashnikov VV, Ivanchenko DD, Bykov VN. The influence of differently polarised microwave radiation on chromatin in human cells. Int J Radiat Biol. 2009 Apr;85(4):322-9.

Shckorbatov YG, Grigoryeva NN, Shakhbazov VG, Grabina VA, Bogoslavsky AM. Microwave irradiation influences on the state of human cell nuclei. Bioelectromagnetics. 1998;19(7):414-9.

Sheikh AQ, Taghian T, Hemingway B, Cho H, Kogan AB, Narmoneva DA. Regulation of endothelial MAPK/ERK signalling and capillary morphogenesis by low-amplitude electric field. J R Soc Interface. 2013 Jan 6;10(78):20120548.

Shiina T, Suzuki Y, Sasaki K, Watanabe S, Taki M. High-efficiency applicator based on printed circuit board in millimeter-wave region. IEEE Transactions on Microwave Theory and Techniques. 2015. 63(10): 3311-3318.

Simicevic N. FDTD computation of human eye exposure to ultra-wideband electromagnetic pulses. Phys Med Biol. 2008 Mar 21;53(6):1795-809.

Simkó M, Mattsson MO. 5G Wireless Communication and Health Effects-A Pragmatic Review Based on Available Studies Regarding 6 to 100 GHz. Int J Environ Res Public Health. 2019 Sep 13;16(18). pii: E3406.

Soubere Mahamoud Y, Aite M, Martin C, Zhadobov M, Sauleau R, Le Dréan Y, Habauzit D. Additive Effects of Millimeter Waves and 2-Deoxyglucose Co-Exposure on the Human Keratinocyte Transcriptome. PLoS One. 2016 Aug 16;11(8):e0160810. doi: 10.1371/journal.pone.0160810.

Stensaas LJ, Partlow LM, Bush LG, Iversen PL, Hill DW, Hagmann MJ, Gandhi OP. Effects of millimeter-wave radiation on monolayer cell cultures. II. Scanning and transmission electron microscopy. Bioelectromagnetics. 1981;2(2):141-50.

Sun S, Titushkin I, Varner J, Cho M. Millimeter wave-induced modulation of calcium dynamics in an engineered skin co-culture model: role of secreted ATP on calcium spiking. J Radiat Res. 2012;53(2):159-67.

Szabo I, Kappelmayer J, Alekseev SI, Ziskin MC. Millimeter wave induced reversible externalization of phosphatidylserine molecules in cells exposed in vitro. Bioelectromagnetics. 2006 Apr;27(3):233-44.

Szabo I, Manning MR, Radzievsky AA, Wetzel MA, Rogers TJ, Ziskin MC. Low power millimeter wave irradiation exerts no harmful effect on human keratinocytes in vitro. Bioelectromagnetics. 2003 Apr;24(3):165-73.

Szabo I, Rojavin MA, Rogers TJ, Ziskin MC. Reactions of keratinocytes to in vitro millimeter wave exposure. Bioelectromagnetics. 2001 Jul;22(5):358-64.

Tadevosyan H, Kalantaryan V, Trchounian A. Extremely high frequency electromagnetic radiation enforces bacterial effects of inhibitors and antibiotics. Cell Biochem Biophys. 2008;51(2-3):97-103.

Thielens A, Martens L, Joseph W. Can body-worn devices be used for measuring personal exposure to mm waves? Bioelectromagnetics. 2017 Apr;38(3):239-242.

Thors B, Colombi D, Ying Z, Bolin T, Tornevik C. Exposure to RF EMF from Array Antennas in 5G Mobile Communication Equipment. IEEE Access 2016; DOI: 10.1109/ACCESS.2016.2601145

Thors B, Furuskär A, Colombi D, Törnevik C. (2017). Time-Averaged Realistic Maximum Power Levels for the Assessment of Radio Frequency Exposure for 5G Radio Base Stations Using Massive MIMO. IEEE Access, 5, 19711-19719.

Titushkin IA, Rao VS, Pickard WF, Moros EG, Shafirstein G, Cho MR. Altered calcium dynamics mediates P19-derived neuron-like cell responses to millimeter-wave radiation. Radiat Res. 2009 Dec;172(6):725-36.

Tong Y, Yang Z, Yang D, Chu H, Qu M, Liu G, Wu Y, Liu S. Millimeter-wave exposure promotes the differentiation of bone marrow stromal cells into cells with a neural phenotype. J Huazhong Univ Sci Technolog Med Sci. 2009 Aug;29(4):409-12.

Torgomyan H, Trchounian A. The enhanced effects of antibiotics irradiated of extremely high frequency electromagnetic field on Escherichia coli growth properties. Cell Biochem Biophys. 2015 Jan;71(1):419-24.

Torgomyan H. Effects of low intensity electromagnetic irradiation of 70.6 and 73 GHz frequencies and antibiotics on energy-dependent proton and potassium ion transport by E. coli. Indian J Biochem Biophys. 2012 Dec;49(6):428-34.

Torgomyan H, Hovnanyan K, Trchounian A. Escherichia coli growth changes by the mediated effects after low-intensity electromagnetic irradiation of extremely high frequencies. Cell Biochem Biophys. 2013 Apr;65(3):445-54.

Torgomyan H, Kalantaryan V, Trchounian A. Low intensity electromagnetic irradiation with 70.6 and 73 GHz frequencies affects Escherichia coli growth and changes water properties. Cell Biochem Biophys. 2011 Jul;60(3):275-81.

Trillo MA, Cid MA, Martínez MA, Page JE, Esteban J, Úbeda A. Cytostatic response of NB69 cells to weak pulse-modulated 2.2 GHz radar-like signals. Bioelectromagnetics. 2011 Jul;32(5):340-50.

Vlasova II, Mikhalchik EV, Gusev AA, Balabushevich NG, Gusev SA, Kazarinov KD. Extremely high-frequency electromagnetic radiation enhances neutrophil response to particulate agonists. Bioelectromagnetics. 2018 Feb;39(2):144-155.

Volkova NA, Pavlovich EV, Gapon AA, Nikolov OT. Effects of millimeter-wave electromagnetic exposure on the morphology and function of human cryopreserved spermatozoa. Bull Exp Biol Med. 2014 Sep;157(5):574-6.

Wu G, Sferra T, Chen X, Chen Y, Wu M, Xu H, Peng J, Liu X. Millimeter wave treatment inhibits the mitochondrion-dependent apoptosis pathway in chondrocytes. Mol Med Rep. 2011 Sep-Oct;4(5):1001-6.

Wu GW, Liu XX, Wu MX, Zhao JY, Chen WL, Lin RH, Lin JM. Experimental study of millimeter wave-induced differentiation of bone marrow mesenchymal stem cells into chondrocytes. Int J Mol Med. 2009 Apr;23(4):461-7.

Wu T, Rappaport TS, Collins CM. Safe for Generations to Come. IEEE microwave magazine. 2015;16(2):65-84.

Xu B, Zhao K, Thors B, Colombi D, Lundberg O, Ying Z, He S. Power Density Measurements at 15 GHz for RF EMF Compliance Assessments of 5G User Equipment. IEEE Trans Antennas Propag 2017.

Xu B, Zhao K, Ying Z, Sjöberg D, He W, He S. (2019). Analysis of Impacts of Expected RF EMF Exposure Restrictions on Peak EIRP of 5G User Equipment at 28 GHz and 39 GHz Bands. IEEE Access, 7, 20996-21005.

Yaekashiwa N, Otsuki S, Hayashi S, Kawase K. Investigation of the non-thermal effects of exposing cells to 70-300 GHz irradiation using a widely tunable source. J Radiat Res 59 (2): 116-121.

Ye Y, Chen Y, Su Y, Zou C, Huang Y, Ou L, Chen R. Raman spectral analysis of nasopharyngeal carcinoma cell line CNE2 after microwave radiation. Biochem Cell Biol. 2013 Apr;91(2):67-71.

Yu G, Coln E, Schoenbach K, Gellerman M, Fox P, Rec L, Beebe S, Liu S. (2002). A study on biological effects of low-intensity millimeter waves. Plasma Science, IEEE Transactions on. 30. 1489 - 1496.

Zeni O, Gallerano GP, Perrotta A, Romano M, Sannino A, Sarti M, D'Arienzo M, Doria A, Giovenale E, Lai A, Messina G, Scarfi MR. Cytogenetic observations in human peripheral blood leukocytes following in vitro exposure to THz radiation: a pilot study. Health Phys. 2007 Apr;92(4):349-57.

Zhadobov M, Sauleau R, Le Drean Y, Alekseev SI, Ziskin MC. Numerical and Experimental millimeter-wave dosimetry for in vitro experiments. IEEE Transactions on Microwave Theory and Techniques. 56:2998-3007.

Zhadobov M, Nicolaz CN, Sauleau R, Desmots F, Thouroude D, Michel D, Dréan Y. (2009). Evaluation of the Potential Biological Effects of the 60-GHz Millimeter Waves Upon Human Cells. Antennas and Propagation, IEEE Transactions on. 57. 2949 - 2956.

Zhadobov M, Alekseev SI, Sauleau R, Le Page Y, Le Dréan Y, Fesenko EE. Microscale temperature and SAR measurements in cell monolayer models exposed to millimeter waves. Bioelectromagnetics. 2017 Jan;38(1):11-21.

Zhadobov M, Alekseev SI, Le Dréan Y, Sauleau R, Fesenko EE. Millimeter waves as a source of selective heating of skin. Bioelectromagnetics. 2015 Sep;36(6):464-75.

Zhadobov M, Sauleau R, Le Coq L, Debure L, Thouroude D, Michel D, Le Dréan Y. Low-power millimeter wave radiations do not alter stress-sensitive gene expression of chaperone proteins. Bioelectromagnetics. 2007 Apr;28(3):188-96.

Zilberti L, Arduino A, Bottauscio O, Chiampi M. Parametric analysis of transient skin heating induced by terahertz radiation. Bioelectromagnetics. 2014 Jul;35(5):314-23.

Ziskin MC, Alekseev SI, Foster KR, Balzano Q. Tissue models for RF exposure evaluation at frequencies above 6 GHz. Bioelectromagnetics. 2018 Apr;39(3):173-189.